

DISSERTATION

Heat Transfer Investigations at the Over-Tip Casing of a High Pressure Turbine Stage – Development of Heat Transfer Correlations

ausgeführt zum Zwecke der Erlangung des akademischen Grades eines Doktors der
technischen Wissenschaften unter Leitung von

ao. Univ.-Prof. Dipl.-Ing. Dr.techn. **Reinhard Willinger**
E302
Institut für Thermodynamik und Energiewandlung

eingereicht an der Technischen Universität Wien

Fakultät für Maschinenwesen und Betriebswissenschaften

von

M.Sc. Bart van Duikeren



Wien, am 20-12-2007

Untersuchung des Wärmeübergangs an Führungsringsegmenten von einer Hochdruckturbinenstufe – Entwicklung Wärmeübergangskorrelationen

Kurzfassung der Dissertation

Die Entwicklung von Gasturbinen zielt – auch unter Berücksichtigung ökonomischer und ökologischer Gesichtspunkte – auf eine kontinuierliche Steigerung von Leistung und Wirkungsgrad. Dabei werden inzwischen Brennkammertemperaturen erreicht, die die zulässigen Materialgrenzwerte weit übersteigen, so dass diese thermisch hoch belasteten Bauteile sehr stark gekühlt werden müssen; dazu gehören neben den Turbinenschaufeln auch der Naben- und Gehäusebereich der ersten Stufen. Bislang wurde insbesondere die aero-thermische Belastung der Gehäusesegmente über rotierenden Laufschaufeln nur unzureichend untersucht und beschrieben. Im vorliegenden Bericht wird zu einem besseren Verständnis der treibenden Phänomene beigetragen.

An einer HD-Turbinenstufe wurden bei verschiedenen Betriebszuständen im Windkanal für rotierende Ringgitter, Göttingen, umfangreiche Messungen im Gehäusebereich über dem Rotor durchgeführt; dazu gehören sowohl zeitgemittelte als auch zeitabhängige Strömungsgrößen, wie z.B. der statische Druck an der Wand, die Wandtemperatur und daraus abgeleitet die Wärmeübergangskoeffizienten sowie Heißfilmmessungen. Außerdem wurde das gehäusenahes Strömungsfeld mit stationärer und instationärer Messtechnik untersucht. Die zur Durchführung der Messungen erforderlichen Sensoren bzw. Einbauten wurden entworfen und gefertigt sowie die notwendigen Auswerteverfahren bereitgestellt.

Aus diesen Messungen konnte eine umfangreiche Datenbasis generiert werden, mit der weiterführende Untersuchungen zum Arbeitsumsatz in Spaltströmungen und zum Wärmeeintrag in Ringsegmenten erfolgten. Die Nusseltkorrelation für die ebene Platte wird auf ihre Anwendung auf die Führungsringsegmente überprüft. Die Korrelation wird dabei um Betriebsparameter erweitert, um die erhöhten Wärmeübergangsniveaus im Teillastfall miteinzubeziehen. Ausserdem wird ein Spaltströmungsmodell eingeführt, dass den Unterschied zwischen dem Wärmeübergang in Passage und Spalt untersucht. Schliesslich wird diskutiert, ob teilungsgemittelte Daten als Eingabedaten für die Nusselt-Korrelation verwendet werden können.

Schlagworte:

Wärmeübergang, Heißfilmmessungen, stationäre und instationäre Druckmessungen, Korrelationen, Turbine, Gehäuse ringsegmente, Thermoelement-Array, Teillast, Nusseltzahl

Heat Transfer Investigations at the Over-Tip Casing of a High Pressure Turbine Stage – Development of Heat Transfer Correlations

Abstract

The development of gas turbines aims to an increase of power and efficiency accounting environmental and economical aspects. Meanwhile combustion temperatures reaches values far above of the acceptable material temperatures. Thus the thermal highly loaded components have to be cooled intensive. These parts includes besides the blades, the platform and the casing of the first stages. Up to now the aero-thermal loading of the over-tip casing above the rotor was investigated poorly. This report contributes to a better understanding of the major phenomena governing the heat flux in the over-tip casing region. Using a HP-turbine at different flow conditions, extended measurements were performed at DLR's wind tunnel for rotating cascades, Göttingen, concerning the flow field above the rotor and close to the over-tip casing.

The data collected include time-averaged as well as time-resolved values as i.e. static pressure at the over-tip casing, wall temperatures and calculated heat flux coefficients, hot-film measurements. Additionally the passage near the casing was investigated using probes (steady and unsteady ones). The sensors and inserts necessary to perform the measurements had to be developed and manufactured; the necessary procedures to evaluate the gained data had to be developed, too.

From these investigations an extended data basis was generated and used to proceed in getting information about work process within the tip gap and about the heat flux into linear segments. The Nusselt correlation for a flat plate is investigated for it's applicability at the over-tip casing. The correlation is enhanced with operating parameters to take the elevated heat transfer levels observed at off-design conditions into account. Additionally a tip leakage model is introduced to examine the difference between heat transfer in the passage and in the gap. Finally differences between time-resolved and pitchwise averaged input data with the flat plate correlation are discussed.

Keywords:

turbine, shroud, over-tip casing, rotating cascade, heat transfer, heat flux, hot-films, steady and unsteady measurements, array of thermocouples, correlation, Nusselt number, off-design

ACKNOWLEDGEMENTS

I would like to express my sincere gratitude to my advisor, Prof. Dipl.-Ing R. Willinger, for interesting me in challenging field of turbomachinery. Without doubt, this thesis profited greatly from his recommendations.

The department of propulsion technology provided an excellent working atmosphere. I am very grateful to Dr.-Ing P.-A. Gieß for giving me the opportunity to carry out this work and for the great confidence put in me.

Special thanks are due to Dipl.-Ing A. Dannhauer not only for many interesting conversations and for his personal support, but also for all his advice throughout the course of this work. I also would like to thank Dr.rer.nat F. Kost for his valuable suggestions.

The conduction of the tests would have been impossible without the thorough technical support of Dipl.-Ing. E. Schüpferling, Mr. A. Tappe and Mr. M. Tanger. I have benefited immensely from their experience.

A special thank you is reserved for my wife Johanna, for her encouragement and support through all these years.

Large portions of the reported investigations were part of the research project "Äußerer Wärmeübergang an Führungsringsegmenten" (AG-Turbo project no. 2.4.11A) lead by Siemens Power Generation, Mülheim, Germany, and supported by MTU Aero Engines, Munich, Germany. The funding of this project (contract no. 032 7090 L) by the Federal Ministry of Education and Research within the national research & development program "AG-Turbo: 500 MW auf einer Welle" is gratefully acknowledged as well as the scientific and technical support given by the industry partners.

CONTENTS

Contents	v
Nomenclature	vii
1 Introduction	1
2 Scientific background	3
2.1 Flow at the over-tip casing	3
2.2 Previous research into over-tip heat transfer study.....	8
2.2.1 Work process in the tip gap.....	13
3 Experimental setup and measurement techniques	16
3.1 The rotating cascade facility at DLR, Göttingen.....	16
3.2 The turbine stage and measurement program.....	17
3.3 Standard RGG instrumentation.....	19
3.4 Over-tip casing instrumentation	20
3.4.1 Thermocouple+ array	20
3.4.2 Pressure measurement system.....	27
3.4.3 Hot-films	31
3.5 Probes for wake measurements	41
3.5.1 Kulite probe	41
4 Experimental results	46
4.1 Tip gap width	46
4.2 Time-mean results	47
4.2.1 Stator results	47
4.2.2 Time-mean pressure distribution	49
4.2.3 Time-mean adiabatic wall temperature	51
4.2.4 Time-mean heat transfer coefficient	52
4.2.5 Time-mean rotor wake results.....	55
4.3 Time-resolved results	57
4.3.1 Normalised pressure distribution	57
4.3.2 Heat transfer distribution	60
4.3.3 Time-resolved wake results.....	61
5 Correlations of heat transfer coefficient at the over-tip casing	65
5.1 Evaluation of the conventional flat plate heat transfer correlation.....	66
5.1.1 Introduction of Nusselt correlations for the flat plate	66
5.1.2 Averaged flow conditions and axial flow direction	66
5.1.3 Averaged flow conditions along the streamlines	69
5.1.4 Variable flow conditions along the streamline	71
5.1.5 Evaluation of the effect of the upstream boundary conditions	73
5.1.6 Effect of stator wake angle deviation.....	75
5.1.7 Comparison of analytical and experimental results	79
5.2 Influences of time-resolved phenomena	84
5.2.1 Relative fluid flow angle deviation	85
5.3 Tip leakage flow.....	87
5.3.1 Isentropic Mach number distribution	88

5.3.2	Tip leakage model.....	91
5.3.3	Relaminarisation of the tip leakage flow.....	95
5.3.4	Heat transfer in the non-rotating passage with compressible flow	96
5.3.5	Heat transfer in the rotating passage with compressible flow	101
5.3.6	Absolute velocity components.....	102
5.3.7	Averaged heat transfer versus tip gap heat transfer	104
5.3.8	Total temperature deviations caused by the work process	105
6	Formation of the correlation	112
6.1	Correlations	112
6.2	Basic correlation	112
6.3	Enhanced correlation.....	123
6.4	Complete enhanced heat transfer correlation for the over-tip casing.....	124
7	Summary and conclusions	134
	List of literature	137
	List of figures.....	141
	List of tables	143
	List of tables	143
APPENDIX A	Overview of operating key-points	144
APPENDIX B	Tip gap width analysis.....	146
APPENDIX C	Pitchwise averaged Adiabatic wall temperature	149
APPENDIX D	Time-resolved static pressure	151
APPENDIX E	Time-resolved heat transfer	154
APPENDIX F	Calculation of the streamlines path.....	156
APPENDIX G	Isentropic fluid properties.....	157

NOMENCLATURE

Latin Symbols

a	Overheat-ratio	$[-]$
A	Area	$[m^2]$
b	Parabolic coefficient	$[-]$
b	Blade span	$[m]$
c	Speed of sound	$[m/s]$
c	Velocity in absolute frame of reference	$[m/s]$
c_p	Specific heat at constant pressure	$[J/kg \cdot K]$
c_*	Friction velocity	$[m/s]$
C_p	Pressure coefficient	$[-]$
D	Rotor diameter	$[m]$
f_{rec}	Recovery factor	$[-]$
f	Frequency	$[Hz]$
h	Heat transfer coefficient	$[W/m^2 \cdot K]$
K	Acceleration parameter	$[-]$
l	Axial chord length	$[m]$
\dot{m}	Mass flow	$[kg/s]$
M	Mach number	$[-]$
n	Rotational speed	$[min^{-1}]$
Nu	Nusselt number	$[-]$
p	Pressure	$[Pa]$
P	Power	$[W]$
Pr	Prandtl number	$[-]$
q	Heat flux	$[W]$
\dot{q}	Specific heat flux	$[W/m^2]$
r	Radius	$[m]$
R	Gas constant	$[J/kg \cdot K]$
R	Electrical Resistance	$[\Omega]$
Re	Reynolds number	$[-]$
Re_τ	Friction velocity Reynolds number	$[-]$
s	Number of blades	$[-]$
Sh	Sherwood number	$[-]$
t	Time	$[s]$
t	Thickness	$[m]$
T	Temperature	$[K]$
u	Circumferential velocity	$[m/s]$

V	Electrical potential	[V]
w	Velocity in relative frame of reference	[m / s]
W	Specific work	[J / kg]
x	Axial coordinate (normalised with the axial chord length)	[-]

Greek Symbols

α	Flow angle in the absolute frame of reference	[$^{\circ}$]
α	Temperature resistance coefficient	[K^{-1}]
β	Flow angle in the relative frame of reference	[$^{\circ}$]
φ	Circumferential coordinate (normalised with the stator pitch)	[-]
γ	Flow angle relative to the rotor blade camber line	[$^{\circ}$]
κ	Ratio of specific heats	[-]
λ	Thermal conductivity	[$W / m \cdot K$]
μ	Viscosity	[$kg / m \cdot s$]
ν	Kinematic viscosity	[m^2 / s]
Π	Pressure ratio	[-]
ρ	Density	[kg / m^3]
τ	Gap height	[m]
τ	Period time	[s]
τ	Shear stress	[N / m^2]

Subscripts

ax	Axial
abs	Absolute
$conv$	Convection
eff	Effective
ps	Pressure side
rel	Relative
ss	Suction side
$tang$	Tangential
0	Total condition
1	Stator entrance
2	Stator outlet
3	Rotor inlet
4	Rotor outlet

1 INTRODUCTION

The world energy demand is estimated to grow by 2.4% per year¹ (Leydon et al. 1996). Although great efforts are made in providing more renewable energy, the gas turbine will remain the workhorse for the next decades. Furthermore in commercial and military aviation, a sector with similar growth potential, the position of gas turbine is even more dominant. For this reason, further improvement of the overall efficiency of the gas turbine will stay a major economical and ecological issue.

From the thermodynamical laws that govern the turbine, it can be concluded that the most effective way of increasing the efficiency is by raising the turbine entrance pressure and temperature. When an effective cooling scheme is implemented, the fluid temperature may be increased by several hundreds of degrees over the material constraints. However, since cooling air is expensive and reduces the overall efficiency and specific power, the air has to be used economically. For this, detailed knowledge of the heat transfer distribution on the affected areas is necessary, so that an improved cooling scheme accounting for any hotspots can be designed.

The part of the casing that is located directly over the rotor, is called the “over-tip casing” and is located closely behind the combustion chamber. The high temperature of the combustion gases in combination with the presence of strong vortices, caused by the periodic passing of the rotor blades, result in a region with a very high heat transfer. The strongly unsteady behaviour of the flow at the over-tip casing puts high demands on the measurement techniques and the windtunnel. Therefore, despite the great potential for saving coolant, the over-tip casing has been excluded from most research so far.

For this reason, the AG-Turbo programme 1.2.4.11A “Heat transfer at the over-tip casing” was funded. The main objectives of the project are:

- 1) Establishing a database for the validation of numerical algorithms.
- 2) Formulation of a correlation for the calculation of the aerodynamical and thermal loading of the over-tip casing.

¹ Fuel Input for Thermal PG between 2000 and 2020 with European Union Conventional Wisdom scenario

The Windtunnel of Rotating Cascades of DLR, Göttingen is ideally suited for comprehensive time-resolved measurement programs. The selected measurement techniques (Van Duikeren 2004b) included both steady (time-averaged) and unsteady (time-resolved) sensors.

The time-averaged data help to predict the hotspots and are therefore valuable information for quality insurance in industry. Additionally the time-resolved measurements will help to understand the nature behind the heat transfer at this highly unsteady region of the turbine. Furthermore the time-resolved data also form a very good benchmark for newly developed CFD tools.

The results are presented in two reports:

- First, the evaluation of steady data and establishing the database for the validation of numerical algorithms was discussed in Van Duikeren (2006). The appendix covers a comprehensive set of experimental data for the complete measurement matrix.
- Second, in this report a correlation for the calculation of the aerodynamical and thermal loading of the over-tip casing will be formulated. Additional time-resolved data is presented which enables the physical interpretation of the fluid phenomena influencing the heat transfer at the over-tip casing. Since in many cases the averaged input data is preferred when using simple correlations, the difference between the usage of time-resolved and pitchwise averaged data with the correlation is investigated.

2 SCIENTIFIC BACKGROUND

2.1 Flow at the over-tip casing

The gap between the blade tip and the over-tip casing has to be wide enough to accommodate the differential thermal expansion between the rotating turbine wheel and the over-tip casing and the elongation of the rotor due to the high centrifugal force. “In practice the gap is about 1% of the blade height for normal size turbines and about 1.5% for smaller turbines” (Metzger et al., 1991).

The gap enables part of the flow to pass from the pressure side to the suction side of the blade without taking part on the work process. This tip leakage flow has significant implications for stage efficiency and heat transfer durability in high-pressure turbines. According to Schaub et al. (1993), 45% of the losses in the rotor and 30% of the losses in the stage can be attributed to the tip leakage flow for a common modern, high-performance, high-pressure turbine stage. A detailed literature review on the studies of the tip leakage flow in axial turbines is provided by Sjolander (1997).

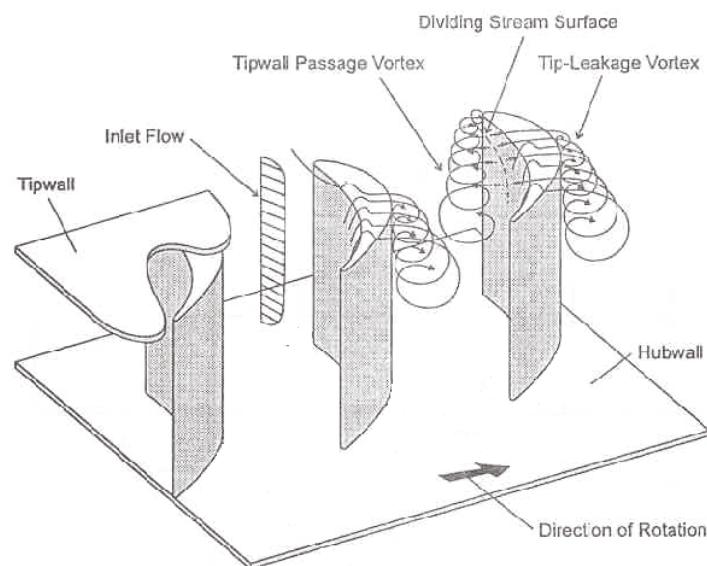


Figure 1: Tip leakage flow (Sjolander, 1997)

Figure 1 shows the main three-dimensional features of the flow in an unshrouded axial-turbine cascade schematically. To avoid unnecessary clutter, the secondary flow at the hub

and the blade wakes have been omitted. The flow at the over-tip casing is dominated by three flow structures:

- Looked upon from the relative frame of reference the biggest part of the over-tip casing is dominated by the tipwall passage vortex. In the passage between any two neighbouring turbine blades of a turbine cascade, a strong longitudinal pressure gradient exists. Additional to this pressure gradient, the flow through the passage is acted upon by a centrifugal force resulting from the curvature of the flow path through the passage. These two forces are in equilibrium:

$$\frac{\partial p}{\partial r} = \frac{dp}{dr} = \frac{\rho c^2}{r} \quad (2.1)$$

The slower which boundary layer flow at the hub and at the over-tip casing experience a reduced centrifugal effect. The flow near these walls drawn by the pressure difference will move, towards the suction side of the passage. The fluid flowing through the centre of the passage will, on the other hand, experience the strongest centrifugal effect and is forced towards the pressure side. This fluid circulation is visible at the upper-half of the passage as a vortex rotating in the opposite direction as the rotor itself.

- The fluid just upstream or inside the tip gap is dominated by the tip leakage flow. The big pressure difference across the blade tip induces a strong acceleration towards the gap. Mayle and Metzger (1982) showed that this acceleration is much larger than the streamwise acceleration that would have existed without a tip-gap. The acceleration is very local and already completed when the fluid enters the gap. “Therefore if a turbulent boundary layer exists on the pressure side of the blade near the tip, the portion of it which enters the gap will relaminarise before it gets there” (Mayle and Metzger, 1982). As an accompanying effect, the thickness of the boundary layer will be reduced greatly.

The acceleration into the gap can even be sufficient to accelerate the flow to sonic conditions: “Since the bulk of the gap flow forms a near two-dimensional flow at almost right angles to the blade mean line, the gap channel effectively forms a convergent divergent nozzle, provided that the separation bubble remains present on the blade tip. Thus the flow could be supersonic in the downstream portion of the flow passage. This does appear to occur in practise” (Sjolander, 1997).

Although the area covered by the tip gap is small compared to the passage, it will be shown in this paper that the tip leakage flow is of outmost importance for the heat transfer at the over-tip casing.

- At the suction side of the tip gap the tip leakage flow re-enters the passage at a very high velocity and under a relative high angle. Consequently the tip leakage flow rolls up and forms the tip leakage vortex. The tip leakage vortex is counter-rotating in respect to the passage vortex. The tip leakage vortex will raise the heat transfer at the over-tip casing, however since the vortex first has to develop, especially the downstream area is affected.

One of the earliest tip leakage models was created by Rains (1954). Rains assumed the chordwise pressure gradients acting on the gap flow were small compared to those normal to the blade. The blade pressure thus only acts to induce a component of velocity normal to the blade. Yaras et al. (1988) further investigated the model and showed that the magnitude and direction of the velocity vectors within the gap are predicted with good accuracy. The tip leakage model is discussed in more detail in section 5.3.2.

Experiments of e.g., Lewis and Yeung (1977) and Yaras et al. (1988) show that the pressure field around the loaded blade is imposed into the endwall with relatively little change. Strong pressure gradients in the spanwise direction from the blade into the wall would imply large spanwise accelerations and large flow velocity components; these are however, largely prevented by the wall (the tip leakage vortex that often forms is generally located somewhat away from the suction surface of the blade, outside the gap, and is thus immaterial to the argument).

The tip leakage models are two-dimensional and do not account for the presence of the relative rotation of the casing. In an operating turbine, the tip leakage flow moves in the opposite direction to the blades (or to the relative motion of the casing), the relative movement establishing a Couette flow. The shape of the velocity profile within the gap depends on whether the flow is shear or pressure dominated. From Figure 2 it is clear that the rotation will lead to a reduction of the gap leakage flow and a decrease of intensity of the tip leakage vortex.

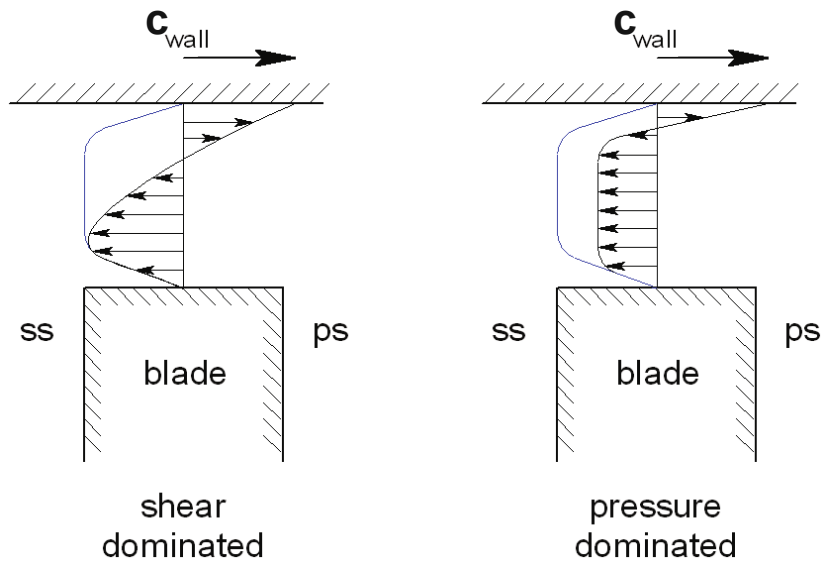


Figure 2: Possible physical mechanisms by which rotation reduces tip leakage flow (Yaras and Sjolander, 1992)

Very detailed measurements of the mean flow in the gap (including relative wall motion) were done by Yaras et al. (1992), the velocity vectors inside the tip gap being shown in Figure 3. The experiments were conducted in a linear cascade with simulated rotation by means of a moving-belt endwall.

The vectors are located at the blade mean line at selected planes from the blade to the endwall (the location being indicated as a percentage of the gap height). Within the gap, the leakage flow obtains a secondary component of velocity directed towards the suction side. This is especially visible at the quarter chord, where the blade loading is at its peak. In this region the fluid flows almost perpendicularly to the mean camber line.

The condition at which the engine flow coefficient is matched to the wall speed is defined as 100% of Engine Equivalent Speed. Figure 3 also shows that the velocity of the flow near to the tip wall is reduced significantly as the wall speed is increased. This is a result of the no-slip condition at the over-tip casing, which is moving in the opposite direction against the flow. The fluid closest to the wall will even flow in the reverse direction; that this is not visible in Figure 3 proves that the boundary layer is thin and that the leakage flow is pressure dominated.

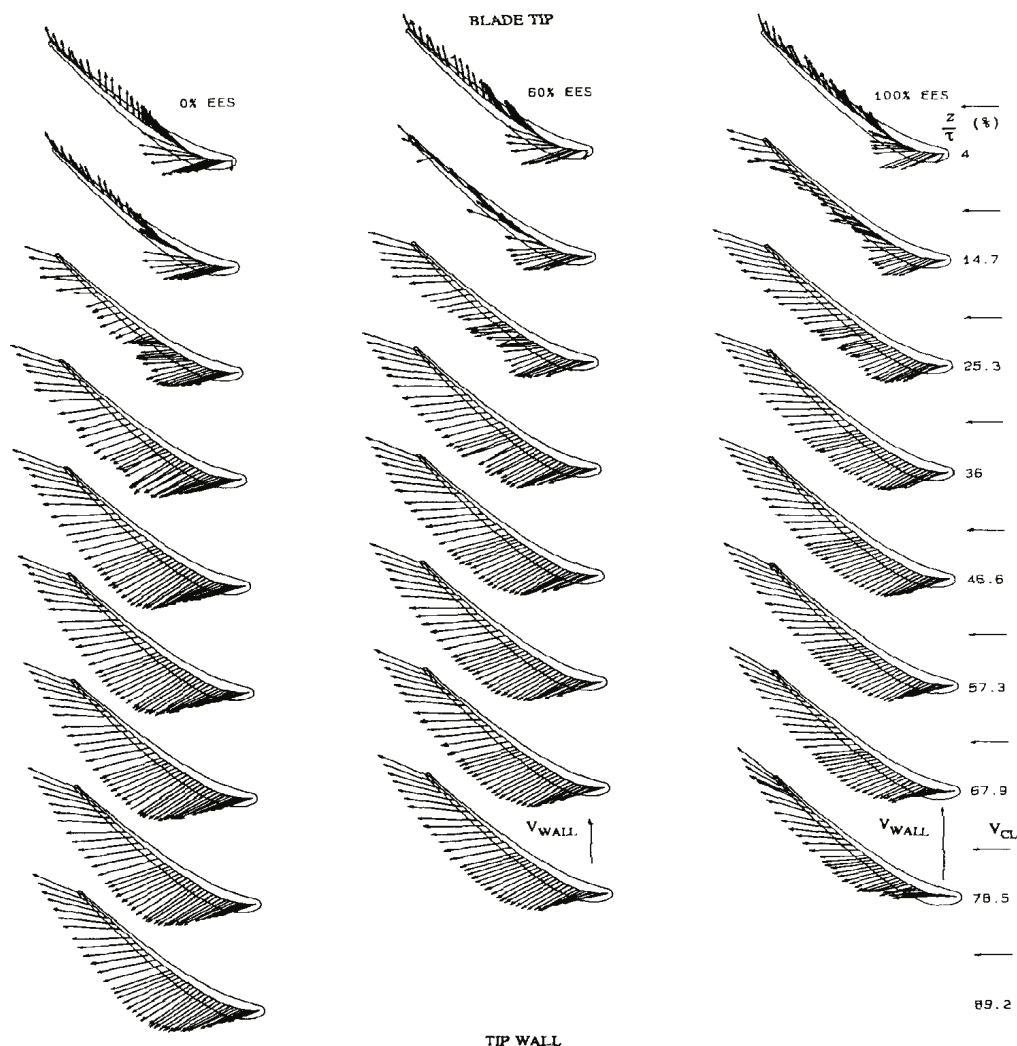


Figure 3: Velocity vectors at different radial positions within the tip gap and different engine equivalent speeds, (Yaras et al., 1992).

A further effect of the rotating blades is noticeable outside the gap, “the passage vortex adjacent to the tip leakage vortex is strengthened by the scraping effect of the blades on the tip-wall boundary layer. It is worth pointing out that the blade tips do not have to intrude physically into the tip wall boundary layer for this scraping effect to occur: the pressure field created by the blades is sufficient to introduce this effect”, Sjolander (1997).

2.2 Previous research into over-tip heat transfer study

Mayle and Metzger (1982) investigated the influence of the relative motion on the heat transfer on a modelled over-tip casing. The experiments were conducted with a disk edge, simulating the relative motion between tip and over-tip casing. Their experiment shows no measurable effects of the moving wall on the average tip heat transfer. Mayle and Metzger showed that the heat transfer at a point inside the gap correlates with:

$$Nu = 0.036 Re^{0.8} Pr^{0.33} \quad (2.2)$$

The first study on the over-tip heat transfer under realistic testing conditions was conducted by Guenette et al. (1985). The experiments were conducted in a short duration test rig which reproduced all of the full scale non-dimensional turbine operating parameters. The experiments included variation of the rotational speed (3x) and Reynolds number (2x).

The measured parameters, static pressure, adiabatic wall temperature, heat transfer rate and Nusselt number show a strong reduction along the blade chord. The time-averaged Nusselt number distribution at the over-tip casing for all of these conditions is shown in Figure 4.

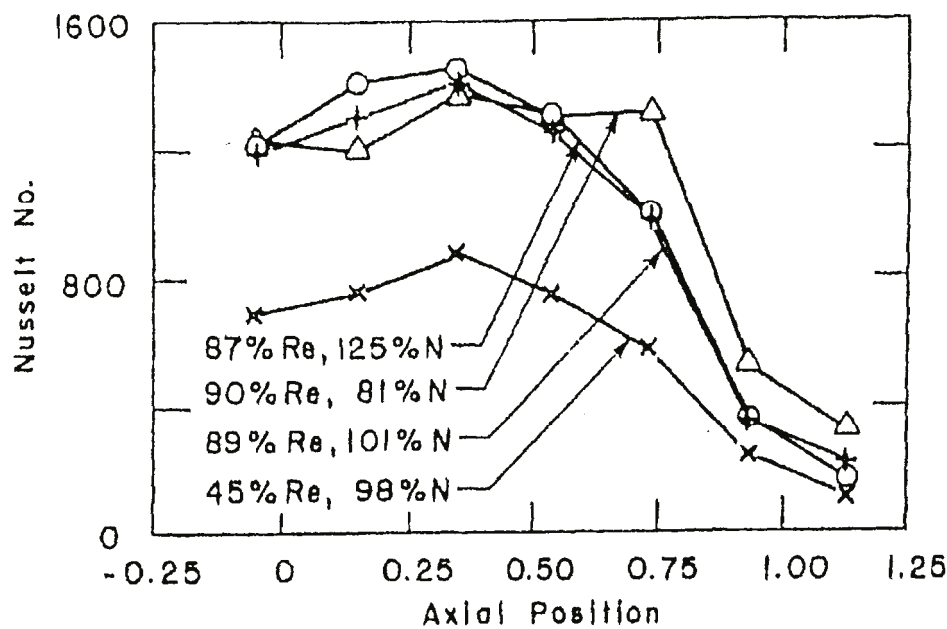


Figure 4: Nusselt distribution at the over-tip casing, (Guenette et al., 1985)

The most significant feature of the graph is the reduction of the Nusselt number along the axial position. This is primarily caused by the changes of Reynolds number, which decreases through the turbine as the flow is decelerated and expanded.

The variation of the Reynolds levels confirmed that also in a rotating rig the heat transfer correlates with $Re^{0.8}$. This was also the conclusion of Polanka et al. (2002) who also measured under realistic engine conditions with even five different Reynolds numbers.

The Nusselt distribution for the three different rotational speeds shows that unlike the findings of Mayle and Metzger (1982) the heat transfer at the casing is dependent on the rotational speed. At the leading edge the heat transfer is identical for all rotational speeds. This followed by a region where the heat transfer positively correlates with the rotational speed. Guenette et al. (1985) relate this to the incidence angle and the resulting loading of the blade: “At 125% corrected speed, the blade incidence angle is reduced by approximately 10 degrees. This unloads the front half of the airflow but does not influence the aft, supersonic section. This would have the effect of reducing the flow under the blade tip near the leading edge, reducing the heat transfer in this area”. An alternative explanation can be found in the passage flow: since the passage vortex is increased by the increased rotation, the leakage flow is rather unimportant in the most upstream part and the temperature has not been reduced much. Further downstream this last effect gains importance and will cause the heat transfer to correlate negatively with the rotational speed.

Additional to the strong variation of the time-averaged data in axial direction, the time-resolved data also showed strong variations in time. The heat flux measured in the tip gap was found to be up to 80% higher than those measured in the passage. Guenette and his co-workers therefore identified the importance of the relatively small tip gap area as a very important factor for the overall heat transfer at the over-tip casing, “Approximately 45% of the total heat load to the shroud is from the flow under the blade tip, even though this represents only 30% of the total shroud area”.

Metzger et al. (1991) tested the equation (2.2) presented by Mayle and Metzger (1982) on the experimental results of Dunn (1990). The measured and estimated time-averaged over-tip casing heat flux is shown in Figure 5. The figure shows that equation (2.2) can be used for estimations of the complete over-tip casing. The accuracy of the correlation is reasonable, except for the most upstream region and around 75% axial chord length, furthermore no predictions of part-load conditions are made.

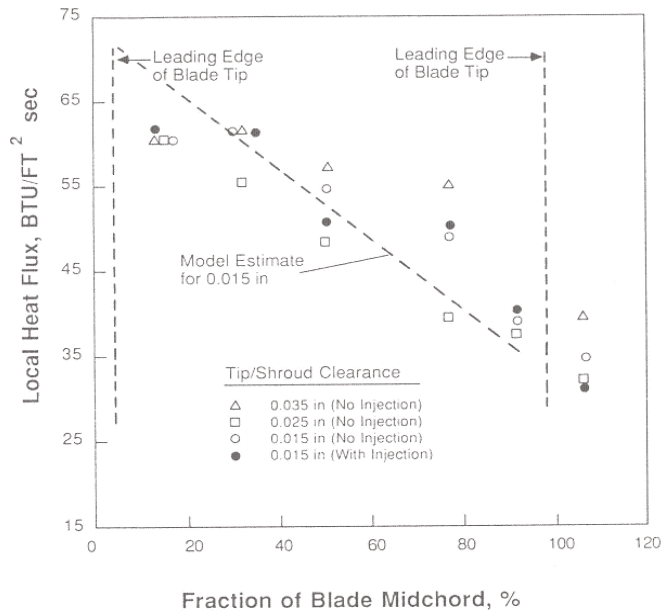


Figure 5: Measured and estimated time-averaged over-tip casing heat flux, (Metzger et al., 1991)

Rhee et al. (2001) and Rhee and Cho (2006) conducted heat/mass transfer measurements at the over-tip casing based on the naphthalene sublimation method. The experiments of the first paper were conducted in a large scale linear cascade and tested the influence of the gap size. The pitchwise averaged Sherwood number was found to vary only little with the tip gap height for all but the smallest tip gap height. The experiments of the second paper were conducted in a low-speed annular cascade. Figure 6 shows the contour plot of the Sherwood number at the over-tip casing.

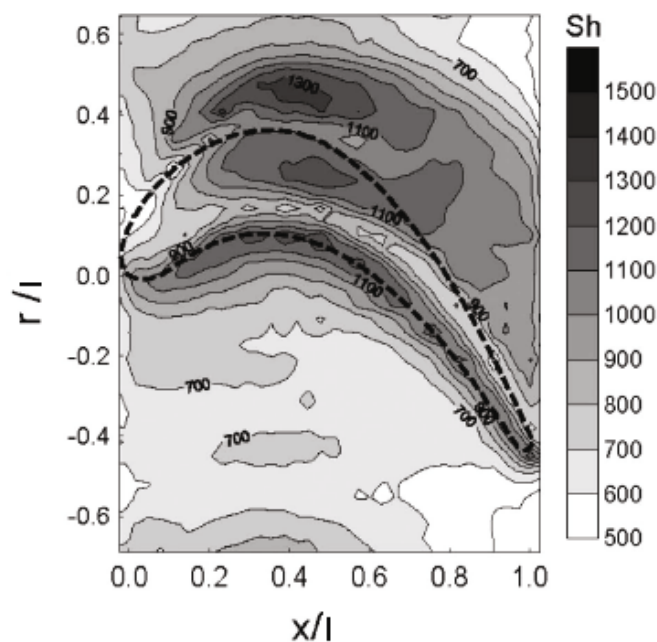


Figure 6: Contour plot of Sh at the over-tip casing, (Rhee and Cho, 2006)

A high heat/mass transfer region is observed along the pressure side due to the flow entrance effect and the acceleration of the tip leakage flow. After the flow enters the tip gap, local valleys are formed in the gap along the pressure side. According to Rhee and Cho those regions are exactly coincident with the blade tip. "This means that the separation bubble on the blade tip blocks the gap and then promotes the acceleration of the gap flow near the shroud (over-tip casing)". "Then, local peak values are shown in the middle of the gap because of the flow transition", the leakage flow will be laminar at the entrance, however it will not stay laminar for the entire gap, since a turbulent boundary layer is more effective in transferring heat the heat transfer will rise (the first peak at the entrance is because the boundary layer is very thin, not because it is laminar). Just outside the suction side edge an additional high heat transfer region is formed. This is presumably due to the upstream tip leakage flow.

Rhee and Cho also examined the effect of rotation (256 *rpm*) on the over-tip casing heat/mass transfer and found the level of the rotating case –due to the reduced tip gap flow- to be 10% lower than that for the steady case.

The research on the heat transfer at the over-tip casing became a big boost by availability of faster and more accurate measurement techniques allowing a better insight in the relative flow field. Detailed studies were conducted by Chana and Jones (2002), Polanka et al. (2002 and 2003) and Thorpe et al. (2004a, 2004b, 2006 and 2007). All three groups conducted their measurements in a blow-down tunnel operating with engine realistic conditions. The time-resolved static pressure was measured with piezo transducers and the heat transfer and wall temperature with thin films.

Chana and Jones (2002) examined the influence of non-uniform inlet temperature on the over tip heat transfer. For the case of the non-uniform inlet conditions the heat was concentrated in the centre of the passage and therefore simulated the temperature field behind the combustion chamber better. They found that overall heat load measured with the more realistic inlet compared to a uniform inlet temperature was significantly lower.

$$Nu = 0.0242 Re^{0.8} Pr^{0.6} \quad (2.3)$$

However other than correlation (2.2), Re is based on the flow velocity through the gap relative to the casing. The gas temperature is the relative temperature at this point. The performance of

the correlation is only shown for a single point inside the tip gap, which is in reasonable agreement with the measured value.

The first paper of Polanka et al. (2002) examines the time-averaged pressure and heat transfer measurements, the second paper of Polanka et al. (2003) describes the time-resolved measurements and computations for the same geometry. Their experiments included Reynolds variation (5x), pressure ratio variation (3x), inlet temperature variation (3x) and cooling air variation (4x).

The pressure ratio only had an effect on the aft portion of the over-tip casing. “The lower pressure ratio resulted in a higher Nusselt number believed to be due to possible separation in the aft portion of the blade. This would have the impact of changing the flowfield in the tip gap and would enhance the heat transfer along the shroud (over-tip casing)”, Polanka et al. (2002).

The change of the gas-to-metal temperature showed to have a big impact on the Nusselt number distribution, as the gas-to-metal temperature decreased, the over-tip casing Nusselt number slope became much steeper. Polanka et al. (2002) formed the driving temperature of the heat transfer using the upstream relative total temperature, this however does not correspond to the true driving temperature. This impact of the gas-to-metal temperature was confirmed by Thorpe et al. (2007).

In the accompanying paper Polanka et al. (2003) concentrate on the base condition and compare the experimental results with numerical results. While the over-tip casing pressure distribution was accurately predicted with the 3-D RANS solver, the heat transfer was overpredicted by a factor of two.

The numerical results showed very high frequencies and high amplitude fluctuations which were absent in the measured data. “These large amplitude fluctuations were physically realistic, and digital filtering in a manner consistent with the experiment revealed that both the peak heat flux and the time-mean on the shroud could be as high as was predicted”. Therefore it is likely that if sensors are used with a too low frequency response to resolve the high heat transfer coefficient peaks inside the tip gap, the measured heat transfer level will be less than the actual heat transfer coefficient level.

The most recent work on the heat transfer at the over-tip casing was performed by Thorpe et al. (2004a, 2004b, 2006 and 2007). The time-averaged and time-resolved data of Thorpe et al. (2004a and 2004b) show in general the same characteristics as the measurements performed by Guenette et al. (1985). However the measurements presented by Thorpe et al. (2004a) were the first to be conducted at multiple circumferential positions allowing the effect of the stator wake on the flow at the over-tip casing to be determined. The influence of the stator vane exit flow features was found to be small compared to the axial changes, although a region of higher heat transfer and higher static pressure has been seen in the vicinity of the stator vane trailing edges. In this region also the adiabatic wall temperature was found to be highest, which can be explained by the reduced amount of lift generated by rotor blade when it is circulated by the stator wake.

This variation of the lift furthermore affects the pressure difference across the tip, and causes a modification of the tip leakage flow speed and direction. “This has a significant impact on the unsteady heat flux to the casing: higher pressure difference produces higher casing heat flux and vice versa” (Thorpe et al., 2004b).

The pitchwise averaged measurements of Thorpe et al. (2004b) show that “around the blade mid axial chord, approximately half of the casing heat load is produced by the tip leakage flow, despite the fact in the circumferential direction the blade thickness is 3.4 times smaller than the passage width”. This corresponds very well with the findings of Guenette et al. (1985).

2.2.1 Work process in the tip gap

Thorpe and his co-workers (2004b) furthermore enable better understanding of the wall temperature fluctuation with the aid of a new model of the work processes in the tip gap. Since the tip leakage flow in contrast to the rest of the fluid does not participate in the work conversion process of the turbine, the total temperature of the tip leakage flow is not reduced, consequently the temperature will be higher than that of other fluid at the same axial position. Thorpe et al. (2004b) found the total temperature in the tip gap to be partially above the stage inlet temperature, this can only occur when in the concerned region work has been added to the fluid. From Euler’s turbine equation follow that the angular momentum and the work are directly linked, for an axial turbine:

$$W = u \cdot (c_{3,tang} - c_{4,tang}) = c_p \cdot (T_{0,3} - T_{0,4}) \quad (2.4)$$

In general in the rotor the work is taken out of the flow by reducing the absolute component of the fluid. However the acceleration inside the gap can result in a local increase of the absolute component. In that case work is added and the total temperature increases. This model is discussed in more detail in section 5.3.8.

Numerical results of Thorpe et al. (2007) show that temperature in the tip gap also depends on the gap length-to-height ratio.

The flow inside the gap is sketched in Figure 7. The combination of the strong spanwise acceleration of the fluid and the sharp corner at the turbine tip results in the formation of a separation bubble at the entrance. This separation bubble will be responsible for a converging flow at the beginning of the passage followed by a region of divergence. This divergence will proceed gradually, consequently the flow will only completely diverge to the size of the gap when the gap length is relatively long e.g. with a thick blade (top sketch). In the case of a short gap (bottom sketch) the fluid has no time to mix.

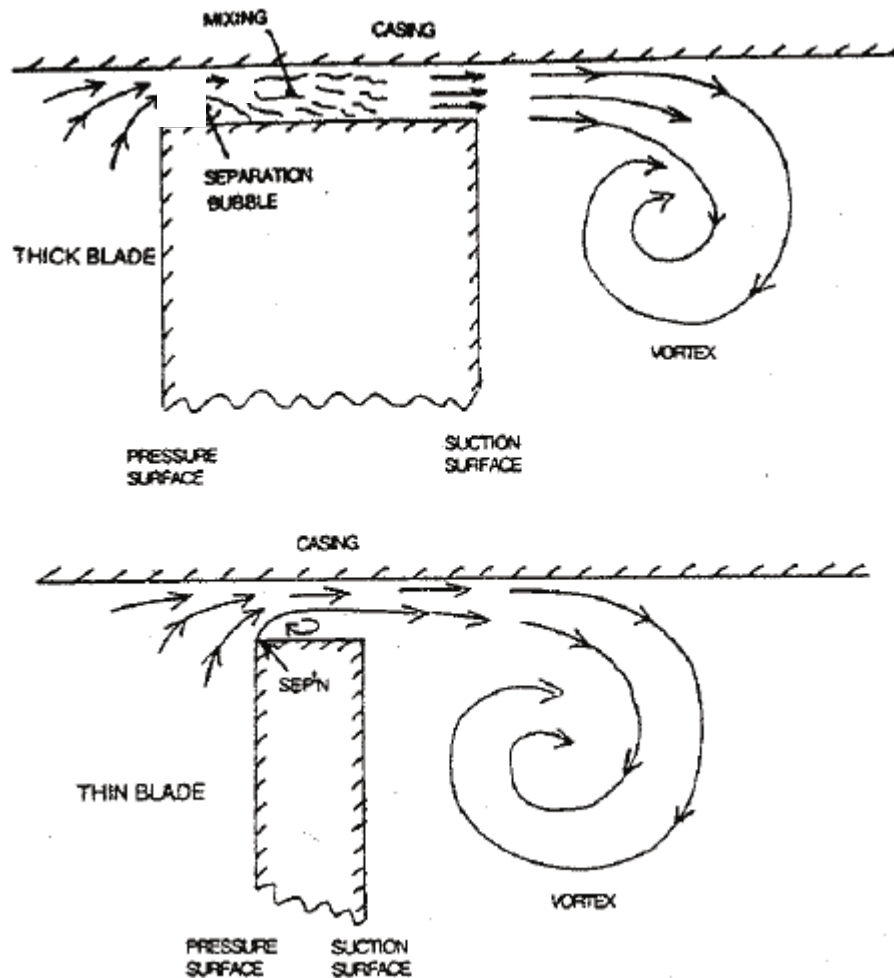


Figure 7: Simple tip gap flow model (Denton, 1993)

The extent of the mixing of the tip leakage flow also has a considerable impact on the tip leakage loss and the turbine tip heat transfer and has therefore been subject of various studies e.g. Heyes and Hodson (1993), Sjolander and Cao (1995) and Willinger and Haselbacher (2000).

Thorpe and his co-workers (2007) found that the mixing also has a direct influence on the heat transfer at the over-tip casing.

- When observing a fluid particle along the streamline over a thick part of the blade tip (e.g. the mid-chord of the blade) in the relative frame of reference, the particle is accelerated into the gap until the narrowest passage at the separation bubble. As a result the (absolute) tangential velocity and absolute total temperature are increased. After passing the separation bubble, the particle will decelerate again and also the (absolute) tangential velocity and absolute total temperature will be reduced. Consequently the absolute total temperature has a peak at the over-tip casing located just above the separation bubble. The total temperature will be lower in the rest of the tip gap
- When observing a fluid particle along the streamline over a thin part of the blade tip (e.g. the trailing edge of the blade), the particle is also accelerated into the gap until the narrowest passage at the separation bubble, but since no mixing occurs, the velocity at the over-tip casing will remain high. Consequently the absolute temperature will remain high, too.

3 EXPERIMENTAL SETUP AND MEASUREMENT TECHNIQUES

The over-tip casing has so far hardly been subject of research. As far as known to the author, this research project is the first program to investigate the heat transfer at the over-tip casing for a wide range of engine realistic conditions.

3.1 The rotating cascade facility at DLR, Göttingen

The Windtunnel of Rotating Cascades of DLR, Göttingen (RGG) is a closed loop windtunnel which can operate at transonic speed with a volume rate up to $15.5 \text{ m}^3 / \text{s}$. A Schematic of the RGG is given in Figure 8. The continuous air supply is delivered by a four stage radial compressor. The rotational speed of the rotor is controlled by a 1.2 MW motor/generator. The temperature of the fluid can be controlled by altering the fraction of the flow passing the cooler.

The fluid is dehumidified by a dehumidifier during the start up of the wind tunnel. The start up procedure takes approximately 60 minutes, this time is also sufficient for the test section to reach adiabatic wall conditions.

The flow is calmed and straightened in the settling chamber. Downstream of the settling chamber the tube contraction towards the cascade inlet is in the order of 20, which results in rather low turbulence levels at the stage entrance (typically around 1.5%).

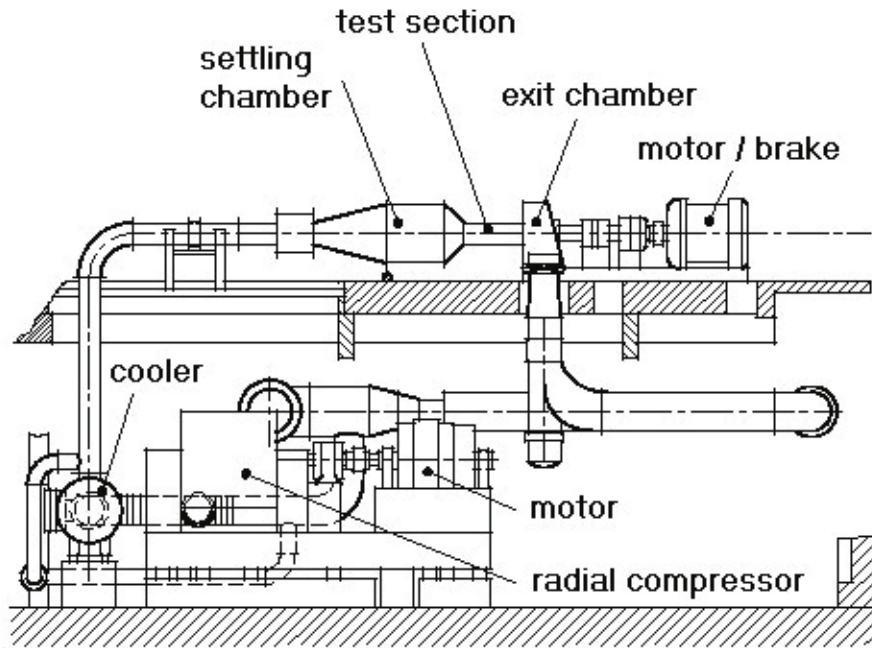


Figure 8: Schematic of the RGG

The RGG enables engine realistic testing conditions to be maintained over a very long period and with an excellent periodicity. However the accompanying complexity of the tunnel exacerbates the instrumentation of the testing objects with the necessary sensors. The use of optical techniques for instance, is possible but very limited. Also the well established thin film technique or Naphthalene sublimation technique is unsuitable or at least problematic for a long duration tunnel such as the RGG.

3.2 The turbine stage and measurement program

The turbine stage used for this project, is the high pressure stage designed by MTU Aero Engines for the German E3E (Environment, Economy and Efficiency) programme. The stage was kindly allocated to the DLR by MTU Aero Engines. A sketch of the stage is given in Figure 9, the key geometrical and operational parameters are given in Table 1. The rotor contains cylindrical blades.

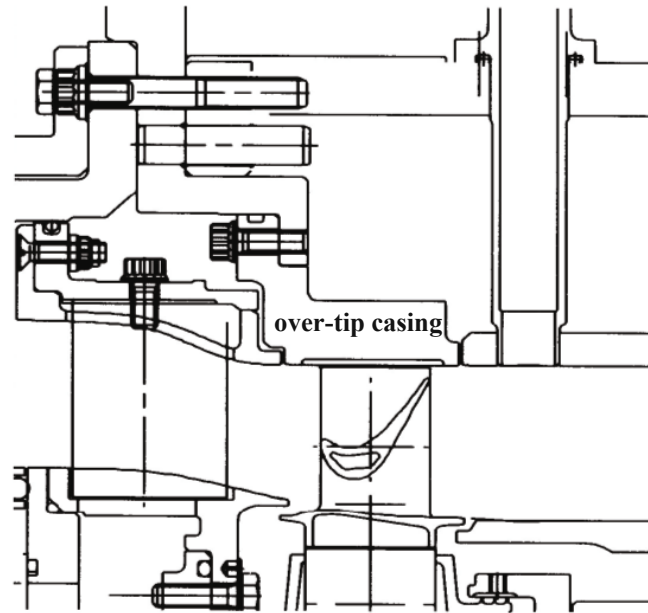


Figure 9: Stage setup in the RGG

settling chamber total pressure	p_{01}	120kPa, 150kPa
settling chamber total temperature	T_{01}	390K
rotational speed	n	8000...10000rpm
pressure ratio	Π	2.3...3.8
Reynolds number	Re	$1.5 \cdot 10^5 \dots 1.8 \cdot 10^5$
stator vane entrance angle	α	0°
number of blades stator/rotor	s	30 / 60
axial chord length stator/rotor	l	35.0mm / 25.0mm
rotor diameter	D_{tip}	547mm
blade span	b	40.0mm
tip gap width normalised with blade span	τ_{cold} / b	0.02

Table 1: Geometrical and operational key-parameters of the high pressure stage

The Reynolds number is based on the stator outlet conditions at mid-height and the rotor chord length. The tip gap width is measured under non-rotating conditions. The gap width is also measured under rotating conditions which is described in paragraph 4.1.

As described in the introduction, the first stage high pressure turbine is cooled by a large portion of cooling air. Also both the stator and the rotor of the E3E HP-turbine stage are

equipped with a state of the art cooling configuration. This configuration is used in order to get a realistic representation of the flow, in total 17% cooling air is used in this stage relative to main flow at entrance. The cooling effectivity of the cooling scheme is not discussed further in this report, but the coolant is necessary for establishing the boundary conditions when operating the stage.

Measuring program

One objective of this project is to enhance the tip leakage models for off-design cases. Therefore a comprehensive measurement matrix was formed of the following three parameters: inlet total pressure (2x), rotational speed (4x) and pressure ratio (5x). The measurement matrix is shown in Table 2. Fields representing the completed measurement conditions are marked with “+”. Fields outside the operating conditions of the RGG are marked with a “-“. The circled conditions represent the selected operating conditions where additional time-resolved wake measurements were conducted.

$p_{01} = 120kPa$ $n \setminus \Pi$	2.30	2.56	2.91	3.38	3.80
10000	⊕	+	⊕	+	⊕
9500	+	+	+	+	+
9000	+	+	⊕	+	⊕
8000	⊕	+	⊕	+	⊕

$p_{01} = 150kPa$ $n \setminus \Pi$	2.30	2.56	2.91	3.38	3.80
10000	⊕	+	⊕	+	-
9500	+	+	+	+	-
9000	+	+	+	+	-
8000	⊕	+	⊕	-	-

Table 2: Measurement matrix

3.3 Standard RGG instrumentation

The facility is controlled and monitored by means of a “Simatic S5” (by Siemens AG) industrial control system. The total pressure and temperature in the settling chamber are controlled within $\pm 100Pa$ respectively $\pm 0.2K$ of the target value, the deviation of rotational speed of the rotor is kept less than $\pm 1rpm$. The pressure of all pressure taps is gathered simultaneously by a 512 channel pressure scanner (PSI system).

3.4 Over-tip casing instrumentation

The main focus of the measurements is put on the over-tip casing, however there is only little space available for instrumentation. Flexibility in replacing and repairing sensors was created by manufacturing two pockets in the over-tip casing for inserting easy reachable and replaceable “inserts” which are instrumented with different measurement techniques. Figure 10 shows one of the two openings, the other opening is located at 180° at the other side of the tunnel. The two holes located downstream of the rotor are for inserting wake probes. The following sections address the various measurement techniques used.

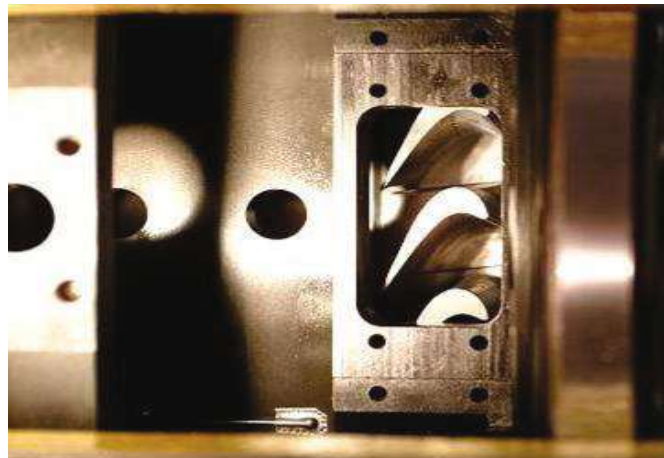


Figure 10: One of the two openings for inserting instrumented parts

3.4.1 Thermocouple+ array

The thermocouple+ array shown in Figure 11 is a heat transfer sensor developed by DLR. The sensor consists of a thin flexible polyimide foil with an integrated thermocouple array and an integrated electrical heater on the rear side. The sensor allows the simultaneous measurement of the steady heat transfer at 25 points. During the experiments these points are spread in the axial direction containing a spacing of 1 mm . The RGG offers the ability to rotate the stator with respect to the sensor, doing this about 250 measurement points per passage can be obtained. The sensor is called thermocouple+ array because it is a thermocouple array, but additionally it has an integrated heating for measuring the heat transfer directly; this additional feature is symbolized by the “+”.

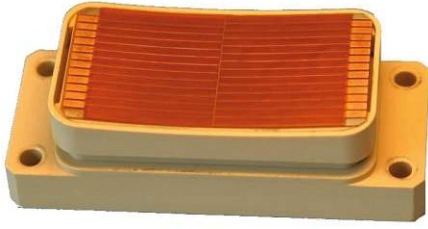


Figure 11: Insert with thermocouple+ array

Constantan circuitry

Copper circuitry

Heating element
(Manganin)

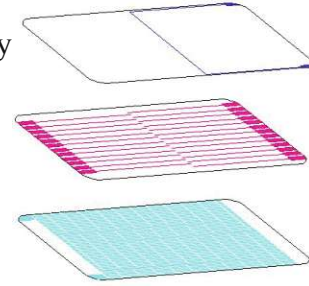


Figure 12: Composition of thermocouple+ array

Figure 12 shows the composition of the thermocouple+ array. The Copper and Constantan circuitry of the top two layers are joint together form the array of thermocouples. The Manganin circuit path on the bottom Polyimide foil acts as a heating element.

The measurement principle of the thermocouple+ array is based upon the simultaneous knowledge of the sensor's internal heat generation per heated area and the distribution of its surface temperature.

The heat transfer coefficient can be calculated from:

$$h = \frac{\dot{q}}{T_{hot} - T_{cold}} \quad (3.1)$$

The heat flux \dot{q} of the electrical heater is generated homogeneously over the entire foil surface. The difference between the wall temperature with heating and without $T_{hot} - T_{cold}$ is measured simultaneously by two separated sensors.

The thermocouple+ array is especially suited for the rotating cascade facility of the DLR, because it doesn't require an optical access, but still provides a precise image with good resolution of the local heat transfer rate. Furthermore the etching process gives a lot of design freedom. For the costs only the initial costs of the layout have been considered. Because the production process is fully automated and the material costs are low the dynamical costs are negligible. The accuracy of the foil is discussed below in some greater detail.

Equation (3.1) shows that for a good accuracy of the sensor both the heat flux and the surface temperatures have to be accurately known.

The heat flux generated by the electrical heater can be determined with great precision, it follows from the layout of the circuitry as well as the power input. The layout with a constant spacing of only 0.1 mm between the successive paths guarantees a homogenous and thus clearly definable heat flux. The power input will be supplied by a DC power supply, the accuracy is within the range of 0.01% of the adjusted power value.

However the generated heat will not be convected completely into the flow. A fraction of the heat is either lost to the back where it will be lost to the surroundings or even worse it will be lost in lateral direction where it can still enter the flow but will cause an additional error in this second region. There are two strategies which are used to counteract this error source:

- 1) The spreading of the heat is reduced by using a very good isolator as wall material. For this reason the insert is manufactured from Poly ether ether ketone (PEEK). PEEK is a semi crystalline thermoplastic and possesses a low thermal conductivity and can sustain temperatures up to 520 K at least.
- 2) When the conduction losses are known the heat flux can be compensated. For this reason a second thermocouple+ array is placed on the backside of the insert, this sensor allows monitoring heat losses towards the back. Information on the lateral losses can be obtained from the neighbouring thermocouples, for this compensation a two-dimensional heat transfer analysis has to be conducted. Since the heat transfer measurement consists of the difference of $T_{hot} - T_{cold}$ the spreading of the wall temperature as result of the changing fluid temperature has no influence on the accuracy of the heat transfer coefficient measurement. This is discussed in more detail in the next paragraph.

The surface temperature difference $T_{hot} - T_{cold}$ follows from two separate measurements of the thermocouple+ array. The Copper and Constantan circuitry form thermocouples of type “T”. The voltage output is collected by a Keithely 2100/7100 digital multimeter, which sends the gathered data to a Labview program running on a PC.

The accuracy of the thermocouples is of great influence for the overall performance of the sensor. There is no previous experience with etched thermocouples neither by DLR nor by the

manufacturing company Isabellehütte. Therefore the accuracy of the thermocouples of the sensor was extensively tested.

For moderate temperatures up to 350K a WIKA 9105 commercial calibrator was used. The maximum deviation is 0.3K . The high temperatures were calibrated using a Nikon Laird S270A infrared camera. The measured deviation complies well with the criteria set for class I type T thermocouples. Thus etched thermocouples perform as well as their class I conventional counterparts.

The obtainable accuracy depends for a large extent on the maximum allowable temperature. This maximum temperature is set by the adhesive between the thermocouple+ array and the insert. Experiments were conducted with a variety of adhesives. X280 a two-component epoxy proved to allow an operation temperature $>470\text{K}$. The sensor is further discussed in Van Duikeren 2004a.

3.4.1.1 Heat losses of the thermocouple+ array

Not all of the heat generated by the heating element is convected directly into the fluid. Part of the heat is conducted by the substrate to the backside of the casing where it enters the surroundings. Especially at the edges of the heating element a considerable amount of heat is additionally conducted away in lateral direction.

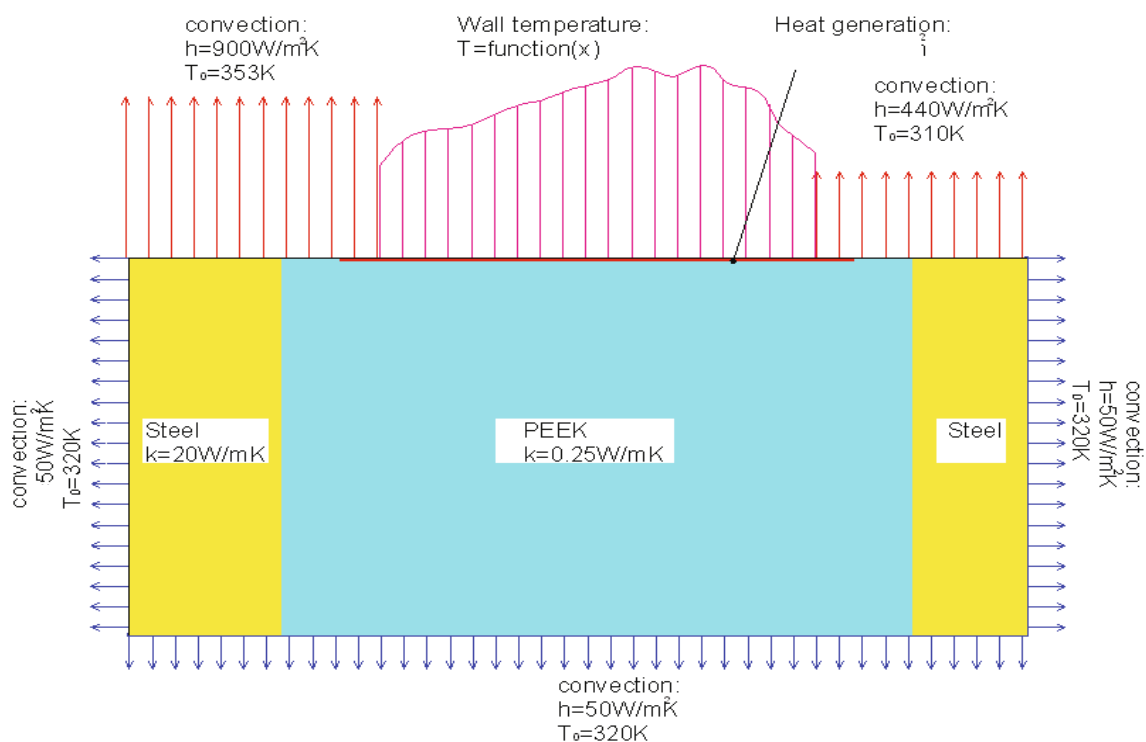


Figure 13: Thermal boundary conditions of the over-tip casing

Consequently the wall heat flux can not be assumed homogeneous, and therefore all heat flows in the substrate have to be determined. For this reason a finite elements model (ANSYS) of the over-tip casing was constructed. A schematic model and the boundary conditions are presented in Figure 13.

The top layer of the thermocouple+ array including the heating circuit is modelled as a layer with isotropic conductivity (in lateral direction the heat has to cross bridges of poor conducting Polyimide substrate). The Polyimide substrate underneath the heating circuit has a thickness of 0.15 mm . The thermocouples are sandwiched in the middle.

	material	conductivity	thickness
heating element	metal/Polyimide	$\lambda_x = 0.38 \frac{W}{m \cdot K}, \lambda_y = 25 \frac{W}{m \cdot K}, \lambda_z = 15 \frac{W}{m \cdot K}$	$t = 50\mu m$
substrate	Polyimide	$\lambda = 0.12 \frac{W}{m \cdot K}$ (isotropic)	$t = 150\mu m$
base	PEEK	$\lambda = 0.25 \frac{W}{m \cdot K}$ (isotropic)	$t = 22mm$
casing	steel	$\lambda = 20.0 \frac{W}{m \cdot K}$ (isotropic)	$t = 22mm$

Table 3: Conductivity of the various sections

The side and back boundary conditions are difficult to determine. As shown in Figure 9, the over-tip casing segment is isolated from other segments by a narrow gap at both sides and air pocket at the backside of the over-tip casing segment. The temperature in the upstream gap can be assumed to be equal to that of the mainstream.

The temperature distribution calculated by ANSYS is shown in Figure 14. The metal (unheated) sides have approximately adopted the temperature of the main flow. The temperature of the heated area corresponds to the experimentally measured values.

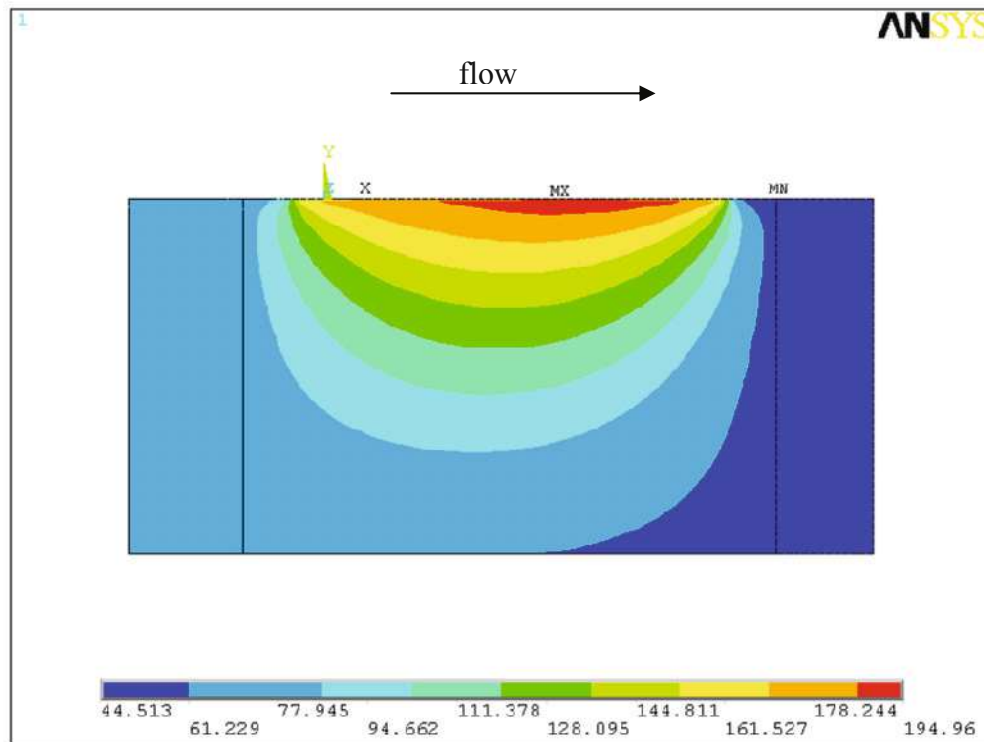


Figure 14: Temperature distribution of the over-tip casing (cross section)

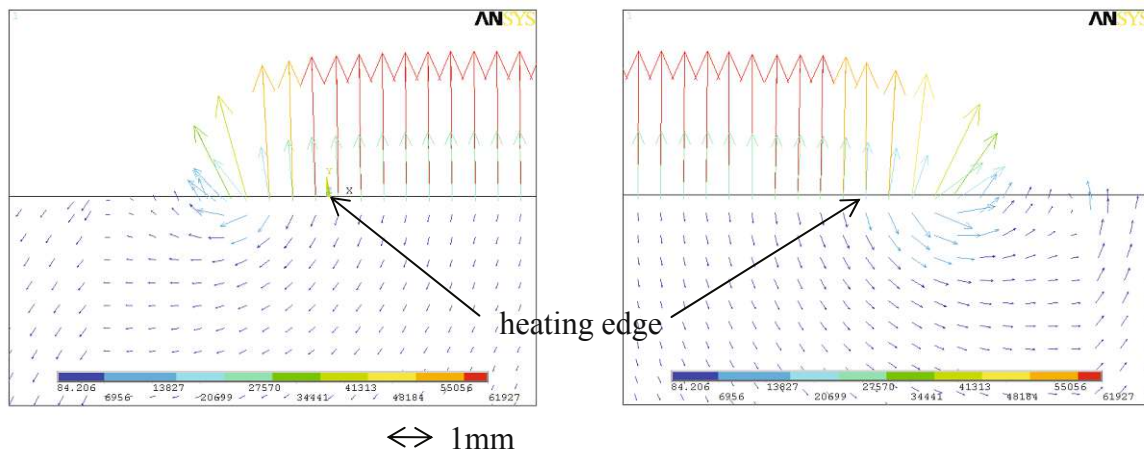


Figure 15: Closeup of the heat flow at the sensor edges

Figure 15 shows a close up of the heat flow at the sensor edges. The red arrows correspond to the grid points at surface located directly on top of the heating. The vertical light blue vectors correspond to the gridpoints in the middle of the heating foil and are consequently approximately half the size of the red ones. Obviously most of the heat is indeed directly transferred into the fluid, however at the edges the lateral conduction does play a significant role.

As already mentioned in the previous section, 5mm under the surface of the sensor additional four thermocouples have been placed. These allow an error estimation of the boundary conditions to be made. The results are shown in Figure 16. The figure shows the measured temperature profile dashed. The readings of thermocouples mounted 5mm deep (marked by *) correspond well with the computed values, which supports the assumed boundary conditions.

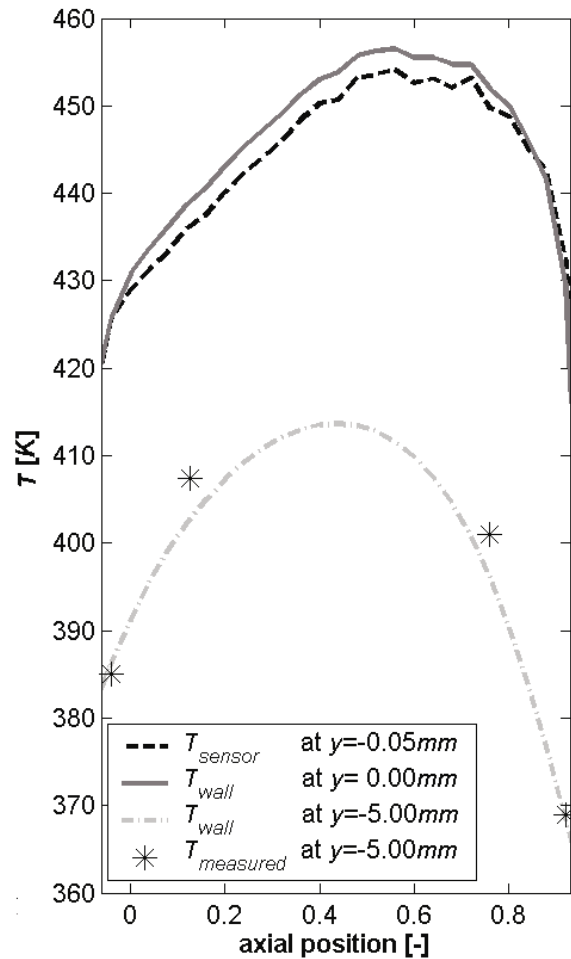


Figure 16: Comparison experimental and computed temperatures

Out of constructional reasons, the thermocouples can not be positioned directly at the surface. Consequently there will be a difference between the wall surface temperature and the sensor temperature. Even a thin isolating layer of $50\text{ }\mu\text{m}$ will, due to the high heat flow rate and resulting steep temperature gradient, result in difference of approximately 2 K .

Depending on the temperature difference between the heated wall temperature and the fluid temperature, this result in an error of approximately 1%.

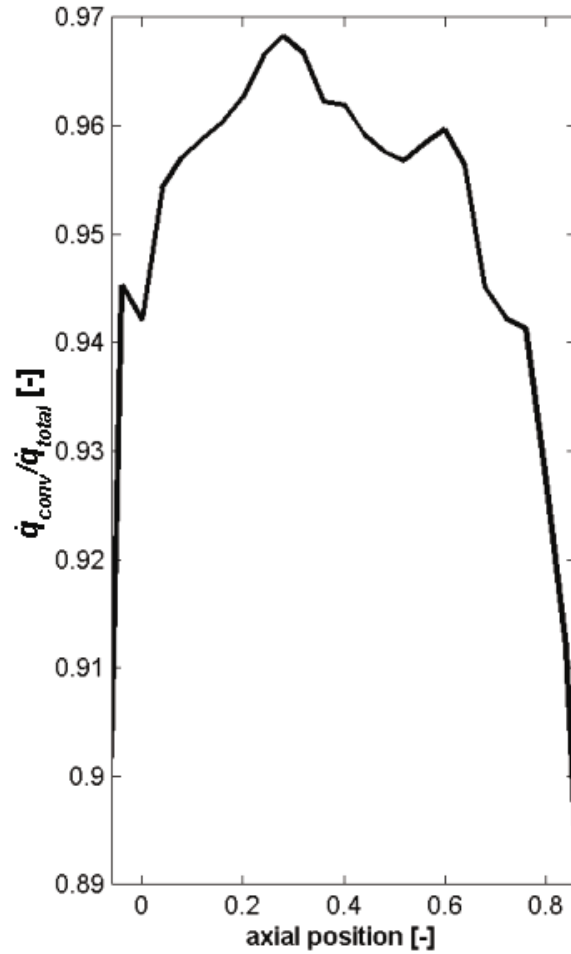


Figure 17: Fraction of generated heat convected into the fluid

Figure 17 shows the resulting part of the heat which is convected into the flow, this curve is virtually independent of the operating condition. The graph can also be used to compensate the heat transfer coefficient distribution.

$$h = \frac{\dot{q}_{total} \cdot \frac{\dot{q}_{conv}}{\dot{q}_{total}}}{T_{hot} - T_{cold}} \quad (3.2)$$

3.4.2 Pressure measurement system

The static pressure is measured by 13 static pressure taps. The data is gathered by a PSI 8400 pressure scanner with an accuracy of $\pm 0.05\%$. The location of the holes is given in Figure 18. The Rotating Cascade Göttingen enables the complete stator to be rotated relative to the rest of the windtunnel. By varying the position of the stator vane relative to the sensors, the sensor experience different stator wake influences. Consequently multiple stator vane settings over one stator pitch enable the complete static pressure at the casing wall to be determined.

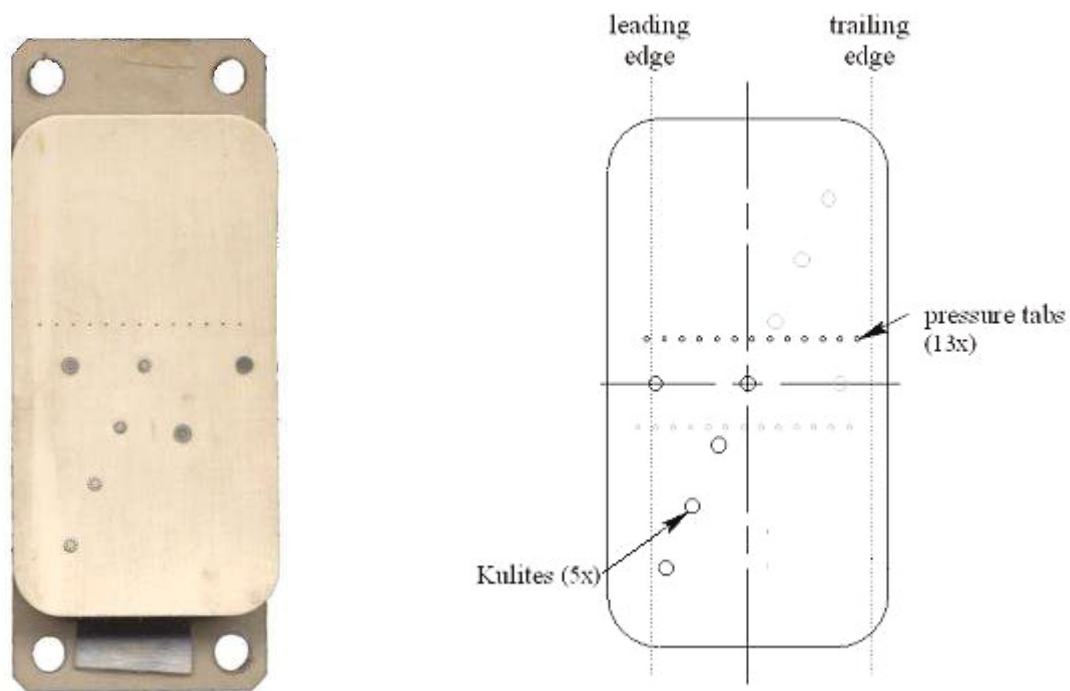


Figure 18: Image and sketch of the steady and dynamical pressure insert

3.4.2.1 Time-resolved data representation

The time-resolved static pressure is measured by five Kulite XCQ-062 dynamic pressure sensors. The location of the Kulites is given in Figure 18, the Kulites are placed on a diagonal line out of construction reason. In the first measurement series five upstream positions are measured. When the first series are completed the instrumented insert is rotated by 180° and four downstream positions are measured (represented in grey in Figure 18). Additionally the middle sensor remains at the same location for both series and is used as a reference. The two step measurement procedure is chosen for reasons of cost-effectiveness. The data is collected by a 4 channel storage oscilloscope. The data is ensemble averaged over 100 samples to enhance the signal-to-noise ratio significantly.

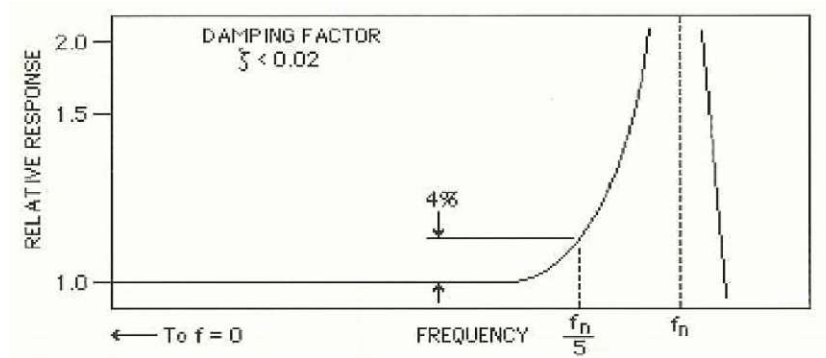


Figure 19: Frequency response of a pressure transducer (Kulite Manual, 2007)

Figure 19 shows the variation of the relative response versus the frequency response. At low frequencies the sensor will be able to correctly measure the varying pressure (relative response ≈ 1). However, when approaching the natural frequency of the sensor, the sensor will overestimate the pressure (relative response > 1). For pressure variations with a frequency under a fifth of the natural frequency the error will be under 4%. Consequently, with a natural frequency of 400kHz , measurements up to 80kHz are feasible. With a blade passing frequency between 8 and 10kHz this will result in 8 to 10 data points per rotor pitch (16 to 20 per stator pitch).

The aim of the Kulite measurements is to generate contour plots of the dynamical casing pressure for distinct stator-rotor settings. These plots represent a good momentary overview of the fluid flow at the casing. A comparison between the different plots for various stator-rotor settings shows the significance of the stator wake effect.

In axial direction a total of 9 sensor positions are available. The stator vane is movable in relation to the rest of the channel and allows positions in the tangential direction to be taken. A step angle of 1° is chosen, these results in 16 steps for $1\frac{1}{4}$ stator vane pitches. Consequently $9 \times 16 = 144$ datasets are generated per operating condition. The measurement grid is shown in Figure 20.

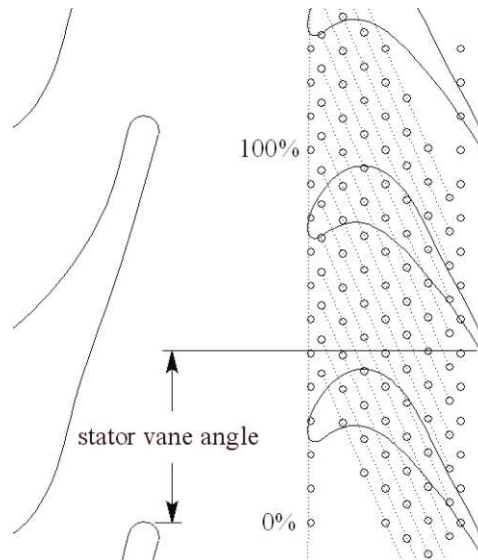


Figure 20: Time-resolved static pressure grid

The individual datasets contain the time-resolved static pressure distribution. Each dataset represents the time-resolved pressure distribution of 4 rotor passings and consists of $4 \times n$ samples. The start of the dataset is initiated by a trigger which is mounted between the casing and the rotor axis. Consequently the trigger point is unaffected by the stator vane-setting.

Figure 21 shows the signal output of the second most upstream Kulite sensor (axial position $x = 0.08$), the different lines represent the various stator vane settings. The horizontal axis consists of the $4 \times n$ samples, of which sample number zero marks the trigger point. The peak clearly indicates the passing of the rotor over the sensor, the suction and pressure side are located respectively left and right of the peak.

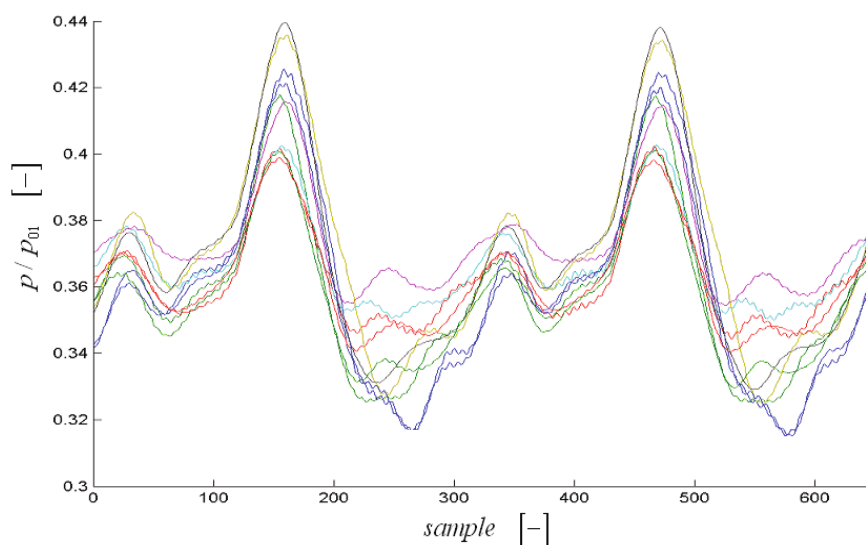


Figure 21: Signals for various stator vane-settings for Kulite sensor 1 ($x=0.08$)

Since the trigger point is unaffected by the stator vane-setting, Figure 21 shows no phase shift, but the location of the stator vane causes a clear variation in the magnitude of the signal.

To construct a correct snapshot of the time-resolved wall pressure for every dataset of the grid, the sample with the accompanying stator-rotor position has to be picked. The sample number can be determined with the following relations.

As shown in Figure 21, every sample represents a unique rotor-sensor position.

$$sample\ nr = \frac{f_{sample}}{360^\circ \cdot (n/60)} \cdot \varphi_{rotor-trigger} \quad (3.3)$$

The sample number needed depends on the ratio of the data acquisition frequency and the demanded position of the rotor in respect to the trigger or vane.

For instantaneous images the relative position between the rotor and the stator is per definition equal for all grid points.

$$\varphi_{stator-rotor} = \varphi_{stator-trigger} - \varphi_{rotor-trigger} = const \quad (3.4)$$

Combining (3.3) and (3.4) gives:

$$sample\ nr = \frac{f_{sample}}{360^\circ \cdot (n/60)} \cdot (\varphi_{stator-trigger} - \varphi_{stator-rotor}) \quad (3.5)$$

Out of (3.5) follows that the required sample number for a given $\varphi_{stator-rotor}$ is also dependent of $\varphi_{stator-trigger}$, since this value is different for every stator vane setting the sample numbers used for the grid points are also variable.

3.4.3 Hot-films

3.4.3.1 Operating principle

The hot-film consists of a thin, etched foil, of which the typical dimensions are $0.05 \times 0.1 \times 0.9 mm$. This foil is placed on the wall with the boundary layer of interest. Due to the relative high electrical resistance of the film, the film will heat itself when an electrical potential is placed across the film. This change in temperature also has an influence on the resistance of the film, thus allowing the temperature of the film to be determined. In the so

called “constant temperature mode” a controller continuously adjusts the potential across the film in order to maintain the temperature of the film constant. The sensor layout of the hot-film array is shown in Figure 22. The hot-films are placed on six axial positions. The hot-films are placed diagonally across the insert, so that the individual films do not thermally influence each other.

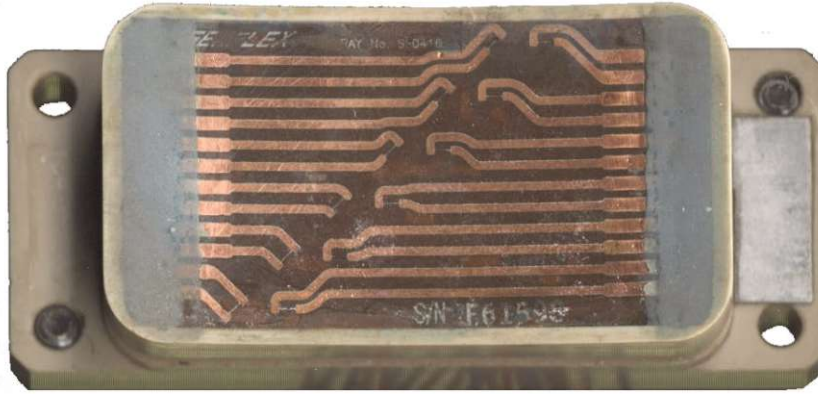


Figure 22: Hot-film array

The relation between the measured voltage and the heat transfer rate at the wall is given by:

$$\frac{V^2}{R} - \frac{V_{loss}^2}{R_{loss}} = q - q_{loss} = A_{eff} \cdot h \cdot (T_{hot} - T_{cold}) \quad (3.6)$$

Where T_{hot} is the operating temperature of the sensor. Rewriting equation (3.6) gives an expression for the heat transfer coefficient:

$$h = \frac{1}{A_{eff} \cdot (T_{hot} - T_{cold})} \cdot \frac{q_{conv}}{q_{total}} \left(\frac{V^2}{R} \right) \quad (3.7)$$

In practice there are two big error sources in equation (3.7):

- I.) The dissipation into the wall is hard to quantify and has an especially adverse consequence on the offset of the heat transfer coefficient. This effect can be eliminated by the in situ calibration of the time-mean hot-film signal with assistance of the thermocouple+ array.

$$h(t) = h_{mean} + h' \quad (3.8)$$

of which h_{mean} is obtained by the thermocouple+ array.

- II.) The size of the effective heated area is a function of the difference between the fluid and the wall temperature. The relative size of the effective heated areas between the different conditions is much better to determine than the absolute size for each temperature

difference apart. For this reason it is chosen to normalise the heat transfer coefficient measured of the downstream hot-films with the heat transfer coefficient measured by the most upstream hot-film:

$$\frac{h_i}{h_1} = \frac{\left(\frac{q_{conv}}{q_{total}} \right)_i \cdot \left(\frac{V_i^2}{R_i} \right) \cdot A_{eff_1} \cdot \left(\frac{T_{hot_1} - T_{cold_1}}{T_{hot_i} - T_{cold_i}} \right)}{\left(\frac{q_{conv}}{q_{total}} \right)_1 \cdot \left(\frac{V_1^2}{R_1} \right) \cdot A_{eff_i}} \quad (3.9)$$

In the next paragraphs the parameters of equation (3.9) will be presented:

3.4.3.2 Sensor operating temperature

Each measurement sequence is started with the in situ measurement of the cold gauge resistance (the gauge is not actively heated, but the fluid temperature can be as high as 390K). Subsequently the gauge temperature is set by the overheat ratio:

$$T_{hot} = \frac{a}{\alpha_{cold}} + T_{cold} \quad (3.10)$$

where α_{cold} is the sensor temperature coefficient of sputtered Nickel at room temperature. The temperature resistance coefficient is obtained by measuring the resistance of the sensor at various temperatures. The temperature resistance coefficient is defined as:

$$\alpha_{cold} = \frac{R_{hot} - R_{cold}}{R_{cold} \cdot (T_{hot} - T_{cold})} \quad (3.11)$$

The calibration gave for the various hot-films a temperature resistance coefficient of $0.39 \pm 0.02\% / K$, which corresponds well to the factory specification for sputtered Nickel of $0.4\% / K$.

The operating resistance of the sensor can be calculated with:

$$R_{hot} = R_{cold} \cdot (1 + a) \quad (3.12)$$

3.4.3.3 Sensor heating losses

Since a considerable amount of the heat of the hot-film is not convected into the fluid but is conducted into the substrate losses have to be accounted for. According to Haselbach and Nitsche (1996) the ratio between the heat convected into the fluid and the heat losses

conducted into the substrate is only dependent on the boundary conditions and not on the fluid temperature:

$$\frac{q_{conv}}{q_{loss}} = f(Re_\tau) \quad (3.13)$$

The experimentally found relation by Nitsche and Haselbach is shown in Figure 23. The figure shows the ratio of the heat convected into the fluid to that which is lost to the substrate through conduction. The amount of conduction is of course also dependent of the substrate material.

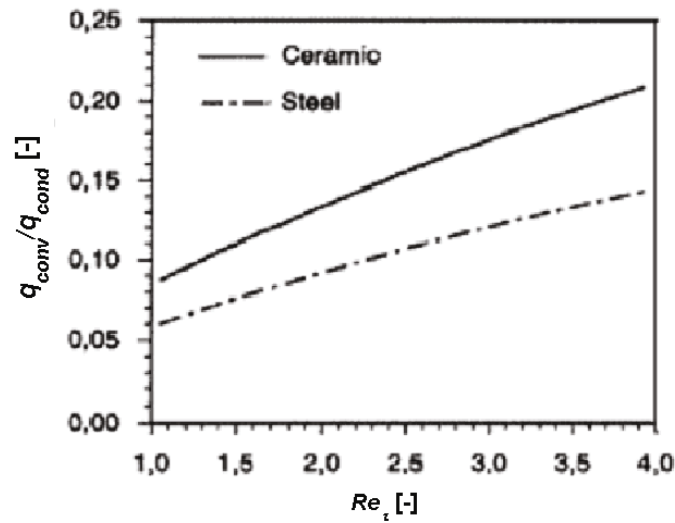


Figure 23: Ratio of convective-to-conductive heat transfer of a hot-film (Haselbach and Nitsche, 1996)

The friction velocity Reynolds number Re_τ is based on the characteristic length of the sensor ($\approx 1.5mm$) and the friction velocity c_* :

$$Re_\tau = \frac{\rho c_* l}{\mu} \quad (3.14)$$

of which:

$$c_* = \sqrt{\frac{\tau_w}{\rho}} \quad (3.15)$$

The shear force can be obtained with the correlations for the fully turbulent plate and a constant main flow (Bejan, 1993):

$$\tau_w = \frac{\rho c^2}{2} \cdot 0.0296 \cdot Re_x^{-0.2} \quad (3.16)$$

The resulting shear stress and friction velocity Reynolds number distribution is shown in Figure 24.

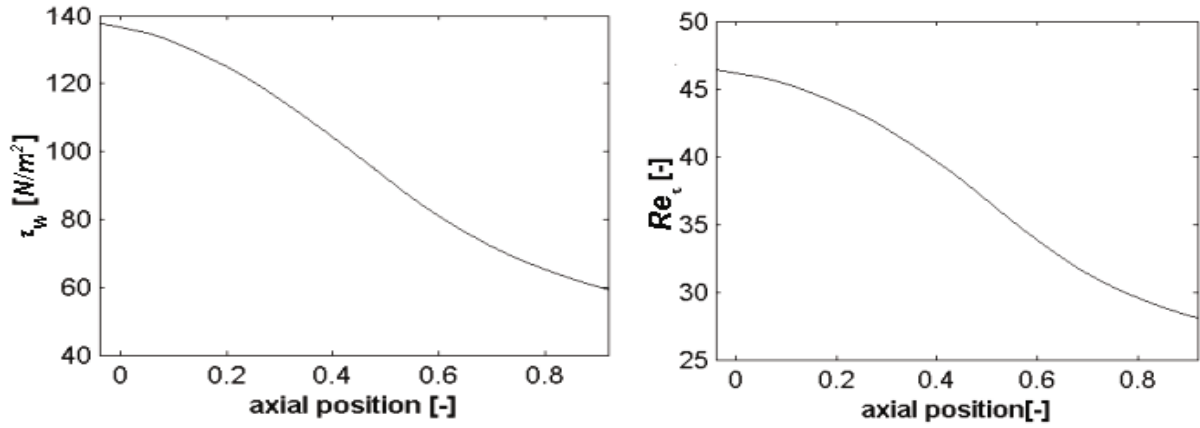


Figure 24: Shear stress and friction velocity Reynolds number distribution at the over-tip casing

The level of Re_τ for the present experiment is higher than that of Haselbach and Nitsche (caused by the higher velocity of the flow of the present measurements). Therefore the curve of Figure 23 is extrapolated.

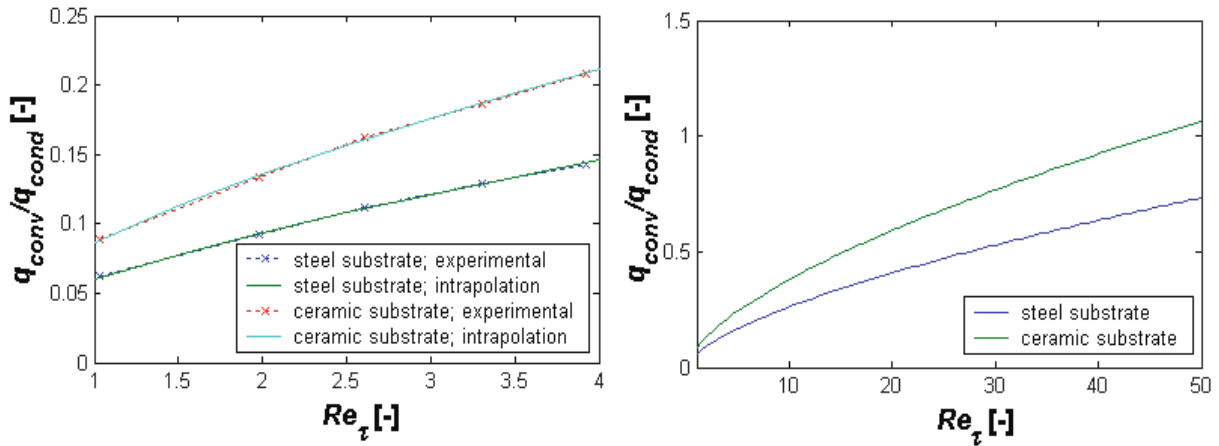


Figure 25: Ratio of convective-to-conductive (loss) heat transfer of a hot-film, calibrated domain (left) extrapolated range (right)

Following equations were found by curve fitting:

$$\frac{q_{conv}}{q_{cond}} \approx 0.06 \cdot Re_\tau^{0.064} \text{ (ceramic substrate)} \quad (3.17)$$

$$\frac{q_{conv}}{q_{cond}} \approx 0.086 \cdot Re_\tau^{0.064} \text{ (steel substrate)} \quad (3.18)$$

The conductivity of the substrate only affects the multiplier of the equation, not the root. The ratio of q_{conv}/q_{total} is more suitable for further representations:

$$\frac{q_{conv}}{q_{total}} = \left(1 + \frac{q_{cond}}{q_{conv}} \right)^{-1} \quad (3.19)$$

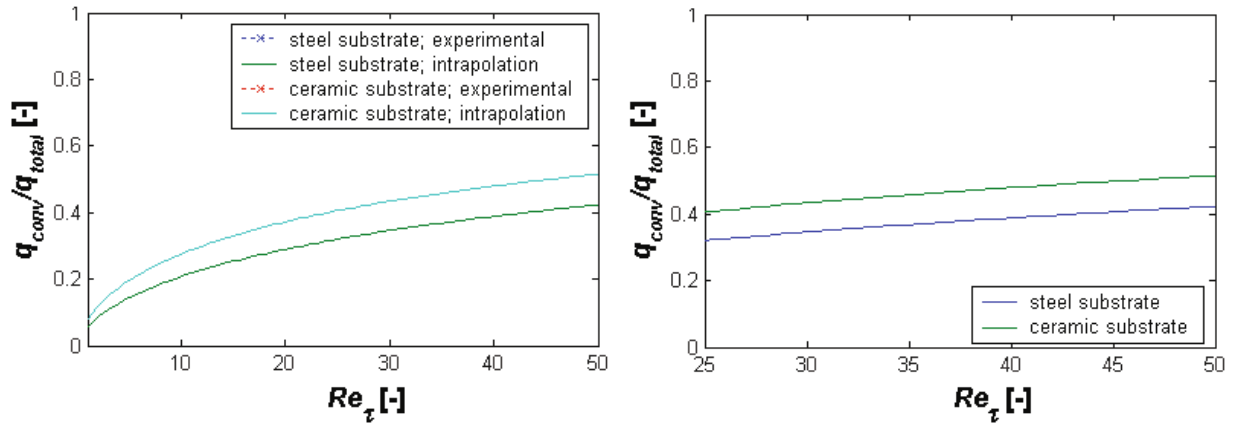


Figure 26: Ratio of convective-to-total heat transfer of a hot-film (left), experimental over-tip casing range (right)

At low velocity the convection will only account for a small part of the heat output, at high velocity the convection part will increase. Figure 27 shows the convective-to-total heat transfer ratio divided by the convective-to-total heat transfer ratio of the first hot-film.

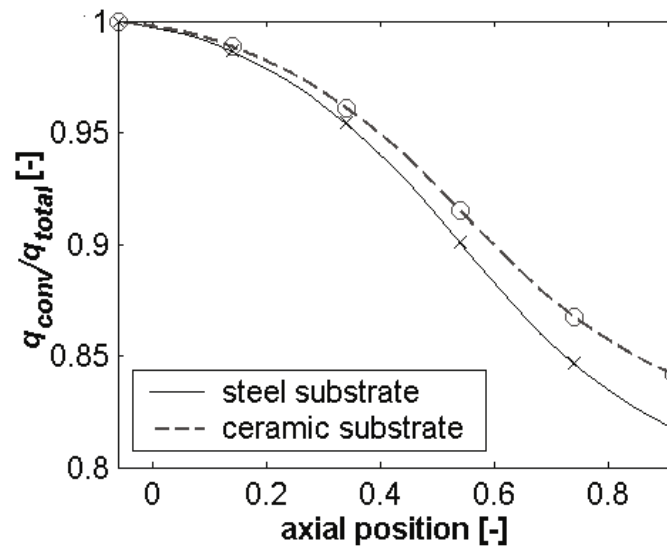


Figure 27: Convective-to-total heat transfer

The actual substrate of the sensor consists of plastic (PEEK), which is a poor conductor. The difference between the conductivity of PEEK and ceramic is much smaller than that between

ceramic and steel. Consequently the empirical relation found for ceramic is assumed to represent a plastic substrate well.

3.4.3.4 Effective heated area

The effective heated area A_{eff} is defined as the size of the virtual area one obtains, when the actual temperature field around the film is represented by a homogenous temperature field T_{hot} which includes the same amount of heat:

$$(\bar{T}_{hot} - T_{cold}) \cdot A_{eff} = \int (T_{hot} - T_{cold}) dA \quad (3.20)$$

There are two methods for determining the size of the normalised effective heated area:

- I.) Integration of the thermal field around the hot-film.
- II.) Comparison of the sensor output of multiple measurements conducted under identical boundary layer conditions but with a different driving temperature.

Integration of the thermal field around the hot-film

Figure 28 shows three close-ups of the thermal image of the heated area of a hot-film for three over temperatures. The lower temperature limit is chosen to be $330K$. Below $330K$ the scatter of the surroundings make the identification of a clear boundary impossible. Consequently the effective area can be determined with:

$$h \cdot A_{eff} \cdot (T_{hot} - T_{cold}) = h \cdot \sum_{>330K} (A_{pix} \cdot (T_{pix} - T_{cold})) \quad (3.21)$$

$$A_{eff} = \frac{\sum_{>330K} (A_{pix} \cdot (T_{pix} - T_{cold}))}{T_{hot} - T_{cold}} \quad (3.22)$$

Table 4 gives an overview of the effective area for three different over temperatures.

over temperature ΔT	140K	180K	220K
effective area A_{eff}	1.09mm ²	0.89mm ²	0.79mm ²

Table 4: Effective heated area of a hot-film for three over temperatures

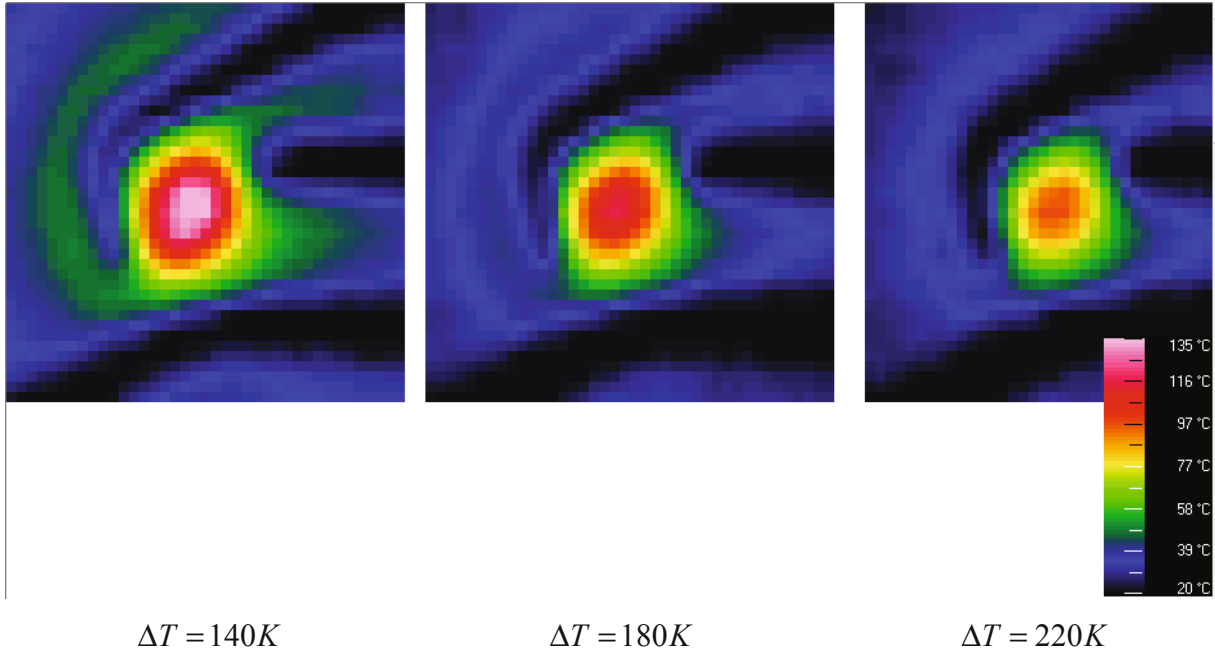


Figure 28: Thermal image of the heated area of a hot-film for three over temperatures

Comparison of successive measurements

If at least two (successive) measurements taken under the same flow conditions –and therefore having the same heat transfer coefficient at the wall- but with a different over temperature, equation (3.7) can be transformed to:

$$\frac{1}{A_{eff_1} \cdot (T_{hot_1} - T_{cold_1})} \cdot \left(\frac{q_{conv}}{q_{total}} \right)_1 \cdot \left(\frac{V_1^2}{R_1} \right) = \frac{1}{A_{eff_j} \cdot (T_{hot_j} - T_{cold_j})} \cdot \left(\frac{q_{conv}}{q_{total}} \right)_j \cdot \left(\frac{V_j^2}{R_j} \right) \quad (3.23)$$

Because the relative loss is equal for the equal flow conditions of both measurements, the loss factor can be crossed out, furthermore the fluid temperature remains equal:

$$\frac{A_{eff_j}}{A_{eff_1}} = \frac{P_j}{P_1} \cdot \left(\frac{T_{hot_1} - T_{cold}}{T_{hot_j} - T_{cold}} \right) \quad (3.24)$$

Figure 29 shows the size of the effective heated area of hot-film at various over temperatures in relation to the hot-film with an over temperature of 200K . The various over temperatures were obtained in situ by six different overheat ratios.

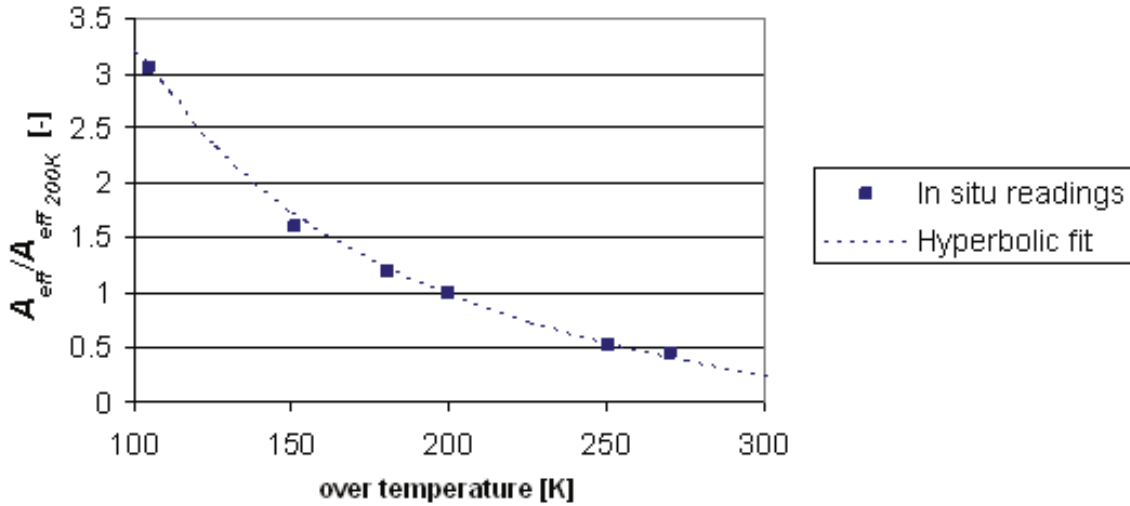


Figure 29: Normalised effective heated area as a function of the over temperature

Table 5 shows that both methods give comparable results.

over temperature ΔT [K]	140K	180K	220K
effective area ratio determined with IR-imaging [-]	1.22	1.00	0.87
effective area ratio determined with thermo couples [-]	1.20	1.00	0.86

Table 5: Comparison effective area ratio of a hot-film for three over temperatures

Now that all parameters of equation (3.7) are known, the normalised distribution of heat transfer coefficient at the over-tip casing can be determined. The results will be presented in section 4.3.2.

3.4.3.5 Time-resolved temperature measurement with hot-films

A further advantage of two successive measurements with unequal driving temperatures is that the time-resolved fluid temperature can be determined. Knowing the normalised effective heated area the equation (3.23) can be rewritten as:

$$T_{cold} = \frac{T_{hot_2} \cdot \frac{V_1^2}{R_1} - T_{hot_1} \cdot \frac{V_2^2}{R_2} \cdot \frac{A_{eff_2}}{A_{eff_1}}}{\frac{V_1^2}{R_1} - \frac{V_2^2}{R_2} \cdot \frac{A_{eff_2}}{A_{eff_1}}} \quad (3.25)$$

Figure 30 shows the time-resolved heating power supplied by the Wheatstone bridge of a hot-film mounted at the over-tip casing at three different overheat ratios.

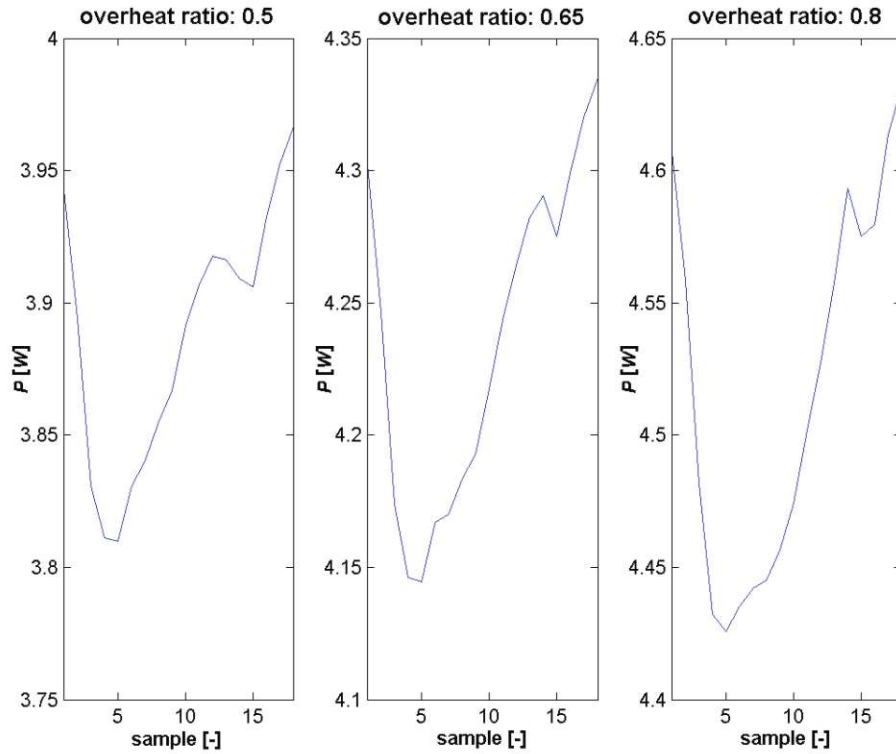
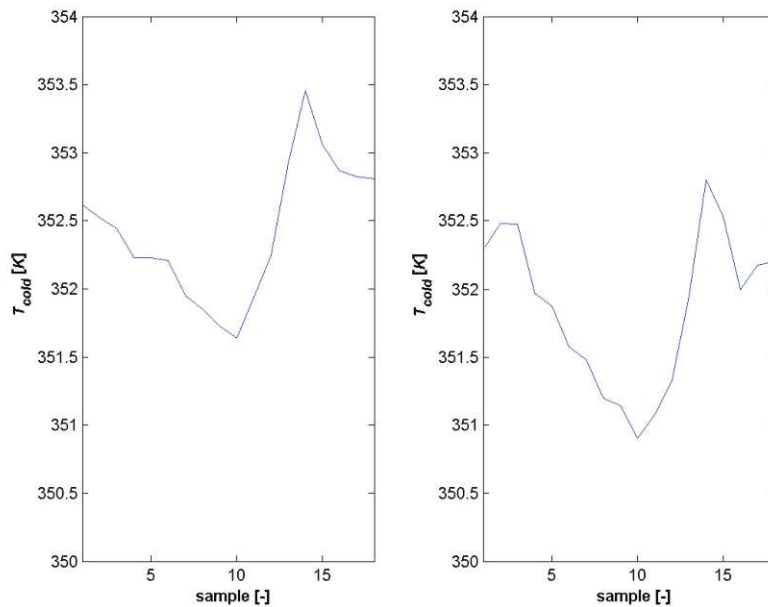


Figure 30: The time-resolved heating power of a hot-film at the over-tip casing for three different overheating ratios



a: Combination overheat ratio 0.50 and 0.65

b: Combination overheat ratio 0.50 and 0.80

Figure 31: Time-resolved wall temperature obtained from two successive hot-film measurements

Figure 31 shows the resulting time-resolved casing wall temperature from equation (3.25). The three signals presented in Figure 30 allow two independent predictions of the wall

temperature. The steady temperature obtained from the thermocouples is $350K$, which means that the level of time-resolved temperature is predicted well but the amplitude is far too small. Obviously the hot-films are capable of measuring the qualitative time-resolved temperature profile but they are too slow to measure the quantitative profile.

3.5 Probes for wake measurements

3.5.1 Kulite probe

The time-resolved wake data is obtained with a Kulite probe. The dimensions of the probe can be taken from Figure 32. The head of the probe consists of two Pitot tubes. The small tube is a steady Pitot tube for obtaining time-mean total pressure. The tube has sharp edges and is $0.5mm$ longer than the rest of the head so that the angle sensitivity is reduced. The pressure is measured by a PSI 8400 pressure transducer. With the aid of a T-fitting the steady pressure is also used as reference pressure for the Kulite. The Kulite is mounted in the tube with the larger diameter and operates in differential mode. The properties of the Kulite (Model Nr. XCS-062) are summarized in table 6.

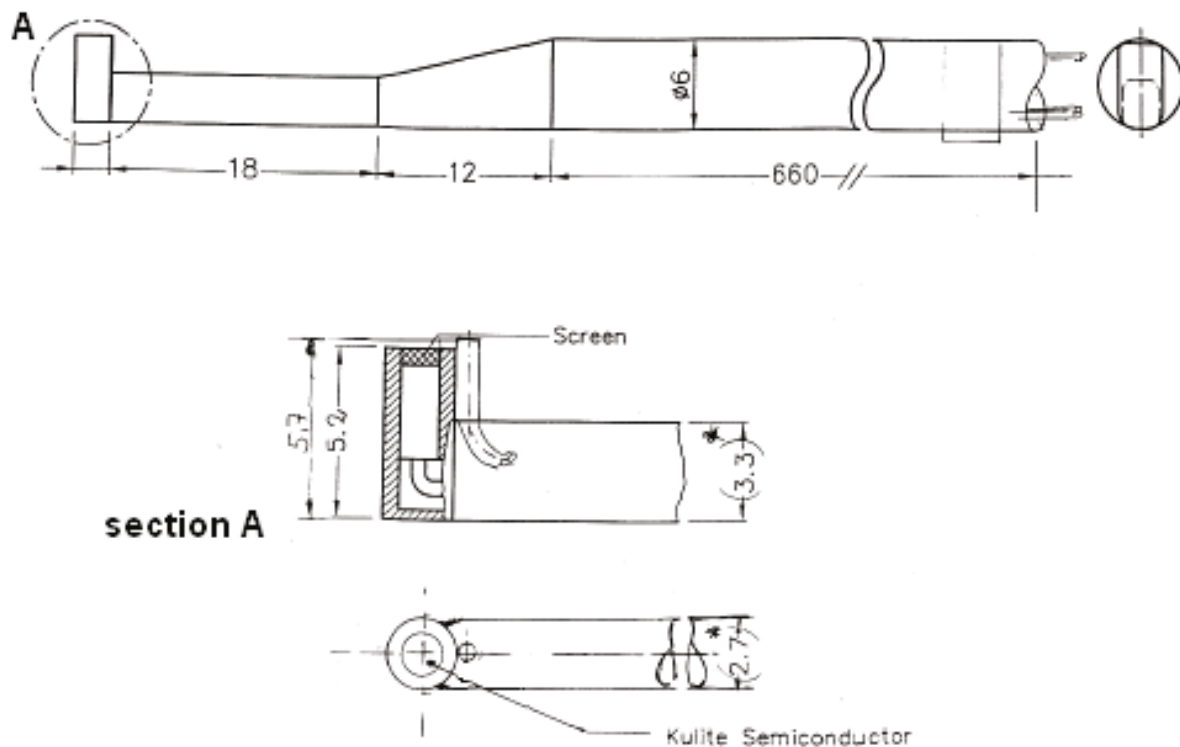


Figure 32: Sketch of the Kulite probe

Operational mode	Differential
Natural frequency (<i>kHz</i>)	175
Pressure range (<i>kPa</i>)	± 35
Full scale output (<i>V</i>)	0.50

Table 6: Properties of the Kulite probe (type: XCS-062)

3.5.1.1 Calibration

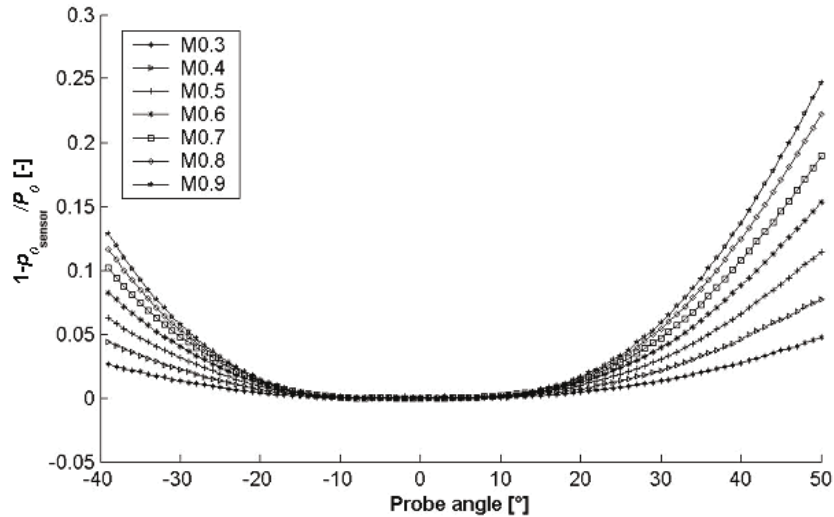
The calibration was conducted in the Probe Calibration Facility (SEG). The SEG is a small wind tunnel especially designed for calibrating probes. The small wind tunnel allows calibration of probes for Mach numbers between $M = 0.2$ and $M = 1.8$, for the pressure range between 10kPa and 300kPa . More details on the SEG can be found in Giess et al. (2000).

First the sensitivity of the Kulite is determined. For this the reference tube is, instead of connected to the steady Pitot tube, connected to the atmosphere. By varying the chamber pressure of the SEG over the complete operating pressure range of the Kulite, the output voltage can be related to the different pressures. Since the Kulite sensor suffers from an offset drift with time this procedure has to be repeated in situ in regular intervals.

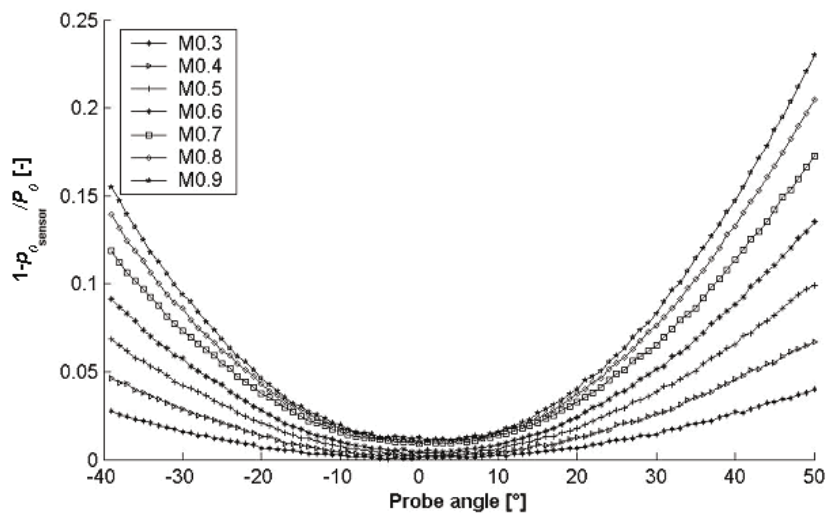
A second point of interest is the gauge pressure of both the steady and the Kulite Pitot tube for different flow angles and different Mach numbers. For this reason calibration curves for 8 Mach numbers between $M = 0.3$ and $M = 0.9$ were created which show the differential pressure as a function of flow angle.

$$C_p = \left(M, (\alpha_{\text{sensor}} - \alpha) \right) = 1 - \frac{P_{0_{\text{sensor}}}}{P_0} \quad (3.26)$$

These calibration curves are shown in Figure 33. The shape of the curves is clearly parabolic and the shape of the parabola becomes sharper with increasing Mach number. Unlike the Kulite sensor the steady Pitot tube has in the middle an interval about $\pm 8^\circ$ at which the signal is insensitive to the flow angle of the fluid. The calibration procedure and the results are described in more detail by Kost (2005).



a: Calibration curves static Pitot tube



b: Calibration curves Kulite probe

Figure 33: Pressure coefficient as a function of the flow angle and Mach number

3.5.1.2 Flow angle analysis

When at each demanded position of the flow field, at least three measurements with different probe angles are made the time-mean and time-resolved total pressure, flow angle and Mach number can be determined. Further precondition is that one probe angle has to be close to the -yet unknown- actual fluid flow angle and the others have to be at a relatively large angle to it, for instance 35° on both sides.

The analysis of the fluid total pressure, angle and Mach number has to be done in two steps. A first approximation is made by a parabolic approximation, then the solution is iteratively improved with the aid of the exact calibration curves described above. A schematic overview of the analysis procedure is shown in Figure 34. As input data the sensor pressure of the

steady Pitot tube can be used, resulting in the calculation of the time-mean values, or the steady Pitot data is combined with the Kulite data and the calculation will result in the time-resolved values.

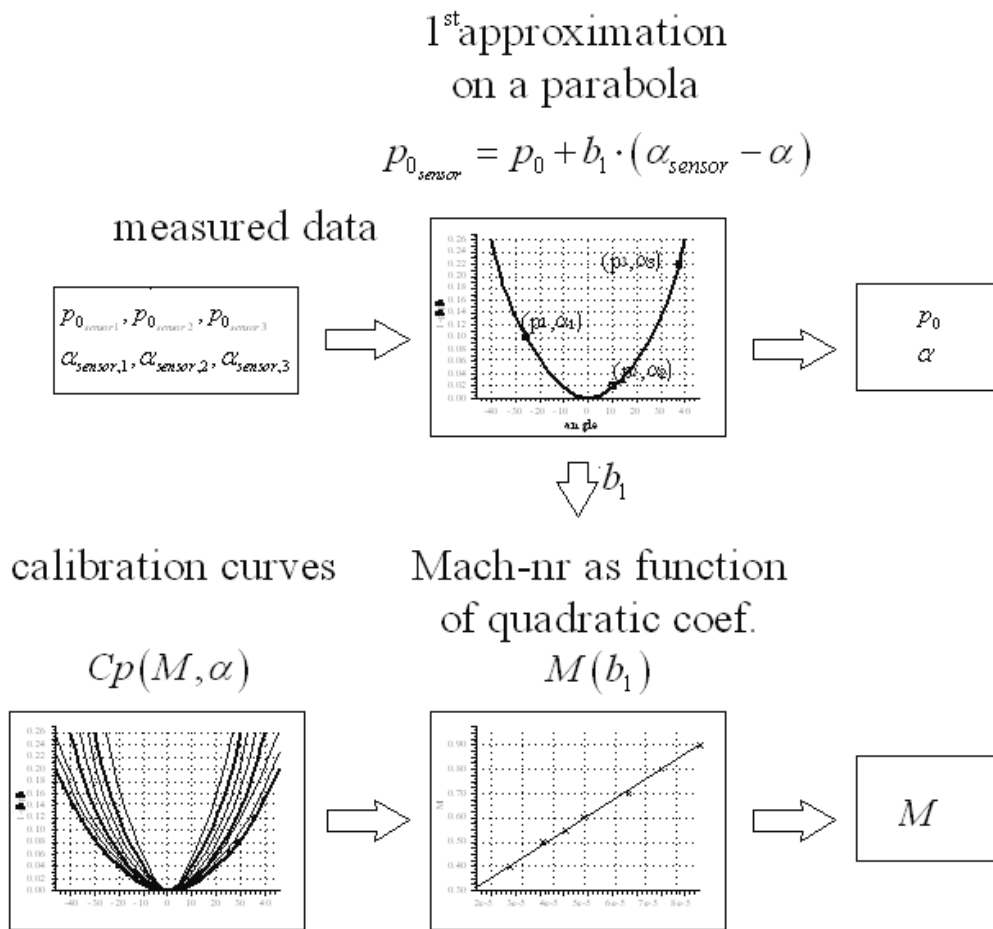


Figure 34: Schematic overview of the wake analysis procedure 1st approximation

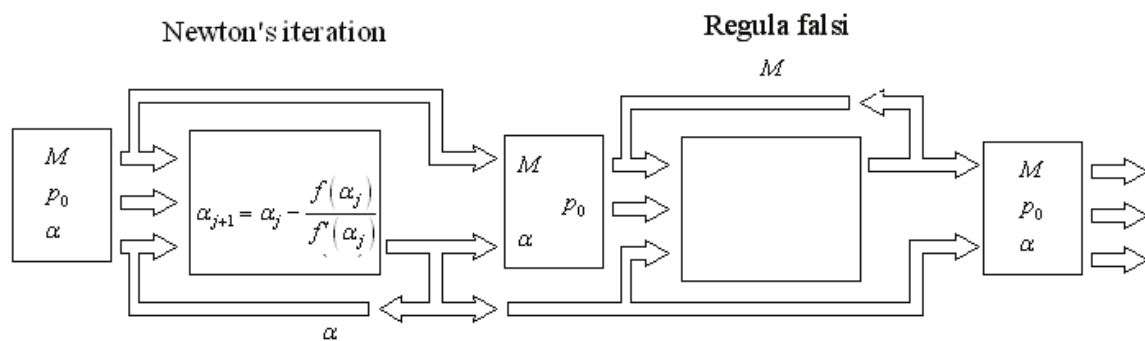


Figure 35: Schematic overview of the wake analysis procedure 2nd iteration

First Approximation

The flow angle and gauge pressure of the three successive measurements are used to construct a parabolic equation of the form:

$$p_{0_{\text{sensor}}} = p_0 + b_1 \cdot (\alpha_{\text{sensor}} - \alpha) \quad (3.27)$$

of which, p_0 and α are the first approximation of the fluid total pressure respectively fluid flow angle. As already observed in Figure 33, the curvature of the parabola is related to the Mach number. The curvature is defined by the quadratic coefficient b_1 . Therefore as a first approximation the Mach number can be found with the aid of b_1 .

$$M = c_1 + c_2 \cdot b_1 + c_3 \cdot b_1^2 \quad (3.28)$$

The flow angle insensitive range of the steady Pitot tube will generally result in a overestimation of the total pressure of the flow.

Iterative improved solution

The first approximation of p_0 can be improved by using the pressure coefficient C_p deduced from the calibration curves presented in Figure 33. Rewriting equation (3.26) gives:

$$p_0 = \frac{p_{0_{\text{sensor},1}}}{1 - C_p(M, (\alpha_{\text{sensor}} - \alpha))} \quad (3.29)$$

$p_{\text{sensor},1}$ is the sensor pressure of the probe placed most directly into the flow, meaning $|\alpha_{\text{sensor}} - \alpha| = \text{Minimum}$. The other pressure readings at the more sideways probe angles are used for improving M, α . This procedure is described in more detail in Kost (2005) and is based on the Newton-method for approximation of α_0 and the Regula falsi method for approximation of M .

4 EXPERIMENTAL RESULTS

This chapter will present the experimental results. First the results of the stator measurements will be shortly discussed. This is followed by the results acquired mainly at the over-tip casing. Finally the rotor wake field measurements will be presented.

Aim of this chapter is to give an overview of all measurements, the complete matrix of various measurements can be found in Van Duikeren (2006). An overview of the key-parameters is given in APPENDIX A.

4.1 Tip gap width

The exact gap width is an essential parameter in the project. The width is mainly affected by the centrifugal forces and thermal elongation. The experiments are conducted at “cold” testing conditions between $310K$ and $490K$. The rotational speeds are between $8000rpm$ and $10000rpm$.

The gap width is measured with two non-contact capacitive distance measuring sensors. Calibration of the sensor is performed with an accurate spinning geared disk with adjustable gap.

As expected, the tip gap width is clearly affected by the rotational speed, whereas the total pressure level and turbine pressure ratio do not have a significant effect on the tip gap size. When adiabatic wall conditions are reached (approximately one hour after start up), also the operating time has no further effect on the tip gap size.

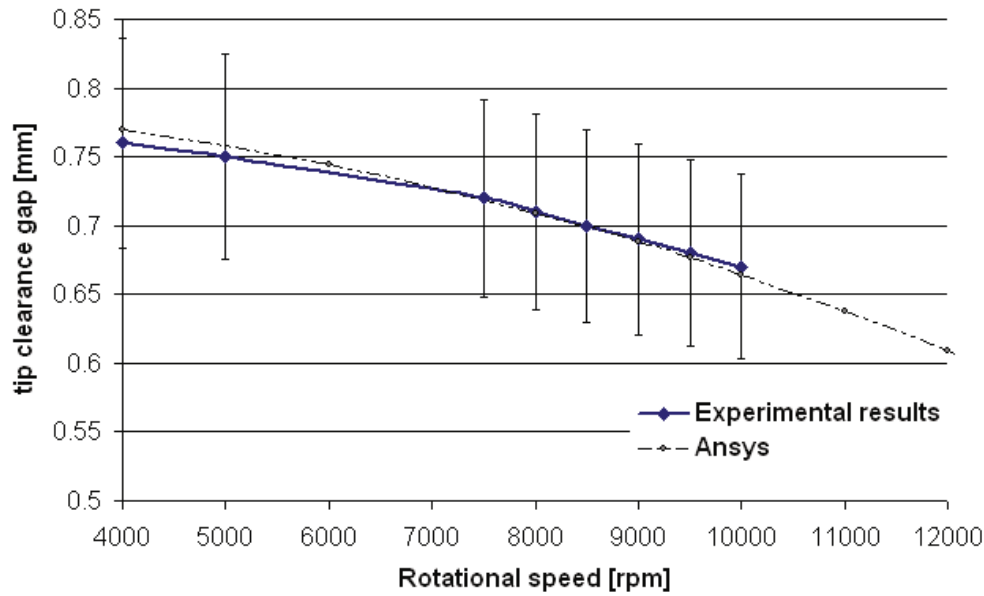


Figure 36: Tip gap size as function of the rotational speed, experimental and computational results

The tip gap size as function of the rotational speed is given in Figure 36, this function can also be expressed by the following empirical formula:

$$\tau(n) \approx 0.79 - \frac{n^2}{7.94 \cdot 10^8} \quad (4.1)$$

where τ is the tip gap size in *mm* and n the rotational speed in *rpm*. The relative high uncertainty range is primarily caused by the difficulty to mount the sensor totally flush after calibration as described above.

The experimental results correspond well with the numerical results, computed at the outset of the project. For the calculations ANSYS was chosen since a finite elements method is best suited for the current task and the moderate costs pose a low threshold. A brief description of the numerical approach of the computation is given in APPENDIX B.

4.2 Time-mean results

4.2.1 Stator results

The inlet flow of the rotor is not homogeneous but affected by the upstream stator and the boundary layers of the casing. The stator, stator casing, and stator hub have been instrumented

with respectively 13, 20 and 16 static pressure taps. The static pressure distribution of the casing is shown in Van Duikeren (2006).

The flow field close to the over-tip casing, located at 0.70 (rotor) chord lengths downstream of the stator vane and 0.15 lengths upstream of the rotor, is measured by four fixed total pressure probes. The tangential orientation angle of the probes is with 78° identical to the geometrical trailing edge angle. Figure 37 shows the results of these probes for an operating condition with a low pressure ratio (left side) and for an operating condition with a high pressure ratio (right side). The horizontal axis shows the tangential position in percentage of the stator vane pitch. Position zero represents the location of the geometrical wake core. This core is defined to start at the stator trailing edge with tangential angle (78°) to the blade. The wake is clearly visible as an area of reduced total pressure (Figure 37 a and b). At 75% blade height the wake flow angle indeed approximates 78° . However, in the vicinity of the casing the wake is deflected more towards the suction side by the action of the passage vortex. Although the four Pitot tubes used are fixed and cannot be turned, the difference between the location of the geometrical and the measured wake core allow the flow angle at the casing to be estimated. The wake angle deviation is at most 3.3° , however this can still result in a big variation of the tangential velocity component which will be discussed in more detail in section 5.1.6.1.

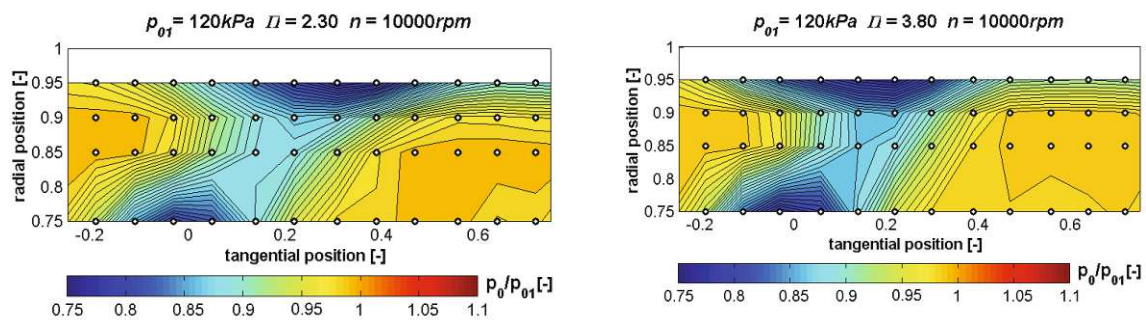


Figure 37: Stator wake total-pressure distribution a) $\Pi = 2.30$ b) $\Pi = 3.80$ (choked flow)

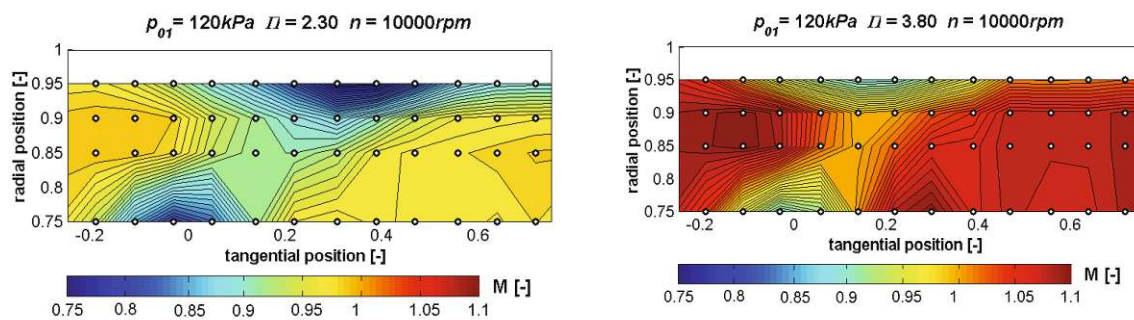


Figure 38: Stator Mach number distribution a) $\Pi = 2.30$ b) $\Pi = 3.80$ (choked flow)

The static pressure holes at casing and hub between the stator and rotor allow the total pressure field to be transferred into a Mach number field (Figure 38a and b). The left figure shows that with a pressure ratio of $\Pi = 2.3$ the wake field is in the high subsonic region but will not choke. It is found that for this the pressure ratio has to exceed $\Pi \approx 3.0$. Figure 39 shows the Mach number field obtained from CFD for the highest pressure ratio. The area between the two dotted lines indicates the measured region.

Rotational speed and pressure level have no significant effect on the wake field at any point of operation tested.

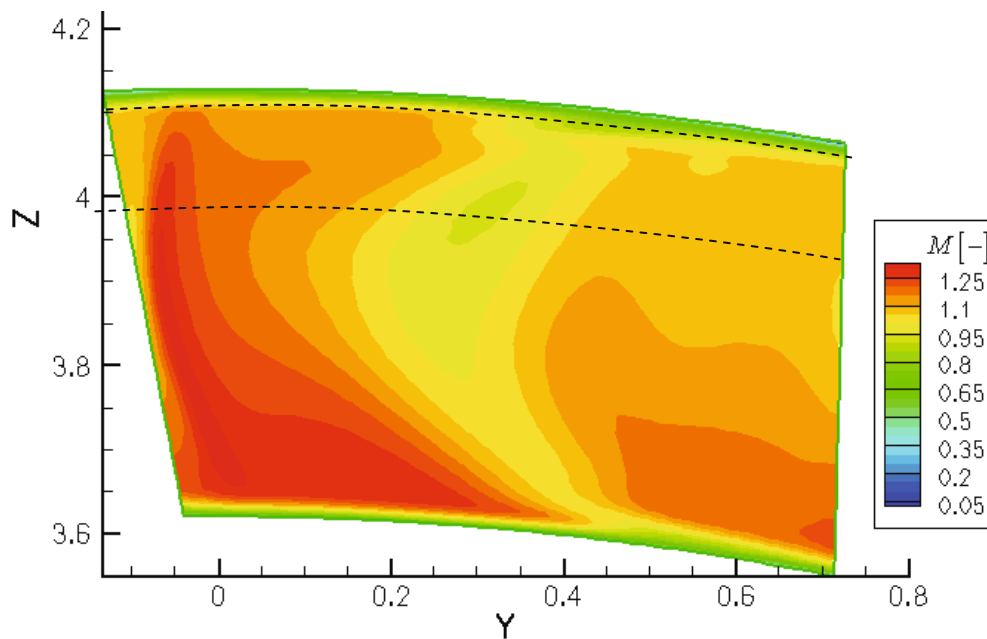


Figure 39: Stator wake Mach field number obtained by CFD (TRACE)

4.2.2 Time-mean pressure distribution

The static pressure distribution at the over-tip casing for various pressure ratios is given in Figure 40. The static pressure is normalised with the total pressure in the settling chamber. The vectors located at $x = -0.15$ represent the position and magnitude of the wake measured by the Pitot tube closest to the casing wall. Similar to the figures of the stator wake, zero and unity of the y-axis mark the geometrical wake core.

There are small but distinct circumferential variations in static pressure at the over-tip casing. This region of high static pressure is caused by the interaction between the stator vane wake and the rotor. Similar results were found by Thorpe et al. (2004a).

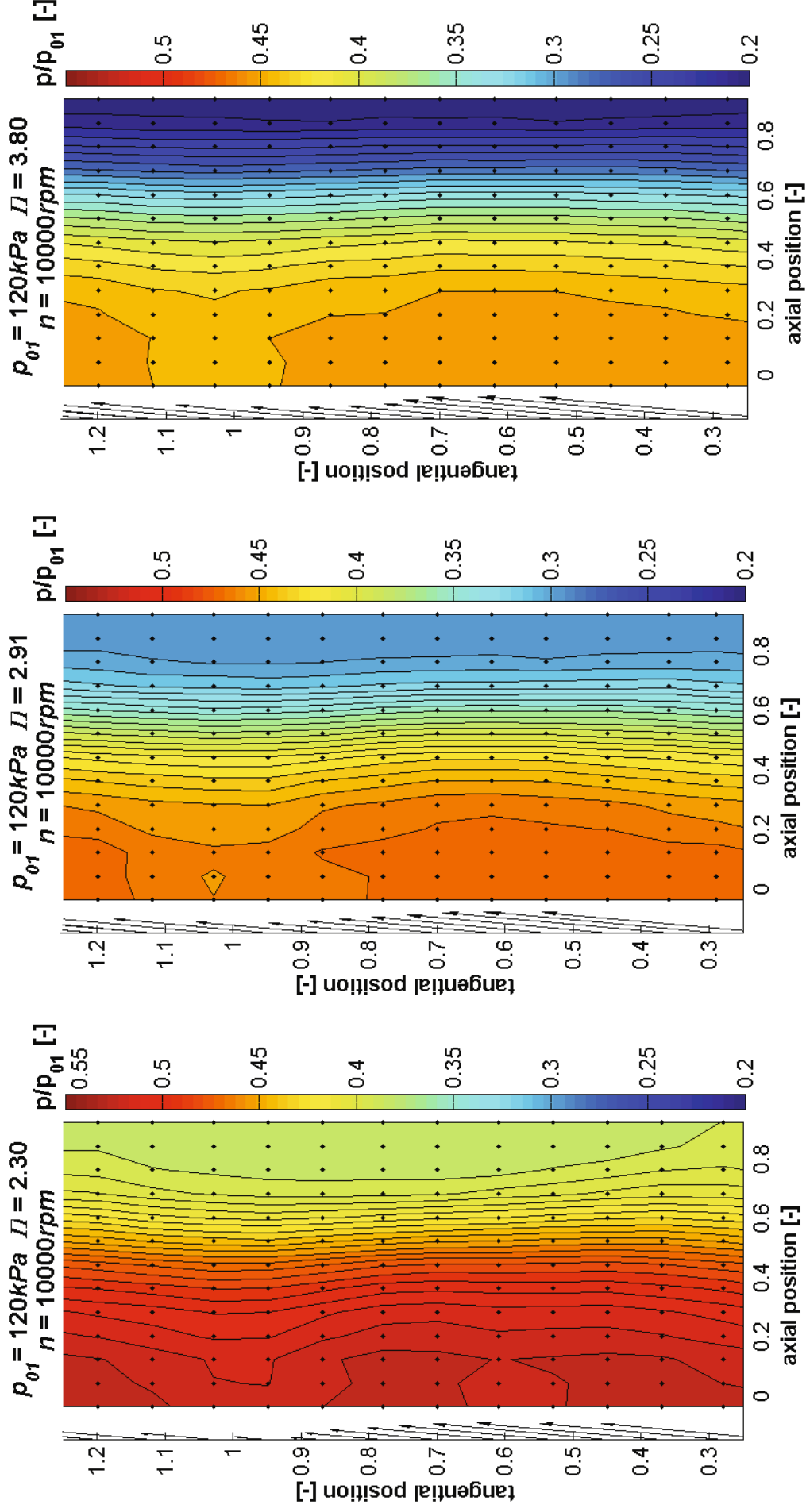


Figure 40: Static pressure distribution at the over-tip casing for a low, middle and high pressure ratio operating condition

The pitchwise averaged static pressure distribution is given in Figure 41. The graph shows a gradual decrease of the static pressure resulting from the increase of the relative velocity of the passage flow. The biggest part of the conversion takes place in the mid-section of the blade between $x = 0.30$ and $x = 0.75$. At a pressure ratio of approximately three, the passage will choke at the throat section of the passage (located at $x = 0.56$). Any further increase of the pressure ratio will only affect the pressure distribution downstream the throat.

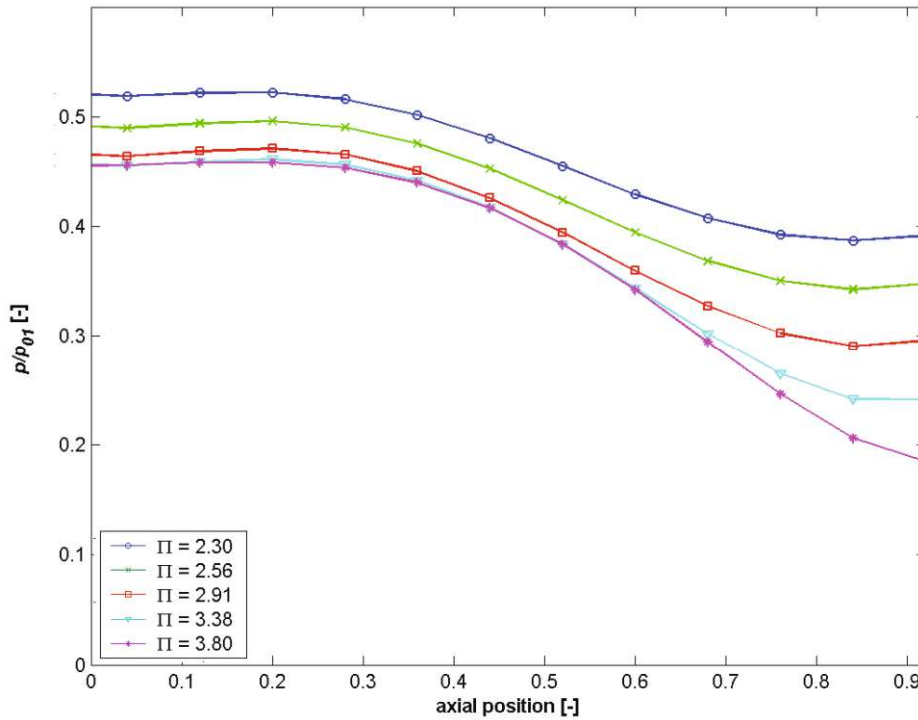


Figure 41: Pitchwise averaged pressure distribution of the over tip casing for various pressure ratios

4.2.3 Time-mean adiabatic wall temperature

The pitchwise averaged adiabatic wall temperature is shown in Figure 42. Since no work is done by the stator, the total temperature of the flow entering the rotor passage –irrespective of the operating condition- equals that of the total temperature in the settling chamber. The difference between the wall temperature and the total temperature at the entrance can however be explained with the recovery factor, which is dependent of the Mach number:

$$f_{rec} = \frac{T_{rec}}{T_0} = \frac{1 + \sqrt[3]{Pr} \frac{\kappa - 1}{2} M^2}{1 + \frac{\kappa - 1}{2} M^2} \quad (4.2)$$

The stator wake Mach number, as shown in Figure 38 and Figure 41, is dependent of the operating condition.

The gradual decrease of the wall temperature, similar to the static pressure profile is caused by the work process of the rotor. However in contrary to the static pressure distribution the adiabatic wall temperature is dependent of the rotational speed. The variance of the time-resolved wall temperature will be discussed in section 5.3.8. The wall temperature of all operating conditions can be found in APPENDIX C.

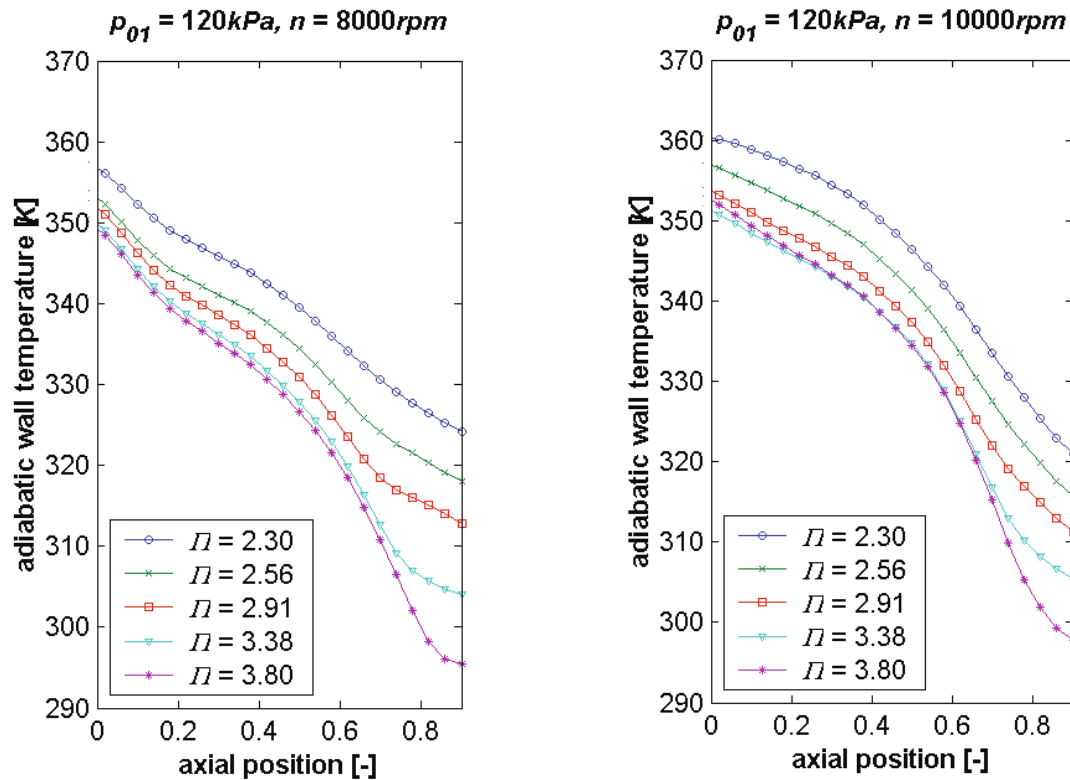


Figure 42: Pitchwise averaged adiabatic wall temperature distribution at the over-tip casing

4.2.4 Time-mean heat transfer coefficient

Figure 43 shows the heat transfer coefficient distribution at the over-tip casing, obtained from the measurement procedure as described in section 3.4.1. The figure accounts for the heat losses inside the substrate as described in 3.4.1.1. Figure 44 shows the heat transfer coefficient distribution at the over-tip casing minus the pitchwise averaged heat transfer coefficient. The figure shows the spatial variations of the heat transfer coefficient.

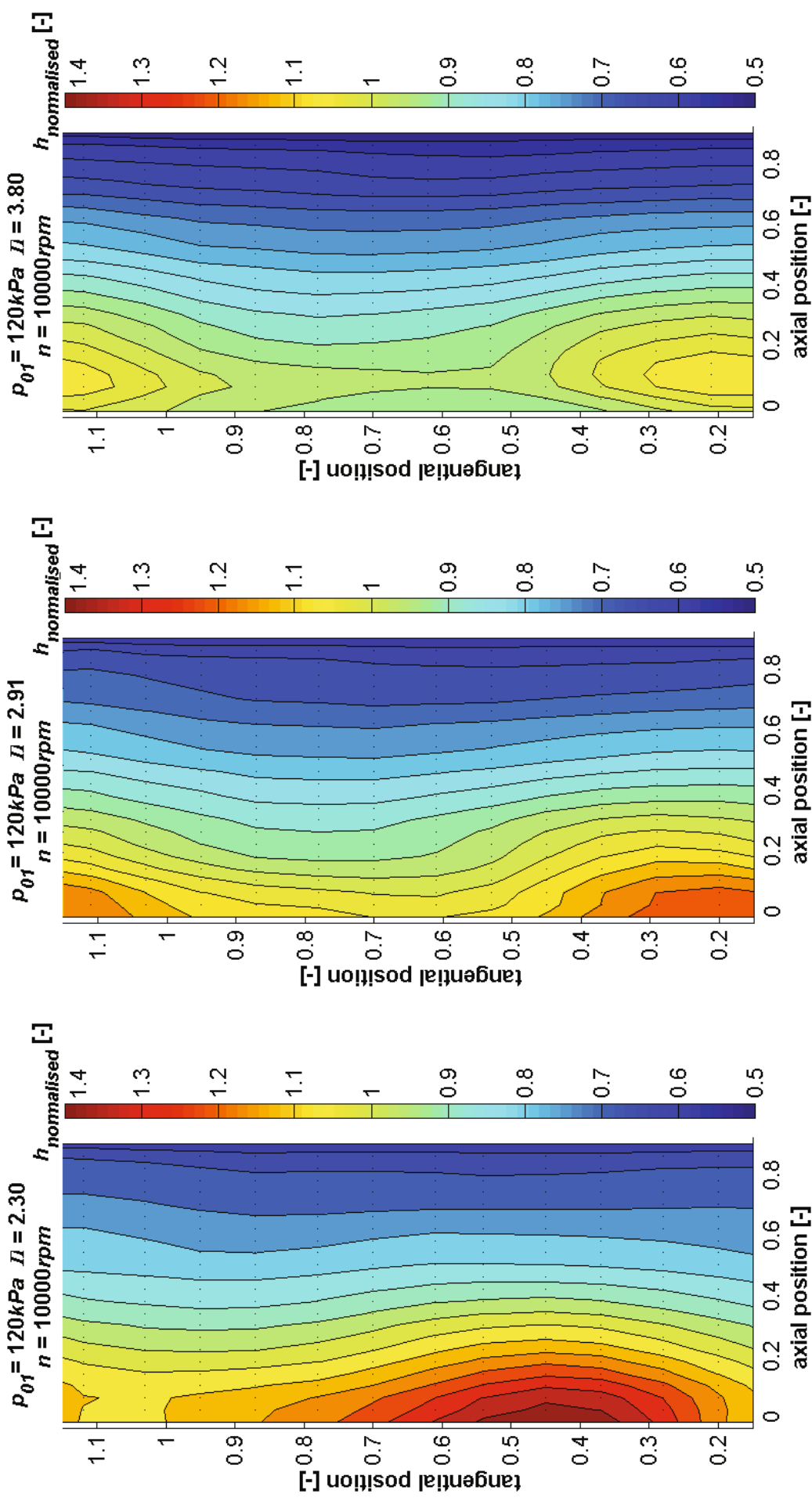


Figure 43: Heat transfer coefficient distribution at the over-tip casing

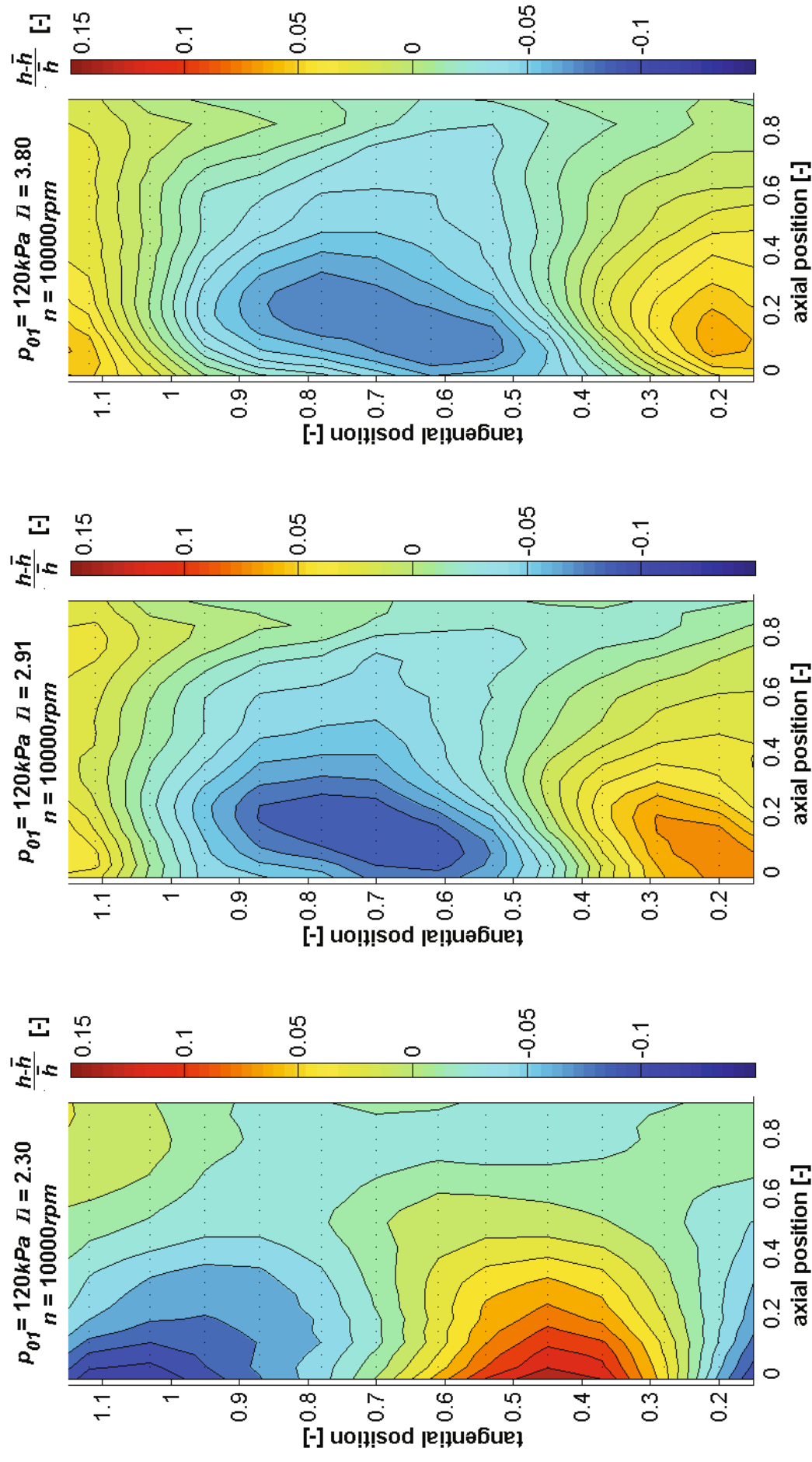


Figure 44: Heat transfer coefficient distribution at the over-tip casing; spatial variations of the pitchwise averaged signal

In chapter 5 a correlation for the prediction of the heat transfer coefficient distribution at the over-tip casing will be presented. Accordingly further interpretation of the pitchwise heat transfer coefficient profile can be found in chapter 5. The circumferential variations can aggravate local heat problems at the casing, this will not be discussed further in this report but is identified as an interesting subject for further research

4.2.5 Time-mean rotor wake results

Figure 45 shows the upper half of the rotor wake field. The measurement plane is located at $x = 0.92$ rotor chord lengths behind the rotor. The origin of the x-axis indicates the tangential position of the trailing edge of the stator vane and serves as geometrical reference and has no fluid dynamical meaning. The rotor moves in counter clockwise direction. The passage flow of the preceding stator is visible as a core of high total pressure in Figure 45. An area with a reduced total pressure indicates a field with increased losses. The stator wake effect, located at 0% vane-pitch is especially visible at mid passage height. At the top quarter the low total pressure is caused by a combination of the passage vortex and the leakage vortex.

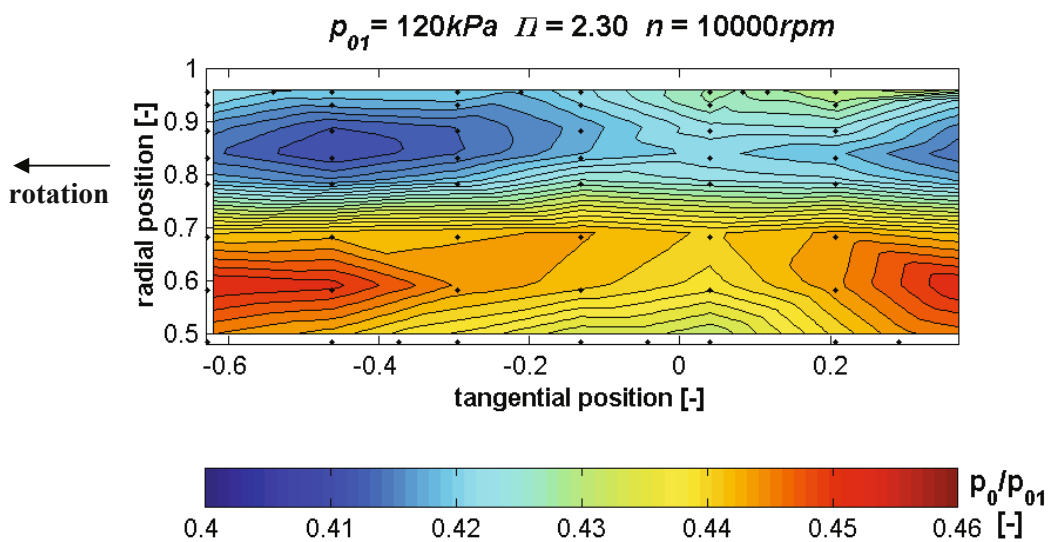


Figure 45: Rotor wake steady total pressure field

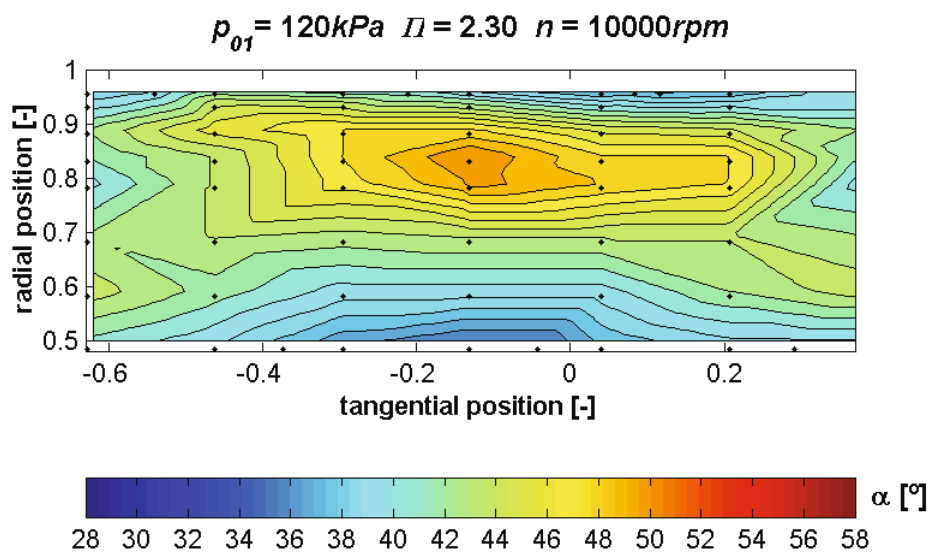


Figure 46: Rotor wake angle field

The location of the passage vortex caused by the stator can be determined best out of the yaw angle distribution shown in Figure 46. The tip gap of the stator is located at the hub; consequently no tip leakage vortex caused by the stator vanes is visible in the upper half of the passage. Figure 47 shows the total temperature distribution of the wake field.

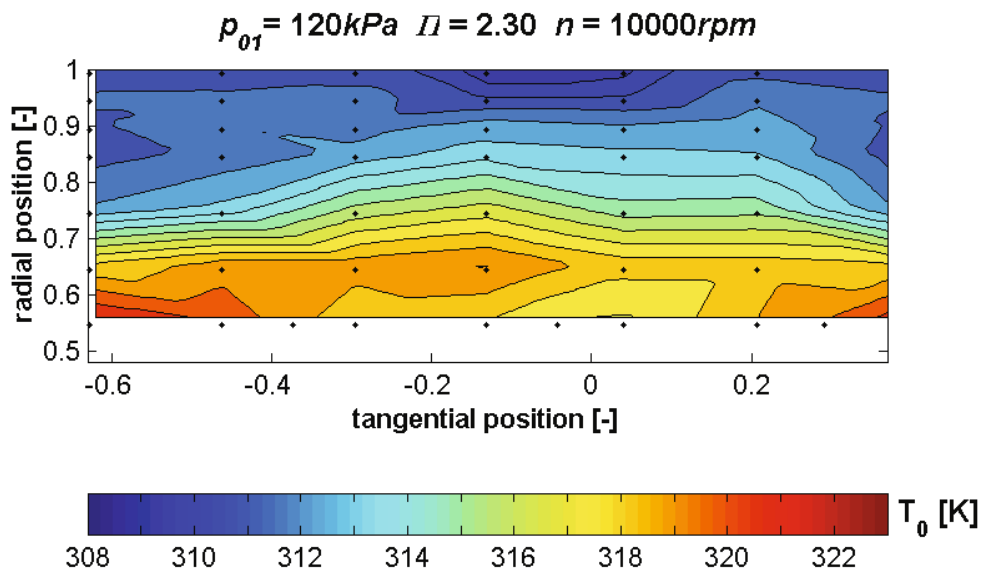


Figure 47: Rotor wake total temperature field

4.3 Time-resolved results

4.3.1 Normalised pressure distribution

Figure 48 shows the time-resolved static pressure distribution at the over-tip casing. In axial position a maximum of nine sensors were used (unfortunately surrounding conditions at the over-tip casing are very harsh which had an adverse effect on the sensor lifetime), the locations of the sensors are indicated by the dashed lines. As shown in section 3.4.2.1, the natural frequency of the sensor of 400kHz will result in approximately 16 to 20 data points per stator pitch. The flow field inside the passage depends on the relative position between the stator and the rotor. In total measurements with 16 different stator vane positions were conducted per operating condition. Figure 48 shows the averaged results of these successive measurements. As a result of the averaging the stator effect is eliminated, which enable better comparison with CFD and other experiments. The figures of other operating conditions can be found in APPENDIX D.

The non-averaged measurements can be used to examine the time-resolved interaction of the stator wake with the rotor. This was shown by Dénos et al. (2001) and Thorpe et al. (2004b), this however is not part of the present report.

Besides the strong gradient in axial direction -which was already shown in the time-averaged static pressure distribution- the most striking feature is the very steep pressure gradient at the pressure side of the blade. At the front part of the blade the flow seems to follow the camber line while at the rear part the flow nearly flows perpendicular to it. This means that the inertia forces of the inlet boundary layer fluids characterize the front part and the pressure gradients inside the gap are more essential at the rear part of the blade (Urban and Vortmeyer 2000). Figure 49 shows the matching CFD computation (TRACE), parallel to the experiments.

The static pressure field in the tip gap is characterised by strong pressure gradients that run approximately normal to the blade pressure surface from about 30% axial chord. This is in contrast to the suction surface, where up to 55% axial chord length, the static pressure gradient is approximately parallel to the local blade tip profile. Beyond 55% axial chord length, the pressure along the suction surface corner of the tip changes only slightly. This can be explained by the fact that the geometrical throat of the blade row intercepts the suction surface at approximately 55% axial chord length. (Thorpe et al. 2004b).

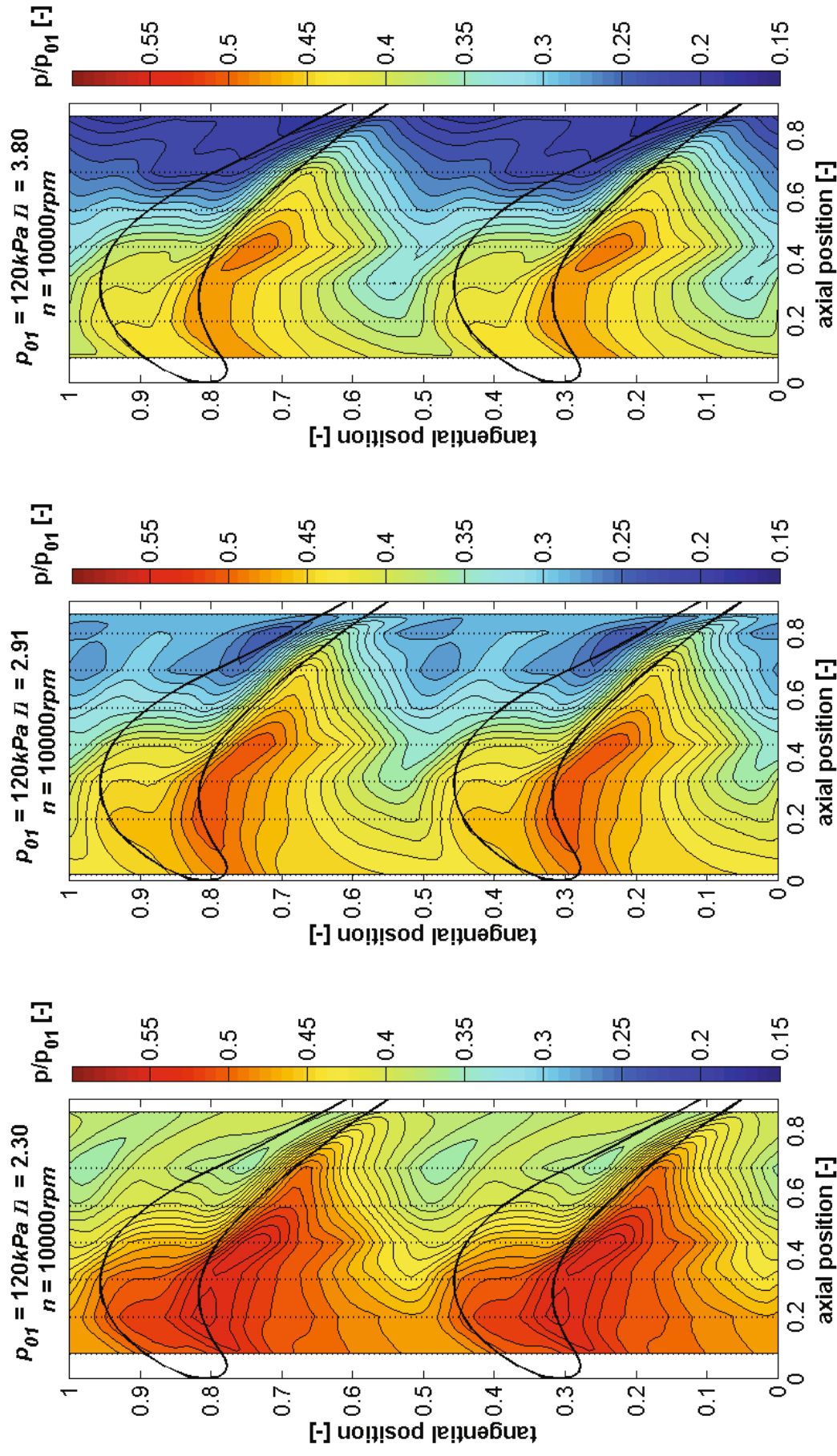


Figure 48: Time-resolved static pressure

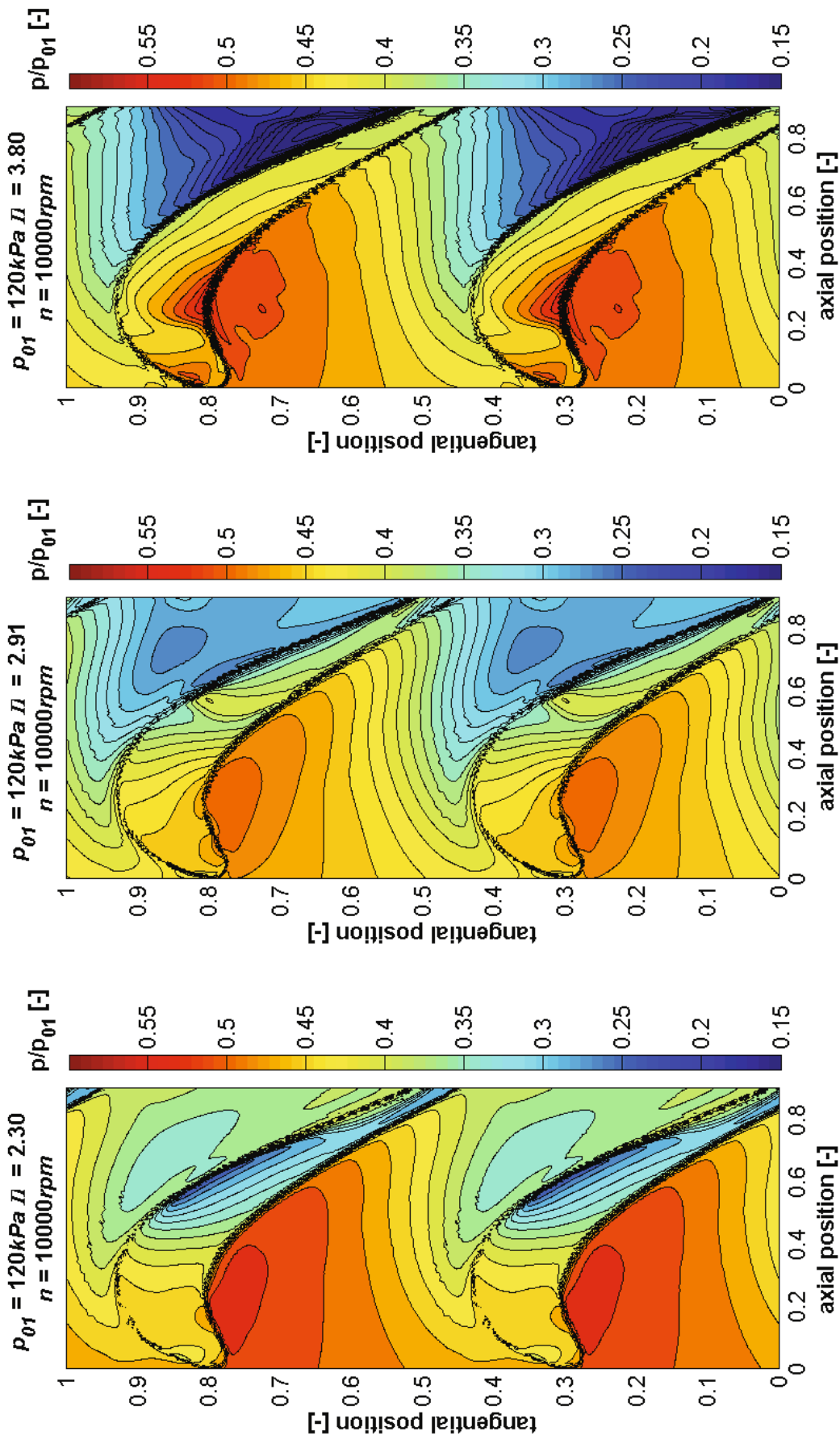


Figure 49: Time-resolved pressure distribution (CFD) (Ochrymiuk, 2007)

Figure 49 shows the results of the time-resolved pressure distribution. The CFD computations show good comparison with the experiments. Further CFD flow field and heat transfer results are presented in Ochrymiuk (2007).

4.3.2 Heat transfer distribution

Figure 50 shows the time-resolved heat transfer coefficient distribution at the over-tip casing. The time-resolved heat transfer coefficient for the operating conditions with $n = 8000\text{rpm}$ can be found in APPENDIX E. The figure clearly shows that the part of the over-tip casing, which is in the relative frame of reference located directly over the blade tip, experiences a significant elevated heat transfer level. At $x \approx 0.45$ this field is divided into two streaks. The streaks are even clearer to identify in Figure 51 where only the alternating part of the heat transfer coefficient distribution is shown.

- I.) The streak at the passage entrance corresponds to the region where the fluid experiences a strong acceleration into the tip gap passage. The acceleration is driven by the big pressure difference between the passage side and the suction side. The acceleration has two effects: it will cause the boundary layer to relaminarise and it will significantly reduce the thickness of the boundary layer. Whereas the relaminarisation has a diminishing effect on the heat transfer, the rejuvenation of the boundary layer has a boosting effect. The existence of the hot streak at the passage proves that the second effect is more dominant. At the passage entrance closer to the leading edge of the blade, this pressure difference has not yet been built up and consequently no high heat transfer region can be seen.
- II.) The second streak at the passage exit represents the region affected by the tip leakage vortex. The tip leakage vortex generally starts at around one quarter of the blade chord ($x = 0.25$) and will from there on increase in size and intensity. The vortex will result in downwashing of the hot fluid into the thermal boundary layer. According to Rhee et al. (2001) an additional reason for the elevated heat transfer coefficient is the flow transition back to the turbulent regime.
- III.) The two streaks are superimposed on a region of general high heat transfer located at the tip gap. This general area with elevated heat transfer is caused by the deflection of the fluid inside the passage in a manner that it does less work and the total temperature is reduced less. This affects the conductivity of air and consequently also the heat transfer coefficient.

The time-resolved heat transfer distribution at the over-tip casing will be discussed further in the second part of chapter 5.

4.3.3 Time-resolved wake results

Figure 52 shows the results of the time-resolved measurements for the operating condition with $p_{01} = 120 \text{ kPa}$, $n = 10000 \text{ rpm}$, $\Pi = 3.80$. The flow angle was obtained with the procedure described in section 3.5.1.2, which proves to be a very effective and accurate method for determining the time-resolved wake angle and the tangential velocity component. The figure shows the presence of the passage vortex, but the tip leakage vortex cannot be identified. The cause for this can be found in the – out of construction reasons - long distance between the rotor trailing edge and the probe.

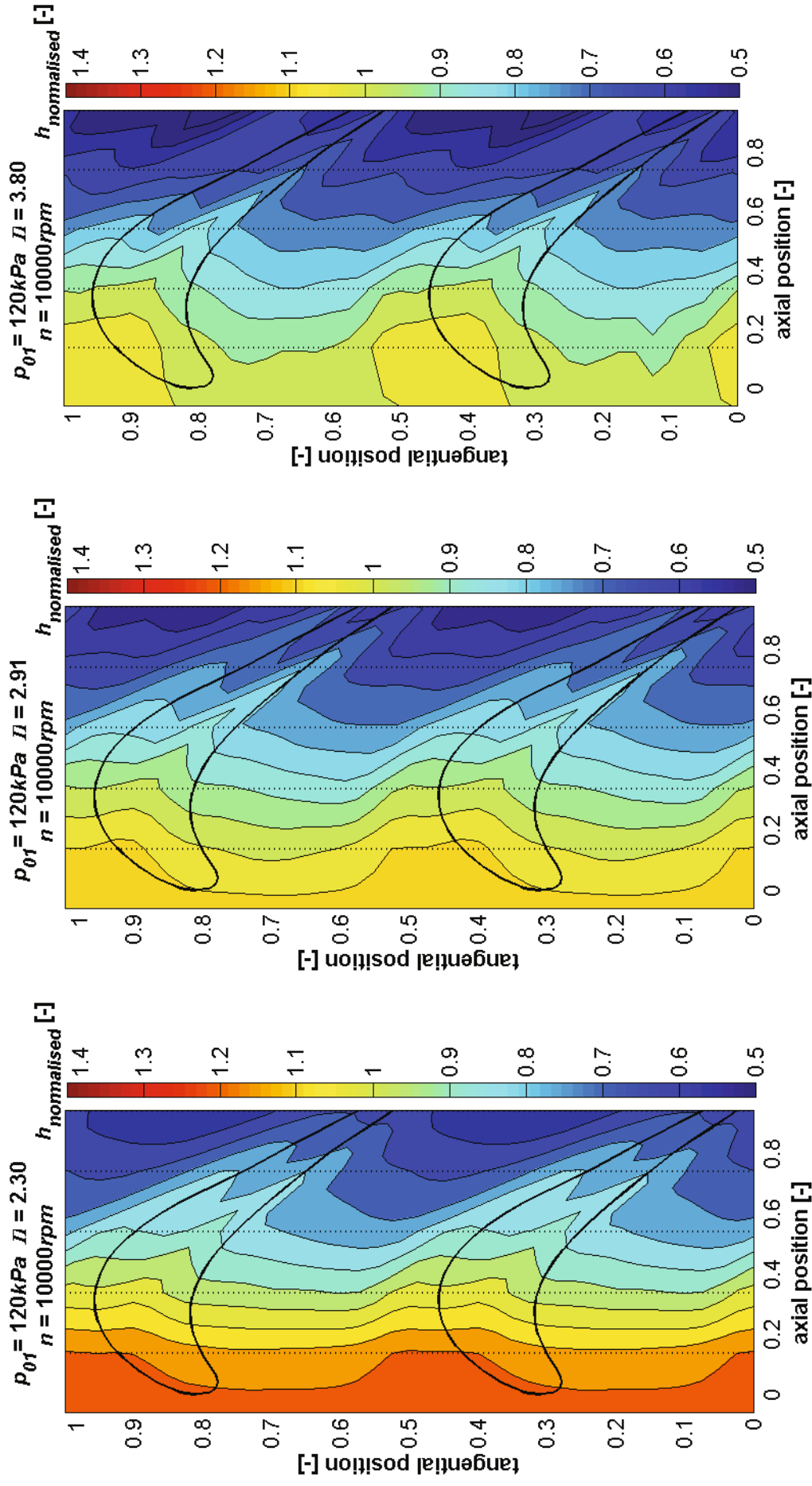


Figure 50: Time-resolved heat transfer coefficient distribution at the over-tip casing

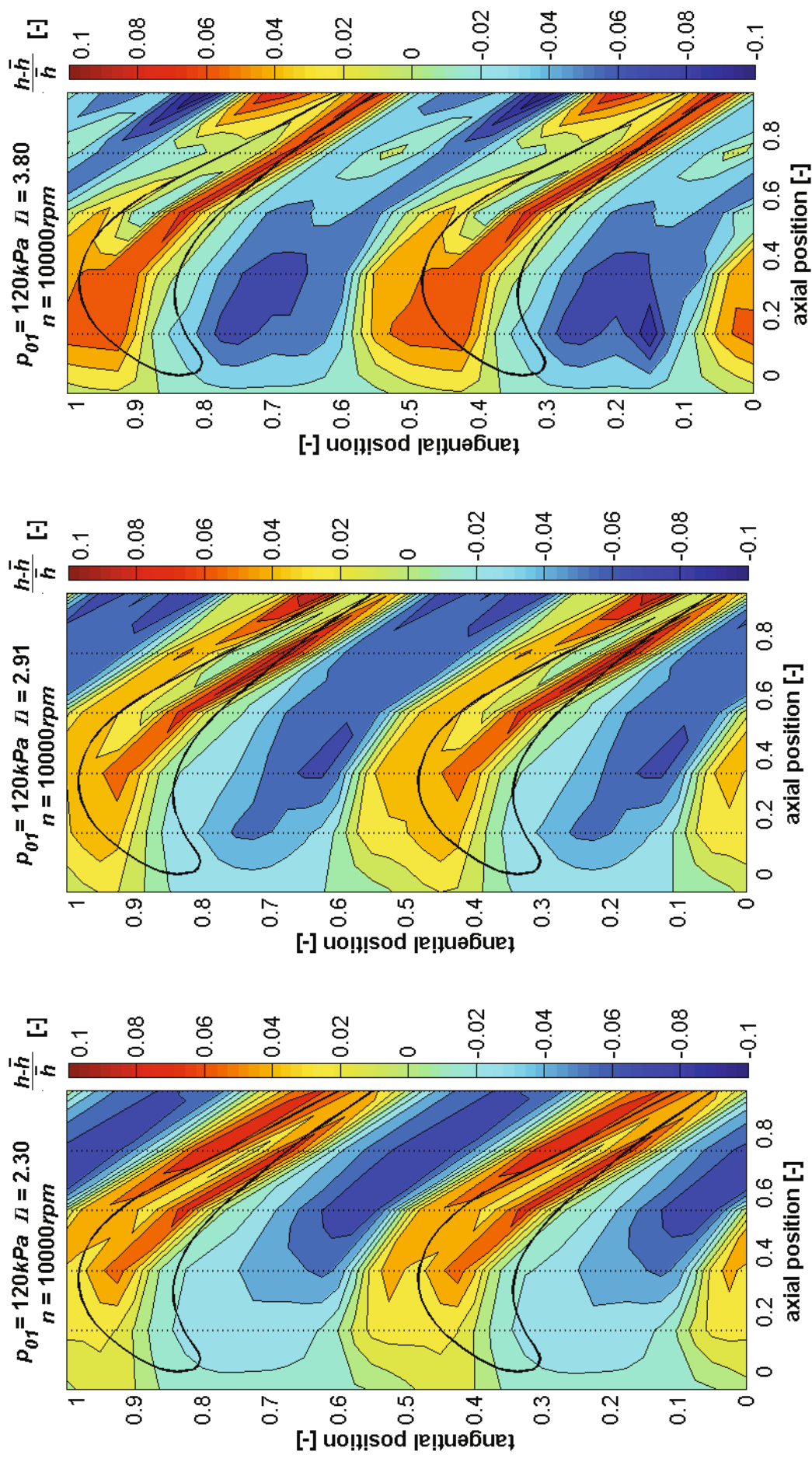


Figure S1: Alternating time-resolved heat transfer coefficient distribution at the over-tip casing

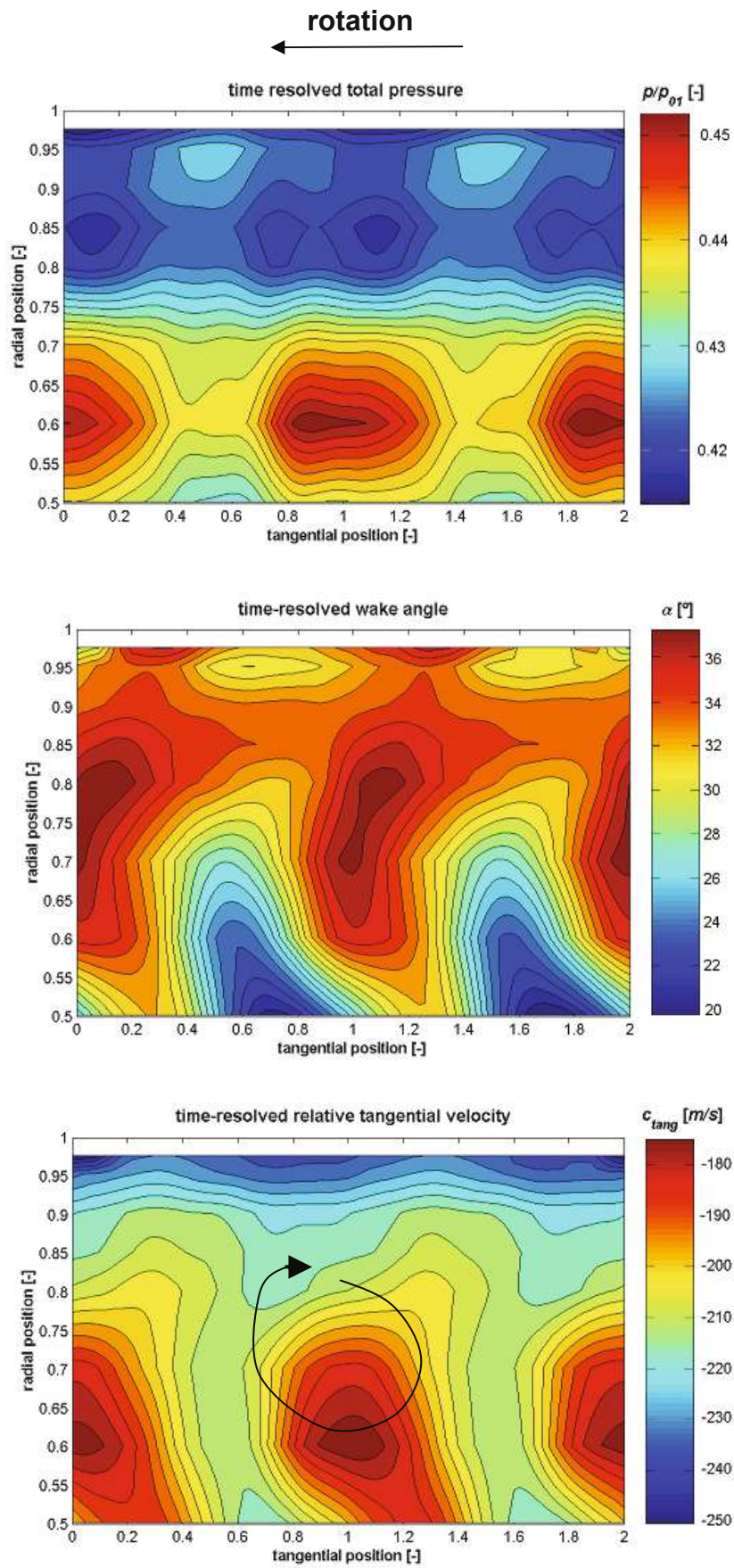


Figure 52: Time-resolved wake results

5 CORRELATIONS OF HEAT TRANSFER COEFFICIENT AT THE OVER-TIP CASING

Although the flow at the over-tip casing is very complex, the most logical starting point for any heat transfer correlation is that of the flat plate. It can be assumed that the boundary layer at the over-tip casing – excluding some regions which will be discussed in section 5.2 - will be fully turbulent. Metzger et al. (1991) showed that the conventional heat transfer correlation for the turbulent boundary layer:

$$Nu = 0.0296 \cdot Re^{4/5} \cdot Pr^{1/3} \quad (5.1)$$

can be successfully used to estimate the expected heat flux at the over-tip casing including the variation in the axial direction. This report aims to explore the validity of equation (5.1) for turbine stages operating under engine realistic conditions and extending the equation for the off-design conditions.

In the first part of this chapter, the conventional Nusselt correlations for the flat plate will be evaluated in three steps using:

- 1) averaged flow conditions and axial flow direction.
- 2) averaged flow conditions and flow along the averaged streamlines (camber line).
- 3) variable flow conditions and flow along the averaged streamlines (camber line).

A fourth step will consist of evaluating the effect of the upstream boundary conditions.

Although section 5.1 will show that the Nusselt correlations for the flat plate are a powerful start for the prediction of the over-tip casing heat transfer distribution, in order to extend the range of application for off-design conditions, additional parameters have to be introduced. That will be the subject of the second part of this chapter.

5.1 Evaluation of the conventional flat plate heat transfer correlation

5.1.1 Introduction of Nusselt correlations for the flat plate

The factors of the flat plate correlation are dependent on the acting boundary conditions and the type of heating. The following relevant correlations for the flat plate were taken from Bejan (1992):

I.) Isothermal heating, starting from the edge. This is the most frequent used condition.

$$\text{Nu} = 0.0296 \cdot \text{Re}^{4/5} \cdot \text{Pr}^{1/3} \quad (5.2)$$

II.) Isothermal heating, starting from distance x_0 from the edge.

$$\text{Nu} = 0.0296 \cdot \text{Re}^{4/5} \cdot \text{Pr}^{1/3} \cdot \left[1 - \left(\frac{x_0}{x} \right)^{9/10} \right]^{-1/9} \quad (5.3)$$

III.) Uniform heat flux, starting from the edge.

$$\text{Nu} = 0.0308 \cdot \text{Re}^{4/5} \cdot \text{Pr}^{1/3} \quad (5.4)$$

The local Reynolds and Prandtl number are defined as:

$$\text{Re} = \frac{c \cdot x \cdot \rho}{\mu} \quad (5.5)$$

$$\text{Pr} = \frac{v \cdot \rho \cdot c_p}{\lambda} \quad (5.6)$$

5.1.2 Averaged flow conditions and axial flow direction

For a first approximation, the correlations are fed with the averaged velocity and the fluid properties measured at the over-tip casing. The fluid is assumed to flow axially over the plate. The averaged values are presented in Table 7, and correspond to the values measured for operating point with: total pressure $p_{01} = 120 \text{ kPa}$, rotational speed $n = 10000 \text{ rpm}$ and pressure ratio $\Pi = 2.9$.

fluid velocity	c	265 m/s
density	ρ	0.5 kg/m^3
viscosity	μ	$1.9\text{e-}5\text{ kg/(s}\cdot\text{m)}$
thermal conductivity	λ	$0.0257\text{ W/(m}\cdot\text{K)}$

Table 7: Averaged velocity and fluid properties

The difference between the fluid and the wall temperature (driving temperature) and heat transfer coefficient distribution of the plate for the various cases can be determined with:

$$\Delta T = \frac{\dot{q}}{\text{Nu}} \frac{x}{\lambda} \quad h = \frac{\text{Nu} \cdot \lambda}{x} \quad (5.7)$$

In Figure 53 and Figure 54 the wall temperatures respectively the heat transfer coefficient distributions obtained by the various correlations are shown.

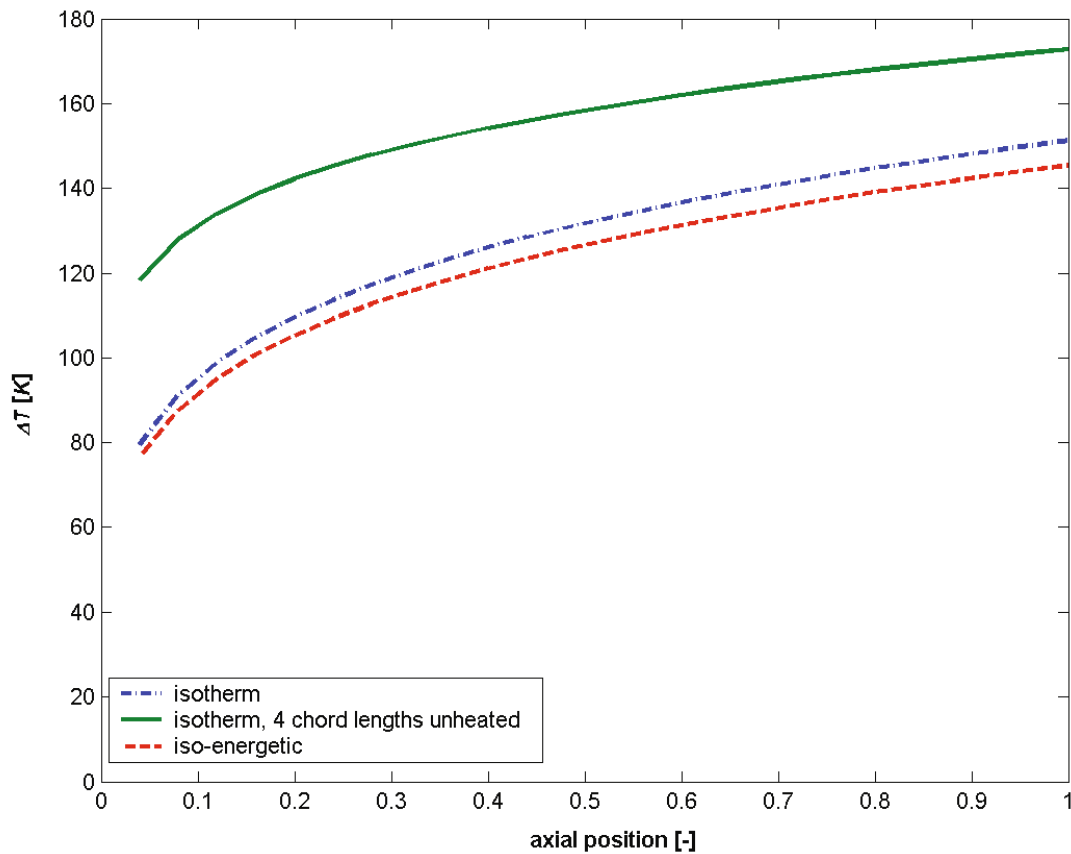


Figure 53: Wall temperature: constant fluid properties, straight flow

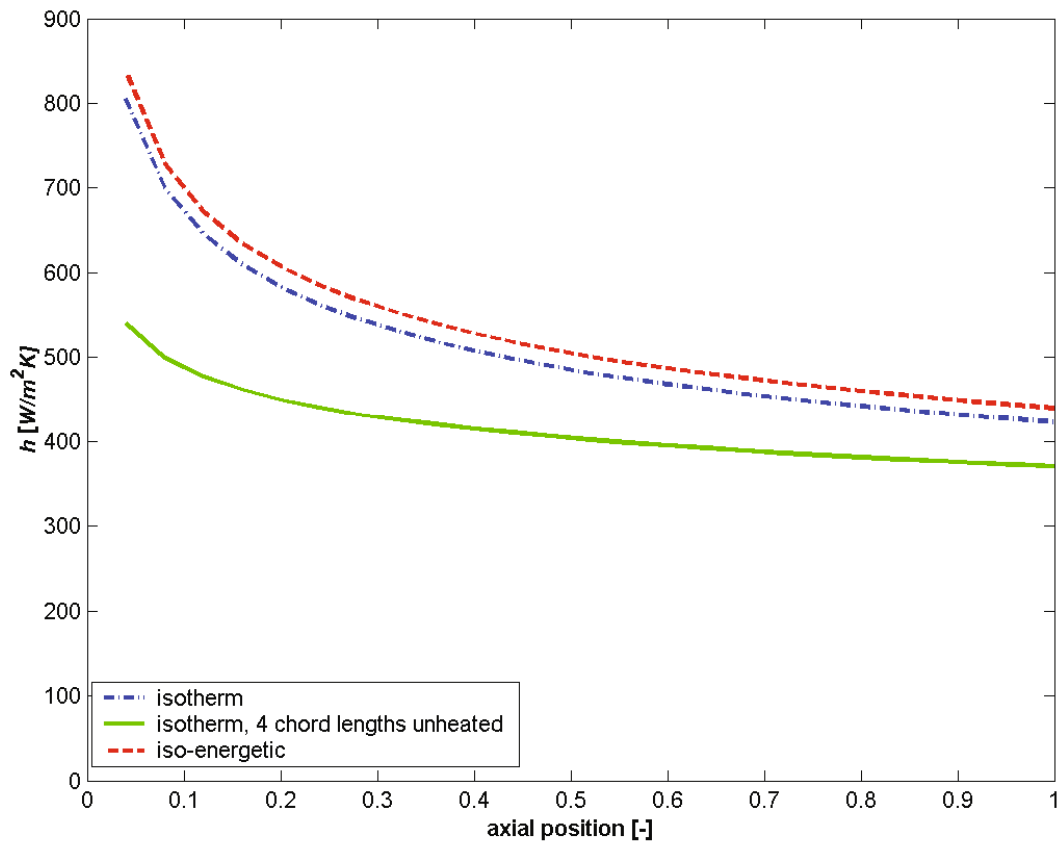


Figure 54: Heat transfer coefficient distribution with constant fluid properties, straight flow

As described in section 3.4.1.1, the over-tip casing is heated electrically with uniform heat flux. Out of constructional reasons it is impossible to heat the whole turbine stage; accordingly there will always be an upstream starting point of the heating area (the significance of this boundary condition will be discussed further in section 5.1.5). Consequently a mixture of equation (5.3) and (5.4) would be most suited. However since an analytical formula for a uniformly heated wall not starting from the edge is not known (at least not to the author), equation (5.3) is chosen as basis for further examination. The difference between isothermal and isoenergetic conditions is only small. According to Bejan (1993) the local Nusselt number for a wall with uniform heat flux is only 4% greater than that of the isothermal case.

When the heating does not start at the edge of the plate (an unheated segment is located upstream of the heating), a viscous boundary layer is already developed before it reaches the start of the heating. The thicker boundary layer is reducing the convection of heat from the plate into the main flow, this will cause the plate to heat up more and the heat transfer will be reduced.

The unheated length of four chord lengths corresponds to the path length between the stator trailing edge and the beginning of the heating, when the flow angle between the stator and rotor measures 78° (the stator wake angle flow will be discussed more deeply in section 5.1.6). It is assumed that due to the strong acceleration at the stator, the boundary layer will be thin. In section 5.1.5 the length will be varied to examine the sensitivity of this parameter.

5.1.3 Averaged flow conditions along the streamlines

Figure 55 shows the averaged streamlines in the rotor passage, calculated with a one-dimensional streamline calculation method. This method is described in APPENDIX F. The figure shows the streamlines at the over-tip casing for various operating conditions.

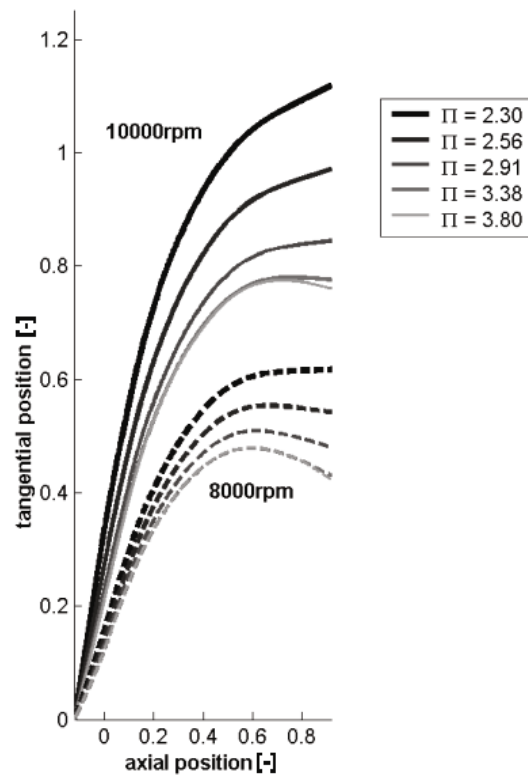


Figure 55: Streamlines at the over-tip casing

In the previous section the flow over the over-tip casing was assumed to be axial. Figure 55 clearly shows that especially at entrance the streamlines are far from axial. This means that the boundary layer has - from an axial perspective - more time to establish. The influence of the change of the pathlength over the over-tip casing on the wall temperature and heat transfer coefficient are shown in Figure 56 respectively Figure 57 for the operating point with: total pressure $p_{01} = 120kPa$, rotational speed $n = 10000rpm$ and pressure ratio $\Pi = 2.9$.

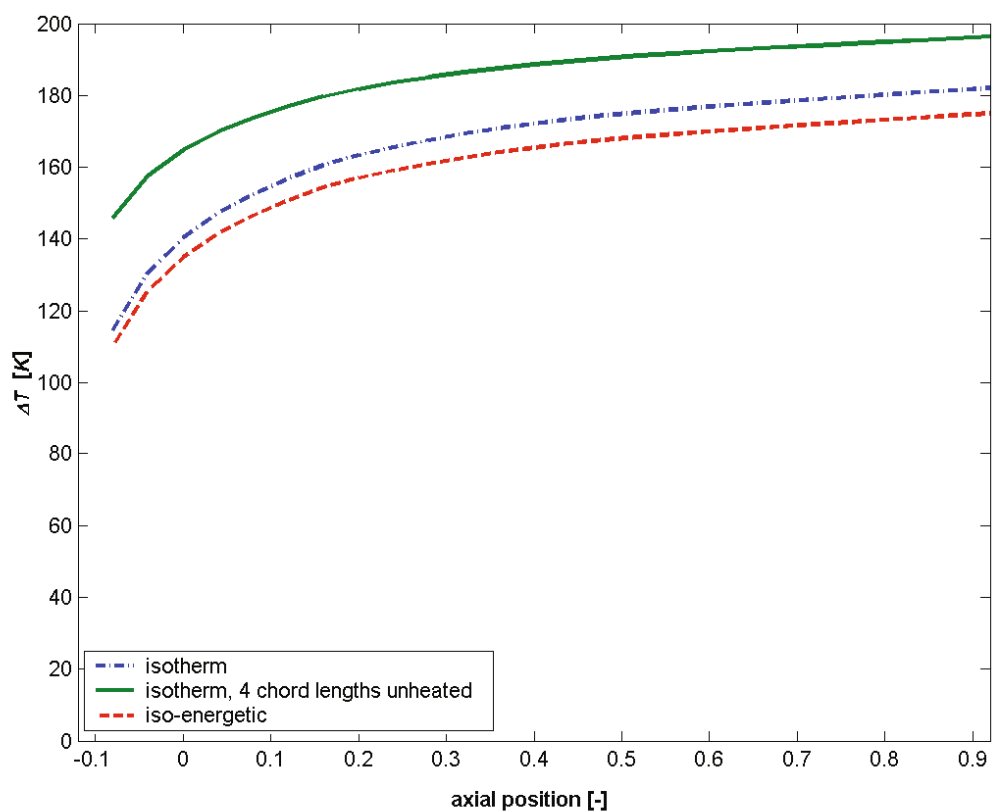


Figure 56: Wall temperature: constant fluid properties, curved flow path

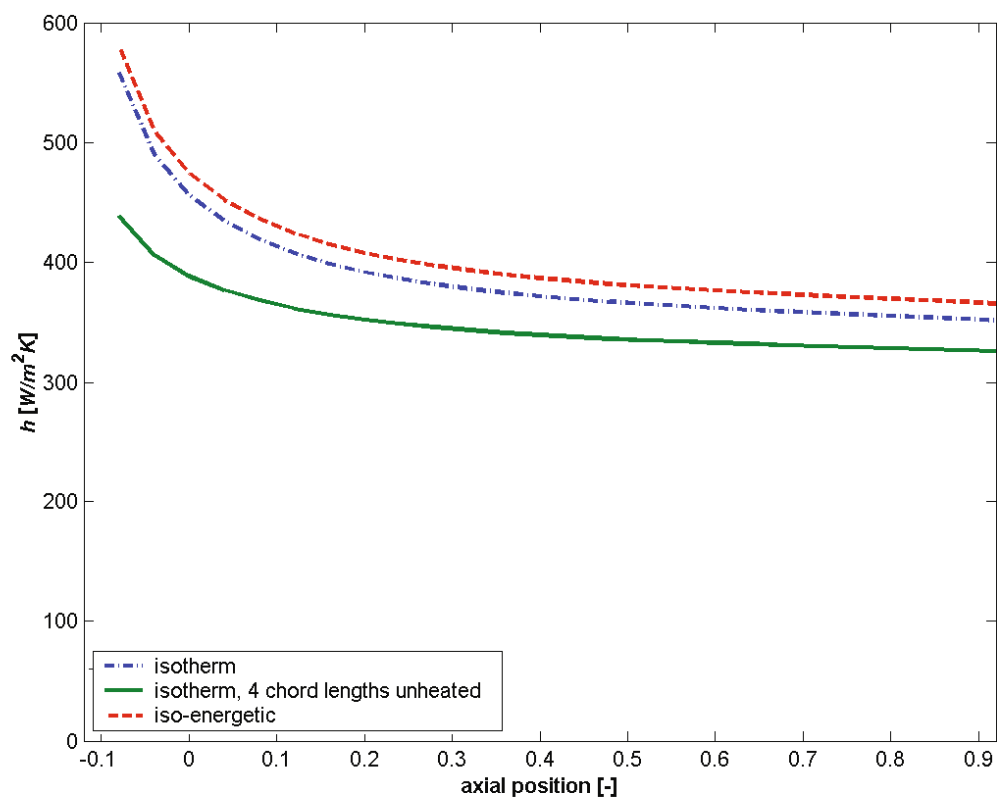


Figure 57: Heat transfer coefficient with constant fluid properties, curved flow path

5.1.4 Variable flow conditions along the streamline

The level of complexity and realism can be further improved by using the actual static pressure and static temperature distribution of the flow at the over-tip casing. The static pressure distribution is directly measured (section 4.2.2), the static temperature distribution is obtained via the measured wall temperature (as described in APPENDIX G). The axial distribution of fluid properties for one operating point ($p_{01} = 150kPa, n = 10000rpm, \Pi = 2.9$) are shown in Figure 58 and Figure 59. The local Reynolds and Nusselt numbers are calculated by inserting the progressive averaged properties (averaged between start und local coordinate) in correlation (5.3). The progressive averaged properties of interest are shown by the dashed lines.

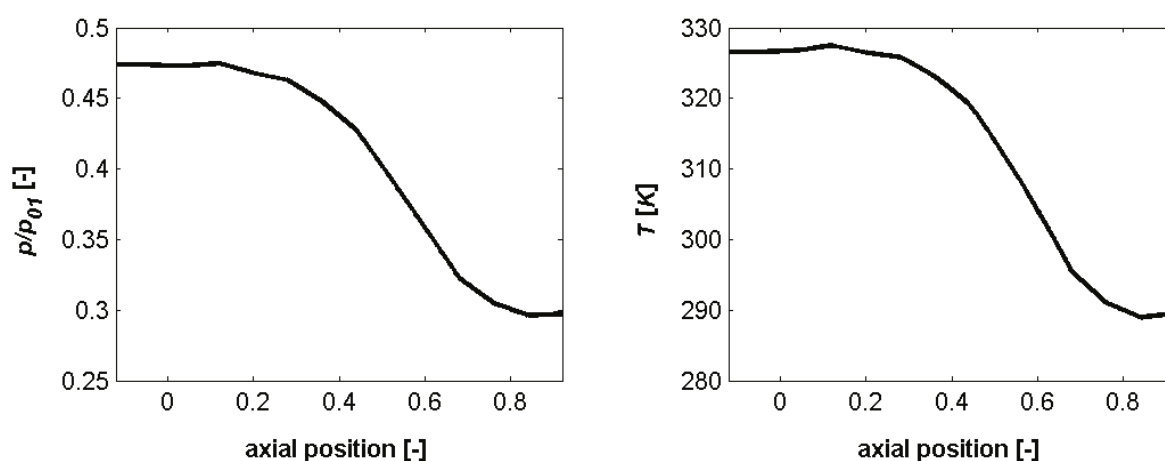


Figure 58: Static pressure and static temperature distribution over the over-tip casing (experimental)

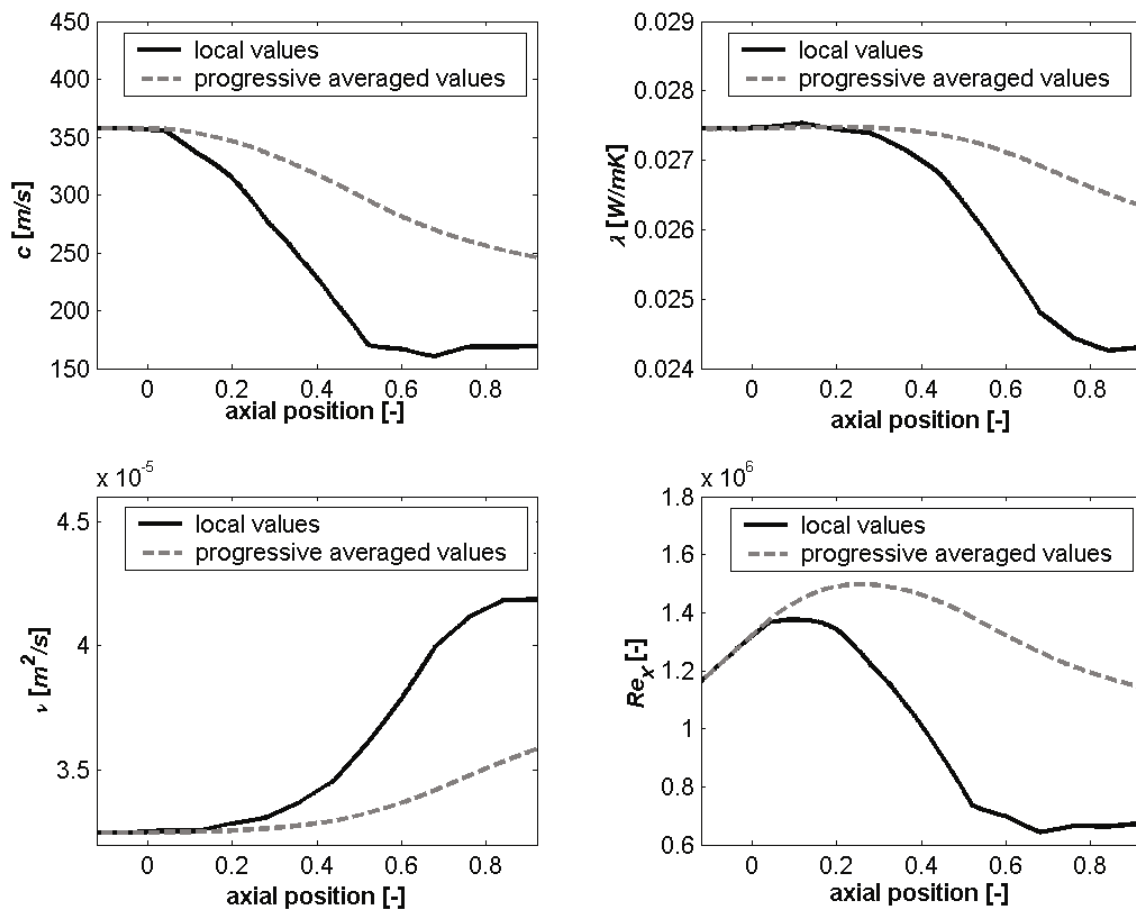


Figure 59: Local and averaged velocity and fluid parameters

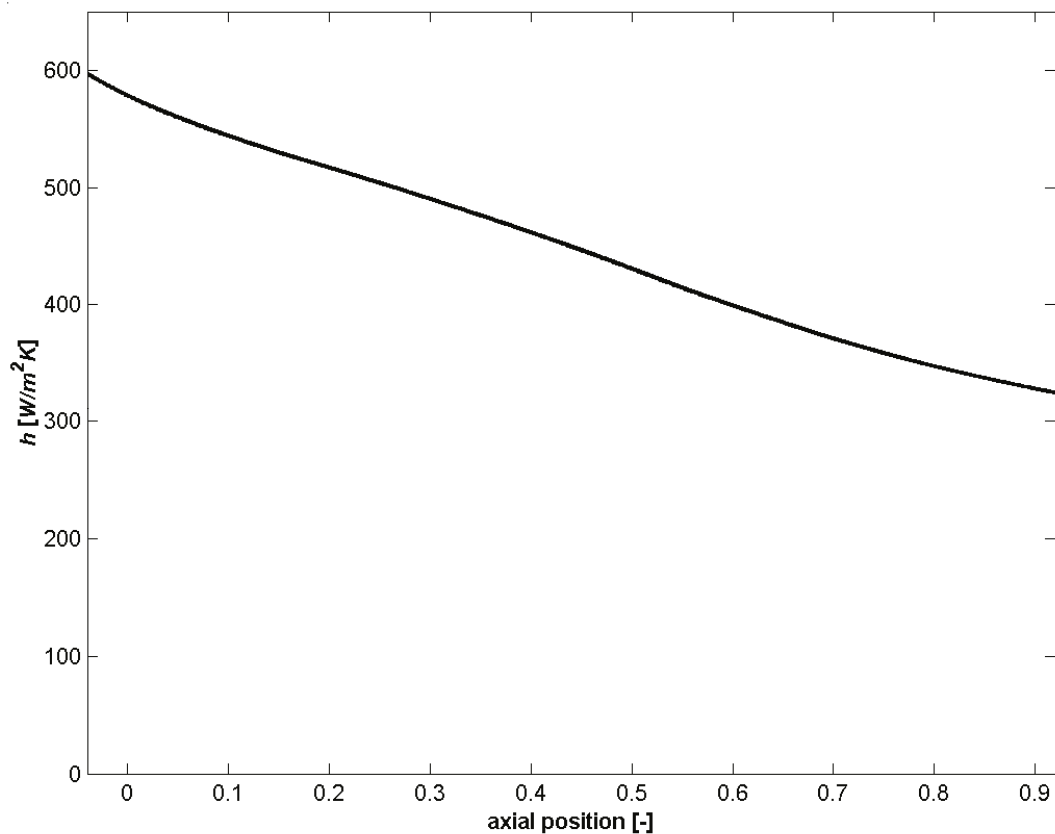


Figure 60: Heat transfer coefficient distribution for condition: $p_{01} = 120\text{kPa}$, $n = 10000\text{rpm}$, $\Pi = 2.9$.

The axial heat transfer coefficient distributions shown in Figure 60 correspond well with the steady heat transfer measurements presented in section 4.2.4 (this does make the correlations of the flat plate a good starting point for any correlations for the over-tip casing region).

5.1.5 Evaluation of the effect of the upstream boundary conditions

In order to examine the influence of the starting point of the heating, the heating area can be (analytically) extended: The starting point of the thermal boundary condition is moved more upstream, the viscous boundary layer remains unchanged. Consequently with an additional heating of four chord lengths, the starting point of the thermal and viscous boundary layer are identical. The resulting heat transfer coefficient distribution is presented in Figure 61.

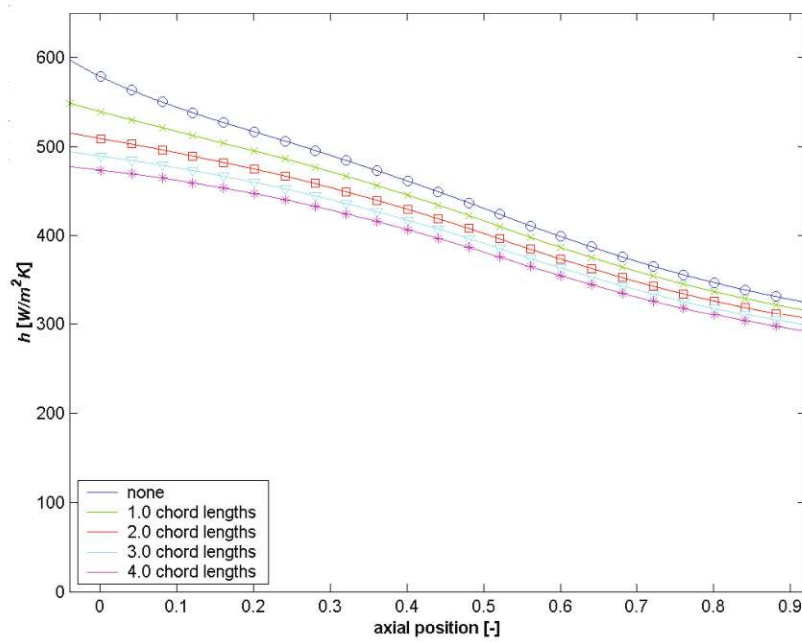


Figure 61: Heat transfer coefficient distribution as a function of the extended heating length, condition:
 $p_{01} = 120\text{kPa}$, $n = 10000\text{rpm}$, $\Pi = 2.9$

Figure 61 shows a parameter study of the influence of the length of the additional heating placed directly upstream of the existing heating elements at the over-tip casing (operating point: $p_{01} = 120\text{kPa}$, $n = 10000\text{rpm}$, $\Pi = 2.9$). The strong gradient in the most upstream part ($x < 0.12$) of the passage is caused by the warm-up effect at the beginning of the heating area. With increasing additional heating length the maximum is reduced, but even with very long lengths of 4 chord lengths or more the gradient of the curve remains continuously negative. The downstream part of the passage is hardly affected by the warm-up effect.

The absolute heat transfer level is reduced with increasing heating length (with an infinite heating length the heat transfer coefficient will approach zero). The heat transfer distribution of the real gas turbine is best represented when the thermal boundary layer length equals that of the viscous boundary layer. It is assumed that the viscous boundary layer is renewed by the strong acceleration at the stator. The path length between the stator and the rotor corresponds to approximately four chord lengths.

The warm-up effect is an inevitable effect for any quantitative measurement technique (thermocouples, IR-thermography, Naphthalene sublimation or liquid crystals) which deals with continuous flow conditions and restricted heating space.

5.1.6 Effect of stator wake angle deviation

As shown in equation (5.3) and (5.5) the path length is an important parameter for the local heat transfer coefficient. The path length between the stator and rotor is primarily set by the absolute wake angle of the stator, this principle is illustrated in Figure 62. A shallow (more axial) wake angle will result in a more direct path. This gives the boundary layer less time to develop and to become thicker and also allows the boundary layer to lose less heat before it encounters the over-tip casing. Consequently a shallower wake angle will cause a higher heat transfer level in the rotor passage.

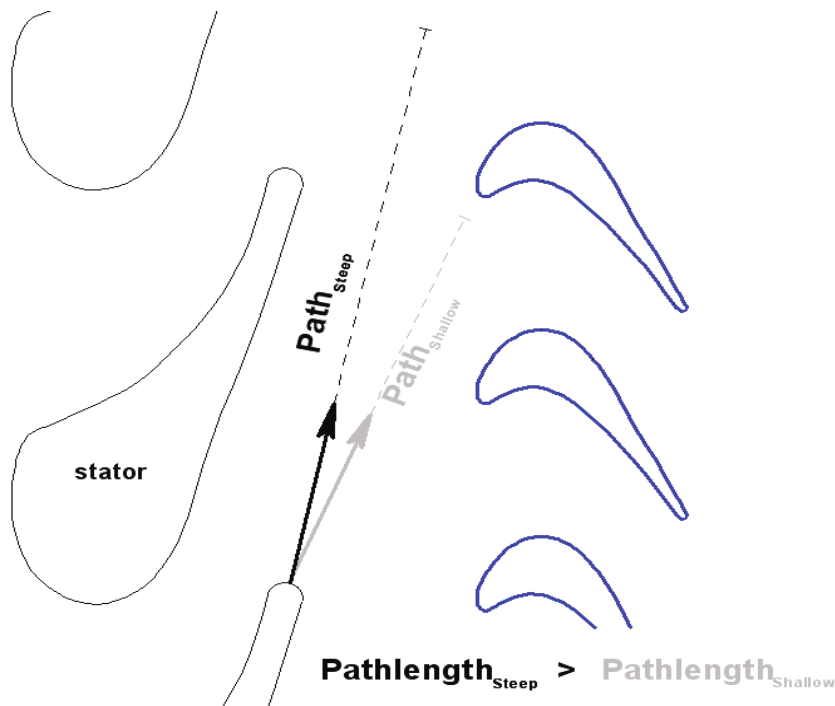


Figure 62: Sketch of the influence of the stator wake angle on the path length between the stator and rotor entrance

Figure 63 shows the heat transfer coefficient at rotor entrance ($x = 0$) as function of the average flow angle between stator and rotor. The heat transfer is normalised on value corresponding to the geometrical wake angle at 78° . This effect is independent of the fluid velocity and therefore valid for all operating conditions.

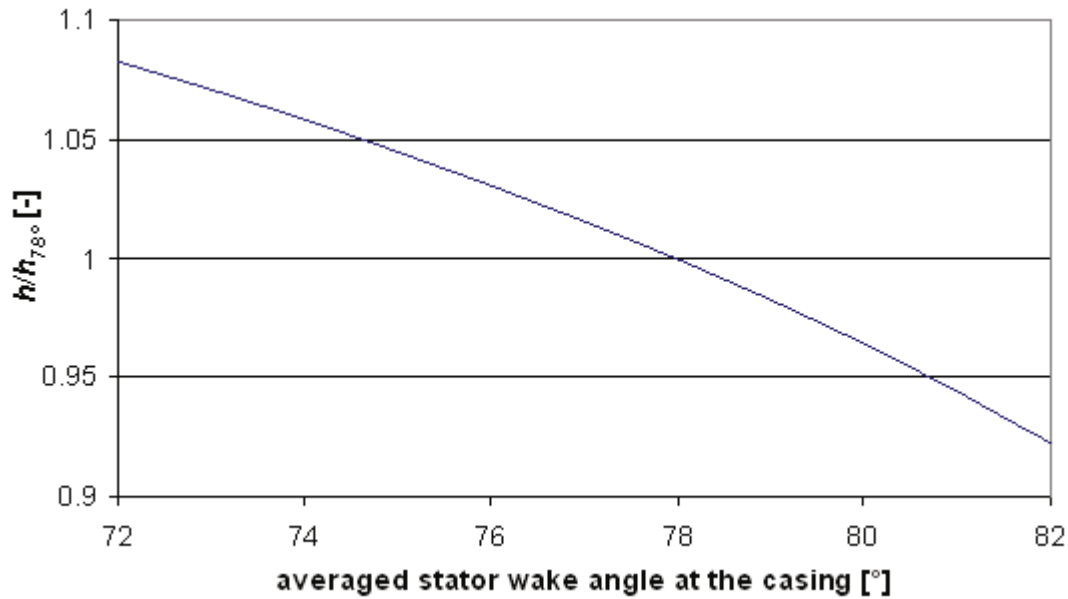


Figure 63: Heat transfer coefficient at the rotor entrance as function the stator wake angle

The geometrical wake angle of the stator vane is 78° . With the aid of the continuity-equation the homogeneous wake angle can be determined to be $\approx 76^\circ$.

5.1.6.1 Fluid flow angle deviation caused by the passage vortex

The passage vortex arises from the shifting of the radial equilibrium within the boundary layer. In the passage between two neighbouring turbine blades of a turbine cascade a strong longitudinal pressure gradient exists. Additional to this pressure gradient, the flow through the passage is acted upon by a centrifugal force resulting from the curvature of the flow path through the passage. These two forces are in equilibrium:

$$\frac{\partial p}{\partial r} = \frac{dp}{dr} = \frac{\rho c^2}{r}. \quad (5.8)$$

In the vicinity of the wall, the velocity of the flow is reduced due to the wall friction and therefore the equilibrium is disturbed: the centrifugal force is reduced and the pressure force becomes more dominant. As a result, the slower fluid near the wall flows more towards the suction side of the passage. This additional velocity component, which is directly perpendicular to the main stream, is called the secondary flow and is observable as a curvature of the flow. The unequal curvature of different fluid layers is often manifest in the form of a vortex. The over turning of the fluid at the casing is observable in various literature sources (e.g. Kost and Nicklas (2001) and Willinger (2002)).

Figure 64a and b show the stator wake Mach number distribution at respectively 75% and 95% of the passage height. It is assumed that the averaged wake angle at 75% passage height corresponds to that of the main – by the passage vortex unaffected - passage flow. Both figures display a region of reduced velocity caused by the stator wake. Since the minimums of the graphs of Figure 55a are found on the same position it can be concluded that the flow angle of the main passage flow is independent of the prevailing pressure ratio. The graphs of Figure 55b however show that in proximity of the wall the location of the stator wake is dependent on the pressure ratio. With increasing pressure ratio, the pressure gradient becomes more dominant and the wake angle increases. Table 8 lists the stator wake angle at 75% and 95% passage height and the resulting angle modification. This variation might seem small, however as shown in Figure 63 a 3.3° change of the stator wake angle causes a decrease of the heat transfer coefficient at the passage entrance of approximately 5%. Additionally the table shows that a change of the pressure ratio can alter the stator wake angle by about 1.6° . The results of Figure 64 were obtained at 95% passage height, it can be expected that the secondary component closer to the wall be even stronger and therefore increasing the total effect.

pressure ratio	2.30	2.56	2.91	3.38	3.80
stator wake angle at $h = 75\%$	$76,1^\circ$	$76,1^\circ$	$76,1^\circ$	$76,1^\circ$	$76,1^\circ$
stator wake angle at $h = 95\%$	77.8°	77.9°	78.3°	78.9°	79.4°
difference	1.7°	1.8°	2.2°	2.8°	3.3°

Table 8: Stator wake angle deflection caused by the passage vortex

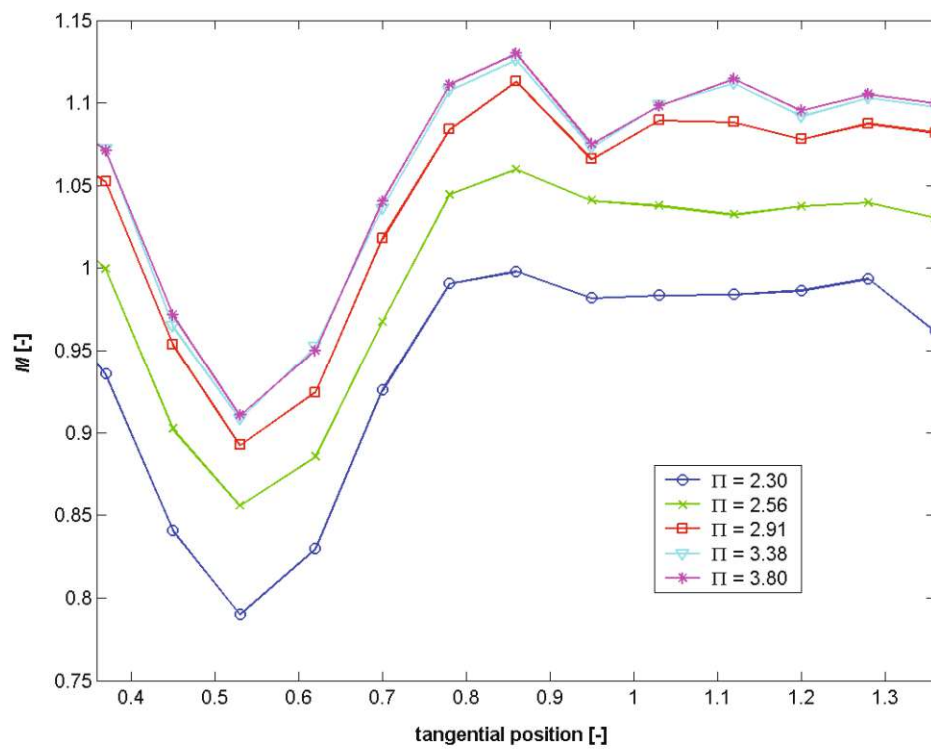


Figure 64a: Stator wake Mach number distribution at $h = 0.75$ passage height

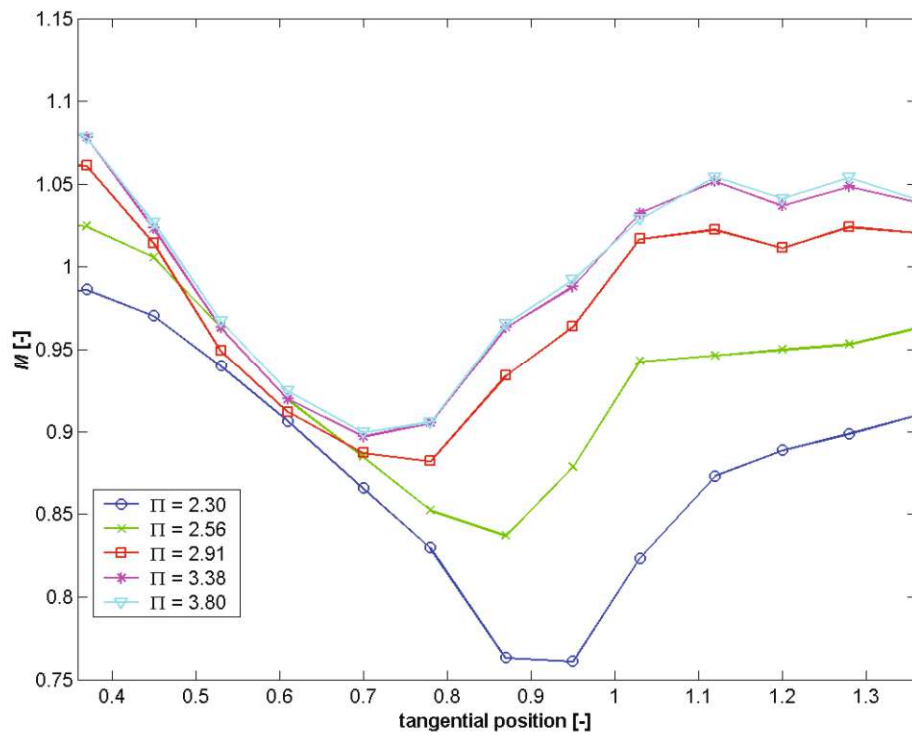


Figure 64b: Stator wake Mach number distribution at $h = 0.95$ passage height

5.1.7 Comparison of analytical and experimental results

Figure 65(a to h) show the experimental heat transfer results (solid lines) as obtained in section 4.2.4 and the analytical heat transfer results (dashed lines) as obtained in section 5.1.4. The flat plate correlation gives a good first prediction of the heat transfer coefficient over the complete over-tip casing. Also the strong influence of the Reynolds number -represented by the two different pressure levels- is well accounted by the correlation. Consequently the flat plate correlation offers a proper basis for an enhanced heat transfer model for the over-tip casing.

The figure furthermore shows that the heat transfer level is constantly underestimated by the correlation. Obviously there are additional heat transfer raising effects which are not accounted for by the flat plate correlation. These effects will be the topic of the second part of this chapter.

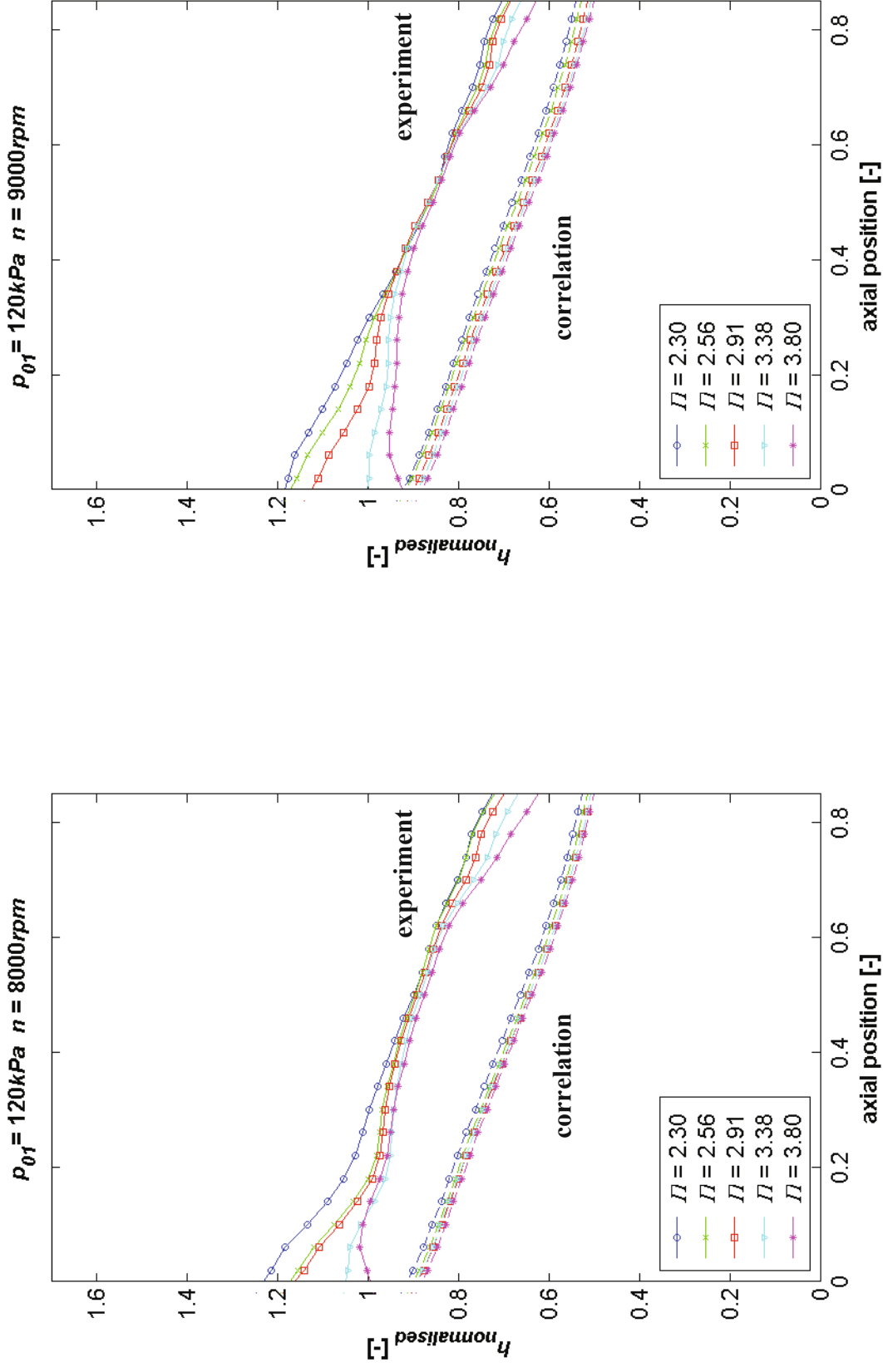


Figure 65a (right) and b (left): Experimental and analytical heat transfer coefficient distribution

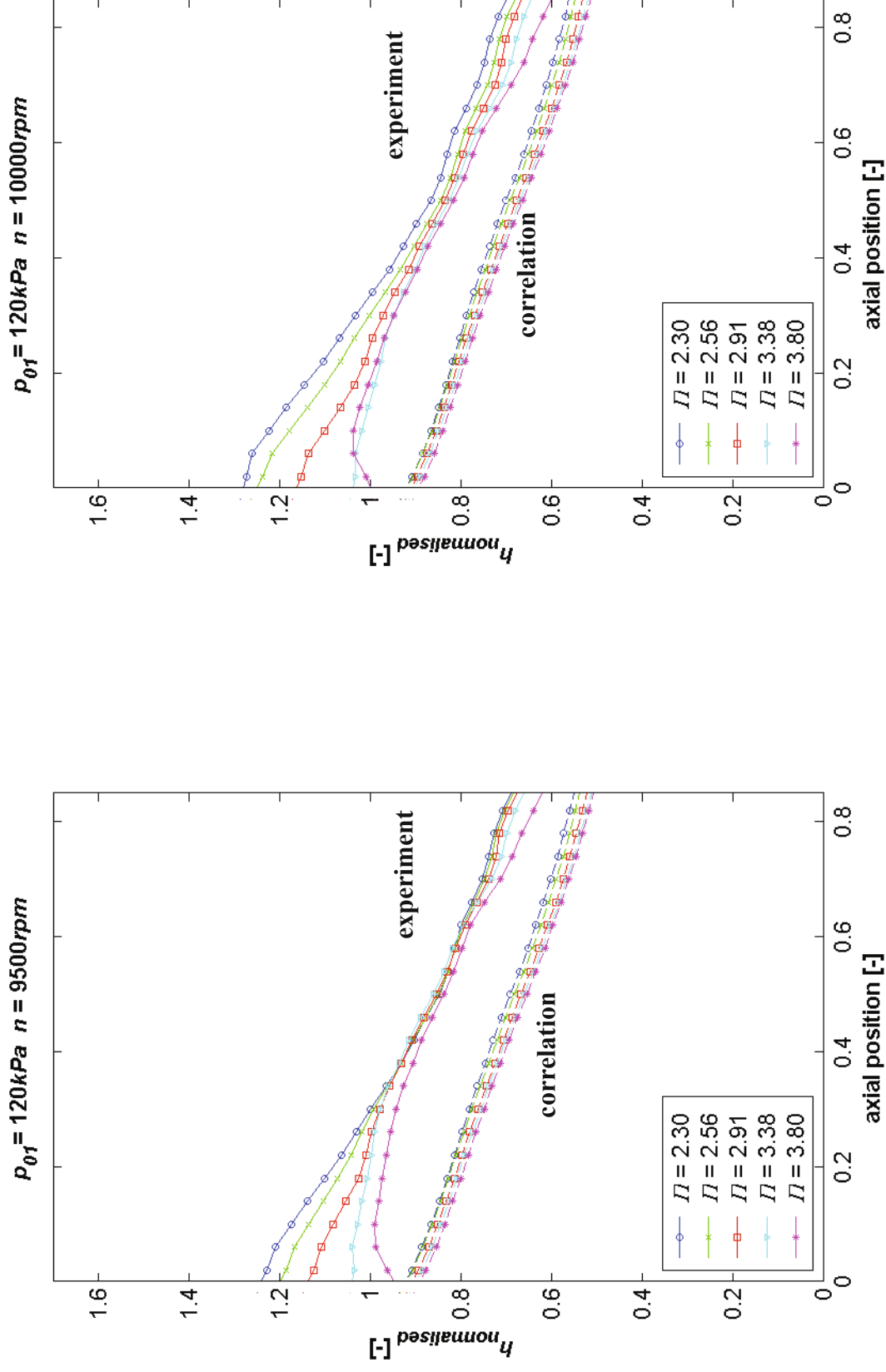


Figure 65c (right) and d (left): Experimental and analytical heat transfer coefficient distribution

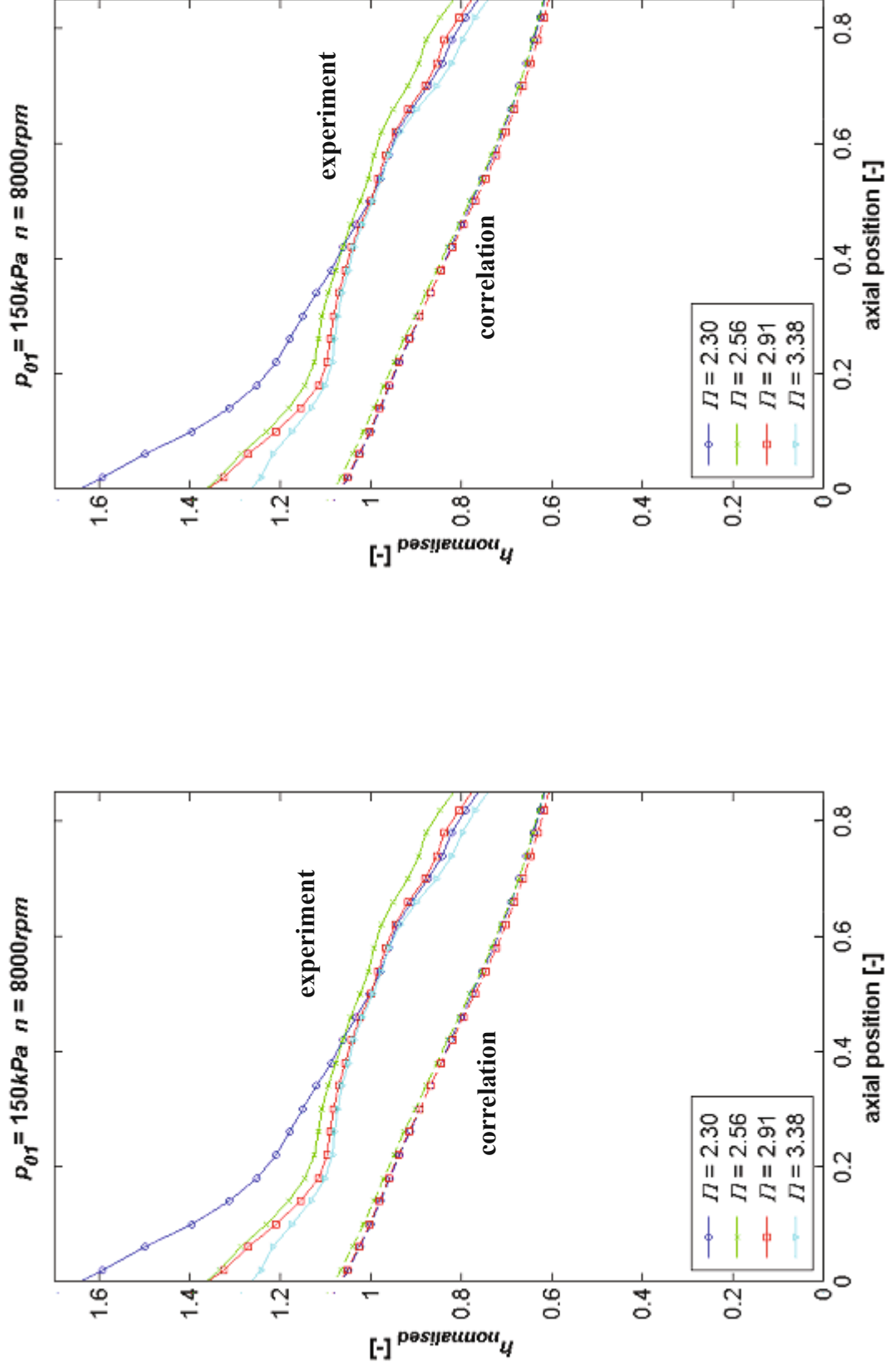


Figure 65e (right) and f (left): Experimental and analytical heat transfer coefficient distribution

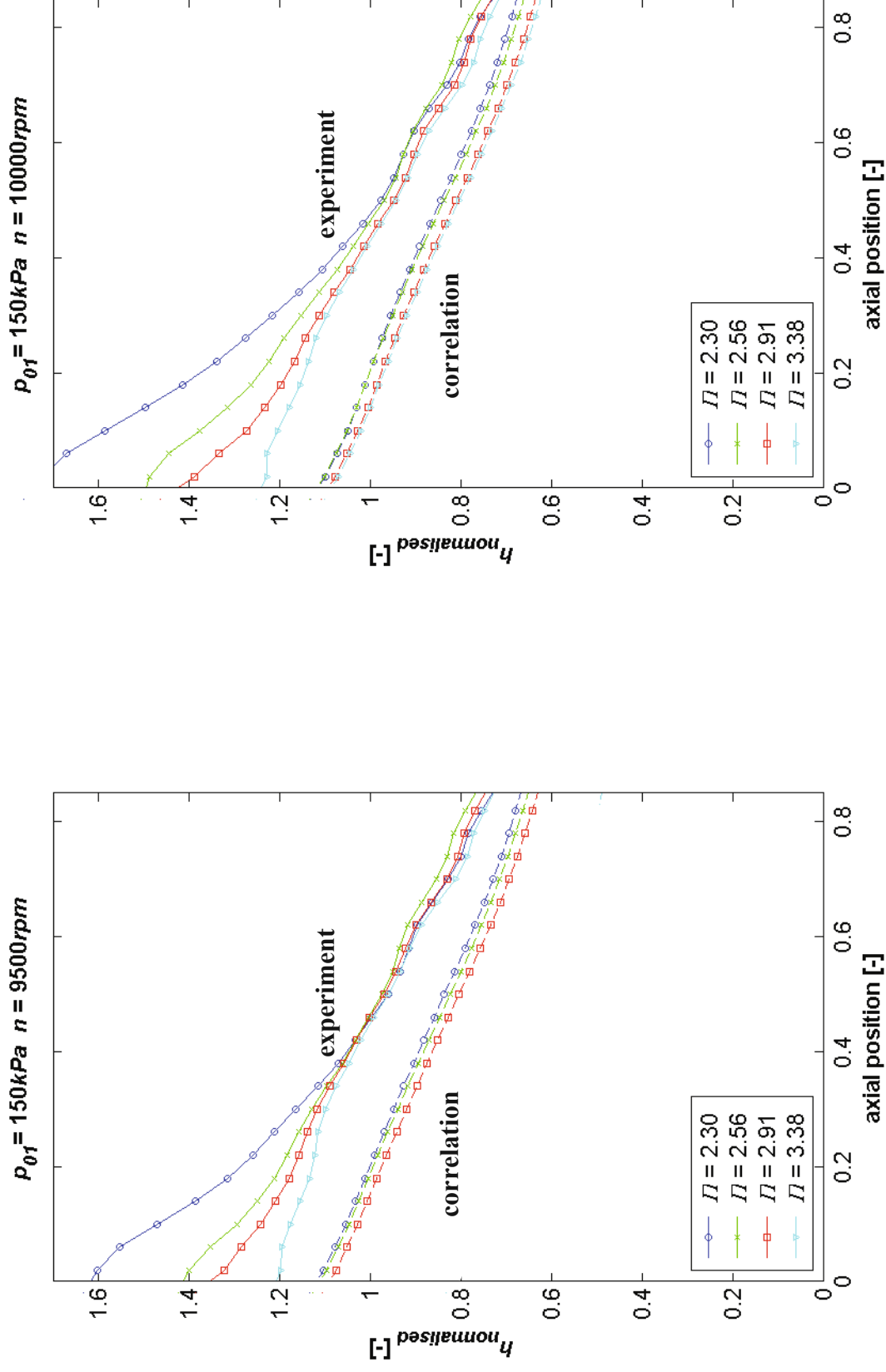


Figure 65g (right) and h (left): Experimental and analytical heat transfer coefficient distribution

5.2 Influences of time-resolved phenomena

The first part of this chapter consisted of introduction of the flat plate correlation together with a parameter study of the factors which affect the pitchwise averaged flow properties. It was found that the flat plate correlation:

- predicts the regression of the heat transfer coefficient along the axial chord very well.
- correlates very well with the total pressure (Reynolds number) along the whole axial chord.
- correlates very well with pressure ratio and rotational speed at $x > 0.3$.
- is - despite the complexity of the flow at the over-tip casing - a sound starting point for the development of an enhanced heat transfer model.

The experiments also showed that the heat transfer coefficient is underestimated for all operating conditions. Furthermore in the upstream region of the blade the experimental results show a divergence which can not be explained with the current correlation. Obviously the study of the pitchwise averaged parameters only is insufficient to explain the heat transfer at the complete over-tip casing accurately. Furthermore the boundary layer over the complete over-tip casing has so far been assumed to be fully turbulent and assumed to grow continuously, however in reality the flow is more complex.

Figure 66 shows two sketches representing the heat transfer coefficient distribution typical for a low pressure ratio (left) and a high pressure ratio (right) operating condition. In the figure the four primary flow effects responsible for the heat transfer are identified:

- I. The main part of the heat transfer is accounted by flat plate correlation (section 5.1.4), the correlation also accounts for the variations of the absolute stator wake angle (section 5.1.6).
- II. The divergence at the upstream part of the over-tip casing is caused by the misalignment of the flow entering the rotor passage and the leading edge of the rotor. It will be shown in section 5.2.1 that the misalignment and the resulting increase of the heat transfer coefficient is especially strong for the operating conditions with a low pressure ratio, whereas the operating conditions with the highest pressure ratio – which corresponds best with the design condition - will not experience an increase of the heat transfer coefficient. The effect is limited to the upstream region of the over-tip casing.

- III. In the mid-section, where the pressure difference across the blade is biggest the tip leakage flow plays a prominent role in the understanding of the time-resolved heat transfer at the over-tip casing. For this reason a tip leakage model is introduced in section 5.3.2, which helps to quantify the influence of the various phenomena in the remaining sections.
- IV. Eventually the tip leakage flow will re-enter the passage flow where it will form the tip leakage vortex. The influence of the tip leakage vortex is especially strong in the rear-section of the passage.

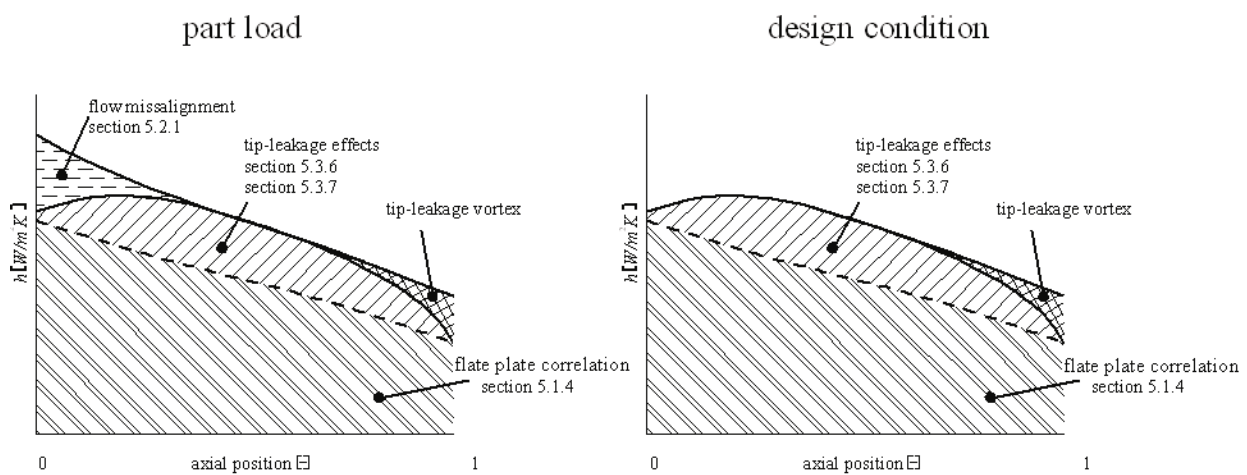


Figure 66: Sketch introducing the main heat transfer phenomena at operating conditions for a typical low and high pressure ratio

5.2.1 Relative fluid flow angle deviation

The leading edge region ($x < 0.15$) of the rotor profile is designed to guide the incoming flow into the passage with as little disturbance as possible. The direction of the incoming flow however depends on the operation condition. Obviously the rotational speed of the rotor is one of the key-parameters, but also the stator wake velocity (which depends on the pressure ratio over the turbine stage) has a significant influence. Figure 67 shows the relative flow angle at rotor entrance as function of the pressure ratio and the rotational speed. The figure shows that the relative flow angle at the entrance can vary as much as 40° .

The rotor blade is mainly optimised for a defined design condition and the matching angle of incoming flow. In consequence, the guidance of the flow is not optimal for all other operating

points. Both in lower partload and higher overload, the incoming fluid is highly disturbed due to severe misalignment. This will manifest itself in the boundary layer as a region of strong turbulence with possible locally separation of the boundary layer. Consequently the heat transfer will be significantly higher. Figure 68 shows the correlation of the relative flow angle with the heat transfer coefficient at the rotor entrance ($x = 0$). The incoming flow angle at the design condition is approximately 50° and corresponds well with the location of the minimum of the two curves.

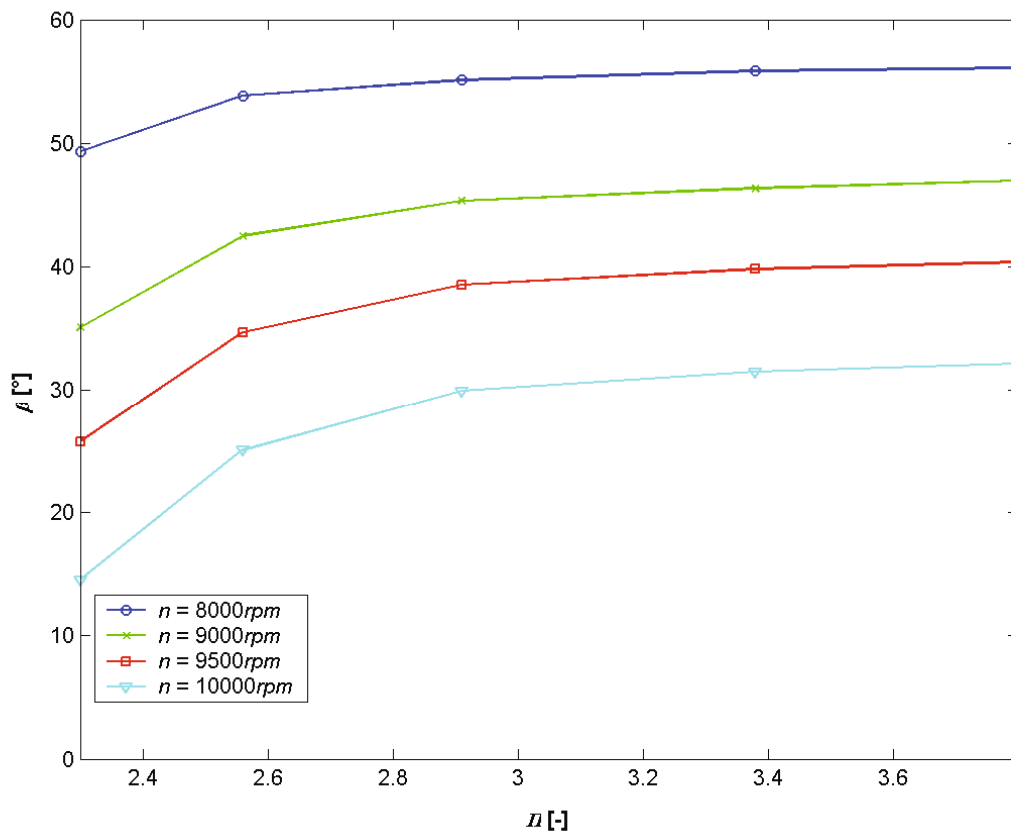


Figure 67: Relative flow angle at rotor entrance as function of pressure ratio and rotational speed

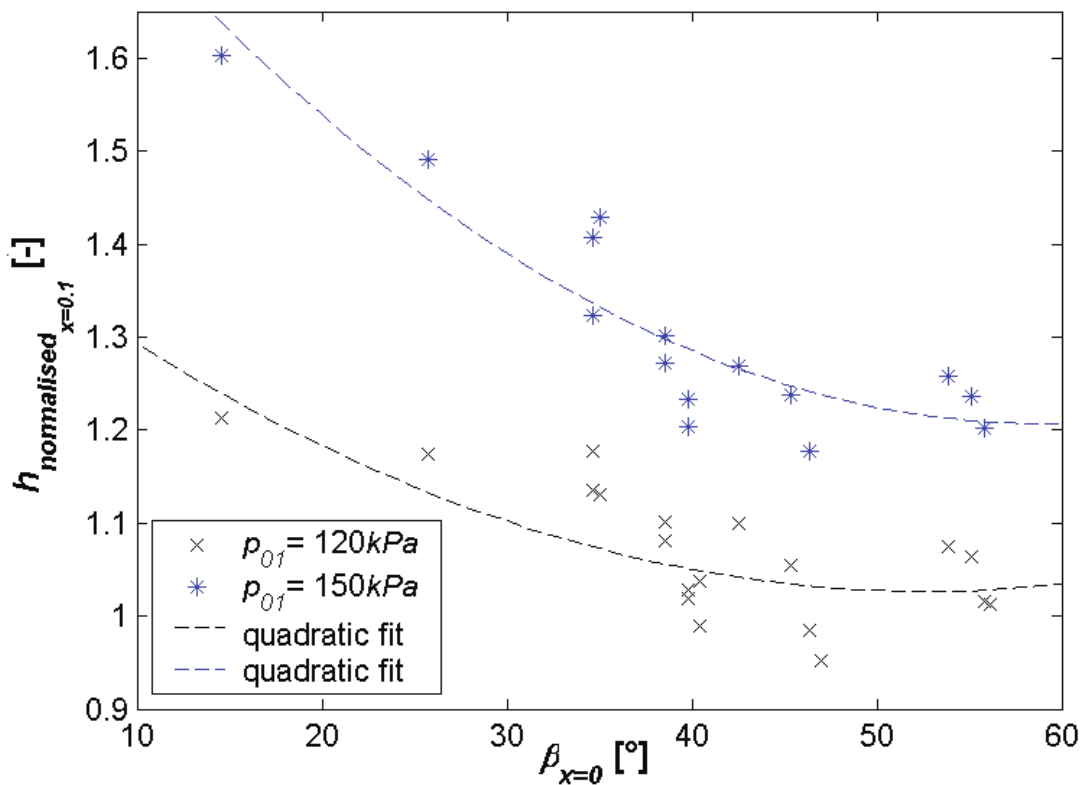


Figure 68: Correlation of the relative flow angle and heat transfer coefficient at rotor entrance

The additional heat transfer caused by the misalignment of the incoming flow can be as much as 13% of the total heat transfer and is therefore identified as an important factor for determining the heat transfer level in the upstream region of the over-tip casing.

5.3 Tip leakage flow

The tip leakage flow is responsible for multiple effects which cause a great increase of the heat transfer inside the tip gap and have - despite the relative small area of the tip gap - a significant influence on the heat transfer of the whole over-tip casing. As a result of the extensive measurement series, of which the results are presented in chapter 4, a great number of experimental data concerning the gap region has been gathered. However, due to the severe constraints set forward by the rotating system, some experimental parameters (e.g. total pressure and flow direction distribution) could not be measured directly inside the gap, despite great technical effort. Before introducing the actual tip leakage model, the isentropic Mach number distribution in the passage and tip gap will be presented.

5.3.1 Isentropic Mach number distribution

The Mach number can be determined directly out of the total-to-static pressure ratio. In the relative frame of reference of the rotor, no work is done by the fluid, when furthermore losses are neglected and $p_{0,rel}$ can be assumed to be constant. The total pressure is obtained by the Pitot measurements (section 4.2.1), the static pressure in- and outside the gap was obtained by the Kulite measurements (section 4.3.1). The isentropic relative Mach number can be determined with:

$$M_{rel} = \sqrt{\frac{2}{\kappa-1} \left(\left(\frac{p_{0,rel}}{p} \right)^{\frac{\kappa-1}{\kappa}} - 1 \right)} \quad (5.9)$$

In reality the flow especially in proximity of the wall will experience losses. The wake measurements showed that the total loss over the rotor is about 5%. Considering that the losses are generated linearly along the chord equation (5.9) can be enhanced.

Figure 69 shows the instantaneous static pressure measured when the entrance of the tip gap (pressure side) respectively the exit of the tip gap (suction side) crosses the sensor-array. The averaged pressure measured by the pressure taps is shown by the dashed line. The characteristics of the averaged static pressure distribution were already discussed in section 4.2.2. The pressure difference across the gap, which is absent at the leading edge, will grow until it is fully established between 0.08 and 0.20 axial chord lengths. From there on the pressure difference remains relatively constant. Figure 70 and Figure 71 show the isentropic relative Mach number corresponding to the static pressure presented in Figure 69. The graph shows that except for a low pressure ratio the relative velocity of the tip leakage flow will be supersonic. The overexpanded tip leakage flow was examined by Moore and Elward (1992) and Moore et al. (1998).

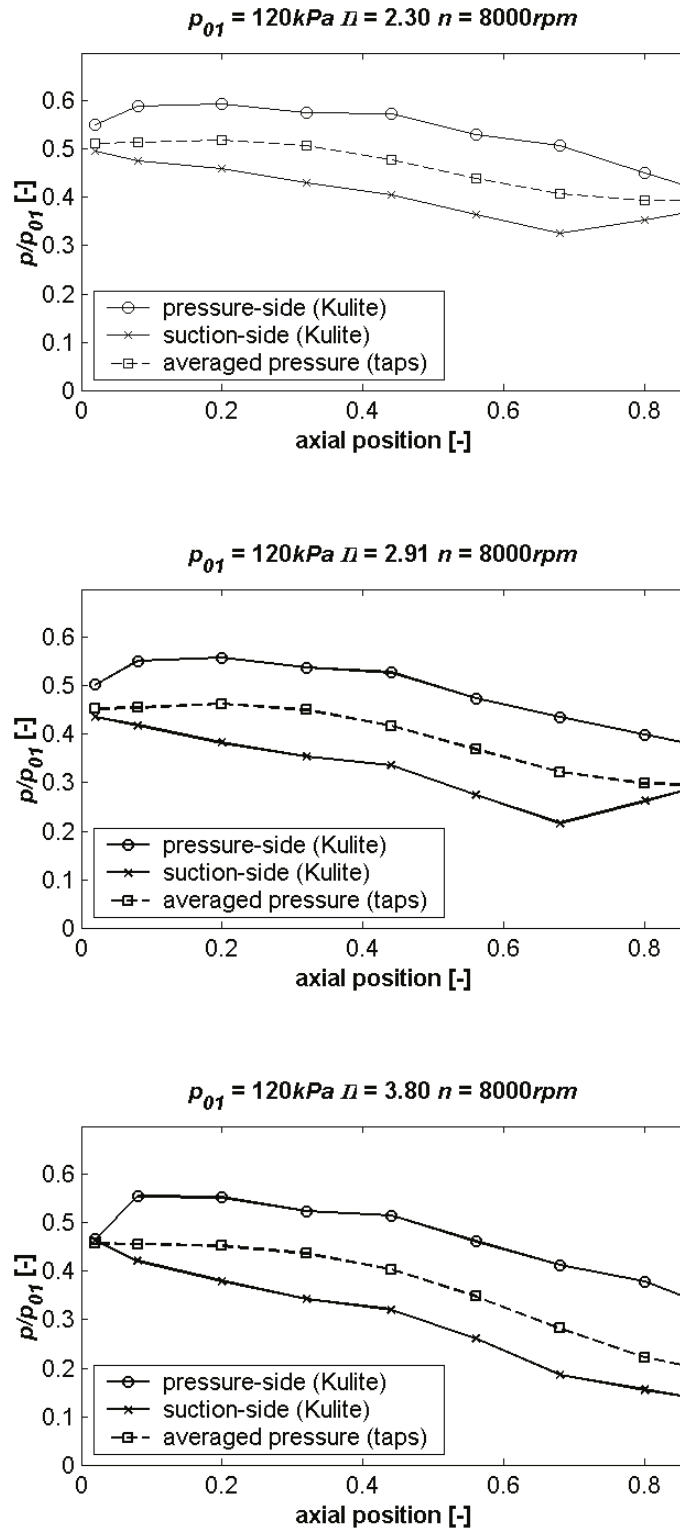


Figure 69: Time-resolved static pressure corresponding to the tip gap entrance and exit for various operating conditions

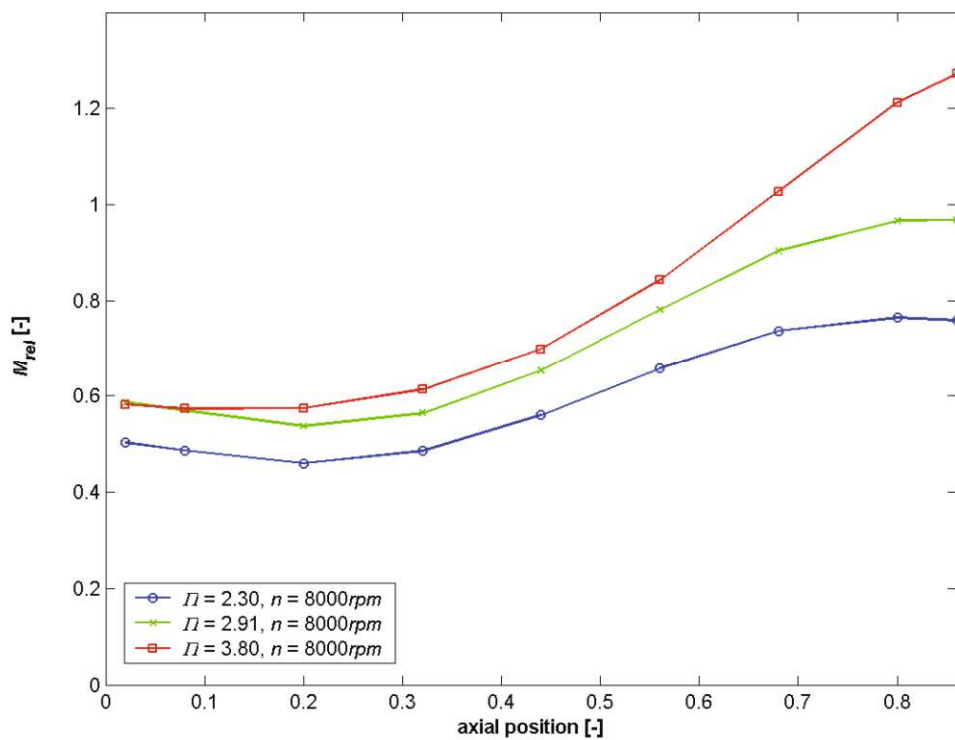


Figure 70: Averaged isentropic relative Mach number for various operating conditions

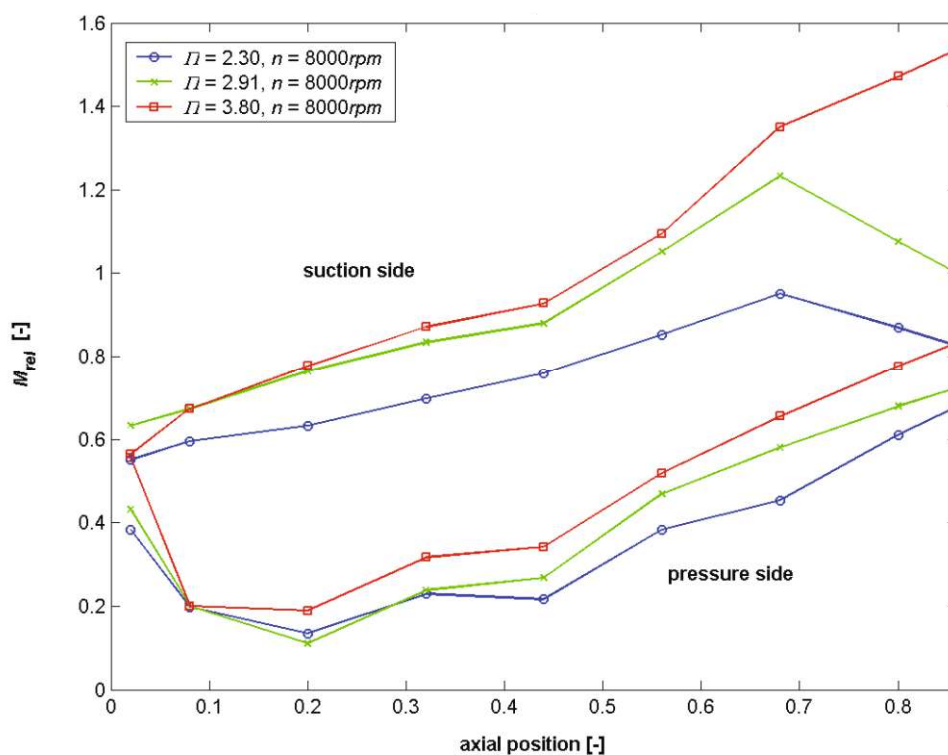


Figure 71: Isentropic relative Mach number distribution for various operating conditions

5.3.2 Tip leakage model

In order to determine the absolute velocity of the tip leakage flow inside the gap, the relative flow angle of the tip leakage flow has to be determined. Yaras et al. (1988) summarised three assumptions which can be used for the fluid entering the tip gap:

- I. No work is done by the fluid entering the gap (this will be discussed in paragraph 5.3.8 in more detail) and there are no losses therefore:

$$\begin{aligned} p_{0,rel} &= \text{const} \\ \rho_{0,rel} &= \text{const} \\ T_{0,rel} &= \text{const} \end{aligned} \quad (5.10)$$

- II. The tangential velocity of the fluid before it is accelerated into the gap is assumed to be related to the static pressure at the pressure side (as shown in Figure 71).
- III. The pressure gradient parallel to the camber line of the blade is small. Consequently, the parallel velocity remains constant. The pressure difference driving the flow into the gap therefore acts to increase only the normal component of velocity. Figure 48 shows that this assumption is valid at the entrance of the gap, however at the exit the pressure gradient parallel to the gap can be significant. Therefore, the present tip leakage model can only be used inside the gap.

Applying the previous three assumptions, the normal component of the tip leakage flow can be determined with:

$$\begin{aligned} p_{0,PS} &= p_{PS} \cdot \left(1 + \frac{\kappa-1}{2} (M_{rel,PS_{normal}})^2 \right)^{\frac{\kappa}{\kappa-1}} \\ p_{0,SS} &= p_{SS} \cdot \left(1 + \frac{\kappa-1}{2} (M_{rel,SS_{normal}})^2 \right)^{\frac{\kappa}{\kappa-1}} \end{aligned} \quad (5.11)$$

of which $M_{rel,PS_{normal}}$ and $M_{rel,SS_{normal}}$ are the normal component of the relative Mach number. Before the fluid is accelerated into the gap $M_{rel,PS_{normal}} = 0$. The big pressure gradient at the pressure side of the blade (as shown in Figure 48) shows that the acceleration is already completed at the entrance of the gap, therefore $M_{rel,tip_{normal}} = M_{rel,SS_{normal}}$. Using (5.10) gives:

$$p_{PS} = p_{SS} \cdot \left(1 + \frac{\kappa-1}{2} (M_{rel,tip_{normal}})^2 \right)^{\frac{\kappa}{\kappa-1}} \quad (5.12)$$

The normal component of the tip leakage flow consequently can be written as:

$$M_{rel,tip,normal} = \sqrt{\frac{2}{\kappa-1} \left(\left(\frac{p_{PS}}{p_{SS}} \right)^{\frac{\kappa-1}{\kappa}} - 1 \right)} \quad (5.13)$$

The resulting relative flow angle and the tip leakage flow velocity can be taken from the velocity triangles (as shown in Figure 72):

$$\gamma_{tip} = \arctan \left(\frac{M_{rel,tip,normal}}{M_{rel,PS}} \right) \quad (5.14)$$

$$M_{rel,tip} = \sqrt{M_{rel,tip,normal}^2 + M_{rel,PS}^2} \quad (5.15)$$

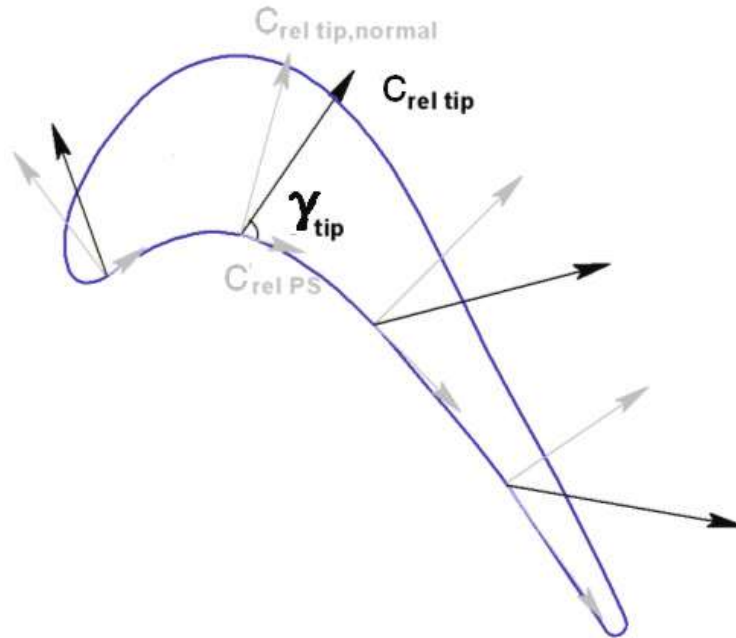


Figure 72: Velocity triangles of the tip leakage flow

The outcome of equation (5.14) and equation (5.15) together with the velocities (Mach numbers) of the passage at the suction side and pressure side of the blade are shown in Figure 73 and Figure 74. The relative flow angle in the region upstream 30% of the axial chord length is probably overestimated since assumption III is in that region only partially valid.

The velocity measured in the passage near the exit of the gap ($M_{rel,SS}$) must - assuming no losses at the exit - be similar to the velocity of the tip leakage flow ($M_{rel,tip}$). Figure 74 shows

that this constraint is satisfied for all operating conditions. This supports the previous assumptions made in the beginning of this section.

When the tip leakage flow re-enters the passage it will form a vortex –the tip leakage vortex– this formation will generally involve significant losses. The losses lead to a reduction of the total pressure. However the isentropic Mach number does not account for local variations of the total pressure. The losses therefore do not affect the isentropic Mach number. This explains why the resemblance between $M_{rel,SS}$ and $M_{rel,tip}$ is so strong and does also improve the confidence in the analytical determined $M_{rel,tip}$. It also implies that the isentropic $M_{rel,SS}$ will most likely be too high in the regions with losses. This is no problem since the region containing the tip leakage vortex is too complex for the flat plate correlation and has to be tackled with a separate correlation.

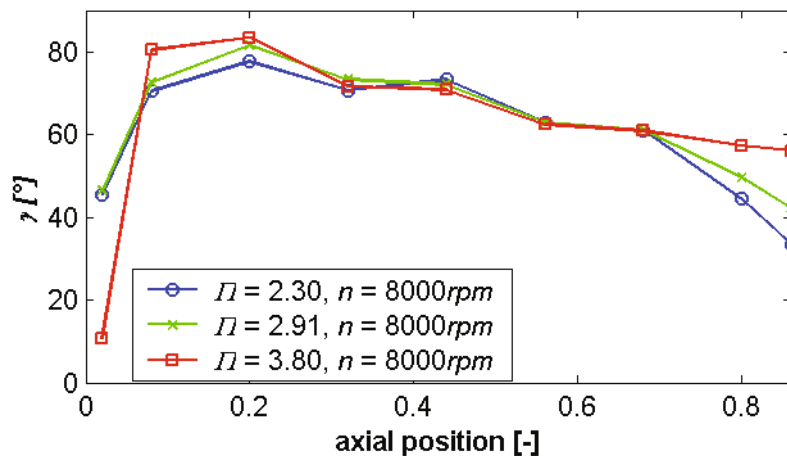


Figure 73: Flow angle of the tip leakage flow relative to the blade contour at the gap entrance

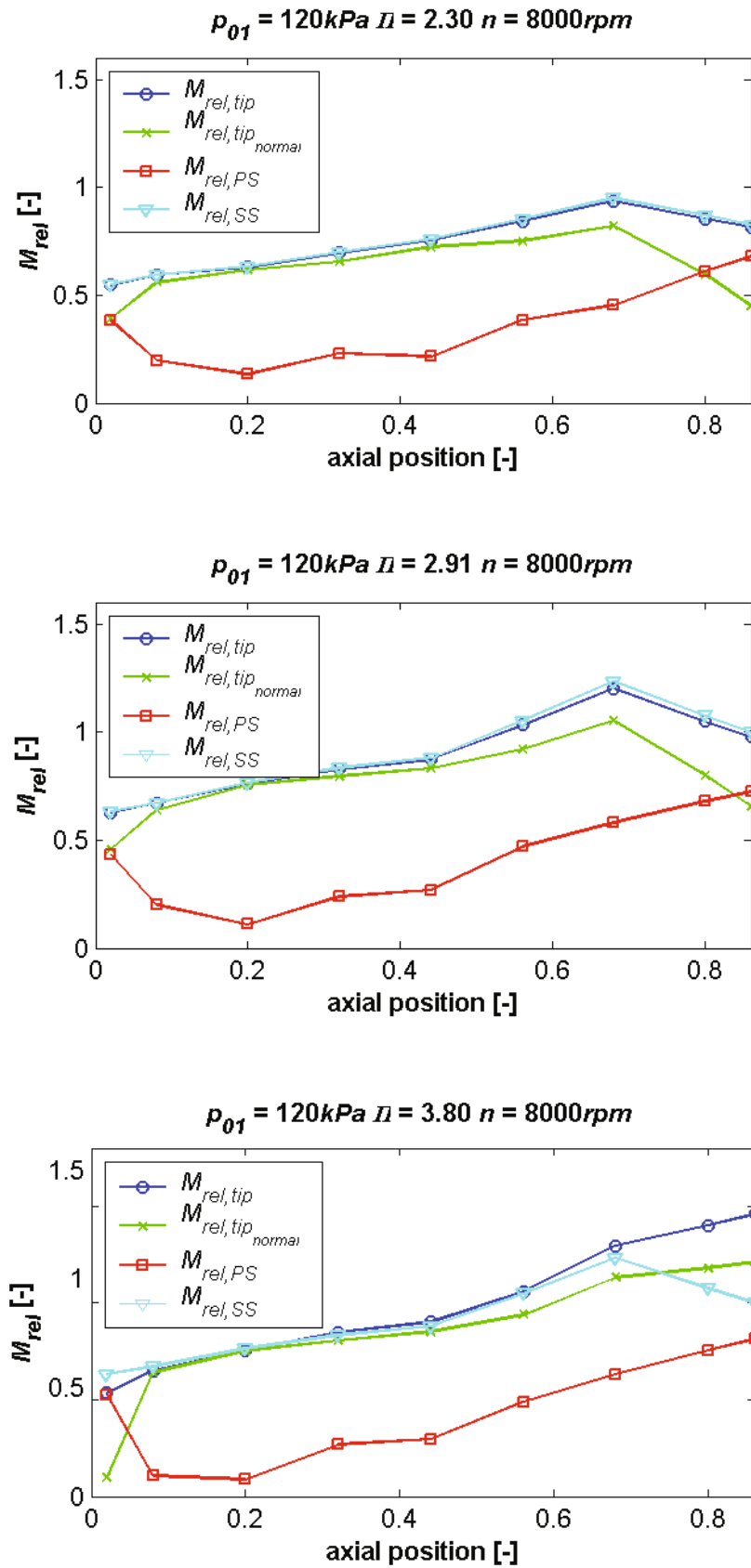


Figure 74: Magnitude of the Mach number components of the tip leakage flow for various operating conditions

5.3.3 Relaminarisation of the tip leakage flow

The big difference between the Mach number just outside the gap ($M_{rel,PS}$) and just inside the gap ($M_{rel,tip}$) as shown in Figure 74 imply a strong acceleration at the entrance of the tip gap. Mayle and Metzger (1982) found that the acceleration caused by the huge pressure difference between both sides of the blade - especially in the forward half of the blade -, can be much larger than the streamwise acceleration (in the relative frame of reference) that would have existed if the leakage was not present. Acceleration and deceleration of the main flow have a big impact on the boundary layer. The boundary layer is defined as that part of the flow for which the velocity is retarded by more than one percent due to the wall friction.

An acceleration of the main flow will decrease the boundary layer thickness. In the case of the thermal boundary layer this means that the wall is less surrounded by a protective layer and the heat transfer rate will increase. The acceleration however not only influences the thickness of the boundary layer, but also the state of the boundary layer. The main parameter for the state of the boundary layer is the Reynolds number:

$$Re = \frac{c \cdot x}{\nu} = \frac{\text{inertia forces}}{\text{viscous forces}} \quad (5.16)$$

In general the boundary layers within a rotor cascade can be assumed to be fully turbulent and to be relatively thick. Whether the acceleration at the tip gap entrance is sufficient for relaminarisation to occur can be determined with the acceleration parameter K presented by Mayle and Metzger (1982):

$$K = \frac{\pi}{2} \frac{1}{Re_{tip}}, \quad (5.17)$$

of which Re_{tip} is the Reynolds number at the turbine tip as defined as:

$$Re_{tip} = \frac{M_{rel,tip,normal} \cdot \sqrt{\kappa \cdot R \cdot T_{tip}} \cdot \tau \cdot \rho_{tip}}{\mu_{tip}} \quad (5.18)$$

The relative Mach number component perpendicular to the tip gap entrance can be taken from equation (5.13), the static fluid properties are presented in APPENDIX G and the tip gap height is given by equation (4.1). Relaminarisation is believed to occur when:

$$K > 3 \cdot 10^{-6} \quad (5.19)$$

For the operating conditions mentioned in the report the acceleration parameter (K) is between $2 \cdot 10^{-4}$ and $8 \cdot 10^{-4}$, which is about two orders of magnitude higher than necessary for relaminarisation to occur. Turbulent boundary layers are characterised by chaotic flow where heat exchange is facilitated by unsteady vortices which appear on many scales. This makes the heat transfer in the turbulent regime far more effective than that of the laminar regime where the heat transfer is solely based on conduction. The state of the boundary layer (laminar or turbulent) inside the tip gap is important for the heat transfer rate in the gap, however the significant reduction of the boundary layer thickness will generally have a bigger impact on the heat transfer causing an extensive increase of the heat transfer coefficient at the tip gap entrance as also found in Figure 50.

5.3.4 Heat transfer in the non-rotating passage with compressible flow

For the case of the non-rotating passage with

$$M_{abs} = M_{rel} = M \quad (5.20)$$

and a geometry of the passage which allows supersonic velocities to be established, equation (5.16) turns into:

$$\text{Re}(M, x) = \frac{M \cdot \sqrt{\kappa R T(M)} \cdot x \cdot \rho(M)}{\mu(T(M))} \quad (5.21)$$

This function is presented graphically in Figure 75. The maximum is located at unity. In the incompressible regime the Reynolds number is almost exclusively dependent on the velocity, however when the compressible effects increase, the influence of the dynamic viscosity becomes more apparent and will start to dominate at $M > 1.0$.

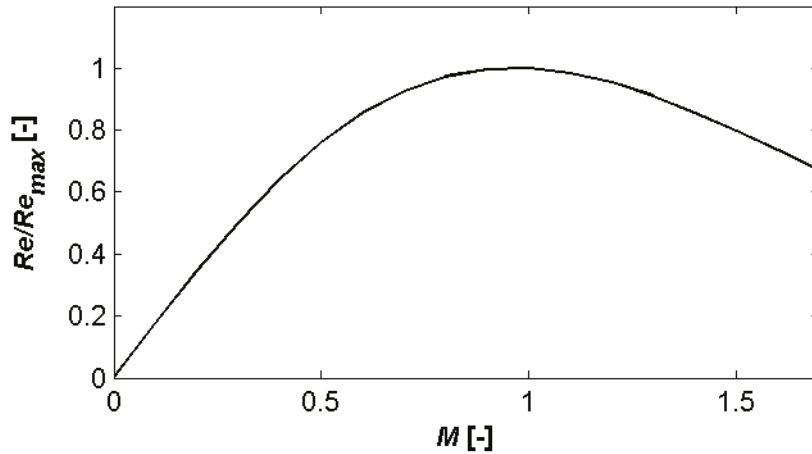


Figure 75: Reynolds number within an isentropic nozzle as function of the Mach number (normalised on the maximum)

The conductivity of air can be assumed to be only dependent of the temperature. The Prandtl number is approximately constant in the temperature and pressure range for the given Mach number variation (VDI-Wärmeatlas, 1984). Therefore, the heat transfer coefficient can be expressed as:

$$h(M, x) \propto \lambda(M) \cdot \text{Re}(M, x)^{4/5} \quad (5.22)$$

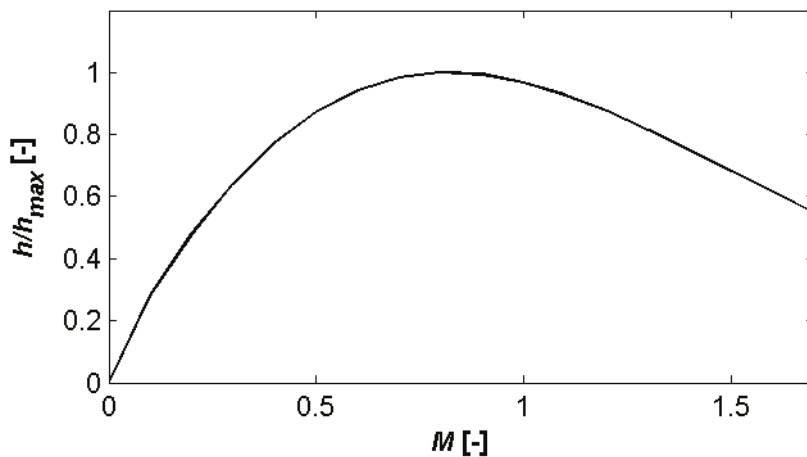


Figure 76: Heat transfer coefficient as function of the Mach number for isentropic flow (normalised on the maximum)

The progression of Figure 76 is very similar to the previous figure. Again the curve shows a maximum, which means that at high velocities the heat transfer coefficient of the wall will reduce with increased Mach number.

The maximum of the curve is however located at $M \approx 0.82$. This shift of the maximum is caused by the temperature dependence of the conductivity of air. The figure clearly shows that the relation between heat transfer coefficient and the Mach number is non-linear.

The flat plate correlation can be either fed with time-resolved or pitchwise averaged input data. Figure 77 sketches the analysis procedures for both possibilities:

- I.) Equation (5.22) gives a relation between the isentropic Mach number and the local heat transfer coefficient. This can be done for every moment in time, allowing complete sets of time-resolved Mach number measurements at the casing to be transferred in a time-resolved heat transfer data set (dashed line in Figure 77). The pitchwise averaged heat transfer can be finally obtained by the integration over one period.
- II.) However often time-resolved data is not available or steady input data is preferable. An example for this is the flat plate correlation which is fed with the experimental data of steady pressure taps. These taps are far too slow to measure the fluctuation of the Mach number caused by the rotor and equals the pitchwise averaged Mach number. The pitchwise averaged value can be entered into the correlation (represented by the solid line in Figure 77) resulting directly in the pitchwise averaged heat transfer coefficient.

In the next paragraphs it will be investigated whether both methods lead to the same result.

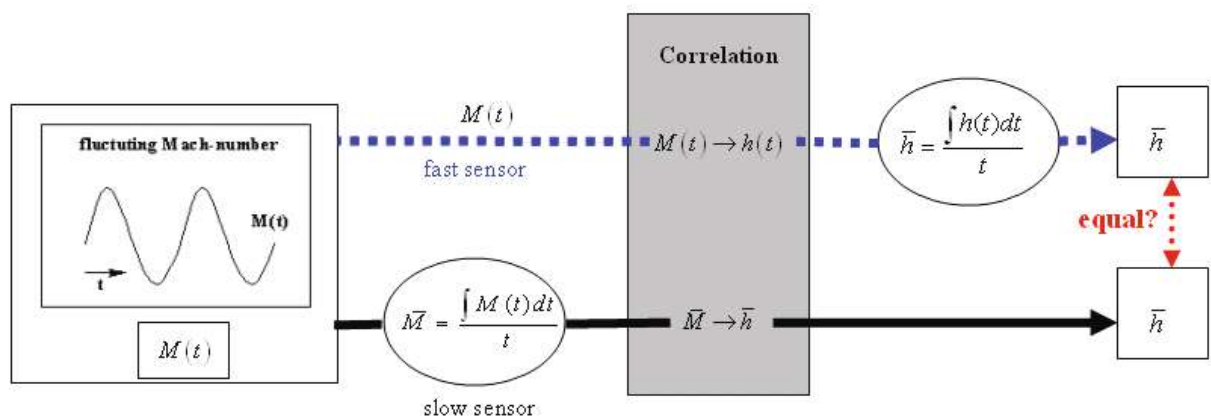


Figure 77: Time-resolved versus pitchwise averaged input data for the flat plate correlation

5.3.4.1 Non-linearity effects of the flat plate correlation in fluctuating flow conditions

Equation (5.22) can be accurately represented by a fourth degree polynomial:

$$h \approx a + bM(t) + c(M(t))^2 + d(M(t))^3 + e(M(t))^4 \quad (5.23)$$

The time-averaged heat transfer coefficient can be determined:

- I.) out of the steady Mach number. The steady Mach number equals the integral of the time-resolved Mach number profile over one period τ :

$$\bar{M} = \frac{\int_0^{\tau} M(t) dt}{\tau} \quad (5.24)$$

Inserting the steady Mach number in equation (5.23) gives:

$$\bar{h} = a + b\bar{M} + c\bar{M}^2 + d\bar{M}^3 + e\bar{M}^4 \quad (5.25)$$

$$\bar{h} = a + b \frac{\int_0^{\tau} M(t) dt}{\tau} + c \left(\frac{\int_0^{\tau} M(t) dt}{\tau} \right)^2 + d \left(\frac{\int_0^{\tau} M(t) dt}{\tau} \right)^3 + e \left(\frac{\int_0^{\tau} M(t) dt}{\tau} \right)^4 \quad (5.26)$$

- II.) out of the time-resolved Mach number. The time-resolved Mach number in equation (5.23) gives:

$$h(t) = a + bM(t) + c(M(t))^2 + d(M(t))^3 + e(M(t))^4 \quad (5.27)$$

$$\bar{h} = \frac{\int_0^{\tau} \left(a + bM(t) + c(M(t))^2 + d(M(t))^3 + e(M(t))^4 \right) dt}{\tau} \quad (5.28)$$

Whether the outcome of equation (5.26) and (5.28) are the same depends on the variation of the time-resolved Mach number:

Time-resolved Mach number is constant

When the Mach number is constant over the whole period:

$$M(t) = C \quad (5.29)$$

Than:

$$\bar{M} = \frac{\int_0^{\tau} M(t) dt}{\tau} = \frac{\int_0^{\tau} C dt}{\tau} = C \quad (5.30)$$

Inserting (5.30) in (5.26) gives:

$$\bar{h} = a + bC + cC^2 + dC^3 + eC^4 \quad (5.31)$$

Inserting (5.29) in (5.28) gives:

$$\bar{h} = \frac{\int_0^{\tau} (a + bC + c(C)^2 + d(C)^3 + e(C)^4) dt}{\tau} \quad (5.32)$$

$$\bar{h} = a + bC + cC^2 + dC^3 + eC^4$$

As expected the results of equation (5.26) and (5.28) are equal

Time-resolved Mach number is not constant

When the Mach number of the flow at the casing is not constant in time, but for instance has a sawtooth fluctuation component:

$$M(t) = t \quad (5.33)$$

Then:

$$\bar{M} = \frac{\int_0^{\tau} M(t) dt}{\tau} = \frac{\int_0^{\tau} t dt}{\tau} = \frac{\tau}{2} \quad (5.34)$$

Inserting (5.34) in (5.26) gives:

$$\bar{h} = a + b\frac{\tau}{2} + c\frac{\tau^2}{4} + d\frac{\tau^3}{8} + e\frac{\tau^4}{16} \quad (5.35)$$

Whereas inserting (5.33) in (5.28) gives:

$$\bar{h} = a + b\frac{\tau}{2} + c\frac{\tau^2}{3} + d\frac{\tau^3}{4} + e\frac{\tau^4}{5} \quad (5.36)$$

Comparison of equation (5.35) and (5.36) shows that if the flat plate correlation is fed with steady pressure measurements and thereby ignoring the non-linearity of equation (5.22) an error will occur. Consequently the error will be biggest in a region with high fluctuations of the flow as for instance in the tip gap region.

As second parameter for the error estimation is the Mach regime of the undisturbed flow just outside the boundary layer. The first two terms of equation (5.35) and (5.36) are identical, however the higher the term the bigger the discrepancy of the constants, consequently in the subsonic and hypersonic regime where the graph of Figure 76 is relative straight the error will be small whereas in the transonic region where the curvature is biggest the error will be more significant.

5.3.5 Heat transfer in the rotating passage with compressible flow

Since in the rotating cascade the relative Mach number and the absolute Mach number are not equal:

$$M_{abs} \neq M_{rel}, \quad (5.37)$$

Therefore equation (5.16) can not be reduced to equation (5.21). However the Reynolds number can be separated into a fluid property (dependent on the relative frame of reference) and a fluid velocity (dependent on the absolute frame of reference) part:

$$\frac{Re(M_{rel})}{M_{abs}} = \frac{\sqrt{kRT(M_{rel})} \cdot \rho(M_{rel})}{\mu(T(M_{rel}))} \cdot x \quad (5.38)$$

Since the influence of the absolute Mach number is linear, all the non-linear effects are combined in the fluid properties. The magnitude of the non-linearity will therefore be in the same order as presented in the previous section. The distribution of the normalised Reynolds number is shown in Figure 78.

Analogue the expression for the heat transfer coefficient can be split:

$$h(M_{rel}) \propto \lambda(M_{rel}) \cdot Re(M_{rel})^{4/5} \quad (5.39)$$

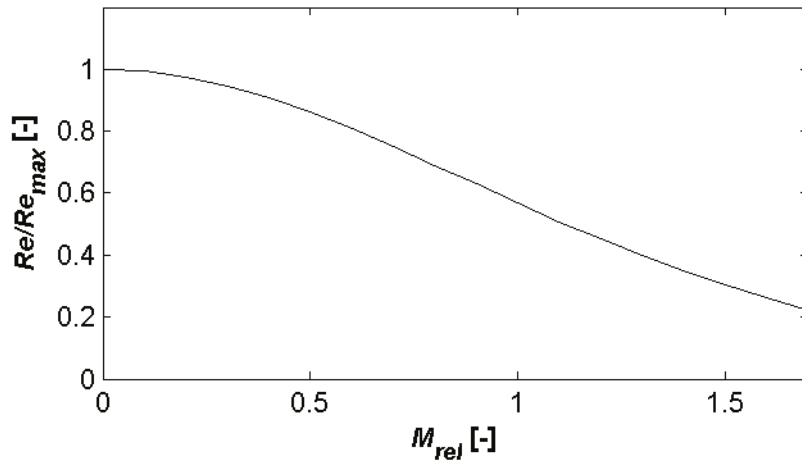


Figure 78: Normalised Reynolds number as function of the Mach number

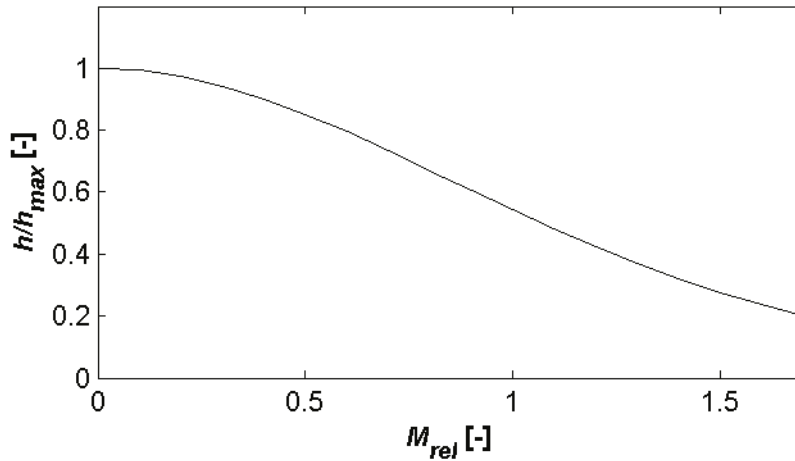


Figure 79: Normalised heat transfer coefficient as function of the Mach number

In the rotating cascade the Reynolds number and heat transfer coefficient can only be determined when both the relative and absolute velocities are known. The calculation of the relative Mach number was already presented in section 5.3.2, in section 5.3.6 the absolute Mach number profile will be determined.

5.3.5.1 Non-linearity effects of the flat plate correlation in fluctuating flow conditions (rotating system)

Since equation (5.39) can also be accurately represented by a fourth grade polynomial the procedure presented in paragraph 5.3.4.1 can also be executed on equation (5.39). This means that also in a rotating cascade - when the heat transfer can not be measured directly but it has to be determined with the aid of correlations - there will be a discrepancy between the output of a correlation fed with steady data and the true time-averaged heat transfer coefficient.

However opposite to the non-rotating cascade in the rotating cascade the curvature of the graph in Figure 79 in the range of typical Mach numbers $[M = 0.3, M = 1.3]$ is small and consequently the potential error will also be small.

5.3.6 Absolute velocity components

Knowing both the magnitude and angle of the tip leakage flow, the relative Mach number can be easily transferred into the absolute system of reference. The resulting absolute velocity components are given in Figure 80.

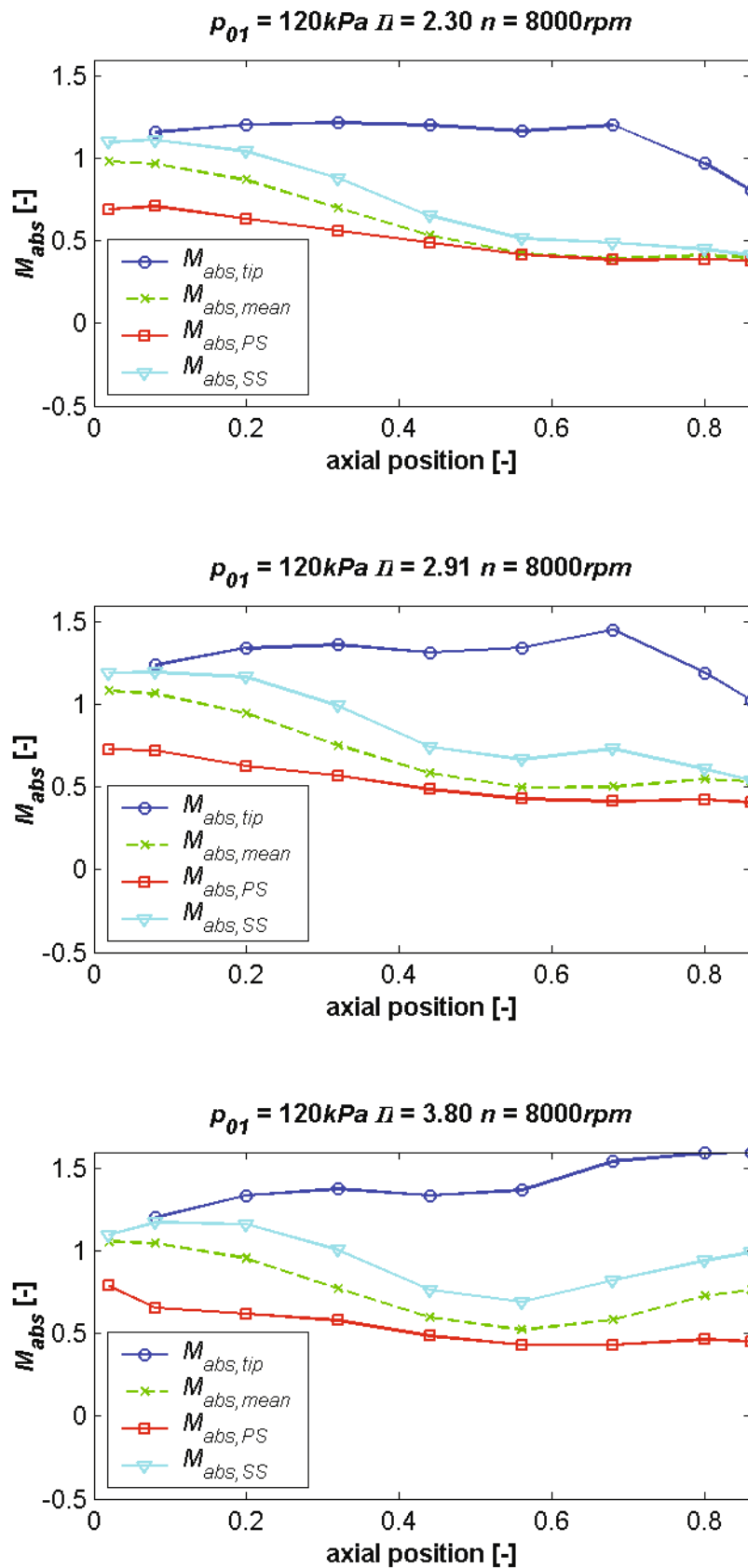


Figure 80: Absolute tip leakage and passage flow Mach number for various operating conditions

5.3.7 Averaged heat transfer versus tip gap heat transfer

In section 5.3.5 the equation for the heat transfer in the rotating cascade was presented:

$$\frac{\text{Re}(M_{rel})}{M_{abs}} = \frac{\sqrt{\kappa RT(M_{rel})} \cdot \rho(M_{rel})}{\mu(T(M_{rel}))} \cdot x \quad (5.38)$$

The relative Mach number was determined in section 5.3.2 and the absolute Mach number was calculated in the previous section. The resulting heat transfer coefficient for the complete passage and the tip gap is shown in Figure 81.

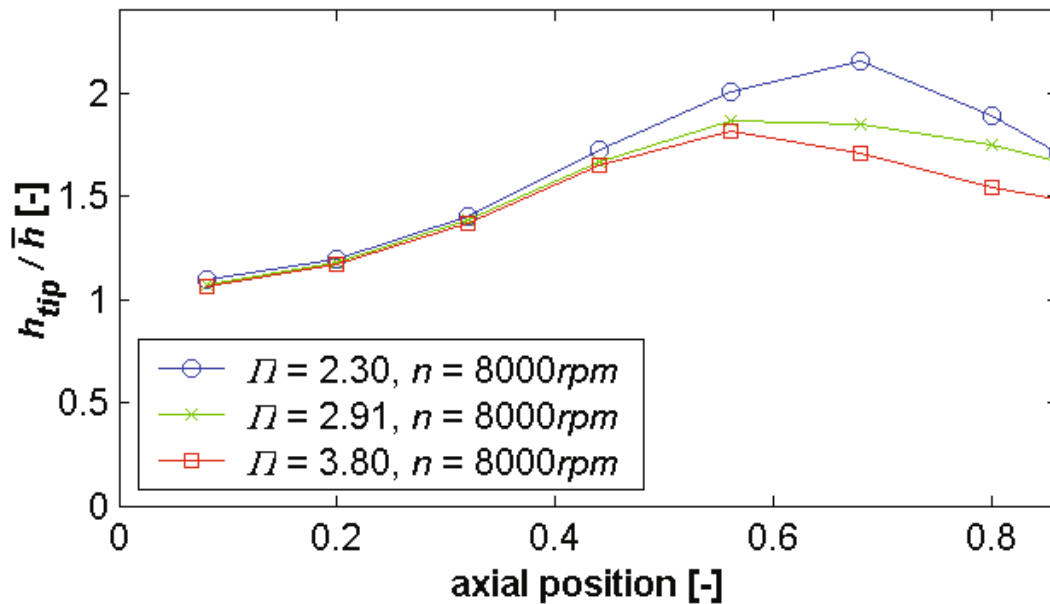


Figure 81: Ratio between the heat transfer coefficient in the passage and in the gap

The figure clearly shows that the heat transfer coefficient in the tip gap is much higher than the pitchwise averaged heat transfer coefficient. The heat transfer coefficient in the tip can be up to twice as high as that of the pitchwise averaged case. The increased level is caused by the very high absolute velocity of the tip leakage flow. In Figure 80 it was shown that the absolute Mach number distribution up to approximately $x = 0.6$ is virtually independent of the operating condition. The curves only diverge at an axial position downstream of $x = 0.6$, a similar pattern is shown in Figure 81.

5.3.8 Total temperature deviations caused by the work process

From Euler's turbine equation follows that the work produced by a turbine is related to the change in angular momentum passing through it:

$$W = \frac{P}{\dot{m}} = u_3 c_3 \sin \alpha_3 - u_4 c_4 \sin \alpha_4 \quad (5.40)$$

For an axial turbine $u_3 = u_4$ and $c_{\text{tang}} = c \sin \alpha$ gives:

$$W = u \cdot (c_{3,\text{tang}} - c_{4,\text{tang}}) \quad (5.41)$$

The angular momentum of the fluid is graphically represented by the velocity triangles of Figure 82. The continuous deflection of the fluid will result in a continuous extraction of energy from the fluid, this causes a proportional reduction of the total temperature of the fluid.

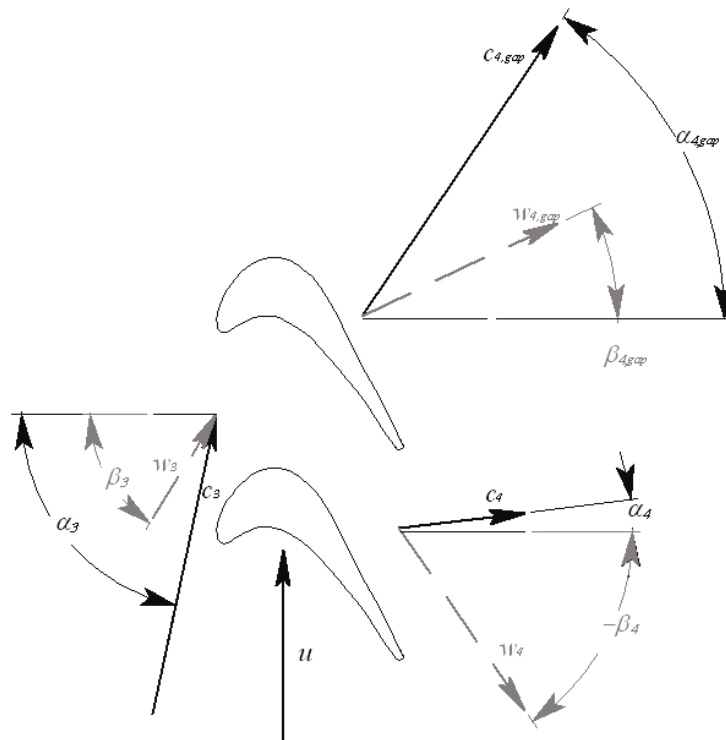


Figure 82: A schematic diagram that illustrates the velocity triangles for the blade inlet, blade passage and over-tip leakage flows. (Thorpe et al., 2004b)

The tangential component of both passage flow and tip leakage flow can easily be obtained from the tip leakage model presented in the previous section. The results are shown in Figure 83.

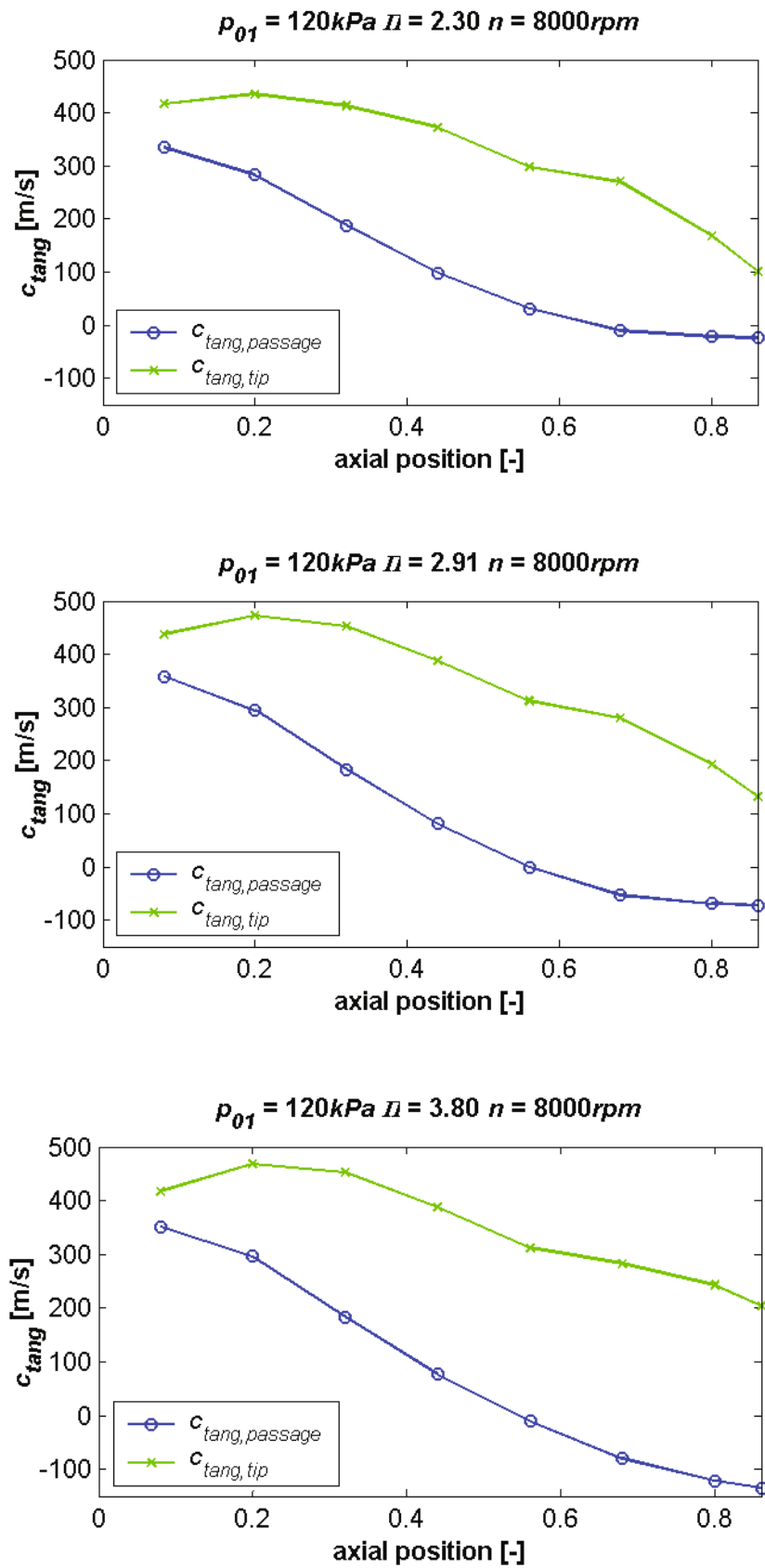


Figure 83: Tangential velocity of the tip leakage and passage flow for various operating conditions

The curves of the passage flow show a continuous decrease of the absolute tangential velocity. This indicates that the work is done along the whole chord length of the blade, most energy is converted in the mid-section where the gradient is the steepest. The total decrease over the blade is a measure for the total work output of the turbine and increases with increasing pressure ratio.

Since the tip leakage flow is not deflected by the blade it does not take part in the work conversion process of the turbine, this is observable in Figure 83 by the smaller gradient of the curves corresponding to the tip leakage flow. Since the tip leakage flow increases with the pressure ratio the difference between the two curves also becomes larger.

In the upstream part of the gap the tangential velocity locally increases. According to the Euler equation this means that in this region there is actually work added to the tip leakage flow. The local increase of the specific enthalpy was first reported by Thorpe et al. (2004b): “It is apparent that the direction of the over-tip leakage flow is significantly different to that of the flow in the blade passage. In fact, the leakage fluid can have an absolute circumferential velocity that is above that at rotor inlet, indicating that work is done on this fluid and that its total temperature will be above that at inlet to the blade passage”.

The amount of energy extracted out of the fluid has a great influence on the stagnation enthalpy and consequently the total temperature of the fluid.

$$c_p \cdot (T_{0,3} - T_{0,4}) = u \cdot (c_{4,tang} - c_{3,tang}) \quad (5.42)$$

The increase of the total temperature has a direct influence on the driving temperature difference at the over-tip casing. Inside the gap the total temperature will be higher than outside the gap. According to Thorpe et al. (2004b) in a real gas turbine these temperature fluctuations are typically between 200K and 400K. Therefore the driving temperature will increase and the amount of heat entering the over-tip casing will be increased. Thermocouples and even hot-films are too slow to register the time-resolved total temperature peaks inside the gap.

Figure 84 shows the total temperature distribution of the passage flow and tip leakage flow for various operating conditions. The total temperature profile was obtained from the static temperature profile and the absolute Mach number distribution as shown in Figure 80.

$$T_{0,abs} = T \cdot \left(1 + \frac{k-1}{2} M_{abs}^2 \right) \quad (5.43)$$

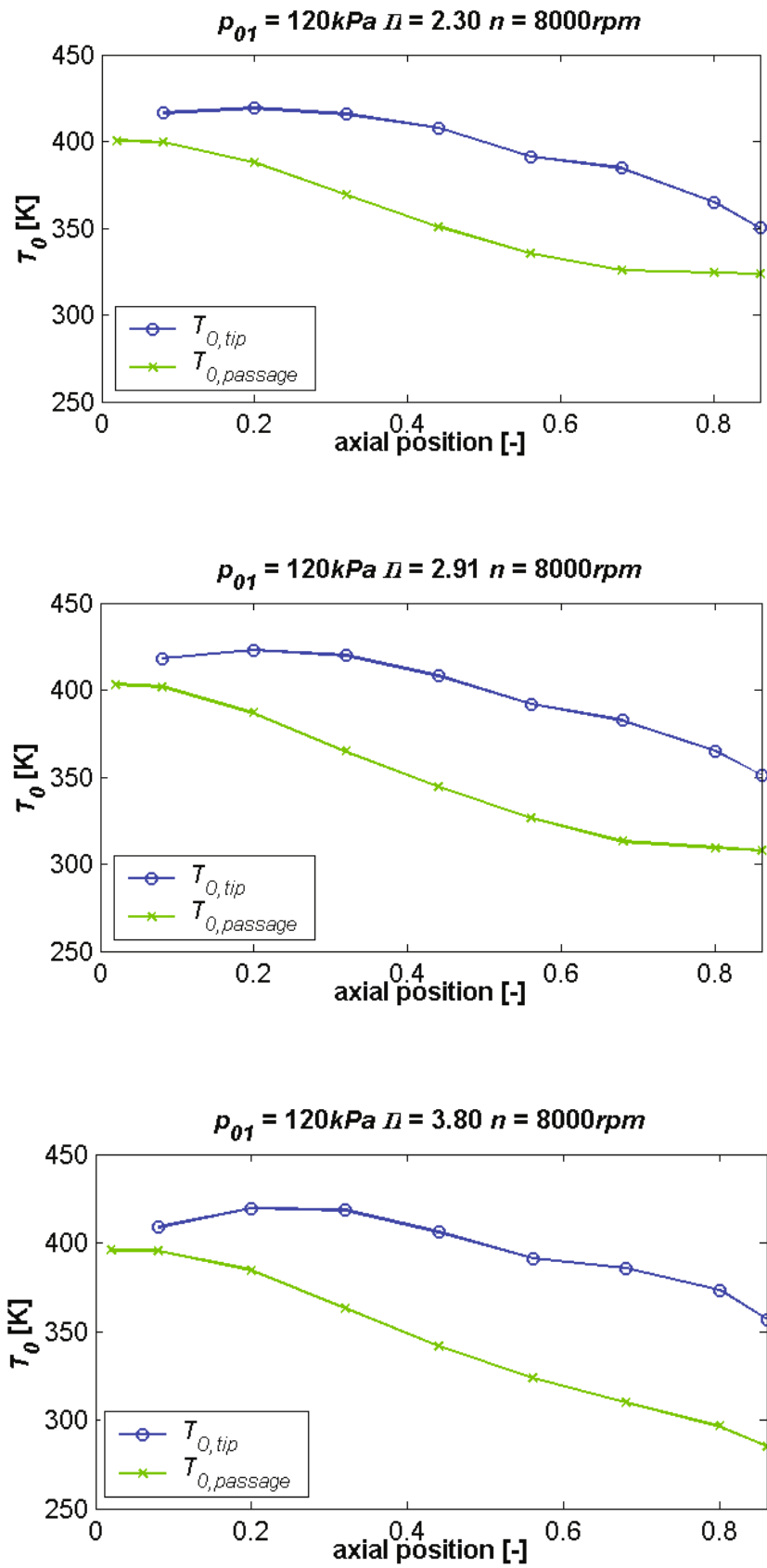


Figure 84: Total temperature distribution of the tip leakage flow and the passage flow for various operating conditions

The figure shows great resemblance with Figure 83, which can be easily explained with equation (5.42).

Since the temperature difference between the passage flow and the tip leakage flow is coupled with the pressure difference over the blade both distribution profiles are similar. The maximum difference is located at mid-chord or slightly downstream of mid-chord and can be as much as $80K$.

5.3.8.1 Influence of the fluctuation of the driving temperature

In section 5.3.5 the effect of the time-response of the static pressure taps on the averaged heat transfer coefficient distribution was examined. It was found that non-linear effects originating from the fluid properties can cause a significant time-averaging discrepancy. In this section the influence of the fluctuation of the total temperature on the time-averaged heat transfer coefficient distribution is examined.

If the sensors have a time-response which is insufficient to register the time-resolved total temperature peaks inside the gap, the total temperature inside the gap is underestimated and the driving temperature overestimated.

Accordingly in reality the heat transfer coefficient inside the gap will be higher than the measured values. In complement the heat transfer outside the gap will be lower than measured.

The steady temperature measured by a thermocouple equals:

$$\Delta \bar{T} = \frac{\int_0^{\tau} \Delta T(t) dt}{\tau} \quad (5.44)$$

The steady heat transfer coefficient determined with this temperature equals:

$$\bar{h} = \frac{\dot{q}}{\Delta \bar{T}} = \frac{\dot{q}}{\left(\frac{\int_0^{\tau} \Delta T(t) dt}{\tau} \right)} \quad (5.45)$$

The steady heat transfer coefficient determined with the time-resolved temperature, followed by an integration over one period equals:

$$\bar{h} = \frac{\left(\int_0^\tau \frac{\dot{q}}{\Delta T(t)} dt \right)}{\tau} \quad (5.46)$$

Equation (5.45) and (5.46) are equal when the driving temperature is constant, but when the driving temperature fluctuates equation (5.45) and (5.46) obtain different results. An example is given with the following sawtooth function:

$$\Delta T(t) = t + C \quad (5.47)$$

Inserting (5.47) in equation (5.45) and (5.46) gives respectively:

$$\bar{h} = \frac{\dot{q}}{\left(\frac{\int_0^\tau \Delta T(t) dt}{\tau} \right)} = \left[\frac{\dot{q}}{\left(C + \frac{\tau}{2} \right)} \right] \quad (5.48)$$

and:

$$\bar{h} = \frac{\left(\int_0^\tau \frac{\dot{q}}{\Delta T(t)} dt \right)}{\tau} = \left[\frac{\dot{q} \ln(\tau + C)}{\tau} \right] = \left[\frac{\dot{q} \ln(\Delta T)}{\tau} \right] \quad (5.49)$$

The result of equation (5.48) and (5.49) is unequal. When the heat transfer coefficient is determined by measuring the driving temperature the frequency response is an important parameter even when only the time-averaged (steady) heat transfer is to be determined. This is especially true for situations where the driving temperature is very small or where the direction of heat transfer is temporarily reversed.

Although all components of the thermocouple+ sensors were selected primarily on the basis of their thermal stability and the heating temperature of the thermocouple+ foil has been set accordingly high, the high entrance temperature of a rotating cascade limits the obtainable driving temperature. As shown in Figure 84 the total temperature of the fluid at mid-chord can fluctuate between 340K (passage) and 400K (tip gap) the driving temperature consequently

varies between $40K$ and $100K$. This means that the heat transfer coefficient measured in the tip gap underestimates the actual heat transfer coefficient by a factor of 2.5. Although the area of the over-tip gap is relatively small the magnitude of the underestimation presented above can have a significant impact on the prediction of the heat transfer at complete over-tip casing.

The hot-films are also influenced by the fluctuation of the fluid temperature, however due to the much higher achievable driving temperature of typically $> 200K$ the underestimation is far less severe and will be in the order of 1.3.

With the procedure described in the previous sections it is possible to perform a correction for the elevated temperatures inside the tip gap and for the undisturbed passage flow. However since the boundary layer flow at the over-tip casing can not be strictly divided into passage flow and tip leakage flow errors have to be accounted for.

6 FORMATION OF THE CORRELATION

6.1 Correlations

In the previous chapter the misalignment in the front-section and the tip leakage flow in the mid-section, were identified as the main contributors to the elevated heat transfer levels at the over-tip casing. It was also shown that with the aid of simple flow models, quantitative predictions are possible for some points at the casing, but not for the complete casing. However, the extensive experimental database presented in chapter 4 and presented more detailed in Van Duikeren (2006) allows – based on the findings of the previous chapter - the formation of correlations which enable quantitative accurate predictions to be made for a wide range of operating conditions. In this chapter, the various steps of the formation of the enhanced correlation will be described, at the end the accuracy of the correlation will be shown.

This chapter the approach to the formulation of the correlation is presented. The coefficients are not directly interchangeable between different turbine designs, and therefore irrelevant to the discussion. In order to protect the design parameters of the manufacturer the coefficients of the empirical correlations have been replaced (c_1, \dots, c_{11}) .

6.2 Basic correlation

In this paragraph, the “basic” correlation is presented which accounts for the heat transfer coefficient of the passage fluid - as determined by the flat plate correlation - and the significant boosting effect of the tip leakage flow. It was shown in Figure 65 that the measured heat transfer coefficient is constantly higher than the analytical heat transfer coefficient.

Furthermore, except for the upstream region where the misalignment plays an important role, the ratio between the experimental and analytical heat transfer coefficient is reasonably constant and only dependent on the rotational speed and on the total pressure. Figure 85 shows this ratio at an axial position of $x = 0.7$ (where the tip leakage is strongest and the misalignment has no effect) and a total pressure of $120kPa$.

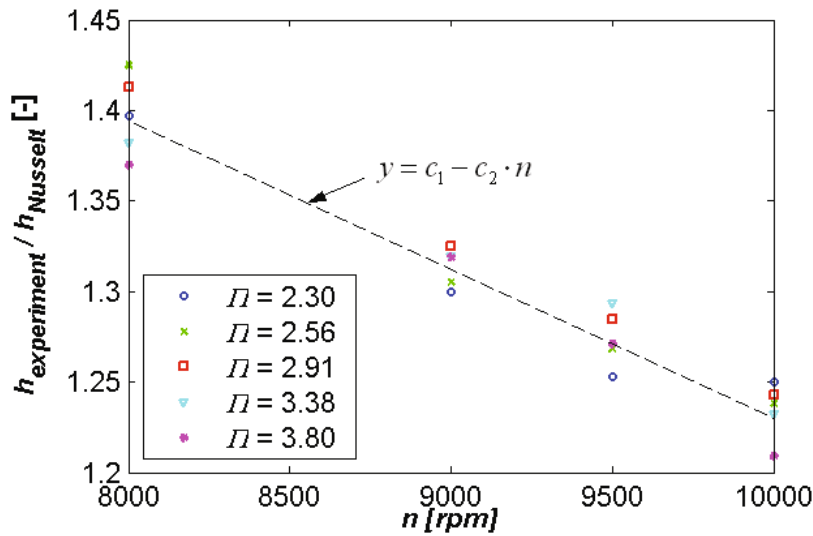


Figure 85: Ratio between the experimental and analytical heat transfer coefficient at $x=0.7$ for $p_{01} = 120kPa$

The figure shows that the discrepancy is biggest for the operating conditions with the lowest rotational speed. The direction of the relative rotation of the casing is opposite to that of the leakage flow, due to the no slip condition at the wall the pressure difference over the gap is reduced. Consequently, the intensity of the tip leakage flow reduces with the increase of the rotational speed. Since the tip leakage flow is responsible for a considerable part of the heat transfer, the heat transfer coefficient strongly correlates with the rotational speed. The dependence of the leakage flow on the rotational speed was studied in detail by Yaras et al. (1992), the reduction of the heat transfer coefficient due to the rotation was also observed by Guenette et al. (1985).

The linear function obtained from Figure 85 can be used to integrate the elevated heat transfer caused by the tip leakage flow in the flat plate correlation:

$$h_{corr_{basic}} = (c_1 - c_2 \cdot n) \cdot h_{flat\ plate} \quad (6.1)$$

Figure 86a to h shows the experimental results (left) and analytical results obtained with the basic correlation as obtained in equation (6.1). The resulting error is shown as well (right). The figure shows a good overall agreement in the mid- and aft-region. However, in the front region, the error can be very significant.

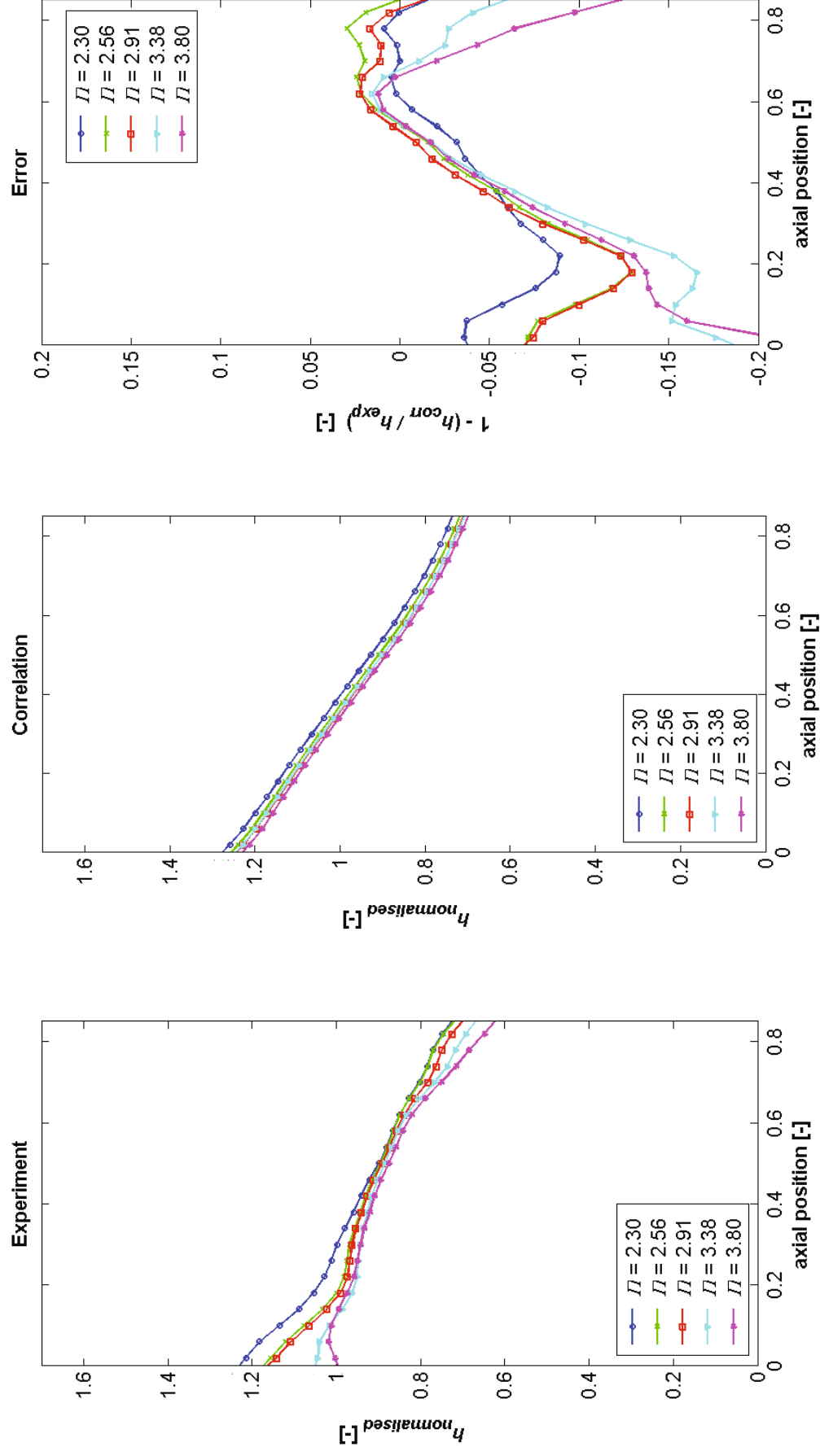


Figure 86a: Experimental (left) and analytical (center) heat transfer coefficient and the resulting error (right) obtained with the “basic” correlation,

$p_{01} = 120kPa, n = 8000 \text{ rpm}$

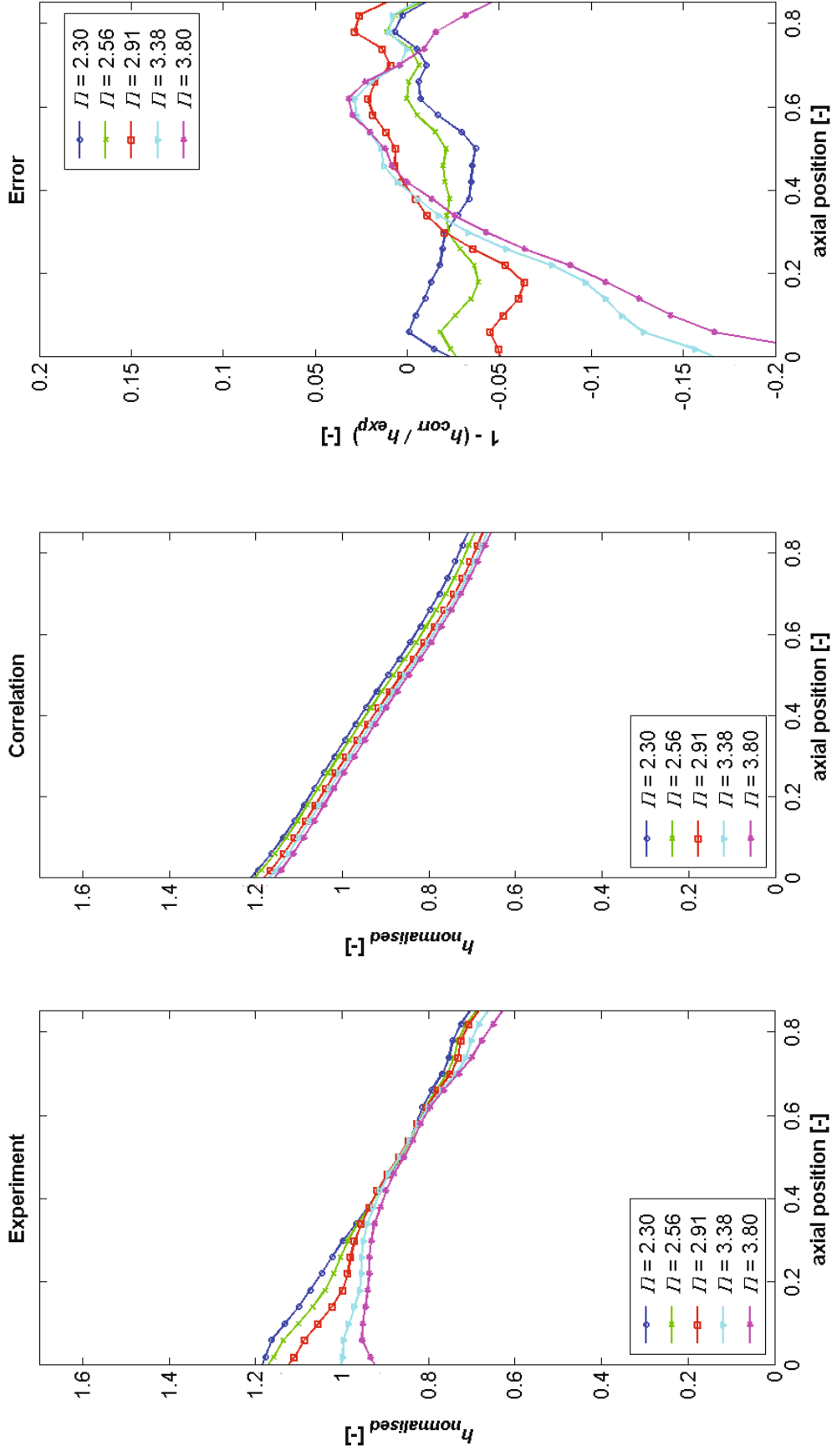


Figure 86b: Experimental (left) and analytical (centre) heat transfer coefficient and the resulting error (right) obtained with the “basic” correlation,

$p_{01} = 120 \text{ kPa}$, $n = 9000 \text{ rpm}$

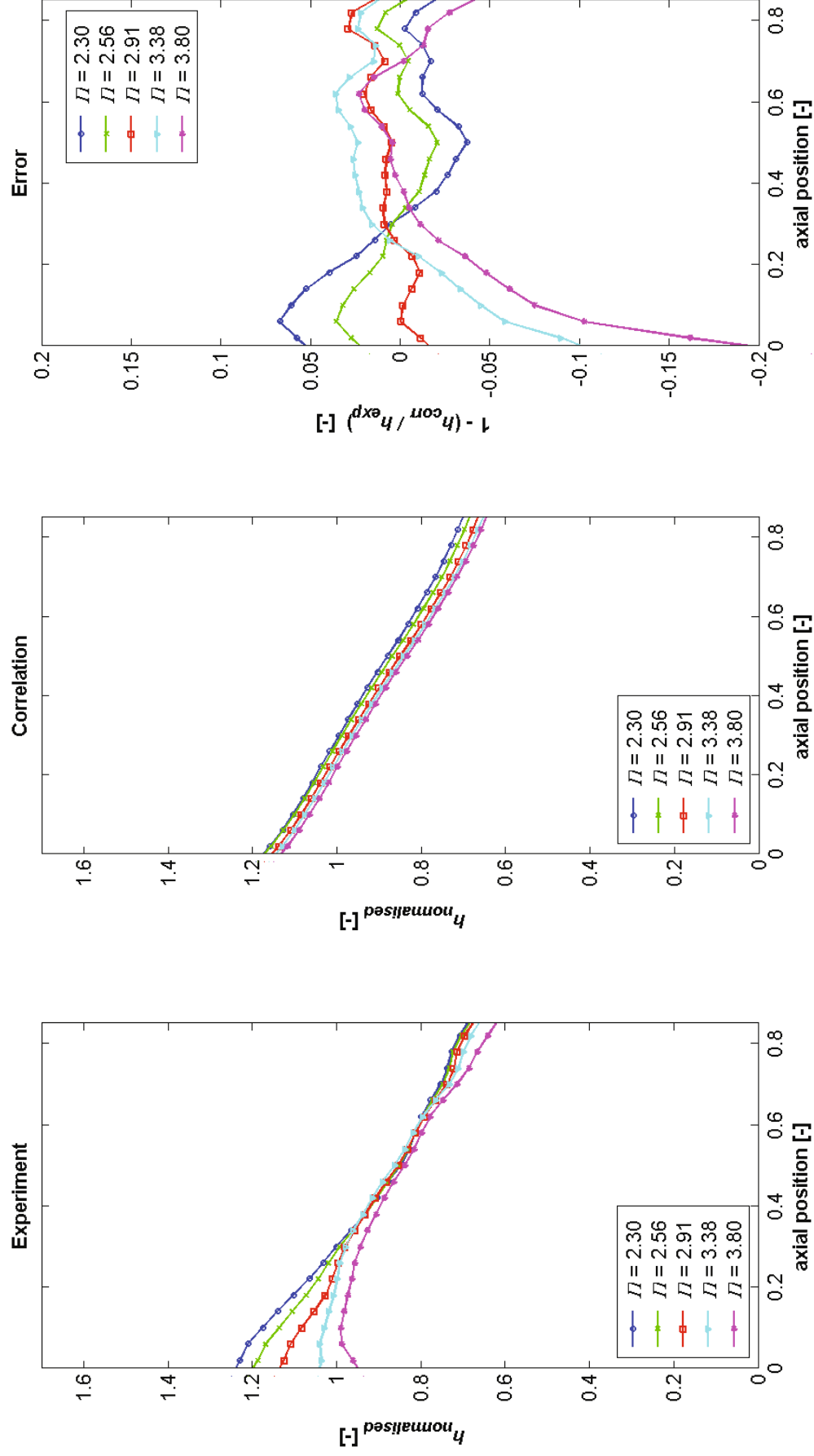


Figure 86c: Experimental (left) and analytical (centre) heat transfer coefficient and the resulting error (right) obtained with the “basic” correlation,

$p_{01} = 120 \text{ kPa}$, $n = 9500 \text{ rpm}$

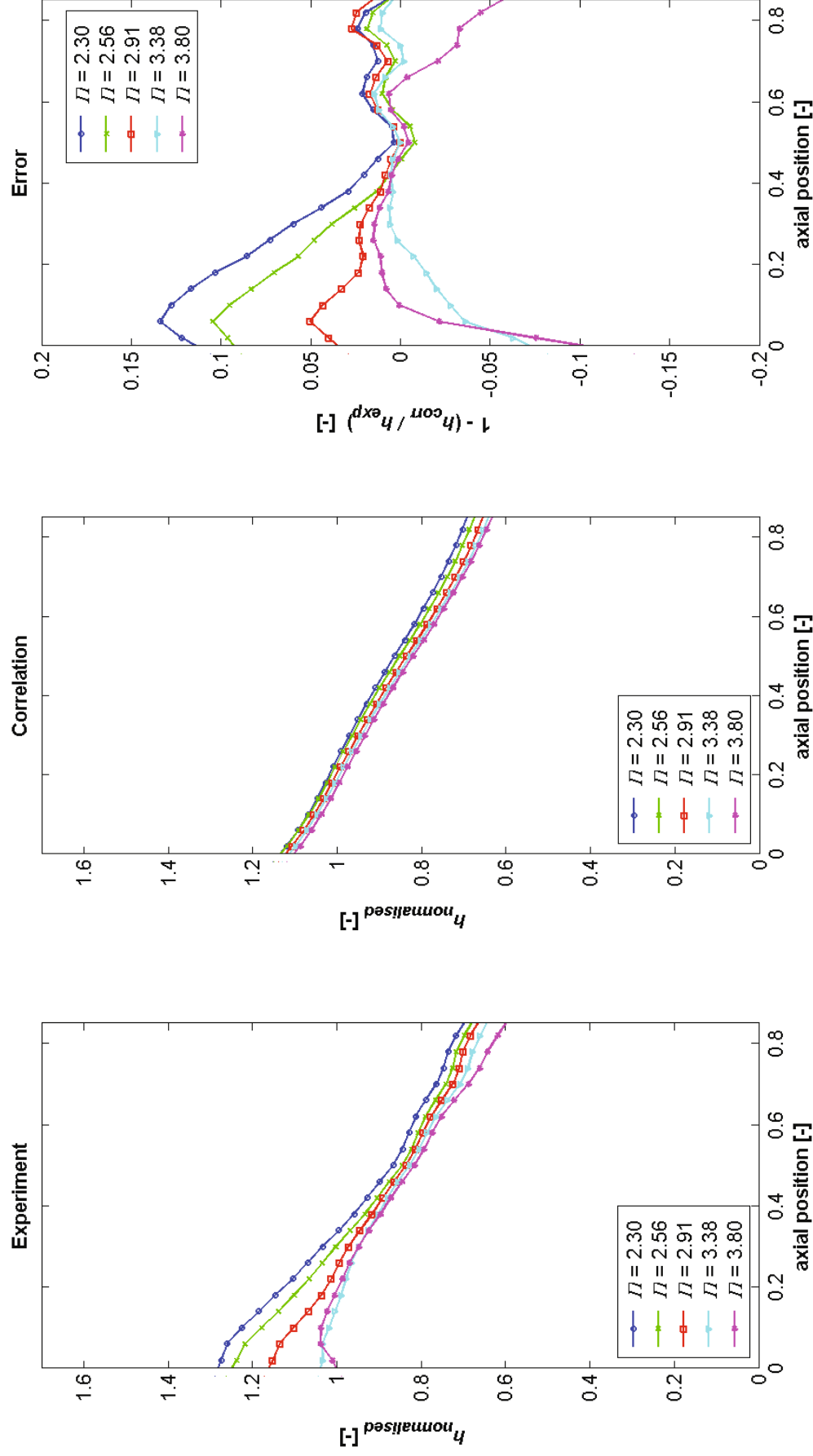


Figure 86d: Experimental (left) and analytical (centre) heat transfer coefficient and the resulting error (right) obtained with the “basic” correlation,

$p_{01} = 120 \text{ kPa}$, $n = 10000 \text{ rpm}$

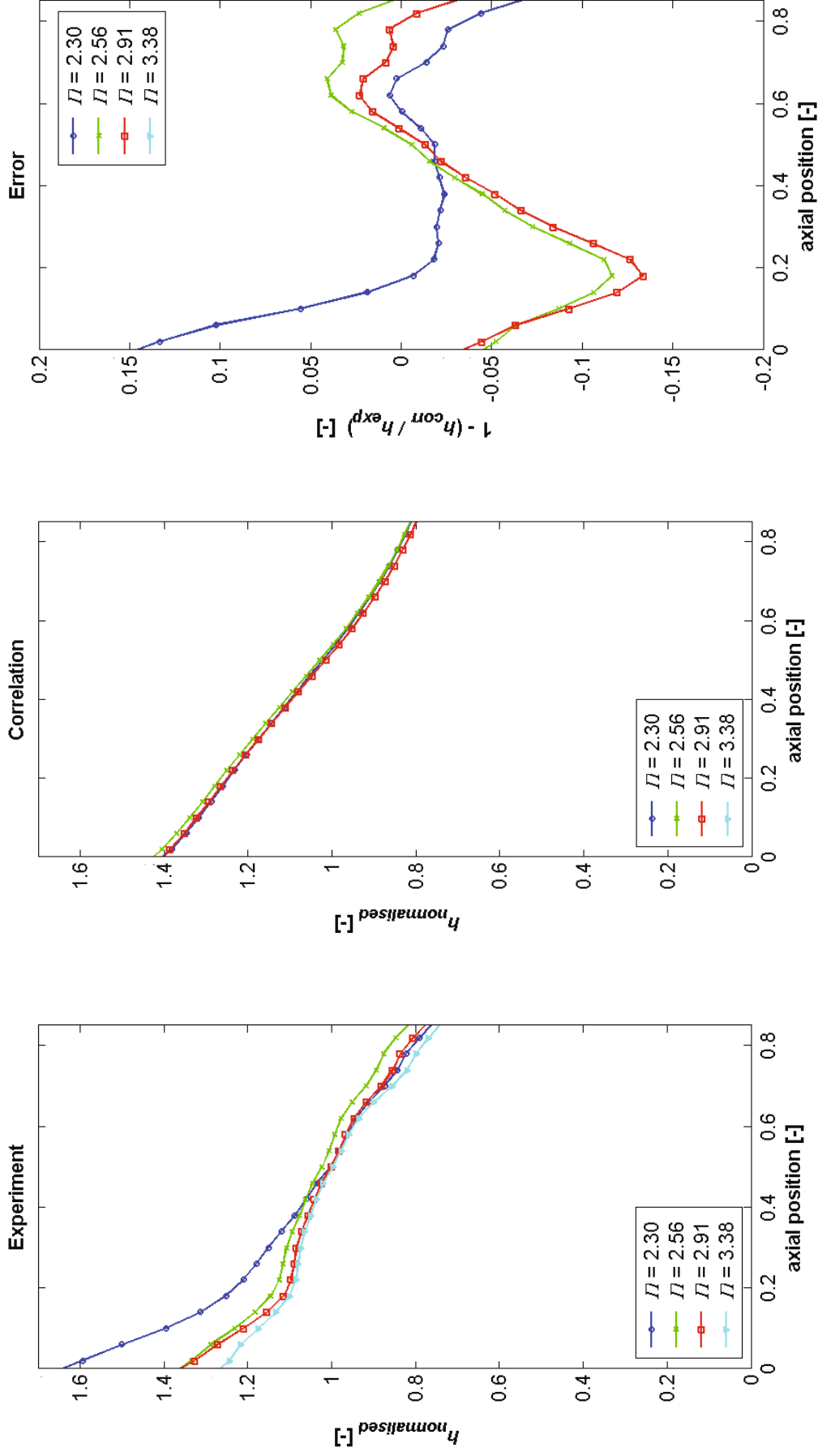


Figure 86c: Experimental (left) and analytical (centre) heat transfer coefficient and the resulting error (right) obtained with the “basic” correlation,

$p_{01} = 150 \text{ kPa}$, $n = 8000 \text{ rpm}$

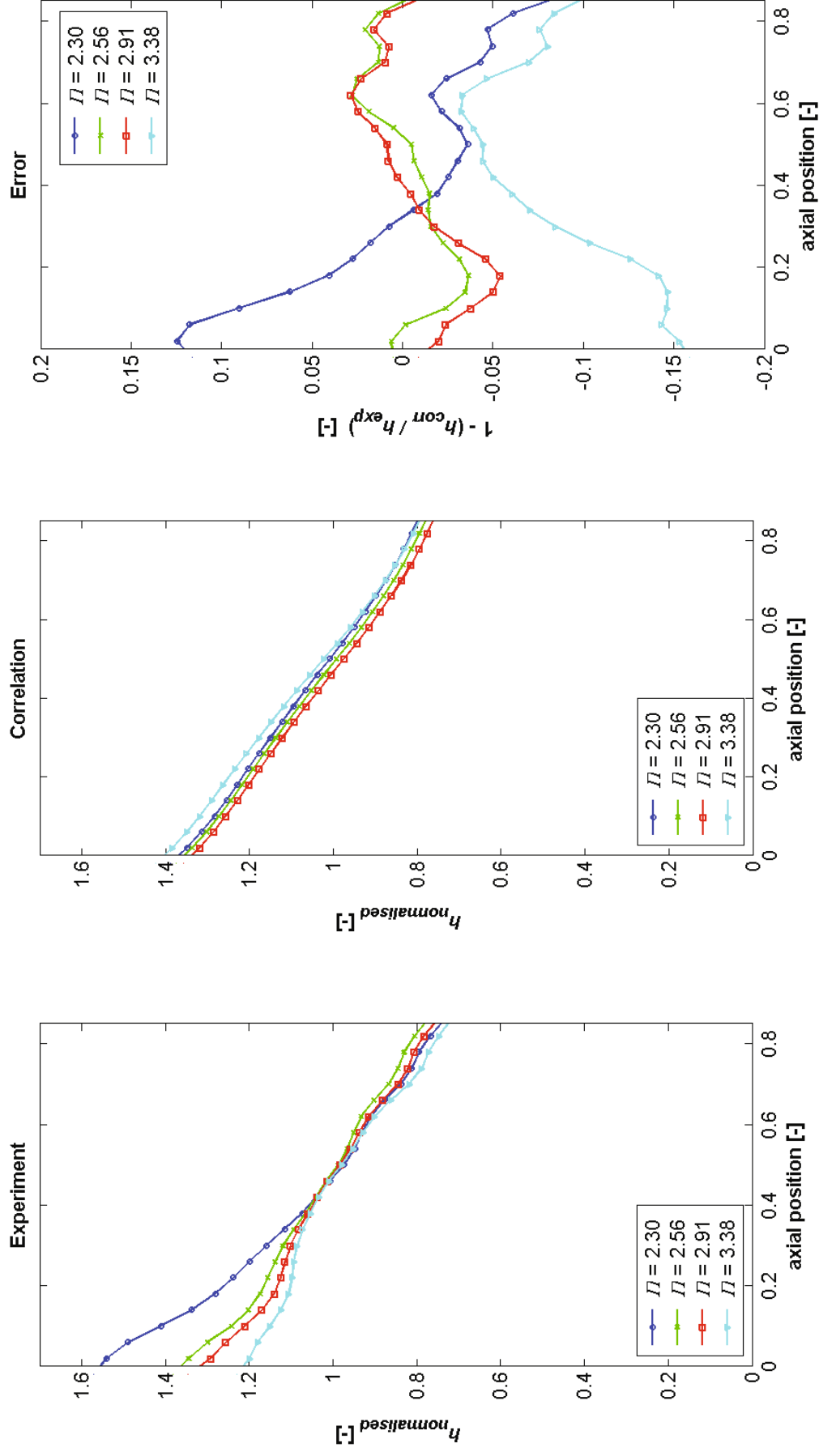


Figure 86f: Experimental (left) and analytical (centre) heat transfer coefficient and the resulting error (right) obtained with the “basic” correlation,

$p_{01} = 150 \text{ kPa}$, $n = 9000 \text{ rpm}$

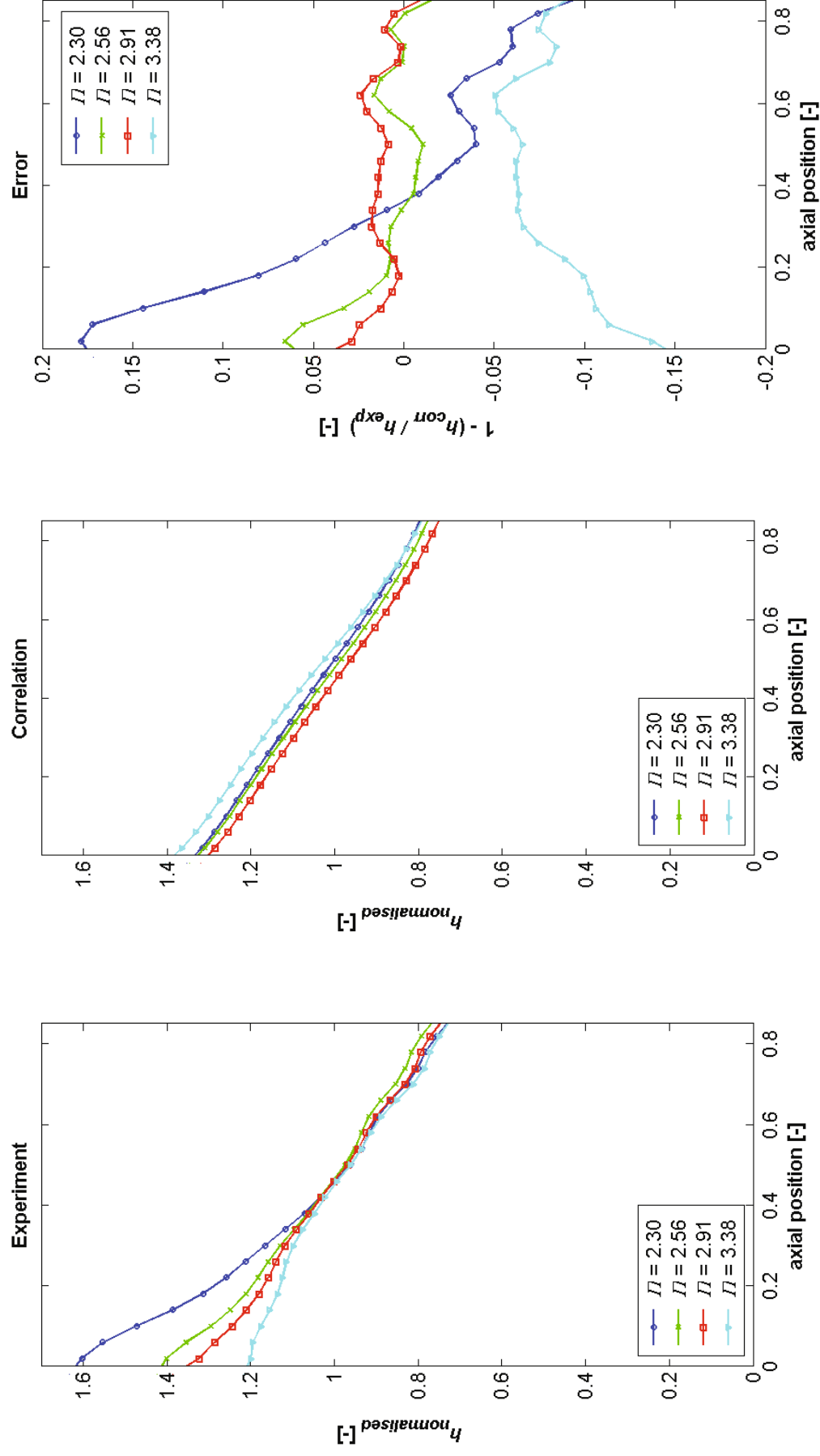


Figure 86g: Experimental (left) and analytical (center) heat transfer coefficient and the resulting error (right) obtained with the “basic” correlation,

$p_{01} = 150 \text{ kPa}$, $n = 9500 \text{ rpm}$

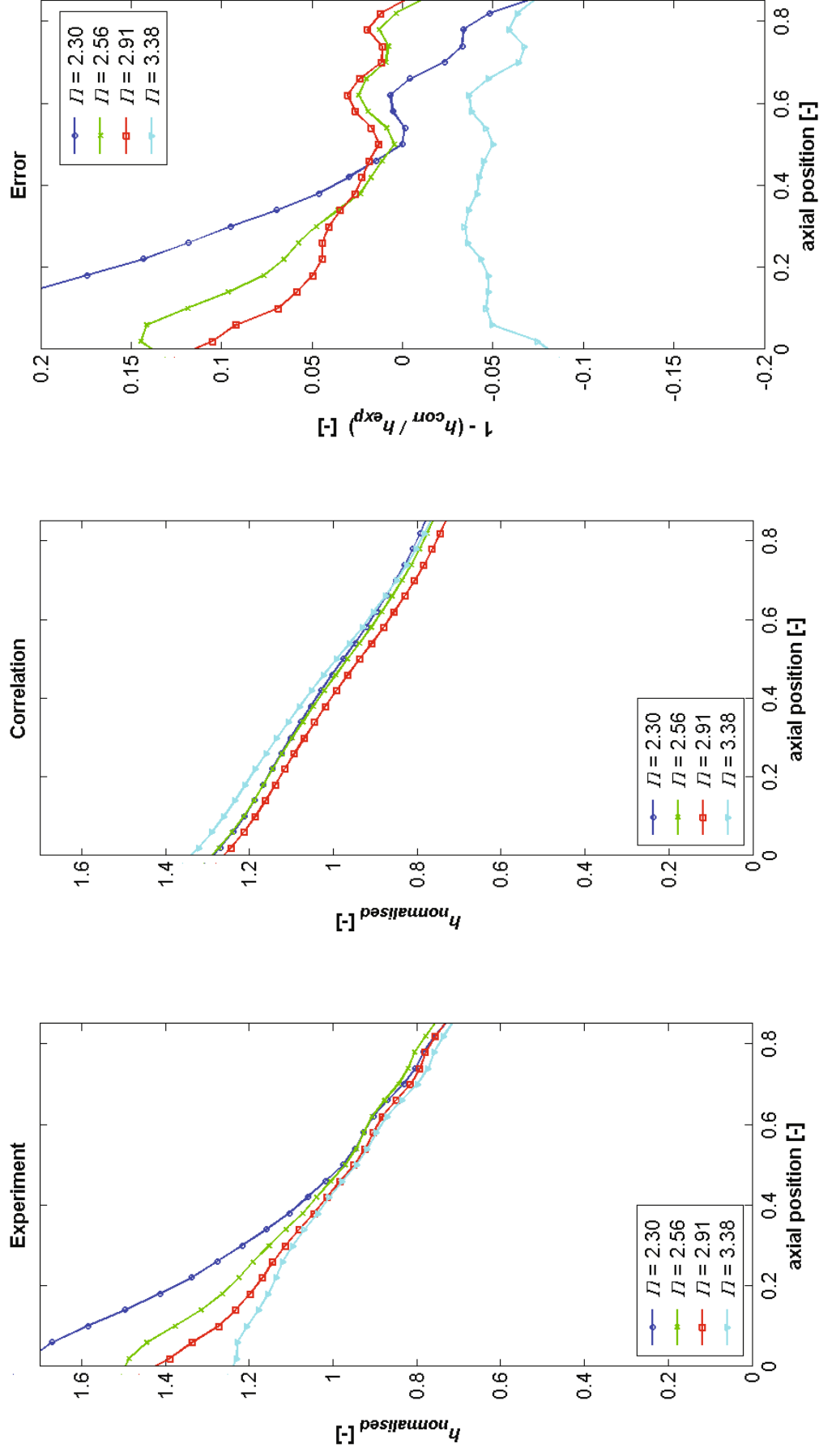


Figure 86h: Experimental (left) and analytical (centre) heat transfer coefficient and the resulting error (right) obtained with the “basic” correlation,

$p_{01} = 150kPa, n = 10000 \text{ rpm}$

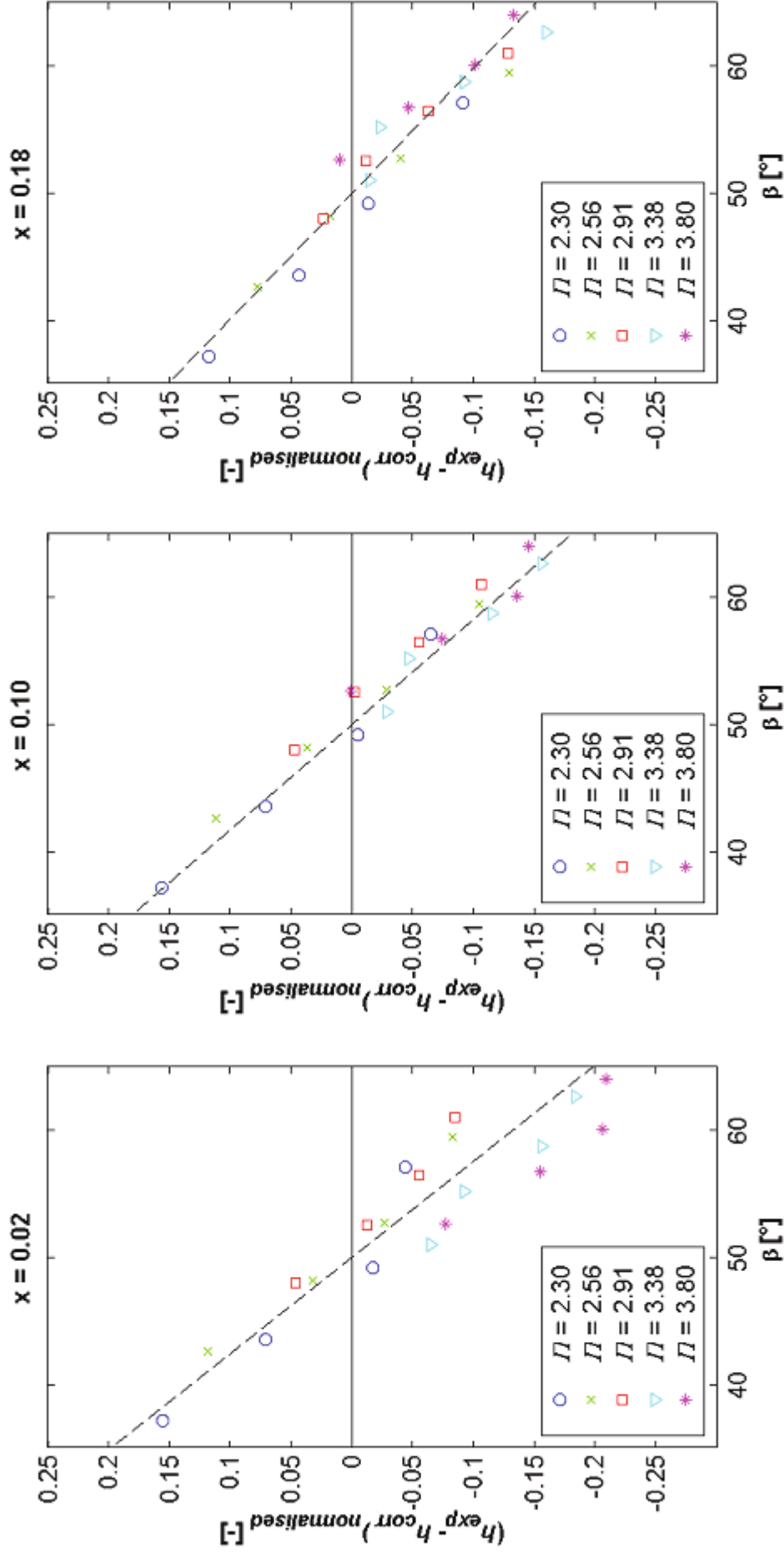


Figure 87: Heat transfer coefficient as function of the relative flow angle at rotor entrance at three different axial positions for $p_{01} = 120kPa$

6.3 Enhanced correlation

The enhanced correlation additionally accounts for the strong variation of the heat transfer levels observed in the upstream area of the over-tip casing caused by the misalignment of the inlet fluid and the rotor blade. In the next step the magnitude of the flow misalignment in the front-region of the over-tip casing will be examined. The magnitude of the elevated heat transfer coefficient caused by the misalignment is defined as:

$$h_{\text{misalignment}} = h_{\text{experiment}} - h_{\text{basic}} \quad (1.1)$$

As discussed in paragraph 5.2.1, there is a correlation between the relative flow angle of the fluid entering the rotor and $h_{\text{misalignment}}$. Figure 87a to c show this relation for the operating conditions with $p_{01} = 120 \text{ kPa}$ at three different axial positions. The three figures show strong

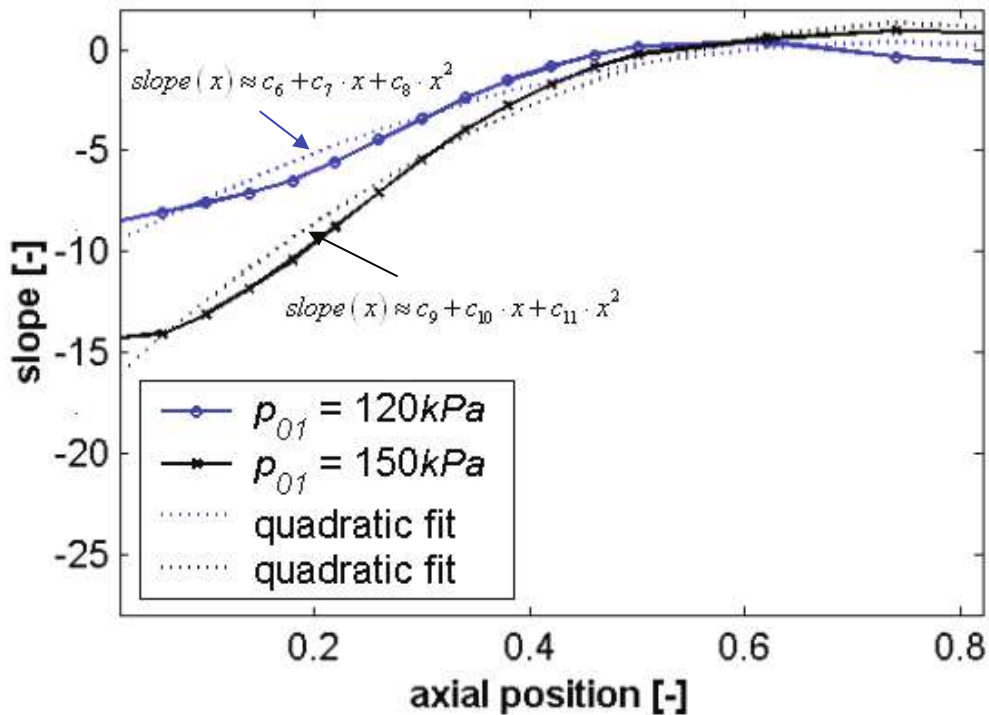


Figure 88: Slope of the correlation as function of the axial position

linear correlation, furthermore all fitted lines (dashed) intersect the x-axis at the same position. Only the gradients of the lines are different, the gradient of the line corresponding to the most upstream region ($x = 0.02$) is steepest. This can be explained by the fact that the impact of the misalignment at the entrance region of the rotor is strongest. At the passage entrance, the misalignment will be biggest. Downstream the entrance the blade guides the

flow into the “correct” direction, which reduces the interference in the flow. The fitted line is defined as:

$$h_{misalignment}(x, \beta) = slope(x) \cdot (\beta - c_4) \quad (1.4)$$

The gradient can be determined for every axial position, the result is shown in Figure 88. The slope as function of the axial position can be fitted by a quadratic function. A quadratic function is chosen since it is simple and supplies adequate results.

$$slope(x) \approx c_6 + c_7 \cdot x + c_8 \cdot x^2 \quad [p_{01} = 120kPa] \quad (1.5)$$

$$slope(x) \approx c_9 + c_{10} \cdot x + c_{11} \cdot x^2 \quad [p_{01} = 150kPa] \quad (1.6)$$

The total increase of the heat transfer caused by the misalignment is:

$$h_{misalignment}(x, \beta) = (c_6 + c_7 \cdot x + c_8 \cdot x^2) \cdot (\beta - c_4) \quad [p_{01} = 120kPa] \quad (1.7)$$

$$h_{misalignment}(x, \beta) = (c_9 + c_{10} \cdot x + c_{11} \cdot x^2) \cdot (\beta - c_5) \quad [p_{01} = 150kPa] \quad (1.8)$$

6.4 Complete enhanced heat transfer correlation for the over-tip casing

The total heat transfer coefficient at the over-tip casing finally can be expressed as:

$$h_{corr_{enhanced}} = (\beta - c_4) \cdot (c_5 + c_6 \cdot x + c_7 \cdot x^2) + h_{corr_{flat\ plate}} \cdot (c_1 - c_2 \cdot n) \quad [120kPa] \quad (1.9)$$

$$h_{corr_{enhanced}} = (\beta - c_5) \cdot (c_9 + c_{10} \cdot x + c_{11} \cdot x^2) + h_{corr_{flat\ plate}} \cdot (c_3 - c_2 \cdot n) \quad [150kPa] \quad (1.10)$$

with β being the averaged relative flow angle at the rotor entrance, $h_{corr_{flat\ plate}}$ the averaged heat transfer obtained by the flat plate correlation as stated in equation (5.7) and n the rotational speed of the rotor in *rpm*. The flat plate correlation allows the heat transfer level coefficient of other pressure (Reynolds) levels to be determined.

The results are plotted in Figure 89a to h. The left row shows the experimental values, the middle row shows the corresponding predictions obtained by the enhanced correlation, and the right row shows the resulting error. The figure shows a good overall agreement between

the experiment and the correlation. The discrepancy of the equation (1.9) and equation (1.10) compared to the experimental data is generally less than $\pm 5\%$.

A bigger discrepancy is found at the upstream region of the operating conditions at low partload conditions and mainly at the high pressure level (Figure 89e). For these conditions, the experimental heat transfer coefficient is significantly higher than the predicted value. This could be explained with the very strong variation of the inlet flow direction (up to 40° misalignment) which is accompanied by high turbulence at macro scale. Only the heat transfer coefficient for the conditions with a pressure ratio of $\Pi = 3.38$ and $p_{01} = 150 \text{ kPa}$ is constantly over predicted and does not lie in the $\pm 5\%$ range. The reason for this difference could not be traced.

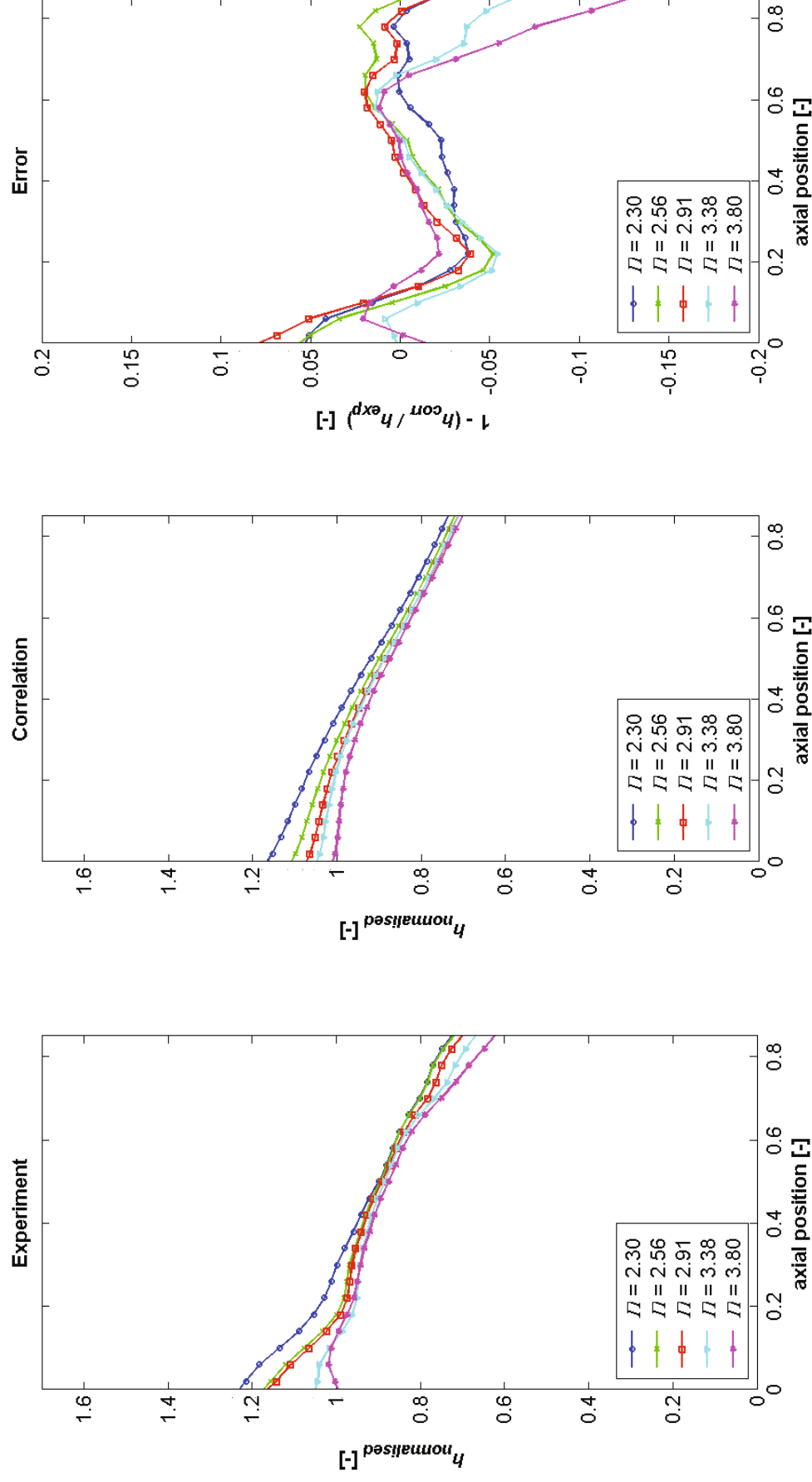


Figure 89a: Experimental (left) and analytical (centre) heat transfer coefficient and the resulting error (right) obtained with the enhanced correlation,

$p_{01} = 120 \text{ kPa}$, $n = 8000 \text{ rpm}$

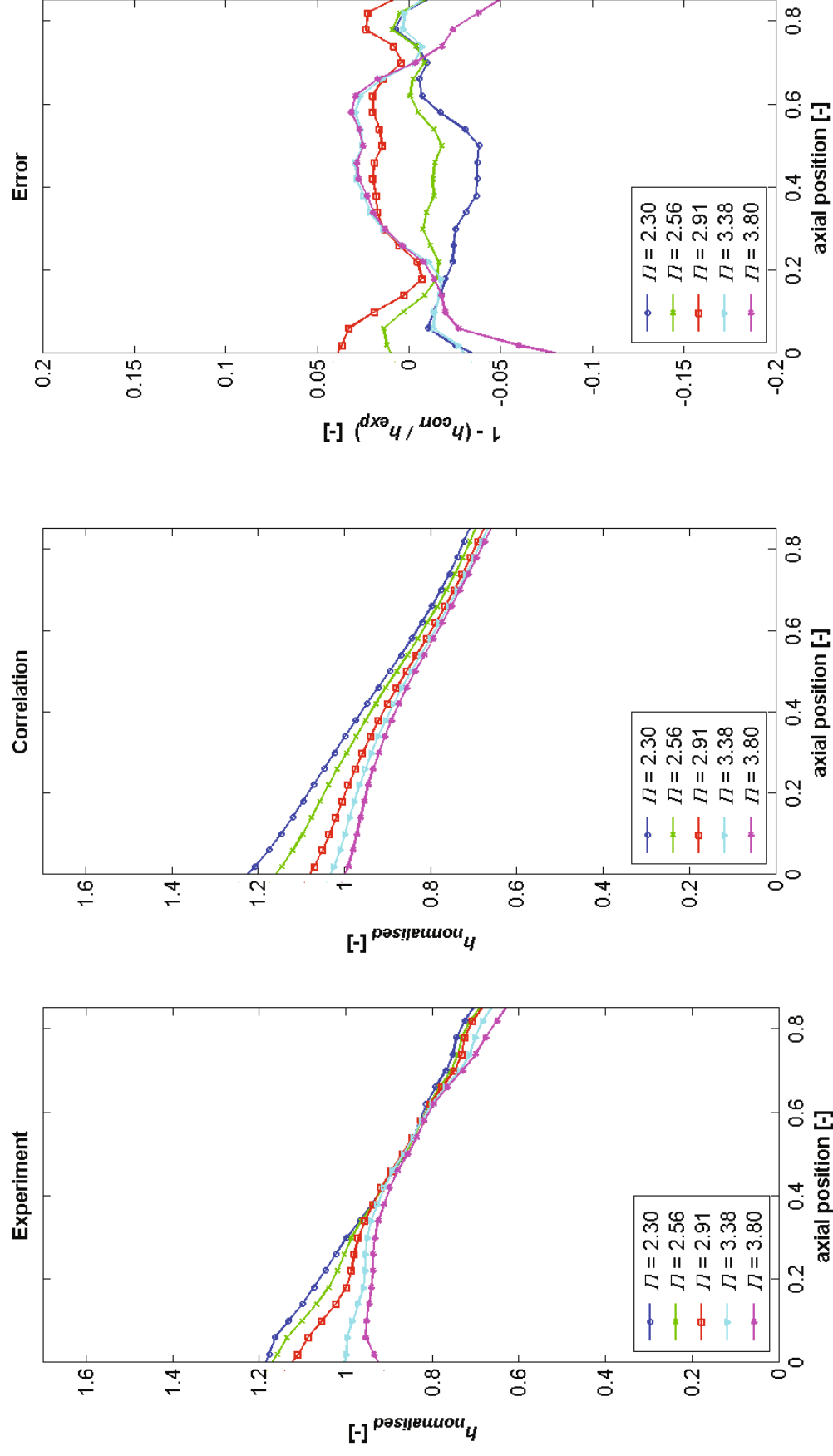


Figure 89b: Experimental (left) and analytical (centre) heat transfer coefficient and the resulting error (right) obtained with the enhanced correlation,

$p_{01} = 120 \text{ kPa}$, $n = 9000 \text{ rpm}$

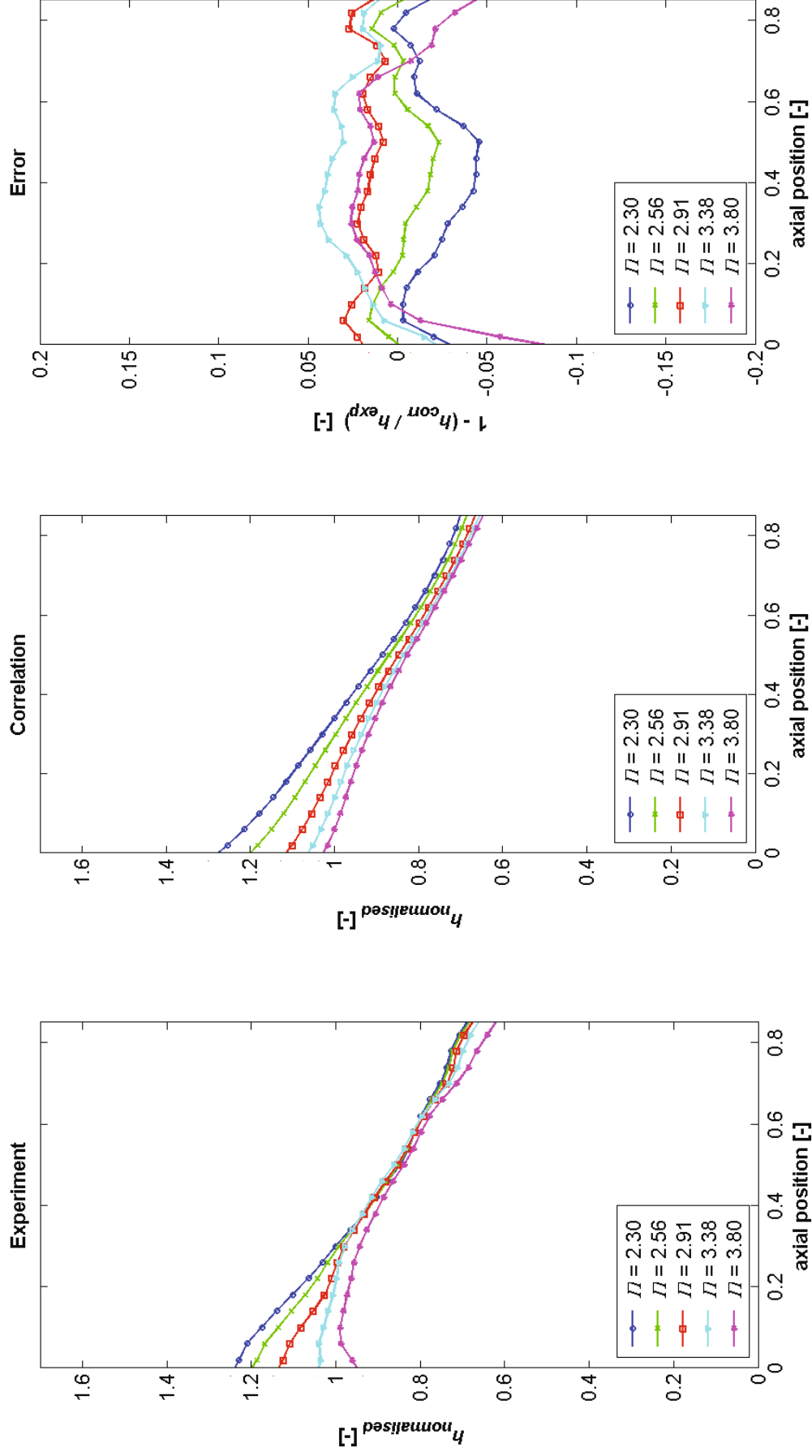


Figure 89c: Experimental (left) and analytical (centre) heat transfer coefficient and the resulting error (right) obtained with the enhanced correlation,

$p_{o1} = 120 \text{ kPa}$, $n = 9500 \text{ rpm}$

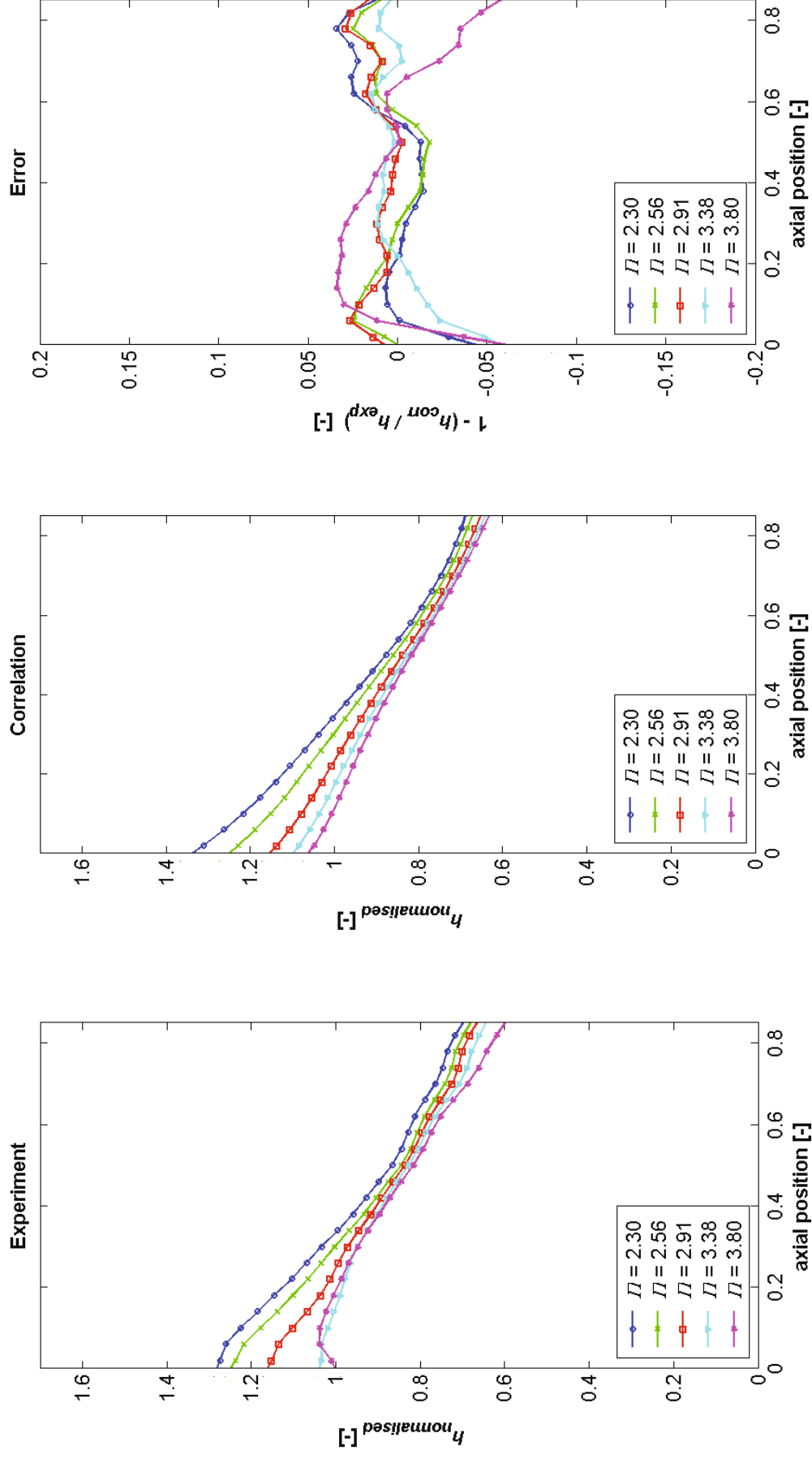


Figure 89d: Experimental (left) and analytical (centre) heat transfer coefficient and the resulting error (right) obtained with the enhanced correlation,

$p_{01} = 120 \text{ kPa}$, $n = 10000 \text{ rpm}$

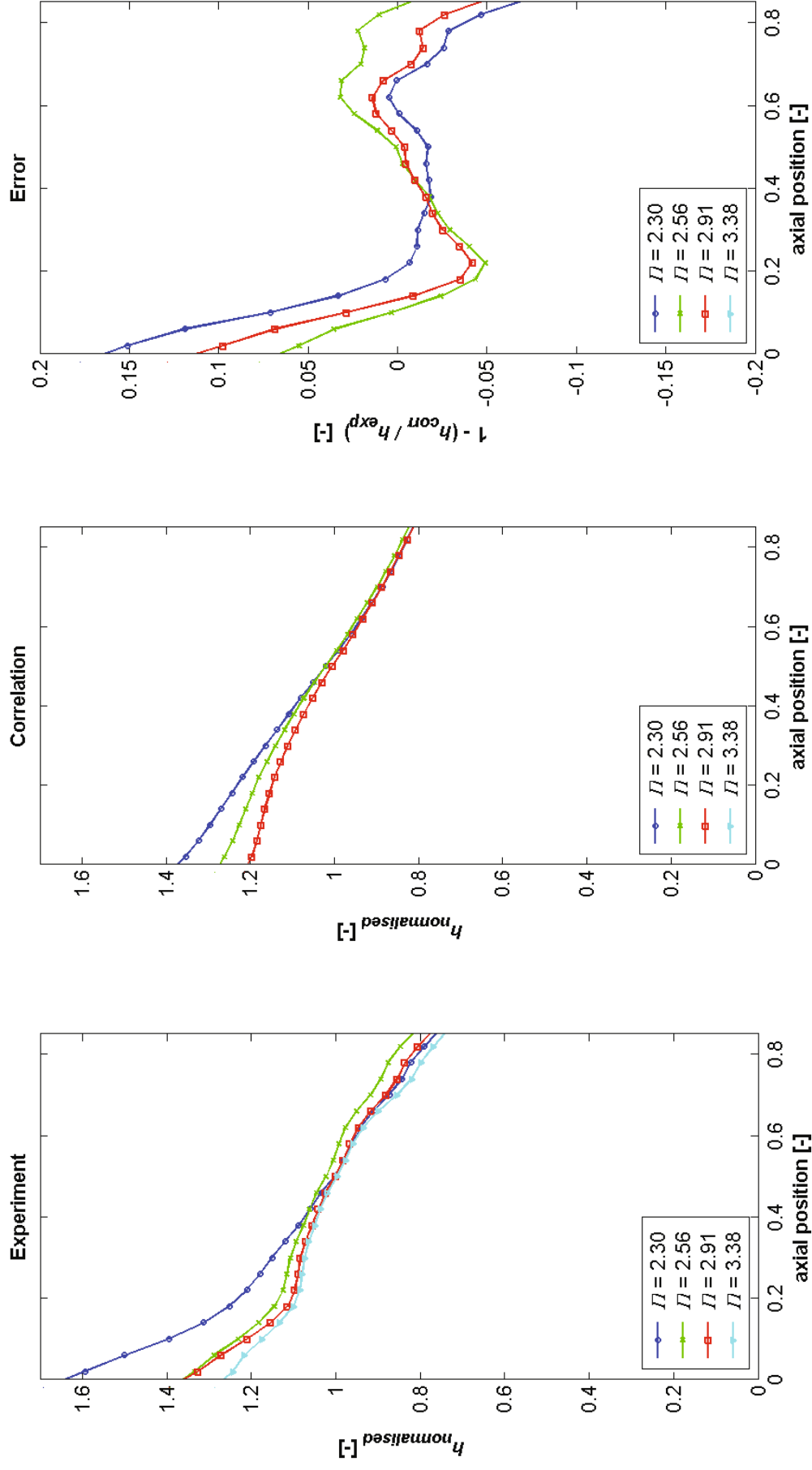


Figure 89c: Experimental (left) and analytical (centre) heat transfer coefficient and the resulting error (right) obtained with the enhanced correlation,

$p_{01} = 150 \text{ kPa}$, $n = 8000 \text{ rpm}$

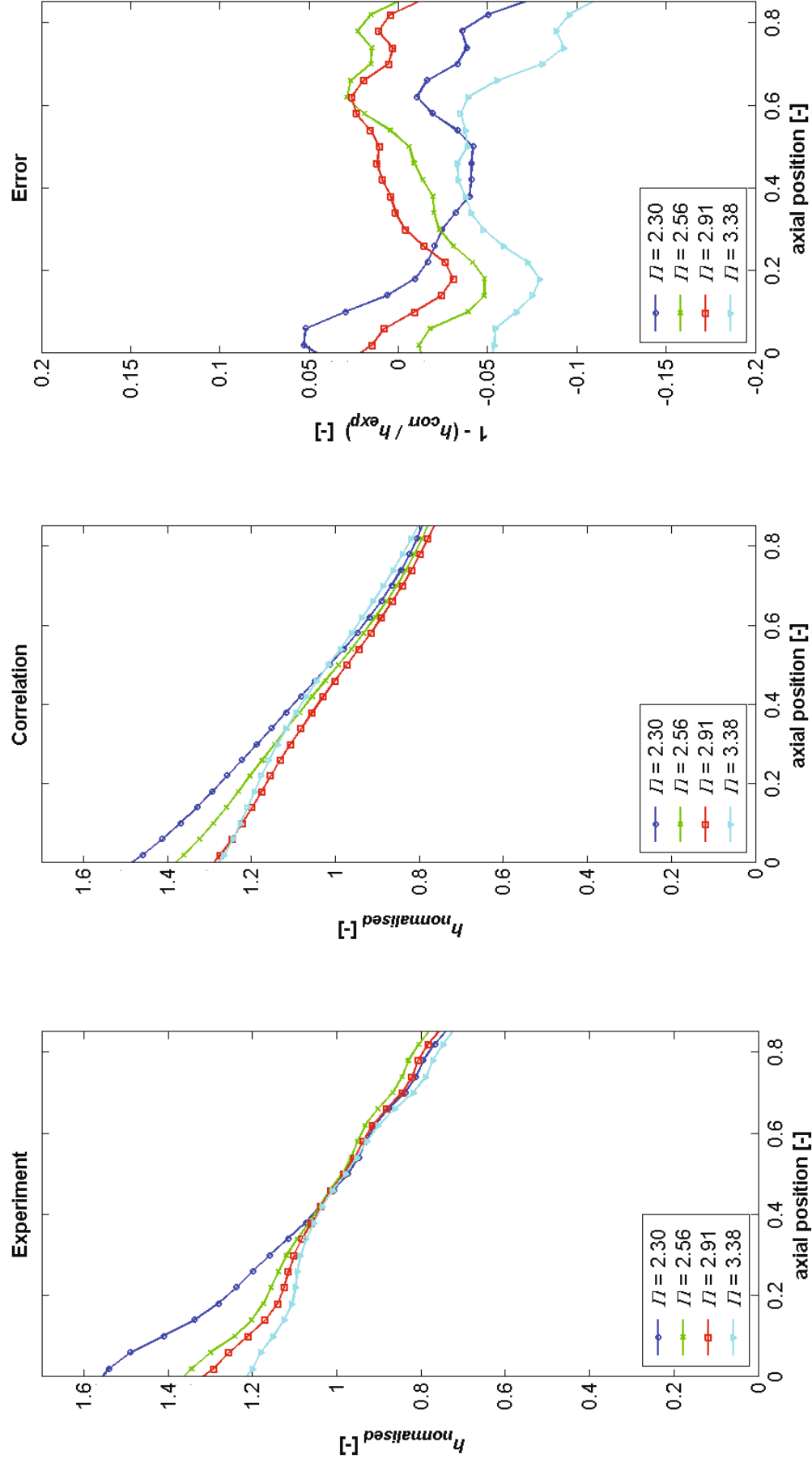


Figure 89f: Experimental (left) and analytical (centre) heat transfer coefficient and the resulting error (right) obtained with the enhanced correlation,

$p_{01} = 150 \text{ kPa}$, $n = 9000 \text{ rpm}$

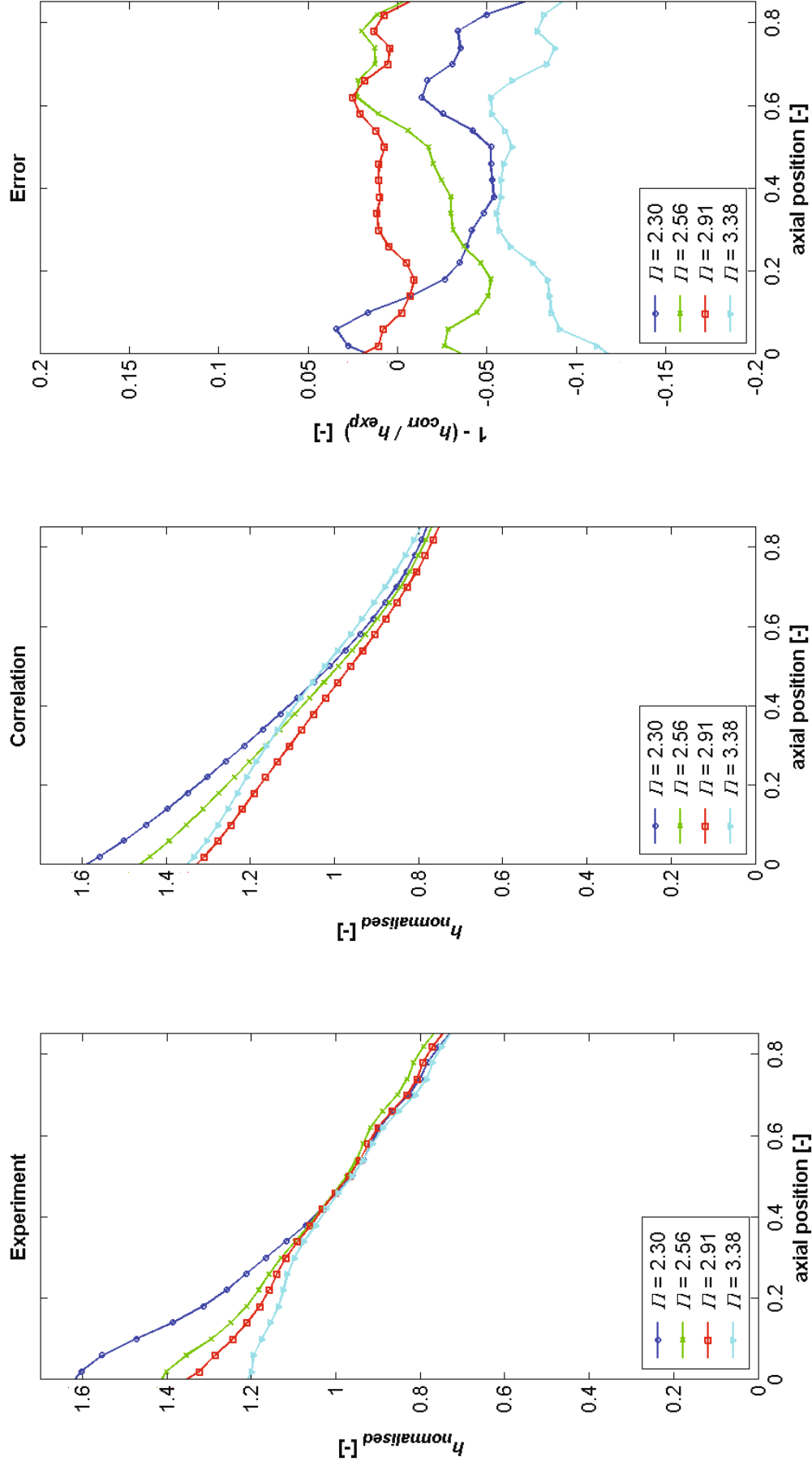


Figure 89g: Experimental (left) and analytical (centre) heat transfer coefficient and the resulting error (right) obtained with the enhanced correlation,

$p_{01} = 150 \text{ kPa}$, $n = 9500 \text{ rpm}$

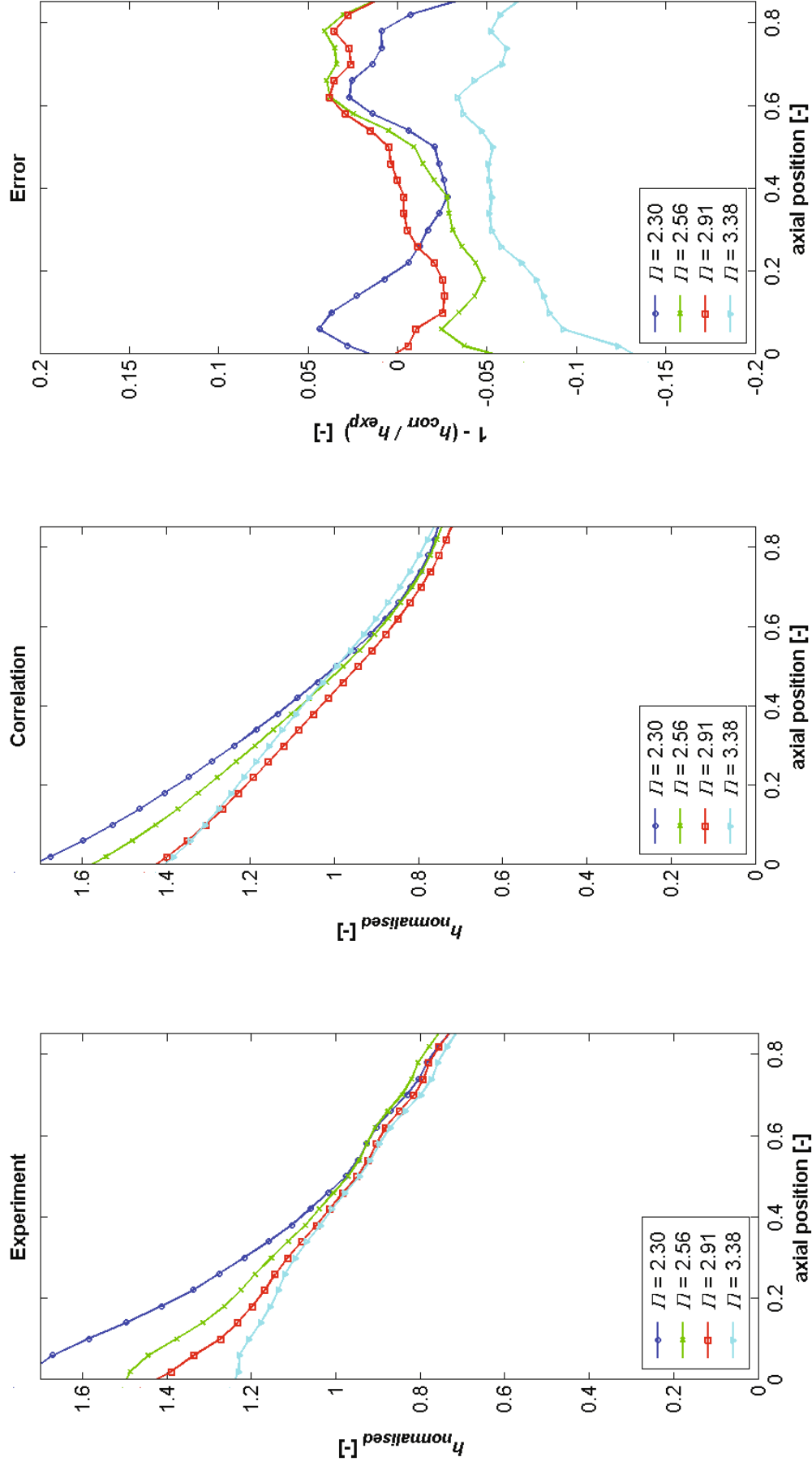


Figure 89h: Experimental (left) and analytical (centre) heat transfer coefficient and the resulting error (right) obtained with the enhanced correlation,

$p_{01} = 150 \text{ kPa}$, $n = 10000 \text{ rpm}$

7 SUMMARY AND CONCLUSIONS

Up to now the aero-thermal load of the over-tip region above rotor blades was investigated insufficiently. Therefore, within the national research and development programme AG-Turbo, the project “Äußerer Wärmeübergang an Führungsringssegmenten” (Heat Transfer at the Over-Tip Casing) was funded to investigate the over-tip flow field of a high pressure turbine stage. The test rig designed and manufactured for an earlier E3E-project by MTU, München, was investigated in DLR’s windtunnel for rotating cascades, Göttingen. The research project was coordinated by Siemens PG, Mülheim. The instrumentation of the rig was modified at DLR to collect data especially from the tip region. Emphasize was given to measure the steady and the unsteady static pressure, heat transfer into the over-tip casing and the complex flow field close to the over-tip casing. A suited set of measuring techniques was selected and adopted within the proceeding investigations. Finally, the rig was instrumented applying:

- steady pressure sensors as static pressure taps in the wall and as Pitot tubes.
- unsteady pressure sensors to get the static wall pressure and to be used with a single-hole-probe to get the flow values.
- a hot-film array for getting unsteady heat transfer on the over-tip casing.
- a thermocouple+ array to get the wall temperature and the heat transfer coefficients.

Applying these measurement techniques many various operation points were investigated in detail; parameters of interest were Reynolds number, pressure ratio and rotor speed.

The following list gives a short summary of the obtained results:

- at established operation points, the width of the tip gap only depends on rotor speed and does not depend on the pressure ratio and the Reynolds number.
- downstream of the stator, the flow field only depends on the pressure ratio and is hardly affected by the Reynolds number and the rotor speed.
- static pressure at the wall strongly depends on the pressure ratio. Temperature and heat flux coefficients are dominated by the pressure ratio, too.
- within the upper quarter of the flow duct downstream of the rotor, the total pressure and total temperature give hints for significantly increasing losses.

On the basis of these experiments a correlation can be formed.

The first step consisted of an investigation of the applicability of the flat plate correlation as basis for the correlation for the heat transfer coefficient at the over-tip casing. It was found that the flat plate correlation:

- predicts the regression of the heat transfer coefficient along the axial chord very well.
- correlates very well with the total pressure (Reynolds number) along the whole axial chord.
- correlates very well with pressure ratio and rotational speed at $x > 0.3$.
- underestimates the heat transfer coefficient for all operating conditions.

The flat plate correlation can – despite the complexity of the flow at the over-tip casing - be used for the prediction of the heat transfer coefficient. The accuracy can be enhanced by investigating the fluid phenomena in the relative frame of reference. The two main contributors for the extra heat transfer were found to be:

- misalignment of the incoming fluid and the rotor blade.
- tip leakage flow.

At the upstream part of the over-tip casing, the heat transfer level is very much affected by the angle of the incoming fluid in relation to the leading edge of the rotor. At the design condition the fluid is guided in the passage without much interference and the turbulence level will remain unaffected. At partload conditions, however, the fluid will hit the front section of the suction side of the blade, resulting in increased turbulence and heat transfer level. In severe cases, the boundary layer flow around the leading edge will separate, which boosts the heat transfer even more. This effect accounts for the bulk of the divergence found in the upstream region.

The heat transfer in the mid-chord is dominated by the tip leakage flow. The tip leakage was found to have multiple effects on the heat transfer coefficient at the over-tip casing. In order to be able to study the tip leakage flow a tip leakage model was introduced in section 5.3.2, which is based on three assumptions:

- I.) no work is done by the fluid entering the gap.
- II.) the tangential velocity of the fluid before it is accelerated into the gap is assumed to be given by the pressure side static pressure at that chordwise position.
- III.) the pressure gradient parallel to the blade camber line is small.

With the aid of the tip leakage model and the flat plate correlations, the heat transfer coefficient in the passage and in the tip gap were determined. It was found that the heat transfer coefficient in the gap can be up to twice as that of the passage. This corresponds well with the findings of Thorpe et al. (2004b). The present tip leakage model predicts the fluid properties in the middle of the passage and in the middle of the gap, it cannot provide the fluid properties of the points in between. This data has to be complemented either experimentally or numerically. When the complete flow field over one period is known, the flat plate correlation (enhanced with the correlation accounting for the misalignment of the flow in the upstream part of the passage) can be used to determine the heat transfer coefficient for each point. The time-averaged heat transfer coefficient is obtained by the integration over one period.

In many cases there is no time or money to complement the data, therefore generally pitchwise averaged data is used. In section 5.3.5, the effect of using steady data as input data was investigated. It was found that an error will be made but in the range of the relative flow velocity found at the over-tip casing, this error will be small.

In section 5.3.8 it was shown that the tip leakage flow is excluded from the work process. Consequently, the total temperature of the tip leakage flow will not be reduced as much as that of the passage flow. This fluctuation of the total temperature over one period can be as much as $80K$, as a result the driving temperature will also fluctuate by $80K$. Especially when the driving temperature is chosen too small, the driving temperature can be temporarily zero or even change sign. This will cause a large error when determining the time-averaged heat transfer coefficient. For this reason the time-resolved temperature should be measured or the driving temperature should be set as high as possible.

LIST OF LITERATURE

- [1] Bejan, A.: Heat transfer. New York. John Wiley & Sons, (1993)
- [2] Chana, K.S., Jones, T.V.: An Investigation on Turbine Tip and Shroud Heat Transfer. Proceedings of ASME Turbo Expo 2002, Amsterdam, the Netherlands, (2002)
- [3] Denton, J.D.: Loss Mechanisms in Turbomachines. ASME Journal of Turbomachinery, Vol. 115, pp. 621-656, (1993)
- [4] Denos, R., Arts, T., Paniagua, G., Michelassi, V., Martelli, F.: Investigation of the Unsteady Rotor Aerodynamics in a Transonic Turbine Stage. ASME Journal of Turbomachinery, Vol. 113, pp. 81-89, (2001)
- [5] Duikeren, B. van: Heat Transfer Measurements at a High Pressure Turbine Shroud. Proceedings of the 17th Symposium on Measuring Techniques in Transonic and Supersonic Flow in Cascades and Turbomachines, Stockholm, Sweden. (2004a)
- [6] Duikeren, B. van: Design of Heat Transfer Instrumentation to be Applied at the Wind Tunnel for Rotating Cascades at DLR. IB 225-2004 A 01, Göttingen, Germany. (2004b)
- [7] Duikeren, B. van: Heat Transfer Investigations at the Over-Tip Casing of a High Pressure Turbine Stage. IB 225-2006 A 05, Göttingen, Germany. (2006)
- [8] Dunn, M.G.: Phase and Time-Resolved Measurements of Unsteady Heat Transfer and Pressure in a Full-Stage Rotating Turbine. ASME Journal of Turbomachinery, Vol. 112, pp. 531-538, (1990)
- [9] Gieß, P.-A., Rehder, H.-J. Kost, F.: A New Test Facility for Probe Calibration Offering Independent Variation of Mach and Reynolds Number. Proceedings of the 15th Symposium on Measuring Techniques in Transonic and Supersonic Flow in Cascades and Turbomachines, Firenze, Italy, (2000)
- [10] Guenette, G.R., Epstein, A.H., Norton, R.J.G., Yuzhang, C.: Time-resolved Measurements of a Turbine Rotor Stationary Tip Casing Pressure and Heat Transfer Field, Proceedings of the AIAA/SAE/ASME/ASEE 21st Joint Propulsion Conference, Monterey, CA, USA, (1985)

- [11] Heyes F. J. G., Hodson H.P.: Measurement and Prediction of Tip Clearance Flow in Linear Turbine Cascades. ASME Journal of Turbomachinery, Vol.115, pp.376-382. (1993)
- [12] Haselbach, F., Nitsche, W.: Calibration of Single-Surface Hot-films and In-Line Hot-Film Arrays in Laminar or Turbulent Flows. Meas. Sci. Technology, Vol. 7, pp. 1428-1438, (1996)
- [13] Kost, F.: Eichung einer *Kulite*-Pitotsonde und Beschreibung der Auswerteprozedur. DLR-interner Bericht IB 225-2005 A 03, Göttingen, Germany, (2005)
- [14] Kost, F., Nicklas, M.: Film-Cooled Turbine Endwall in a Transonic Flow Field: Part I - Aerodynamic Measurements. AMSE Journal of Turbomachinery, Vol. 123, pp. 709-719, (2001)
- [15] Lewis, R.I., Yeung, E.H.C.: Vortex Shedding Mechanisms in Relation to Tip Clearance Flows and Losses in an Axial Fan. British A.R.C. R.&M. 3829, (1977)
- [16] Leydon, M., Decker, J.: European Energy Outlook to 2020 A Scenario Approach http://europa.eu.int/comm/energy/en/etf_2_en.html. Office for Official Publications of the European Communities, Luxemborg. ISBN 92-827-5226-7, (1996)
- [17] Mayle, R.E. and Metzger, D.E.: Heat Transfer at the Tip of an Unshrouded Turbine Blade. Proceedings of the Seventh Int. Heat Transfer Conf., Hemisphere Pub., pp. 87-92, (1982)
- [18] Metzger, D. E., Dunn, M. G., Hah, C.: Turbine Tip and Shroud Heat Transfer. ASME Journal of Turbomachinery, Vol. 113, pp. 502-507, (1991)
- [19] Moore, J., Elward, K.M.: Shock Formation in Overexpanded Tip Leakage Flow. ASME Journal of Turbomachinery, Vol. 115, pp. 392-399, (1992)
- [20] Moore, J., Moore, J.G., Henry, G.S, Chaudhry, U.: Flow and Heat Transfer in Turbine Tip Gaps. ASME Journal of Turbomachinery, Vol. 111, pp. 301-309, (1989)
- [21] Ochrymiuk, T.: Aerodynamic Investigations of the Stationary Flow Field within a HP-Turbine Stage Applying the CFD-Tool TRACE. DLR - IB 225 - 2007 C 04, (2007)

- [22] Polanka, M. D., Clark, A. L., Meininger, M., Praisner, T. J.: Turbine Tip and Shroud Heat Transfer and Loading Part B: Comparisons Between Prediction and Experiment Including Unsteady Effects, Proceedings of ASME Turbo Expo 2003, Atlanta, USA, (2003)
- [23] Polanka, M. D., Hoying, D. A., Meininger, M.: Turbine Tip and Shroud Heat Transfer and Loading Part A: Parameter Effects Including Reynolds Number, Pressure Ratio, and Gas to Metal Temperature Ratio, Proceedings of ASME Turbo Expo 2002, Amsterdam, The Netherlands, (2002)
- [24] Rains, D. A.: Tip Clearance Flows in Axial Flow Compressors and Pumps, California Institute of Technology, Hydrodynamics and Mechanical Engineering Laboratories, Report No. 5, (1954)
- [25] Rhee, D. –H. Cho, H. –H.: Local Heat/Mass Transfer Characteristics on a Rotating Blade with Flat Tip in a Low-Speed Annular Cascade – Part II: Tip and Shroud. Proceedings of ASME Turbo Expo 2006, Barcelona, Spain, (2006)
- [26] Rhee, D. –H. Choi, J. –H, Cho, H. –H.: Effect of Blade Tip Clearance on Turbine Shroud Heat/Mass Transfer, Proceedings of ASME TURPO EXPO 2001, New Orleans, LO, USA, (2001)
- [27] Schaub, U. W., Vlasic, E., and Moustapha, S. H.: Effect of Tip Clearance on the Performance of a Highly Loaded Turbine Stage. AGARD-CP-537 ,Technology Requirements for Small Gas Turbines, Paper 29, (1993)
- [28] Sjolander, S. A.: Secondary and Tip-clearance Flows in Axial Turbines: Overview of tip-clearance effects in axial turbines. VKI Lecture Series, 1997-01, (1997)
- [29] Sjolander, S.A., Cao., D.: Measurements of the Flow in an Idealized Turbine Tip Gap, ASME Journal of Turbomachinery, Vol. 117, pp. 578-584, (1995)
- [30] Thorpe, S.J., Ainsworth, R.W.: The Effects of the Blade Passing on the Heat Transfer Coefficient of the Over-tip casing in a Transonic Turbine Stage. Proceedings of ASME Turbo Expo 2006, Barcelona, Spain, (2006)

- [31] Thorpe, S.J., Miller, R.J., Yoshino, S., Ainsworth, R.W., Harvey, N.W.: The Effect of Work Processes on the Casing Heat Transfer of a Transonic Turbine. Proceedings of ASME Turbo Expo 2007, Montreal, Canada, (2007)
- [32] Thorpe, S.J., Yoshino, S., Ainsworth, R.W., Harvey, N.W.: An Investigation of the Heat Transfer and Static Pressure Field on the Over-Tip Casing of a Shroudless Transonic Turbine Rotor at Engine Representative Flow Conditions. (I). Time-Mean Results, International Journal of Heat and Fluid Flow Vol. 25., pp. 933-944, (2004a)
- [33] Thorpe, S.J., Yoshino, S., Ainsworth, R.W., Harvey, N.W.: An Investigation of the Heat Transfer and Static Pressure Field on the Over-Tip Casing of a Shroudless Transonic Turbine Rotor at Engine Representative Flow Conditions. (II). Time-Resolved Results, International Journal of Heat and Fluid Flow, Vol. 25, pp. 945-960, (2004b)
- [34] Urban, M. F., Vortmeyer, N.: Experimental Investigations on the Thermal Load and Leakage Flow of a Turbine Blade Tip Section with Different Tip Section Geometries. Proceedings of ASME Turbo Expo 2000, Munich, Germany, (2000)
- [35] Verein Deutscher Ingenieure: VDI-Wärmeatlas; Berechnungsblätter für den Wärmeübergang;. 5. erweiterte Auflage, VDI Verlag, Düsseldorf, Germany, (1988)
- [36] Willinger, R.: Sekundär- und Spaltströmung im axialen Turbinengitter unter Teil-, Nenn- und Überlastbedingungen. Fortschritt Bericht VDI Reihe 7 Nr. 433. VDI Verlag, Düsseldorf. Germany, (2002)
- [37] Willinger, R., Haselbacher H.: On the Modelling of Tip Leakage Flow in Axial Turbine Blade Rows. Proceedings of ASME Turbo Expo 2000, Munich, Germany, (2000)
- [38] Yaras, M.I, Sjolander, S.A.: Effects of Simulated Rotation on Tip Leakage in a Planar Cascade of Turbine Blades: Part I – Tip Gap Flow. ASME Journal of Turbomachinery, Vol. 114, pp. 652-659, (1992)
- [39] Yaras, M.I., Yingkang, Z., Sjolander, S.A.: Flow Field in the Tip Gap of a Planar Cascade of Turbine Blades. Presented at the Gas Turbine and Aeroengine Congress and Exposition, Amsterdam, The Netherlands, (1988)

LIST OF FIGURES

Figure 1: Tip leakage flow	3
Figure 2: Possible physical mechanisms by which rotation reduces tip leakage flow	6
Figure 3: Velocity vectors at different radial positions within the tip gap and different engine equivalent speeds.....	7
Figure 4: Nusselt distribution at the over-tip casing	8
Figure 5: Measured and estimated time-averaged over-tip casing heat flux.....	10
Figure 6: Contour plot of Sh at the over-tip casing.....	10
Figure 7: Simple tip gap flow model	14
Figure 8: Schematic of the RGG	17
Figure 9: Stage setup in the RGG.....	18
Figure 10: One of the two openings for inserting instrumented parts.....	20
Figure 11: Insert with thermocouple+ array.....	21
Figure 12: Composition of thermocouple+ array	21
Figure 13: Thermal boundary conditions of the over-tip casing.....	24
Figure 14: Temperature distribution of the over-tip casing	25
Figure 15: Closeup of the heat flow at the sensor edges.....	25
Figure 16: Comparison experimental and computed temperatures.....	26
Figure 17: Fraction of generated heat convected into the fluid.....	27
Figure 18: Image and sketch of the steady and dynamical pressure insert	28
Figure 19: Frequency response of a pressure transducer	29
Figure 20: Time-resolved static pressure grid.....	30
Figure 21: Signals for various stator vane-settings	30
Figure 22: Hot-film array	32
Figure 23: Ratio of convective-to-conductive heat transfer of a hot-film.....	34
Figure 24: Shear stress and friction velocity Reynolds number distribution	35
Figure 25: Ratio of convective-to-conductive heat transfer of a hot-film.....	35
Figure 26: Ratio of convective-to-total heat transfer of a hot-film	36
Figure 27: Convective-to-total heat transfer	36
Figure 28: Thermal image of the heated area of a hot-film	38
Figure 29: Normalised effective heated area as a function of the over temperature.....	39
Figure 30: The time-resolved heating power of a hot-film at the over-tip casing	40
Figure 31: Time-resolved wall temperature obtained from two successive hot-film measurements.....	40
Figure 32: Sketch of the Kulite probe	41
Figure 33: Pressure coefficient as a function of the flow angle and Mach number	43
Figure 34: Schematic overview of the wake analysis procedure 1 st approximation	44
Figure 35: Schematic overview of the wake analysis procedure 2 nd iteration	44
Figure 36: Tip gap size as function of the rotational speed	47
Figure 37: Stator wake total-pressure distribution	48
Figure 38: Stator Mach number distribution	48
Figure 39: Stator wake Mach field number obtained by CFD	49
Figure 40: Static pressure distribution at the over-tip casing.....	50
Figure 41: Pitchwise averaged pressure distribution of the over tip casing.....	51
Figure 42: Pitchwise averaged adiabatic wall temperature distribution at the over-tip casing..	52
Figure 43: Heat transfer coefficient distribution at the over-tip casing	53
Figure 44: Heat transfer coefficient distribution at the over-tip casing	54
Figure 45: Rotor wake steady total pressure field.....	55

Figure 46: Rotor wake angle field.....	56
Figure 47: Rotor wake total temperature field	56
Figure 48: Time-resolved static pressure	58
Figure 49: Time-resolved pressure distribution	59
Figure 50: Time-resolved heat transfer coefficient distribution at the over-tip casing.....	62
Figure 51: Alternating time-resolved heat transfer coefficient distribution.....	63
Figure 52: Time-resolved wake results	64
Figure 53: Wall temperature: constant fluid properties, straight flow	67
Figure 54: Heat transfer coefficient distribution with constant fluid properties, straight flow..	68
Figure 55: Streamlines at the over-tip casing.....	69
Figure 56: Wall temperature: constant fluid properties, curved flow path	70
Figure 57: Heat transfer coefficient with constant fluid properties, curved flow path	70
Figure 58: Static pressure and static temperature distribution over the over-tip casing	71
Figure 59: Local and averaged velocity and fluid parameters	72
Figure 60: Heat transfer coefficient distribution.....	73
Figure 61: Heat transfer coefficient distribution as a function of the extended heating length .	74
Figure 62: Sketch of the influence of the stator wake angle on the path length	75
Figure 63: Heat transfer coefficient at the rotor entrance as function the stator wake angle....	76
Figure 64: Stator wake Mach number distribution.....	78
Figure 65: Experimental and analytical heat transfer coefficient distribution	80
Figure 66: Sketch introducing the main heat transfer phenomena.....	85
Figure 67: Relative flow angle at rotor entrance.....	86
Figure 68: Correlation of the relative flow angle and heat transfer coefficient	87
Figure 69: Time-resolved static pressure corresponding to the tip gap entrance and exit	89
Figure 70: Averaged isentropic relative Mach number.....	90
Figure 71: Isentropic relative Mach number distribution.....	90
Figure 72: Velocity triangles of the tip leakage flow	92
Figure 73: Flow angle of the tip leakage flow relative to the blade contour.....	93
Figure 74: Magnitude of the Mach number components of the tip leakage flow	94
Figure 75: Reynolds number within an isentropic nozzle as function of the Mach number.....	97
Figure 76: Heat transfer coefficient as function of the Mach number for isentropic flow	97
Figure 77: Time-resolved versus pitchwise averaged input data for the flat plate correlation ..	98
Figure 78: Normalised Reynolds number as function of the Mach number	101
Figure 79: Normalised heat transfer coefficient as function of the Mach number	102
Figure 80: Absolute tip leakage and passage flow Mach number.....	103
Figure 81: Ratio between the heat transfer coefficient in the passage and in the gap	104
Figure 82: A schematic diagram that illustrates the velocity triangles	105
Figure 83: Tangential velocity of the tip leakage and passage flow	106
Figure 84: Total temperature distribution of the tip leakage flow and the passage flow	108
Figure 85: Ratio between the experimental and analytical heat transfer coefficient	113
Figure 86: Experimental and analytical heat transfer coefficient and the resulting error obtained with the “basic” correlation,.....	114
Figure 87: Heat transfer coefficient as function of the relative flow angle.....	122
Figure 88: Slope of the correlation as function of the axial position	123
Figure 89: Experimental and analytical heat transfer coefficient and the resulting error obtained with the enhanced correlation	126

LIST OF TABLES

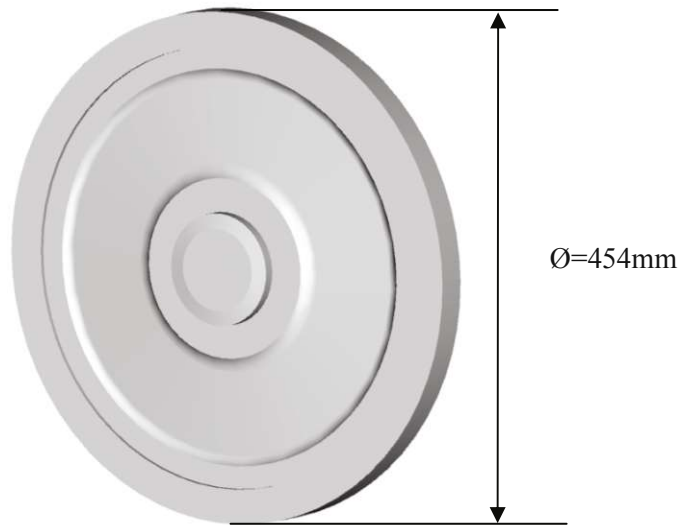
Table 1: Geometrical and operational key-parameters of the high pressure stage.....	18
Table 2: Measurement matrix	19
Table 3: Conductivity of the various sections.....	24
Table 4: Effective heated area of a hot-film for three over temperatures	37
Table 5: Comparison effective area ratio of a hot-film for three over temperatures	39
Table 6: Properties of the Kulite probe (type: XCS-062)	42
Table 7: Averaged velocity and fluid properties.....	67
Table 8: Stator wake angle deflection caused by the passage vortex.....	77

APPENDIX A OVERVIEW OF OPERATING KEY-POINTS

p_{01}	p_{01} / p_{04}	n	T_{01}	Re	p_1 / p_{01}	\dot{m}	Cooling Air		
							$\dot{m}_{stator} / \dot{m}$	$T_{0,stator} / T_{01}$	$p_{0,stator} / p_{01}$
[kPa]	[-]	[rpm]	[K]	[-]	[-]	[kg/s]	[-]	[-]	[-]
120	2.30	10000	388.6	$1.52 \cdot 10^5$	0.991	3.25	0.077	0.793	1.36
120	2.30	9500	388.7	$1.44 \cdot 10^5$	0.991	3.26	0.077	0.793	1.36
120	2.30	9000	389.7	$1.48 \cdot 10^5$	0.991	3.26	0.077	0.791	1.35
120	2.30	8000	387.8	$1.48 \cdot 10^5$	0.991	3.27	0.077	0.795	1.34
120	2.56	10000	389.7	$1.52 \cdot 10^5$	0.991	3.22	0.077	0.791	1.36
120	2.56	9500	389.7	$1.50 \cdot 10^5$	0.991	3.24	0.077	0.791	1.35
120	2.56	9000	389.4	$1.50 \cdot 10^5$	0.991	3.25	0.077	0.792	1.35
120	2.56	8000	389.7	$1.52 \cdot 10^5$	0.991	3.22	0.077	0.791	1.34
120	2.91	10000	389.5	$1.51 \cdot 10^5$	0.991	3.24	0.077	0.791	1.35
120	2.91	9500	389.8	$1.52 \cdot 10^5$	0.991	3.24	0.077	0.791	1.35
120	2.91	9000	389.2	$1.52 \cdot 10^5$	0.991	3.25	0.077	0.792	1.34
120	2.91	8000	388.8	$1.54 \cdot 10^5$	0.991	3.26	0.077	0.793	1.34
120	3.38	9500	388.5	$1.54 \cdot 10^5$	0.991	3.23	0.077	0.792	1.35
120	3.38	8000	388.6	$1.54 \cdot 10^5$	0.991	3.25	0.077	0.793	1.34
120	3.80	10000	389.1	$1.52 \cdot 10^5$	0.991	3.22	0.078	0.792	1.36
120	3.80	9500	389.8	$1.50 \cdot 10^5$	0.991	3.21	0.078	0.791	1.35
120	3.80	9000	390.0	$1.50 \cdot 10^5$	0.991	3.22	0.078	0.790	1.35
120	3.80	8000	389.5	$1.80 \cdot 10^5$	0.991	3.24	0.077	0.791	1.34
150	2.30	10000	389.9	$1.80 \cdot 10^5$	0.991	3.94	0.079	0.790	1.42
150	2.30	9000	388.8	$1.82 \cdot 10^5$	0.991	3.94	0.079	0.793	1.41
150	2.30	8000	388.3	$1.80 \cdot 10^5$	0.992	3.94	0.079	0.793	1.42
150	2.56	10000	389.7	$1.81 \cdot 10^5$	0.991	3.94	0.079	0.791	1.41
150	2.91	10000	389.1	$1.80 \cdot 10^5$	0.991	3.94	0.079	0.792	1.42
150	2.91	9000	389.0	$1.79 \cdot 10^5$	0.992	3.92	0.079	0.792	1.42
150	2.91	8000	389.0	$1.80 \cdot 10^5$	0.991	3.93	0.079	0.792	1.42
150	3.80	10000	389.9	$1.79 \cdot 10^5$	0.992	3.90	0.079	0.790	1.42

$\dot{m}_{rotor} / \dot{m}$	$T_{0,rotor} / T_{01}$	$p_{0,rotor} / p_{01}$	<i>Torque</i>	α_4	$p_{04_{mid}} / p_{01}$	$p_{4_{casing}} / p_{01}$	$p_{4_{hub}} / p_{01}$	$T_{04_{mid}} / T_{01}$
[-]	[-]	[-]	[Nm]	[°]	[-]	[-]	[-]	[-]
0.049	0.793	1.73	196.7	36.7	0.438	0.391	0.392	0.806
0.049	0.793	1.72	208.8	36.7	0.438	0.393	0.393	0.805
0.049	0.791	1.71	223.1	29.0	0.434	0.390	0.391	0.803
0.049	0.795	1.70	247.2	20.4	0.440	0.393	0.394	0.807
0.049	0.791	1.72	222.4	28.3	0.394	0.350	0.351	0.803
0.049	0.791	1.71	236.6	24.2	0.391	0.348	0.349	0.803
0.049	0.795	1.71	250.5	19.7	0.391	0.346	0.347	0.804
0.049	0.791	1.70	278.9	10.9	0.396	0.344	0.344	0.803
0.049	0.791	1.72	254.3	17.0	0.343	0.299	0.300	0.803
0.050	0.790	1.71	268.4	12.8	0.343	0.298	0.298	0.803
0.049	0.791	1.71	283.2	7.4	0.343	0.296	0.296	0.804
0.049	0.792	1.70	311.7	-0.1	0.351	0.292	0.293	0.805
0.049	0.793	1.71	302.3	-4.3	0.295	0.248	0.248	0.806
0.049	0.793	1.70	353.1	-15.7	0.300	0.233	0.233	0.805
0.049	0.792	1.72	312.6	-10.1	0.263	0.212	0.212	0.804
0.050	0.790	1.71	329.5	-14.6	0.263	0.207	0.207	0.803
0.050	0.789	1.71	347.0	-17.7	0.265	0.201	0.201	0.802
0.050	0.790	1.70	383.4	-23.6	0.266	0.185	0.184	0.804
0.045	0.790	1.51	250.4	39.3	0.436	0.392	0.393	0.802
0.045	0.793	1.52	283.2	31.5	0.433	0.391	0.391	0.805
0.045	0.794	1.52	313.5	21.9	0.438	0.392	0.393	0.806
0.045	0.791	1.52	282.0	37.8	0.395	0.351	0.352	0.803
0.044	0.792	1.49	322.1	21.5	0.341	0.300	0.301	0.804
0.045	0.792	1.50	358.0	10.4	0.343	0.297	0.298	0.804
0.045	0.792	1.51	394.9	2.9	0.351	0.293	0.293	0.804
0.045	0.790	1.50	364.5	9.6	0.294	0.251	0.251	0.802

APPENDIX B TIP GAP WIDTH ANALYSIS



Material: 42CrMo4V

Figure B-1: Schematic of the rotor disk

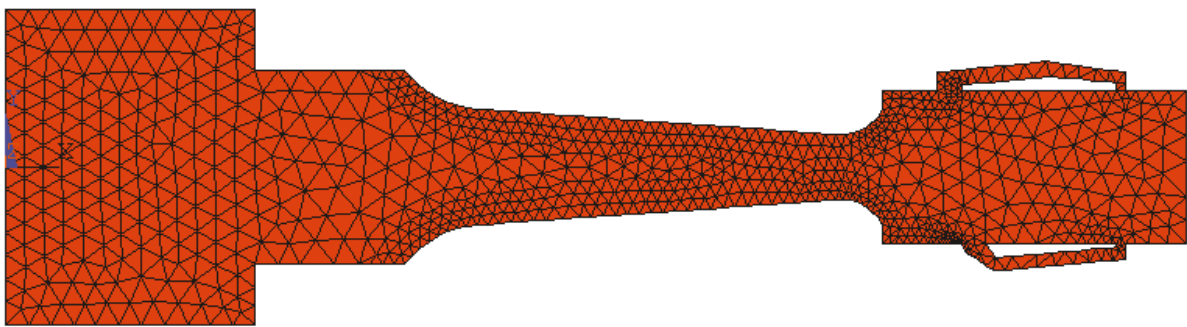


Figure B-2: Finite element mesh of rotor section

Figure B-1 shows a schematic of the rotor disk. The disk diameter is 454mm and is made from one piece of 42CrMo4V steel. The 60 turbine blades have a length of 40mm and mass of $\approx 0.05\text{kg}$ each. For simplicity reasons, the blades are represented by a lumped mass at the rotor tip. An axisymmetric solution was performed with the y-axis taken as axis of symmetry. The finite element mesh of the rotor disk section is shown in figure B-2. Element types “PLANE 2 axisymmetric” were utilized (Triangle 6node 2). The degrees of freedom of rotor disc axis (the leftmost vertical line of figure B-2) were constrained in the x-direction and the centre key-point of the axis was additionally constrained in the y-direction. The rotation of the rotor disk was applied by defining an angular velocity around the global y-axis.

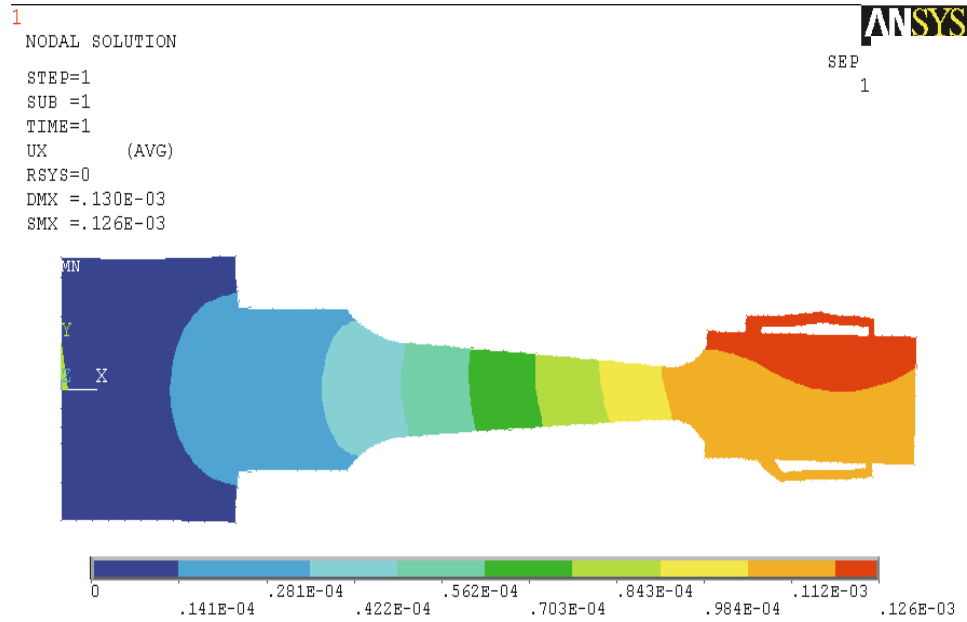


Figure B-3: Radial elongation of the Rotor disk at 10000 rpm

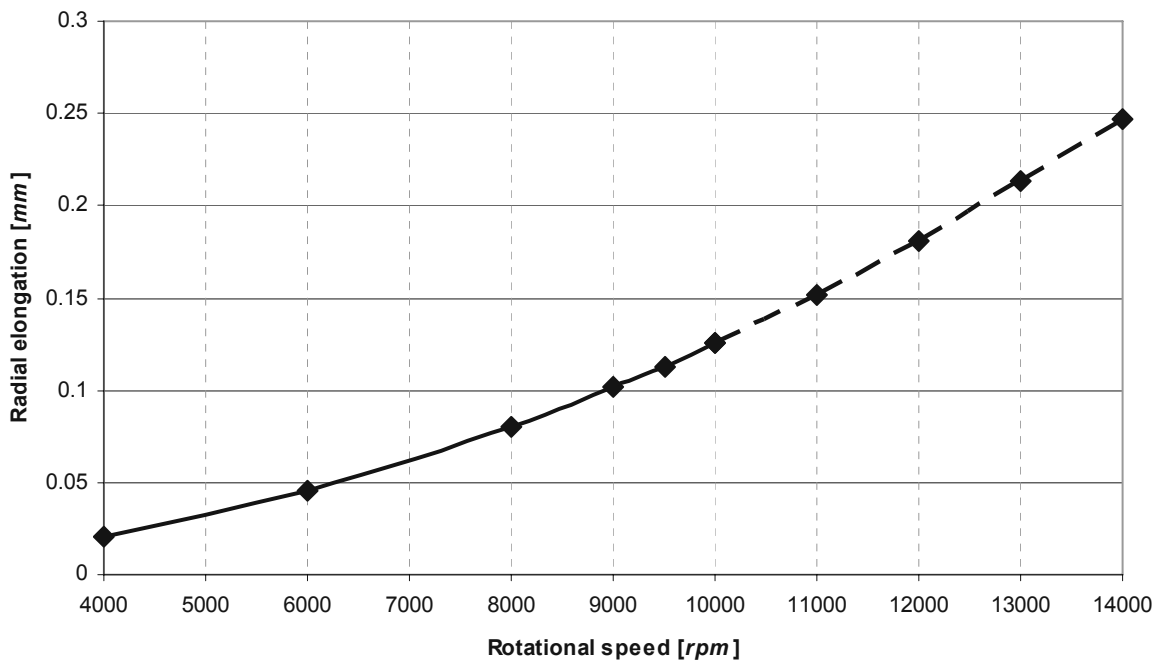


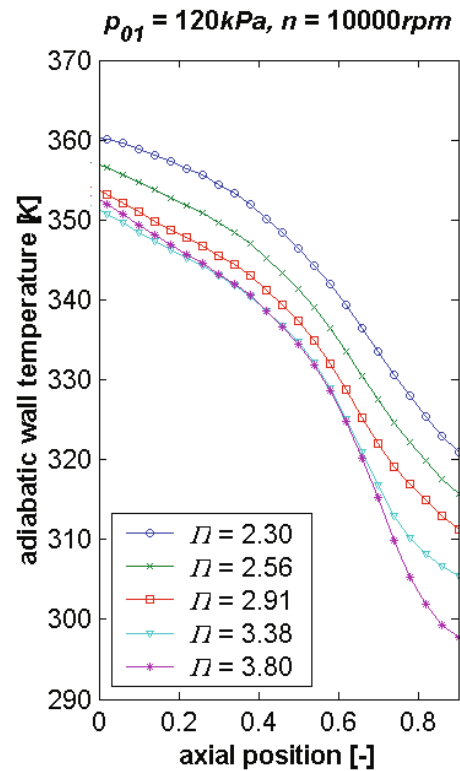
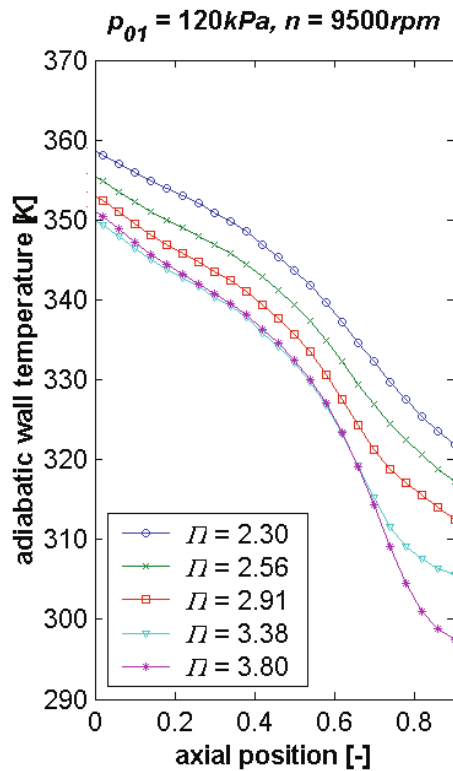
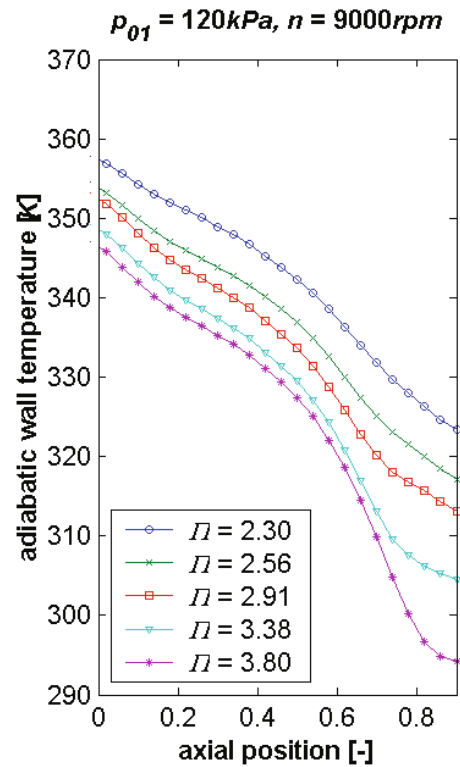
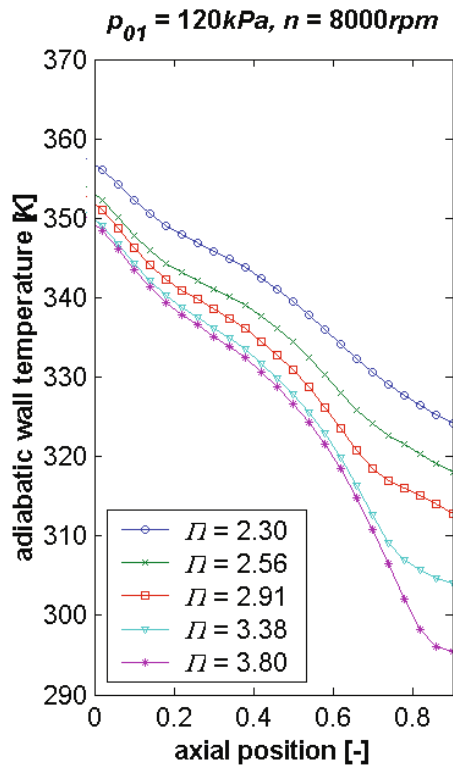
Figure B-4: Elongation of the rotor as a function of the rotational speed

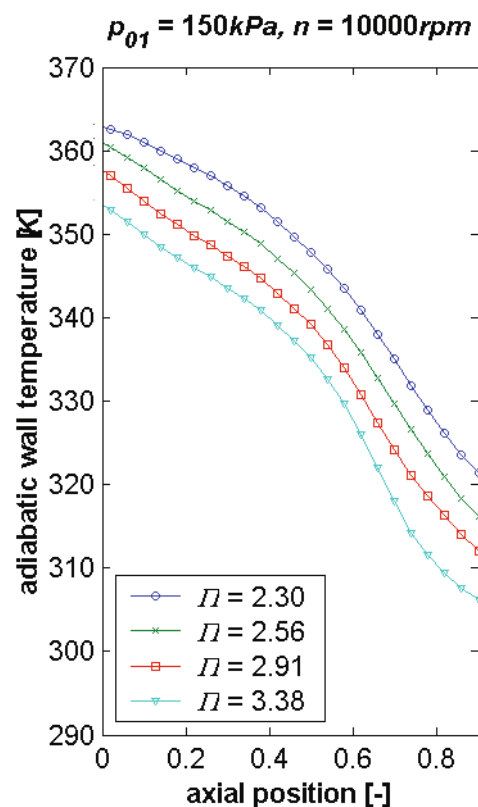
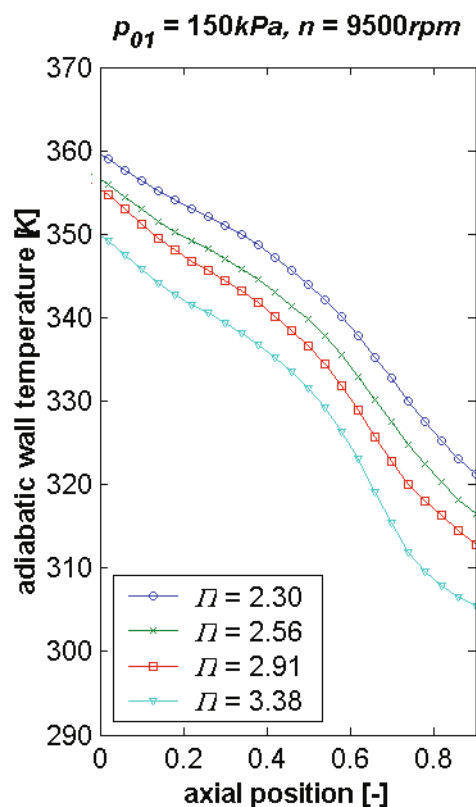
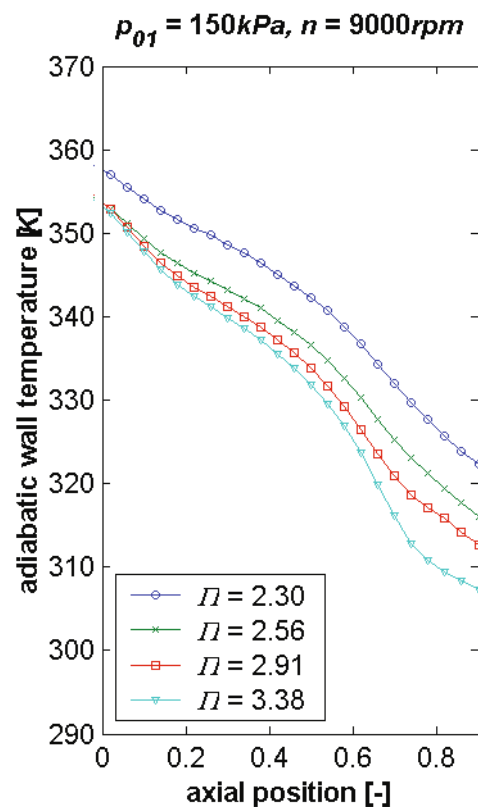
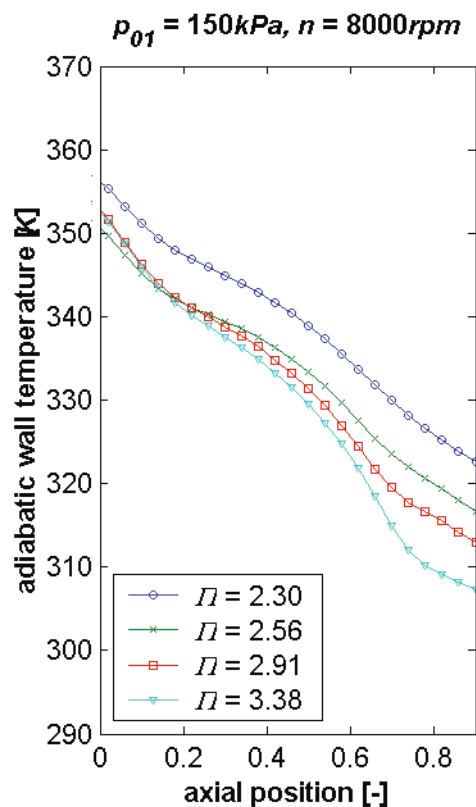
Figure B-3 shows the estimated deflection of 10000rpm, which is the highest rotational speed of the current research program. A function of the radial elongation is given in figure B-4, this function can also be expressed by the following empirical formula.

$$\tau(n) \approx \frac{n^2}{7.94 \cdot 10^8} \quad (1.1)$$

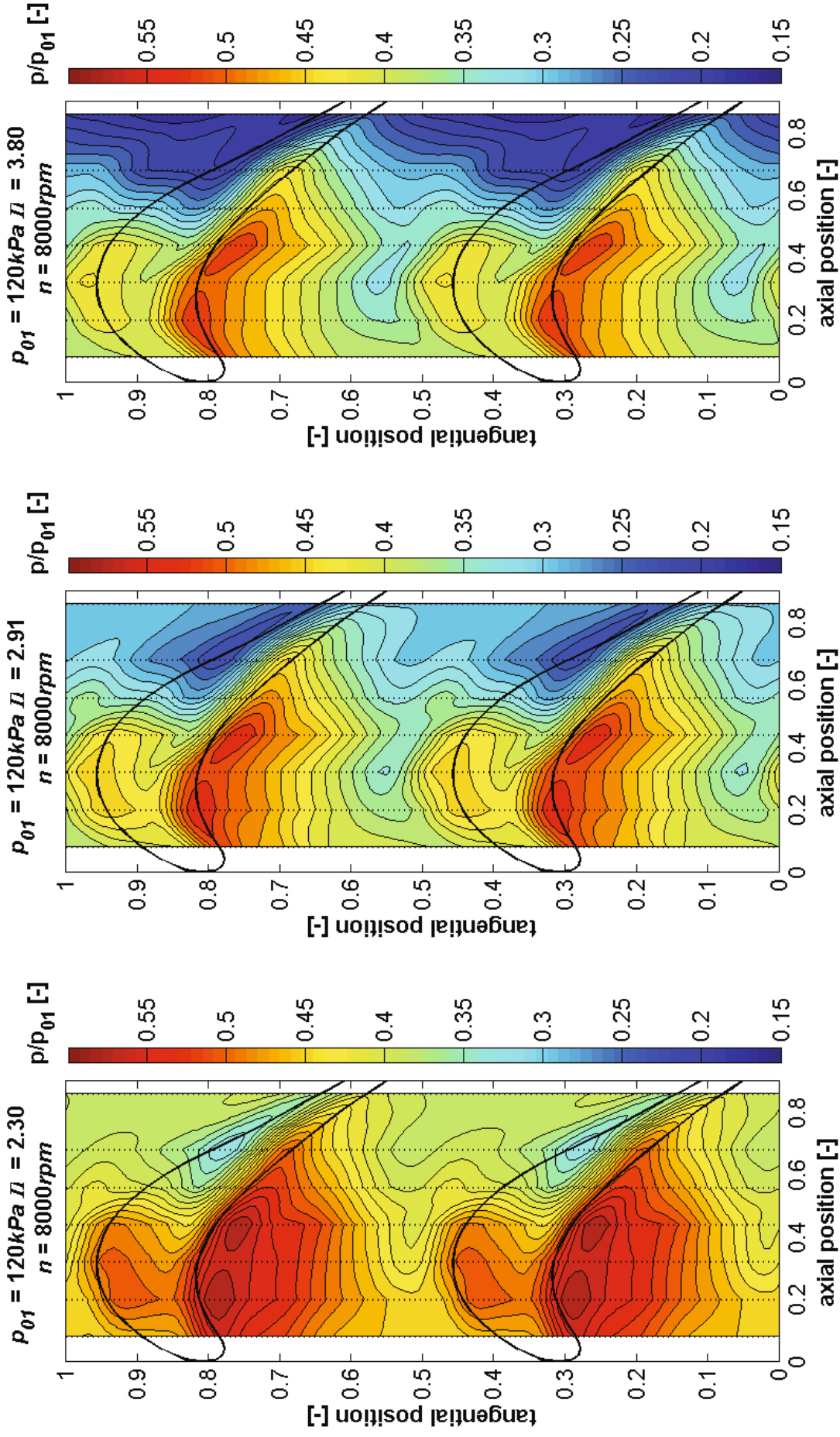
For the actual radial displacement, also the play between the rotor disk and the turbine blades has to be accounted for. This play is estimated to be 0.1mm and is independent of the rotational speed. At rest, the tip gap width is 0.79mm . This means that during the tests the tip gap is reduced to a height between 0.71mm and 0.66mm . This is about 1.7% of the total blade height and is a realistic value for a full scale turbine in operation.

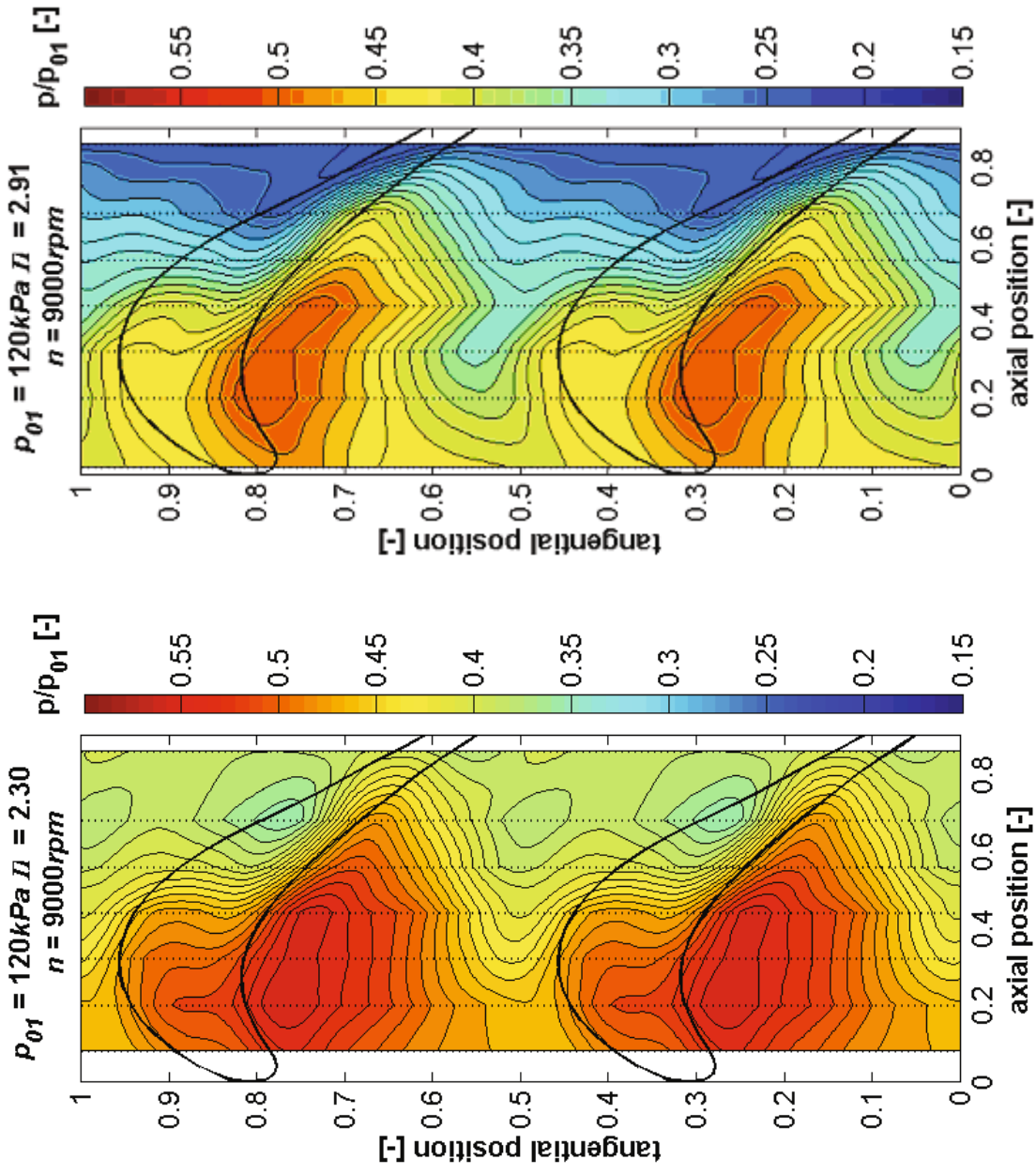
APPENDIX C PITCHWISE AVERAGED ADIABATIC WALL TEMPERATURE

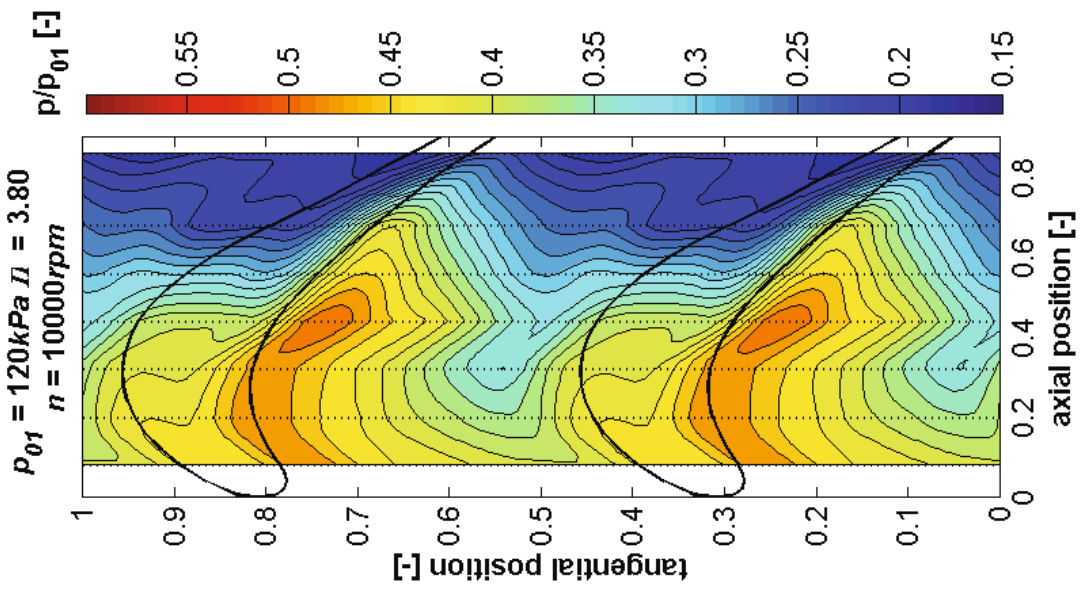
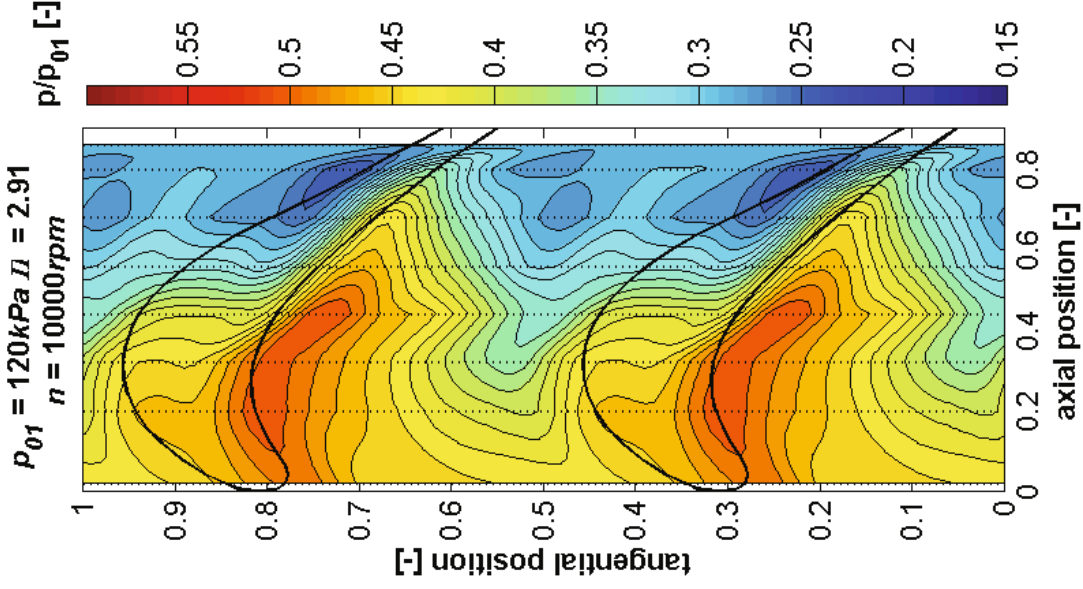
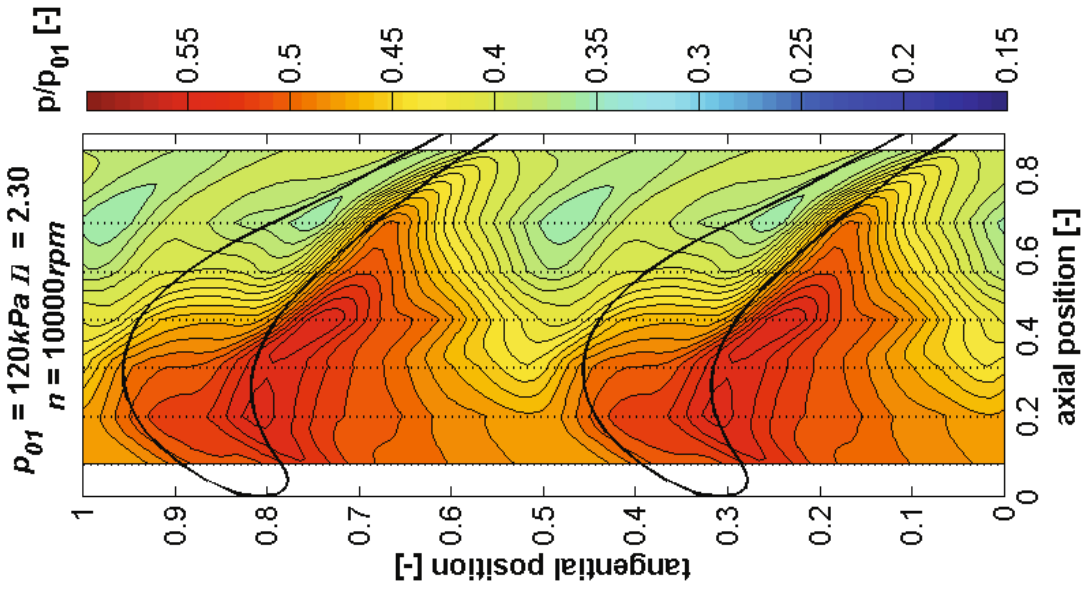




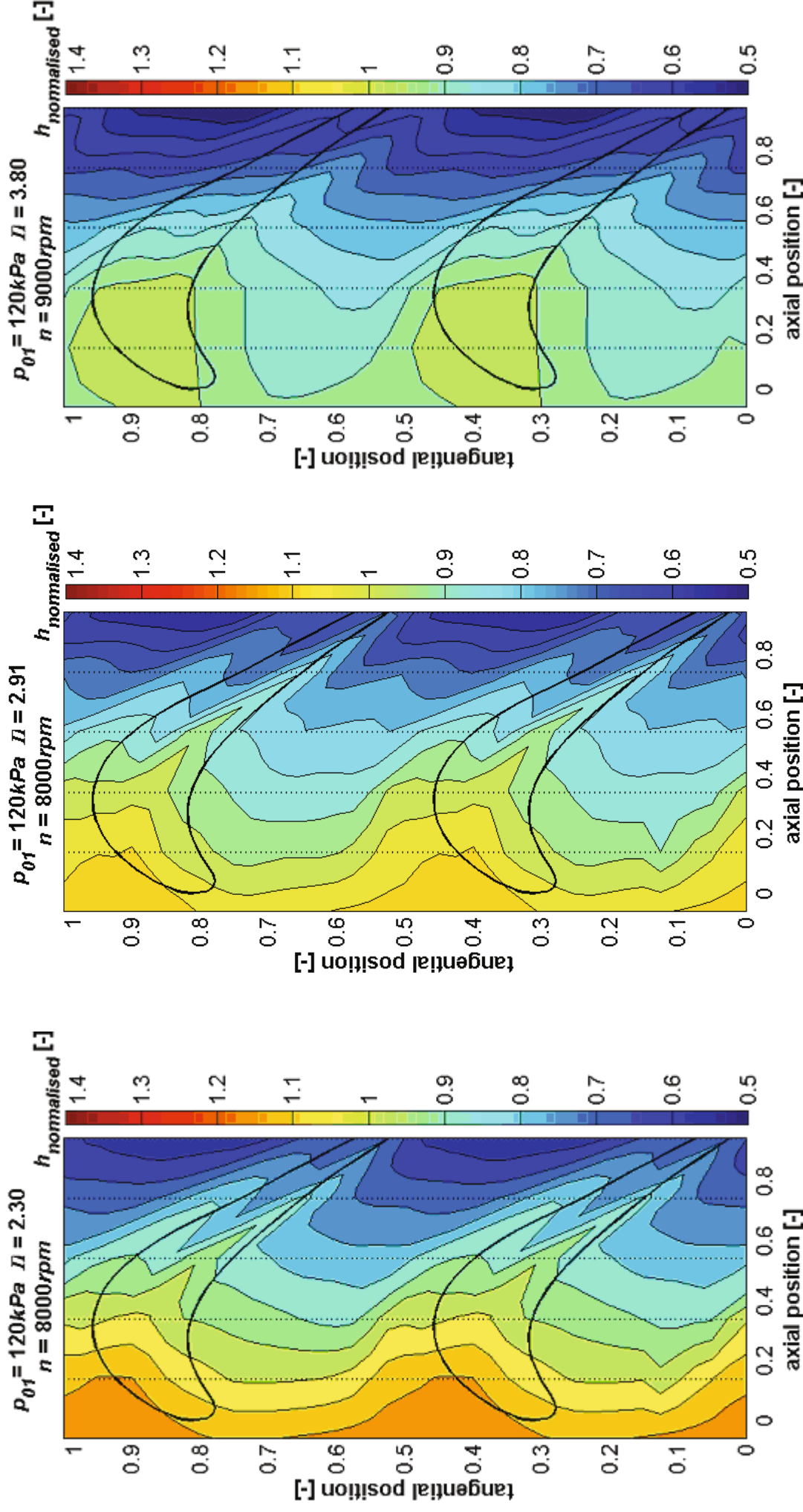
APPENDIX D TIME-RESOLVED STATIC PRESSURE

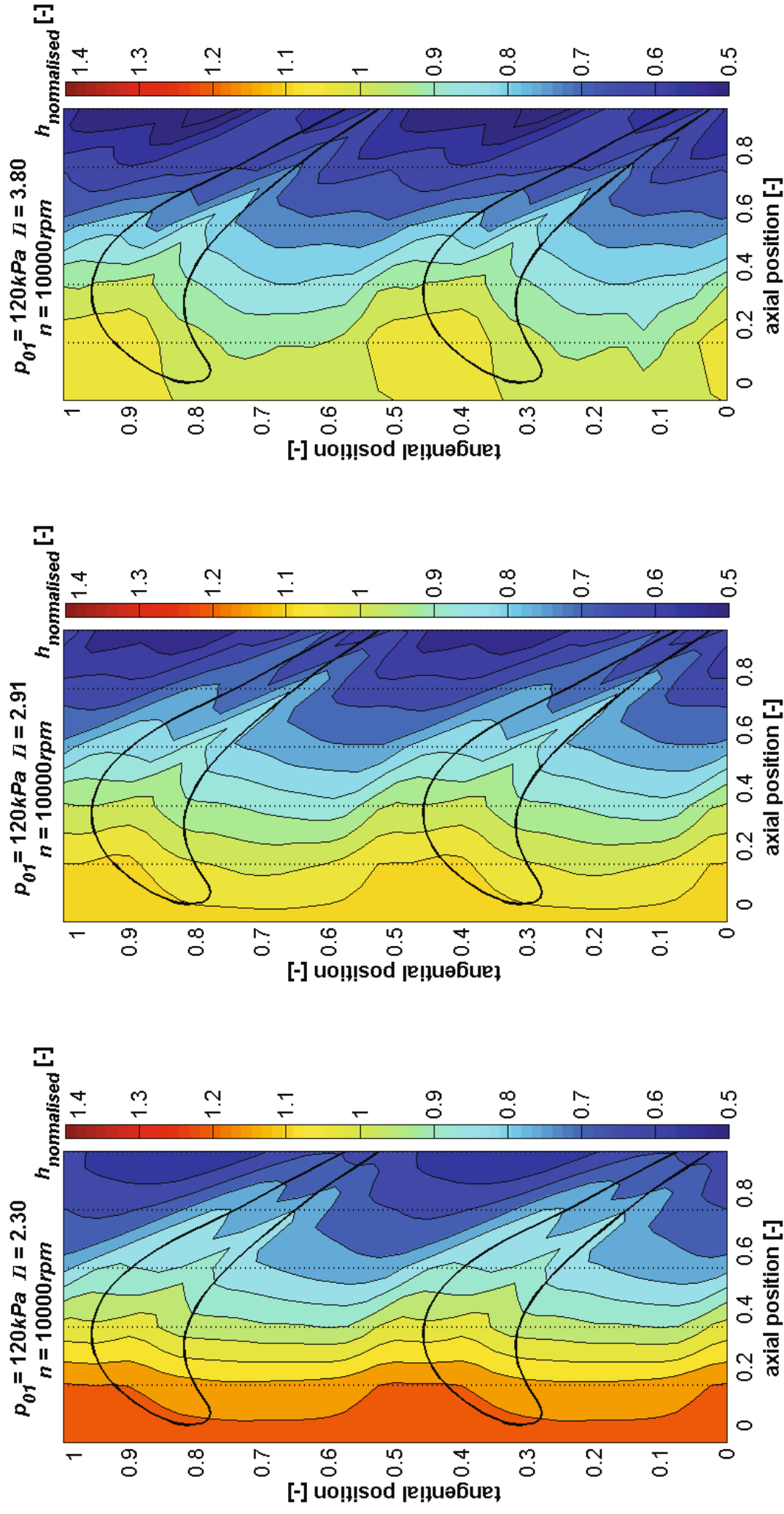






APPENDIX E TIME-RESOLVED HEAT TRANSFER





APPENDIX F CALCULATION OF THE STREAMLINES PATH

The relative total pressure and relative total temperature are defined as:

$$p_{01,rel} = p_1 \cdot \left(1 + \frac{\kappa-1}{2} \cdot M_{rel}^2 \right)^{\frac{\kappa}{\kappa-1}} \quad (1.2)$$

$$T_{01,rel} = T_1 \cdot \left(1 + \frac{\kappa-1}{2} \cdot M_{rel}^2 \right) \quad (1.3)$$

The velocity and density are obtained from the static tubes mounted just upstream the rotor (described in section 4.2.1), these parameters are – assuming no losses - constant in the complete relative reference frame. It is assumed that the losses in the rotor are similar to those measured at the stator and these losses are distributed linear over the rotor.

The relative Mach number as a function of the axial position is obtained from the measured static pressure distribution.

$$M(x)_{rel} = \sqrt{\frac{\kappa-1}{\kappa} \left(\left(\frac{p(x)_{0,rel}}{p(x)} \right)^{\frac{\kappa-1}{\kappa}} - 1 \right)} \quad (1.4)$$

The relative Mach number distribution allows the static temperature, speed of sound and finally the relative velocity to be calculated.

$$T(x) = \frac{T(x)_{0,rel}}{\sqrt{1 + \frac{\kappa-1}{2} M(x)_{rel}^2}} \quad (1.5)$$

$$c(x)_{sound} = \sqrt{\kappa R T(x)} \quad (1.6)$$

$$w(x) = M(x)_{rel} \cdot c(x)_{sound} \quad (1.7)$$

It is assumed that the pitchwise averaged deflection of the relative flow is equal to that of the camber line of the rotor blade. This allows the relative velocity to be divided into an axial and a tangential component.

$$w(x)_{tang} = w(x) \cdot \sin(\beta(x)) \quad (1.8)$$

$$c(x)_{ax} = w(x)_{ax} = w(x)_{rel} \cdot \cos(\beta(x)) \quad (1.9)$$

$$c(x)_{tang} = w(x)_{tang} + u \quad (1.10)$$

APPENDIX G ISENTROPIC FLUID PROPERTIES

Assuming isentropic conditions inside the passage, the density of the fluid at the casing can be expressed as:

$$\rho = \rho_0 \cdot \left(1 + \frac{\kappa - 1}{2} M_{rel, isentropic}^2 \right)^{\frac{\kappa}{\kappa - 1}}, \quad (1.11)$$

of which the total density ρ_0 is assumed to remain constant since no work is done in the relative frame of reference. Analogue the temperature at entrance can be determined:

$$T = \frac{T_0}{1 + \frac{\kappa - 1}{2} M_{rel, isentropic}^2}, \quad (1.12)$$

which is needed for calculating the fluid properties. The conductivity of air as a function of the temperature is obtained by a linear fit through the tabulated data of Bejan (1993).

$$\lambda(T) \approx 0.024 + (T - 273.15) \cdot 7.79 \cdot 10^{-5} \quad [200K \dots 400K] \quad (1.13)$$

The viscosity of air as a function of the temperature is obtained by using the Sutherland formula:

$$\mu(T) = \mu_{suther} \cdot \frac{T_{suther} - C_{suther}}{T - C_{suther}} \cdot \left(\frac{T}{T_{suther}} \right)^{3/2} \quad (1.14)$$

$$\mu_{air}(T) = 1.827 \cdot 10^{-5} \cdot \frac{290.15 - 120}{T - 120} \cdot \left(\frac{T}{290.15} \right)^{3/2}$$

CURRICULUM VITAE

Personal Details

Name:	Bart van Duikeren
Date of birth	
Place of birth	
Nationality	
Family status	

Education

Mechanical Engineering at the University of Twente (NL) and the Vienna University of Technology (AUT)	1996-2004
Diploma at the University of Twente: Master of Science	16.03.2004
Masters Thesis: German Aerospace Center	
Title: Design of Heat Transfer Instrumentation to be Applied at the Wind Tunnel for Rotating Cascades at DLR, Göttingen	

Professional experience

Research assistant at the “Institute of Propulsion Technology” of the German Aerospace Center (DLR) in Göttingen (GER)	2003-2007
--	-----------